THE UNIVERSITY
of ADELAIDE

Energy Systematics and Long Term Performance of the Pierre Auger Observatory's Fluorescence Telescopes

Phong Huy Nguyen

A thesis submitted to the University of Adelaide in fulfilment of the requirements for the degree of Doctor of Philosophy.

School of Physical Sciences
Department of Physics

2018

Abstract

Since the discovery of cosmic rays in the early 20th century, physicists have strived to gain a deeper understanding of the properties behind the universe's most energetic particles. Aiding in this effort has been the development and operation of very large cosmic ray detectors, which have successfully contributed to numerous advancements in the field of cosmic ray astrophysics. The most notable of such detectors is the Pierre Auger Observatory, situated in the Mendoza province of western Argentina, and is the result of an international effort to study cosmic rays of the highest of energies. The Pierre Auger Observatory utilises two well established methods to study enormous particle showers initiated by the interaction of incoming cosmic rays at the top of the Earth's atmosphere. One such method is the detection of faint fluorescence light emitted during the longitudinal evolution of a cosmic ray initiated particle shower, achieved through the specially designed fluorescence detector.

This thesis will investigate the long term performance and stability of the Pierre Auger Observatory's energy scale, with a particular focus on the Observatory's fluorescence detector.

A brief history of the discovery of cosmic rays is presented in Chapter 1, followed by a discussion of the current knowledge of the properties of the cosmic ray flux and possible production mechanisms. Chapter 2 begins with a review of the physics of extensive air showers and shower detection methods, as well as a discussion of several notable cosmic ray experiments, both past and present. This is followed by an extensive discussion of the Pierre Auger Observatory in Chapter 3. Recent notable results and discoveries are highlighted in Chapter 4.

Chapter 5 begins with a discussion of the calibration methods used to monitor the performance of the Observatory's fluorescence detector. This will be followed by an extensive analysis of the long term stability of the Observatory's energy scale. This includes a discussion of notable analyses improvements developed in recent years, and the effect of these improvements on the Observatory's energy scale.

Chapter 6 begins with a discussion of how the night sky background signal is monitored by the Observatory's fluorescence detector. A cross check method is developed to use the night sky background observed

between neighbouring fluorescence telescopes to monitor the stability of their inter-calibration.

In Chapter 7 a cross check method is developed to monitor the long term stability of the fluorescence detector's absolute calibration using stellar photometry. The results are compared with the long term stability of the Observatory's energy scale from Chapter 5.

The results from these studies are summarised in Chapter 8.

Declaration of Originality

I, Phong Huy Nguyen, certify that this work contains no material which has been accepted for the award of any other degree or diploma in my name, in any university or other tertiary institution and, to the best of my knowledge and belief, contains no material previously published or written by another person, except where due reference has been made in the text. In addition, I certify that no part of this work will, in the future, be used in a submission in my name, for any other degree or diploma in any university or other tertiary institution without the prior approval of the University of Adelaide and where applicable, any partner institution responsible for the joint-award of this degree.

I give consent to this copy of my thesis, when deposited in the University Library, being made available for loan and photocopying, subject to the provisions of the Copyright Act 1968.

I also give permission for the digital version of my thesis to be made available on the web, via the University's digital research repository, the Library Search and also through web search engines, unless permission has been granted by the University to restrict access for a period of time

I acknowledge the support I have received for my research through the provision of an Australian Government Research Training Program Scholarship.

Signed: .... Date: ....22 - 02 - 2018.....

Acknowledgements

Firstly I would like to thank my supervisors Bruce Dawson and Jose Bellido. Their eternal patience, wisdom and support have been immeasurable and this would not have been possible without their guidance.

I would like to thank all members, past and present, of the High Energy Astrophysics Group in Adelaide. It has been a pleasure to work with you all and my time as a student has been enjoyable because of your company. In particular I would like to thank Simon, Patrick, James and Alex for providing valuable companionship and banter for the past 8 years.

I would like to thank all members of the Pierre Auger Collaboration for providing me the opportunity to work on such an incredible experiment.

Lastly, I would like to thank my friends and family in particular my parents, Quang and Lan, and my brother, Huy, for their love and continual support of my studies. You taught me the value of hard work and for that I am forever grateful.

Contents

Abstract i

Declaration iii

Acknowledgements iv

1 Cosmic Rays 1
- 1.1 The Cosmic Ray Energy Spectrum . . . 2
- 1.2 Cosmic Ray Acceleration Mechanisms . . . 5
  - 1.2.1 Fermi's Original Theory . . . 5
  - 1.2.2 Diffusive Shock Acceleration . . . 8
- 1.3 Cosmic Ray Sources . . . 10

2 Extensive Air Showers and Cosmic Ray Detection Methods 12
- 2.1 Extensive Air Showers . . . 12
- 2.2 Heitler's Model for Electromagnetic Showers . . . 13
- 2.3 Hadronic Air Showers . . . 15
- 2.4 Detection Methods . . . 17
  - 2.4.1 Ground Arrays . . . 17
  - 2.4.2 Fluorescence Detectors . . . 18
- 2.5 Past and Current Experiments . . . 19
  - 2.5.1 Volcano Ranch . . . 19
  - 2.5.2 Haverah Park . . . 20
  - 2.5.3 Sydney University Giant Air-shower Recorder (SUGAR) . . . 20
  - 2.5.4 Yakutsk . . . 20
  - 2.5.5 Fly's Eye . . . 21
  - 2.5.6 Akeno Giant Air Shower Array (AGASA) . . . 21
  - 2.5.7 HiRes . . . 22
  - 2.5.8 The Telescope Array Experiment (TA) . . . 23

3 The Pierre Auger Observatory **27**
3.1 Surface Detector . . . 27
3.1.1 Station Design . . . 28
3.1.2 Station Calibration . . . 29
3.1.3 Energy Reconstruction . . . 30
3.2 Fluorescence Detector . . . 32
3.2.1 Telescope Design . . . 33
3.2.2 Telescope Calibration . . . 33
3.2.2.1 Absolute Calibration . . . 33
3.2.2.2 Relative Calibration . . . 34
3.2.3 Event Reconstruction . . . 36
3.3 Atmospheric Monitoring . . . 38
3.4 Hybrid Energy Calibration . . . 39
3.5 Auger Enhancements . . . 40
3.5.1 HEAT . . . 40
3.5.2 AMIGA . . . 42
3.5.3 AERA . . . 42
3.5.4 AugerPrime . . . 44

4 Recent Results From Cosmic Ray Experiments **46**
4.1 Energy Spectrum Studies . . . 46
4.2 Mass Composition Studies . . . 49
4.3 Anisotropy Studies . . . 52

5 Monitoring the Energy Scale of the Pierre Auger Observatory **59**
5.1 Calibration Constants . . . 59
5.1.1 Monitor for Camera Performance . . . 62
5.2 Running Cal A Measurements . . . 64
5.3 Calibration Constant Temperature Dependence . . . 66
5.4 Calibration Constant Background Light Dependence . . . 67
5.5 Long Term Stability of the Observatory's Energy Scale . . . 71
5.5.1 Functional Fit to the Long Term Energy Scale . . . 71
5.5.2 Broken Fits to the Energy Scale Ratio . . . 73
5.5.3 Estimating Uncertainties . . . 78
5.6 Improvements to the Aerosol Database . . . 79
5.7 Surface Detector Weather Correction . . . 82
5.7.1 Surface Detector Event Rate . . . 85
5.7.2 Application to the Energy Scale Ratio . . . 88
5.8 Combining Corrections . . . 88
5.8.1 Discussion of Residual Features . . . 90
5.9 Conclusions . . . 92

6 A Cross Check of the Fluorescence Detector Relative Calibration Using the Night Sky Background 94
6.1 The Night Sky Background . . . 94
6.2 Calculating the Night Sky Background Photon Flux . . . 98
6.2.1 Identical Pixel Method . . . 98
6.2.2 K_v Method . . . 100
6.3 Cross Check Method . . . 101
6.4 Results and Discussion . . . 103
6.5 Conclusions . . . 109

7 A Cross Check of the Fluorescence Detector Absolute Calibration Using Stellar Photometry 111
7.1 Choosing a Constant Light Source . . . 112
7.1.1 Identifying Star Signals from FD Night Sky Background Files 114
7.1.2 Functional Form of Star Tracks . . . 117
7.1.3 Characteristics of Star Tracks . . . 119
7.2 Analysis Method . . . 121
7.2.1 Correcting the Rayleigh Atmosphere . . . 121
7.2.2 Correcting Track Modulations . . . 125
7.2.2.1 Simulated Template . . . 125
7.2.2.2 Empirical Template . . . 127
7.2.2.3 Guided Template . . . 127
7.2.3 Fitting Algorithm . . . 129
7.2.4 Spread in the Fitted Absolute Calibration . . . 131
7.3 Analysis of Systematic Errors . . . 134
7.3.1 Broadening of the Point Spread Function . . . 134
7.3.1.1 Direct Measurement of the Point Spread Function . 135
7.3.1.2 Verification of Previously Measured PSF . . . 137
7.3.2 Rayleigh Model Systematic Uncertainties . . . 140
7.3.2.1 Spectrum . . . 141
7.3.2.2 Fluorescence Detector Efficiency . . . 144
7.3.3 Fitting Algorithm . . . 144
7.3.3.1 Angstrom Coefficient . . . 147
7.3.3.2 Choice of Template . . . 148
7.3.4 Systematics Summary . . . 149
7.4 Results and Discussion . . . 150
7.4.1 Sirius . . . 150
7.4.2 Rigel . . . 152
7.4.3 Canopus . . . 153
7.4.4 Comparisons of Star Calibration Measurements . . . 154
7.4.4.1 Sirius and Rigel . . . 154
7.4.4.2 Sirius and Canopus . . . 155
7.5 Comparisons with the Energy Scale Ratio . . . 157

7.5.1 Long Term Drift of the FD Calibration and Energy Scale Ratio 159
7.5.2 Discontinuity in the FD Calibration and Energy Scale Ratio . 162
7.5.2.1 Significant Calibration Events 162
7.5.2.2 Introduction of the Running Calibration 163
7.5.3 UV Filter and Mirror Cleaning Campaigns 164
7.6 Conclusions 167

8 Conclusions and Future Work **169**

References **173**

A Event Quality Cuts **186**

B Photon Flux Uncertainty **187**

C Additional Figures **189**

D Broadening of the Optical Spot **199**

E Rescaling Library Spectra **202**

Chapter 1

Cosmic Rays

Although we may not feel it, we are under constant exposure to various forms of radiation from both natural and man-made sources. Radioactive materials exist naturally in the ground beneath our feet and within materials used to construct buildings. Televisions, smoke alarms and medical machines are examples of man-made radiation emitting sources. In addition to these Earth-based sources, the Earth is under constant bombardment from cosmic rays; mysterious particles originating from regions deep within space [1].

To appreciate the history of cosmic ray physics we must first go back to the late 18^{th} century, when French physicist Charles-Augustin de Coulomb conducted several static electricity inspired experiments using an electroscope; an instrument which took the typical form of a narrow piece of thin gold leaf with one end attached to a small brass strip [2]. As charge is introduced to the instrument, electromagnetic forces act to repel the gold leaf from the brass strip. For an isolated system, it would not be unreasonable to expect the separation of the leaf and strip (in other words, the charge of the system) to remain constant with time. Through his experiments, Coulomb noted that the electroscope would spontaneously (and unexpectedly) discharge overtime, an observation which would later be confirmed independently by Michael Faraday around 1835 [3]. It was concluded that the cause of the electroscope's discharge was the ionisation of the air contained in the instrument, but the cause behind the ionisation still remained a mystery.

Fast forward to the beginning of the 20^{th} century, when British physicist Charles Thomson Rees Wilson revisited the results of spontaneous ionisation in experiments similar to those conducted by Coulomb. Wilson hypothesised that the ionisation may be caused by radioactive rays from outside of the Earth's atmosphere. In an attempt to test his hypothesis, Wilson ventured into a Scottish tunnel with an electroscope with the hopes of measuring a reduction in the radiation levels with respect to those measured above ground. Unfortunately, Wilson's ability to make such measurements was limited by the precision of the measuring apparatus that existed at the time and was consequently unable to confirm his hypothesis [4].

The major breakthrough came in 1912 when Austrian physicist Victor Hess conducted what is considered to be the pioneering experiment in cosmic ray physics. In fact, the experiment was later deemed to be of such significance that Hess would be awarded the 1936 Nobel Prize in physics for his earlier efforts [5]. During a series of heroic high altitude balloon fights, Hess monitored the radiation of his surroundings, making note of any changes during the balloon's ascent. Hess' apparatus indicated a steady decrease in the surrounding environment's ionisation, which Hess would attribute to a weakening of the Earth's radioactivity at those altitudes. This trend would continue until Hess and his balloon reached an altitude of $\sim$ 2000 m at which point Hess began to measure a slow but steady increase in the surrounding ionisation, followed by a rapid increase as he continued to ascend, approaching an altitude of 5000 m. Hess would eventually conclude that the sudden increase in the ionisation must be due to another component of a highly penetrating nature, which entered the Earth's atmosphere from above, emitting radiation in the process. Fittingly, this mysterious source that seemed to originate from beyond the Earth would later be given the label of cosmic rays.

Since their discovery over a century ago, physicists have strived to gain a deeper understanding of cosmic rays - protons and heavier nuclei, with energies far exceeding that of anything created by humans. The astrophysical processes in which cosmic rays are accelerated to such enormous energies, their chemical compositions and where their points of origin are all topics which have formed the foundations of modern day cosmic ray physics.

1.1 The Cosmic Ray Energy Spectrum

The cosmic ray energy spectrum describes the number of particles arriving at Earth as a function of energy (Figure 1.1) and can be described by the following power law.

$$\frac{dN}{dE} \propto E^{-\gamma} \qquad \mathrm{m}^{-2}\mathrm{s}^{-1}\mathrm{sr}^{-1}\mathrm{eV}^{-1} \tag{1.1}$$

where dN is the number flux of particles arriving at the Earth's atmosphere in the energy interval E to $E + dE$ and γ is the spectral index. A single value of $\gamma \sim 3$ describes the spectrum surprisingly well across nearly 10 decades of energy ($\sim 10^{10}$ eV to $\sim 10^{20}$ eV), indicating non-thermal acceleration processes [6]. Upon closer inspection the spectrum appears to deviate from a single power law (indicating a change in the value of γ) which becomes more apparent if the number flux is scaled by some power law of energy, as illustrated in Figure 1.2. These deviations are often referred to as spectral features and begin with a steepening at $\sim 3 \times 10^{15}$ eV (referred to as the *knee*), a further minor steepening at $\sim 10^{17}$ eV (the *second knee*), a distinct flattening at $\sim 3 \times 10^{18}$ eV (the *ankle*), and a suppression of the cosmic ray flux for energies beyond $\sim 6 \times 10^{19}$ eV. Up to the knee γ is ~ 2.7, changing to ~ 3.1 in the region before the ankle before further increasing

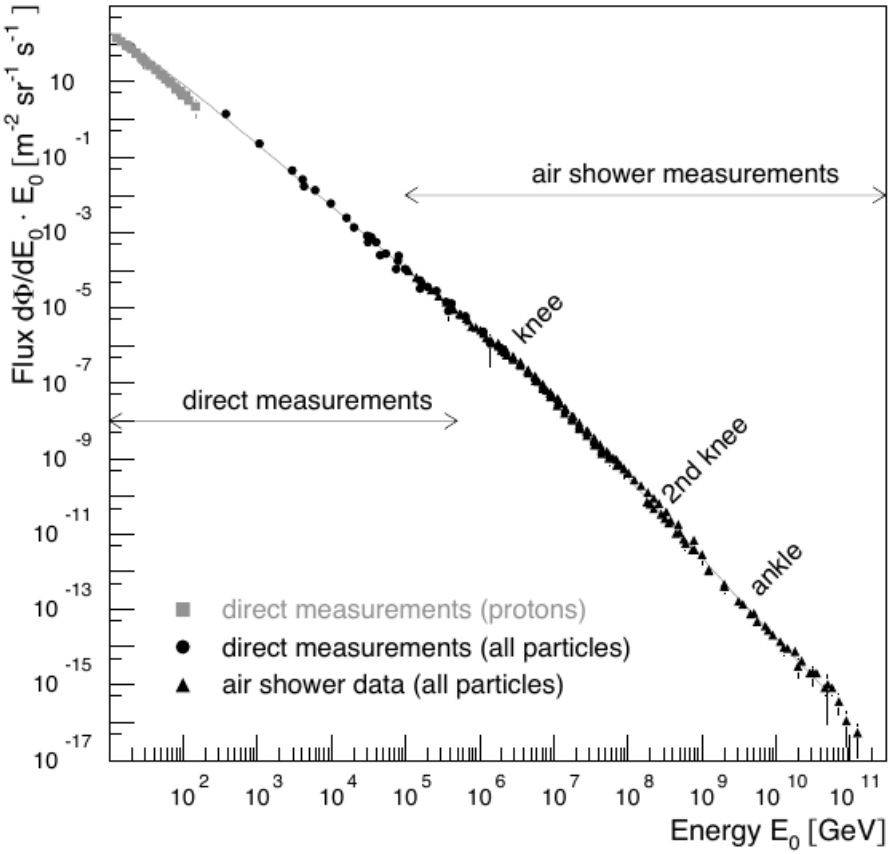

Figure 1.1: The measured cosmic ray spectrum displayed over 10 decades of energy. The figure illustrates the deviation from a single power law over a large energy range. Cosmic rays with energies below $\sim$ 100 MeV can be produced by the Sun. Those with energies up to about $\sim$ 100 TeV are believed to originate from within the galaxy [6].

to $\sim$ 4.1 beyond the flux suppression [6]. The physical reasons driving these spectral features have long been a focal point of cosmic ray studies, and are widely considered to be related to the acceleration mechanisms, origins and propagation of cosmic rays. Recent cosmic ray energy spectrum results are discussed in Section 4.1. In this thesis we will be primarily focussed on cosmic rays with energies around and above the ankle region of the spectrum. These cosmic rays are often referred to as ultra high energy cosmic rays (UHECR).

A suppression of the flux occurs above the ankle at an energy of approximately 6×10^{19} eV. This feature was first predicted by Greisen and later independently by Zatsepin and Kuz'min shortly after the discovery of the cosmic microwave background radiation (CMBR) by Penzian and Wilson in 1965 [8–10]. The Greisen-Zatsepin-Kuz'min (GZK) effect predicts that UHECR will experience energy loss through photo-pion and pair production interactions with CMBR photons. Ultra high energy protons (p) will interact with CMBR photons (γ_{CMBR}) through pair

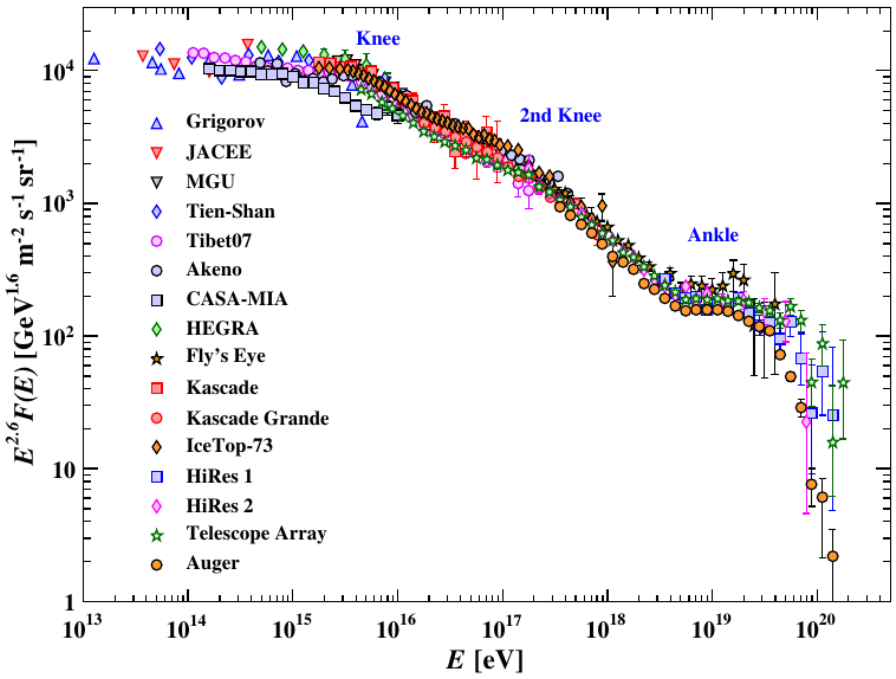

Figure 1.2: Measurements of the cosmic ray energy spectrum through different experiments. The vertical axis is scaled by a factor of $E^{2.6}$ to accentuate the structures of the spectrum. The spectrum shown here begins at an energy of 100 TeV [7].

production

$$p + \gamma_{CMBR} \longrightarrow p + e^+ + e^- \tag{1.2}$$

in which p loses energy through the production of an e^+e^- pair, as well as photo-pion production

$$p + \gamma_{CMBR} \longrightarrow n + \pi^+ \tag{1.3}$$

$$p + \gamma_{CMBR} \longrightarrow p + \pi^0 \tag{1.4}$$

in which a neutral or charged pion are created.

Nuclei larger than protons are expected to experience attenuation through interactions with photons (CMB, infra-red, optical and ultraviolet) through pair production and photodisintegration channels [11, 12]. For a heavy nucleus of mass A, these interactions are summarised in Equations 1.5 (pair production) and 1.6 (photodisintegration).

$$A + \gamma_{CMBR} \longrightarrow A + e^+ + e^- \tag{1.5}$$

$$\begin{aligned} A + \gamma_{CMBR} &\longrightarrow (A-1) + N \\ &\longrightarrow (A-2) + 2N \end{aligned} \tag{1.6}$$

where N is either a proton or neutron.

The shape of the cosmic ray spectrum indicates a flux which rapidly decreases as a function of increasing energy. For energies exceeding $\sim 10^{14}$ eV this presents a significant experimental challenge as cosmic rays at these energies arrive at the Earth's outer atmosphere too infrequently for direct detection through instruments installed on high altitude balloons or satellites. A solution is found in the form of ground-based detectors with extremely large collection areas, designed to detect cosmic rays indirectly through the study of secondary particles produced during a cosmic ray induced particle shower. This concept is discussed in greater detail in Chapter 2.

1.2 Cosmic Ray Acceleration Mechanisms

The mechanisms through which cosmic rays can be accelerated to potentially enormous energies still remains as one of the great mysteries in cosmic ray astrophysics. Numerous creation and acceleration scenarios have been proposed for cosmic rays, which can broadly be categorised as either *top-down* or *bottom-up* models.

Top-down models presume that cosmic rays (in particular those of the highest energies) are the decay products of extremely massive exotic particles (referred to as X particles) that may be remnants from the early universe [13]. Several of these models predict the production of a large fraction of high energy photons as part of the decay process of X particles. Top-down models have recently fallen out of favour as a possible production mechanism following results obtained by the Pierre Auger Observatory (Chapter 3), which have enabled strict upper limits to be placed on the photon fraction across a broad energy range [14, 15].

Bottom-up models are formulated on the acceleration of charged particles from low to high energies within a source region. Currently, the most widely accepted model was proposed by Italian physicist Enrico Fermi, who hypothesised that cosmic rays from within the galaxy gradually gain energy through multiple interactions with moving magnetised plasma. In this Section we will briefly overview Fermi's original theory for cosmic ray acceleration. This will be followed by a discussion of how the original theory was modified to describe the interaction of a cosmic ray across an astrophysical shock, a model commonly referred to as diffusive shock acceleration. The following Section will be largely based on the work described in [16] and the references therein.

1.2.1 Fermi's Original Theory

Fermi's original theory, also referred to as 2^{nd} order Fermi acceleration, is modelled on the interaction of a cosmic ray as it passes through an interstellar medium (ISM) gas cloud during its propagation through the galaxy. In this model, a cosmic ray enters an ISM gas cloud, which itself is moving at some velocity with respect to the motion of the galaxy, scattering off irregularities in the cloud's magnetic

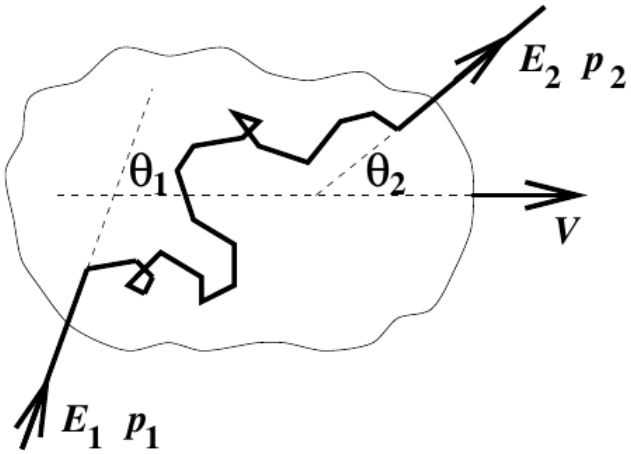

Figure 1.3: Diagram depicting the interaction of a cosmic ray with an ISM cloud travelling at a velocity of v [16].

field before eventually emerging from the cloud having experienced a change in energy and subsequent acceleration.

Consider the scenario depicted in Figure 1.3 in which a cosmic ray of energy E_1 and momentum p_1 enters an ISM cloud moving at velocity v. The cosmic ray enters the cloud in a direction of θ_1 with respect to the cloud's motion and exits at θ_2 with energy E_2 and momentum p_2. In the reference frame of the cloud (from here onwards denoted by the primed superscript) there is no change in energy as scattering interactions are collisionless and therefore, the scattering between the cosmic ray and the more massive ISM cloud is considered to be elastic. Additionally, the direction at which the cosmic ray emerges is also randomised due to scattering interactions within the cloud. With the application of Lorentz transformations between the laboratory reference frame and that of the ISM cloud, the fractional change in the laboratory energy, $(E_2 - E_1)/E_1$, can be estimated. Transforming from the laboratory frame to the cloud frame gives:

$$E_1^{'} = \gamma_{cloud} E_1 (1 - \beta_{cloud} \cos\theta_1) \tag{1.7}$$

where $\beta_{cloud} = v/c$ and $\gamma_{cloud} = 1/\sqrt{1 - \beta_{cloud}^2}$. The energy at which the cosmic ray leaves the cloud (in the cloud's reference frame) can be written as:

$$E_2^{'} = E_1^{'} \tag{1.8}$$

where $E_1^{'}$ is given in Equation 1.7. Transforming back to the laboratory frame gives:

$$E_2 = \gamma_{cloud} E_2^{'} (1 + \beta_{cloud} \cos\theta_2^{'}) \tag{1.9}$$

combining Equations 1.8 and 1.9

$$E_2 = \gamma_{cloud}^2 E_1 (1 - \beta_{cloud} \cos\theta_1)(1 + \beta_{cloud} \cos\theta_2^{'}) \tag{1.10}$$

The fractional change in energy can then be written as

$$\frac{\Delta E}{E} = \frac{(E_2 - E_1)}{E_1} = \frac{1 - \beta_{cloud}\cos\theta_1 + \beta_{cloud}\cos\theta_2^{'} - \beta_{cloud}^2 \cos\theta_1 \cos\theta_2^{'}}{1 - \beta_{cloud}^2} - 1 \tag{1.11}$$

To find the average fractional change in energy, $\langle \Delta E \rangle / E$, we must first determine appropriate average values for $\cos\theta_1$ and $\cos\theta_2^{'}$ (denoted by $\langle \cos\theta_1 \rangle$ and $\langle \cos\theta_2^{'} \rangle$, respectively). Within the ISM cloud, the cosmic ray may undergo several scattering interactions with magnetised irregularities and so its direction is randomised. Therefore,

$$\langle \cos\theta_2^{'} \rangle = 0 \tag{1.12}$$

For the average value of $\langle \cos\theta_1 \rangle$, we must consider the rate at which cosmic rays enter the cloud at different angles. For a particle moving at velocity v_p, the probability per unit solid angle of colliding with a cloud of velocity v at angle θ_1 is proportional to $(v_p - v\cos\theta_1)$. For cosmic rays, which are moving at ultra-relativistic velocities, $v_p \rightarrow c$, the collisional probability distribution can be written as

$$\frac{dP}{d\Omega_1} \propto (1 - \beta_{cloud}\cos\theta_1) \tag{1.13}$$

recalling that $\beta_{cloud} = v/c$. Using Equation 1.13, we can estimate the value of $\langle \cos\theta_1 \rangle$

$$\langle \cos\theta_1 \rangle = \int \cos\theta_1 \frac{dP}{d\Omega_1} d\Omega_1 \; / \int \frac{dP}{d\Omega_1} d\Omega_1 = \frac{-\beta_{cloud}}{3} \tag{1.14}$$

Substituting Equations 1.12 and 1.14 into Equation 1.11 we find that the average fractional change in the energy of the cosmic ray can be expressed as

$$\frac{\langle \Delta E \rangle}{E} = \frac{1 + \beta_{cloud}^2/3}{1 - \beta_{cloud}^2} - 1 \simeq \frac{4}{3}\beta_{cloud}^2 \tag{1.15}$$

From Equation 1.15 it can be seen that the average fractional energy gain is positive and second order in β_{cloud}. However, since $\beta_{cloud} << 1$, the average energy gain is very small because the number of (approaching) collisions resulting in an energy gain are almost balanced by (following) collisions which result in an energy loss. Due to its inefficiency in accelerating cosmic rays to extremely high energies, Fermi's original theory was later modified to describe acceleration at the shocks of supernovae, through a process referred to as diffusive shock acceleration.

1.2.2 Diffusive Shock Acceleration

In an attempt to find a more efficient theory for cosmic ray acceleration to extremely high energies, Fermi's original theory was later modified to describe the acceleration of cosmic rays across astrophysical shocks. For the following example, the acceleration of a cosmic ray across a supernova shock will be discussed but what follows is generally applicable to other astrophysical shocks (such as those associated with the jets of active galactic nuclei and gamma ray bursts). During a supernova explosion, several solar masses worth of material are ejected, moving in an outward direction at speeds of $V_p \sim 10^4\,\mathrm{km\,s^{-1}}$ [16]. The velocity at which this material is ejected is far greater than that of the speed of sound in the surrounding ISM ($\sim 10\,\mathrm{km\,s^{-1}}$), resulting in the formation of a shock which propagates radially outwards at a velocity V_s. An important feature of this model is the concentration of the ISM and its associated magnetic field in the regions surrounding the shock front.

Consider the scenario shown in Figure 1.4 which depicts the interaction of a cosmic ray of energy E_1 and velocity V_p with a shock front. The modified theory begins with a cosmic ray bouncing back and forth across the supernova shock, experiencing an energy change upon interacting with the surrounding magnetic irregularities on either side. Similar to Fermi's original theory, the average fractional energy change, $\Delta E/E$, can be estimated by calculating average values for the interaction angles $\langle \cos\theta_1 \rangle$ and $\langle \cos\theta_2' \rangle$. By considering the rate at which cosmic rays cross the shock from both directions, it can be shown that for isotropic cosmic rays,

$$\langle \cos\theta_1 \rangle = -\frac{2}{3} \tag{1.16}$$

and

$$\langle \cos\theta_2' \rangle = \frac{2}{3} \tag{1.17}$$

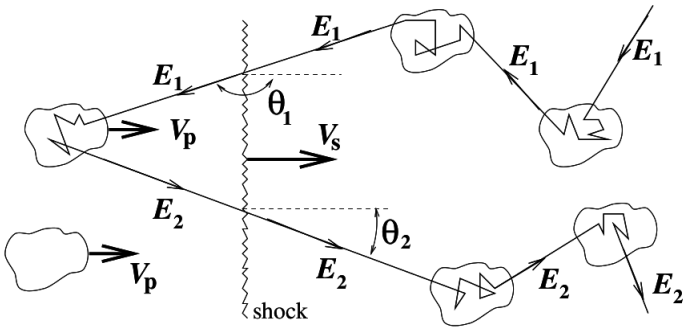

Figure 1.4: Figure demonstrating a particle with velocity V_p interacting with a shock front of velocity V_s [16].

It can be shown that the average fractional energy change can be expressed as

$$\langle \frac{\Delta E}{E} \rangle = \frac{1 - \beta_p \langle \cos\theta_1 \rangle + \beta_p \langle \cos\theta_2^{'} \rangle - \beta_p^2 \langle \cos\theta_1 \rangle \langle \cos\theta_2^{'} \rangle}{1 - \beta_p^2} - 1 \tag{1.18}$$

where $\beta_p = V_p/c$. For $\beta_p << 1$, we find that

$$\frac{\langle \Delta E \rangle}{E} \simeq \frac{4}{3}\beta_p = \frac{4}{3}\frac{V_p}{c} = \frac{4}{3}\left(\frac{R-1}{R}\right)\frac{V_s}{c} \tag{1.19}$$

where R is the compression ratio which, based on shock hydrodynamic theory, has a typical value of 4 for the case of strong shocks [16]. Equation 1.19 can be further simplified to

$$\frac{\langle \Delta E \rangle}{E} \simeq \frac{V_s}{c} = \beta_s \tag{1.20}$$

which is first order in β_s. Owing to the linearity of Equation 1.20, diffusive shock acceleration is often referred to as 1^{st} order Fermi acceleration. In contrast to 2^{nd} order Fermi acceleration, collisions in the modified theory are all 'head-on' collisions, in which magnetic irregularities are always approaching. As each collision results in a gain in energy, diffusive shock acceleration is therefore considered to be a more efficient cosmic ray acceleration mechanism compared to Fermi's original theory. By considering the probability of a cosmic ray encountering the shock multiple times, it can be shown that for strong shocks (where $R = 4$) the differential energy spectrum produced from this model can be described with an inverse power law with an index of $\gamma \sim 2$, slightly lower than that measured through cosmic ray experiments.

By taking into consideration the size of an accelerating region, an expression predicting the maximum energy attainable through diffusive shock acceleration can be derived. As the Larmor radius (r_L, defined in Section 4.3) approaches the accelerator's size, it becomes increasingly difficult to contain the cosmic ray within the accelerating region. From this basic dimensional argument, the maximum energy (E_{max}) to which a cosmic ray can be accelerated is given by

$$E_{max} \leq \gamma ZeBR \tag{1.21}$$

where γ is the Lorentz factor of the shock matter, Ze is the charge of the particle, B is the strength of the magnetic field and R is the linear dimension of the accelerating region. It should be noted that Equation 1.21 does not include an efficiency factor. The criterion set by Equation 1.21 can be depicted through the Hillas diagram (Figure 1.5) which illustrates the requirements for acceleration to energies beyond 10^{20} eV. It is evident that very few astrophysical regions are capable of accelerating particles to such enormous energies, as this requires either highly condensed objects with powerful magnetic fields or enormously extended objects.

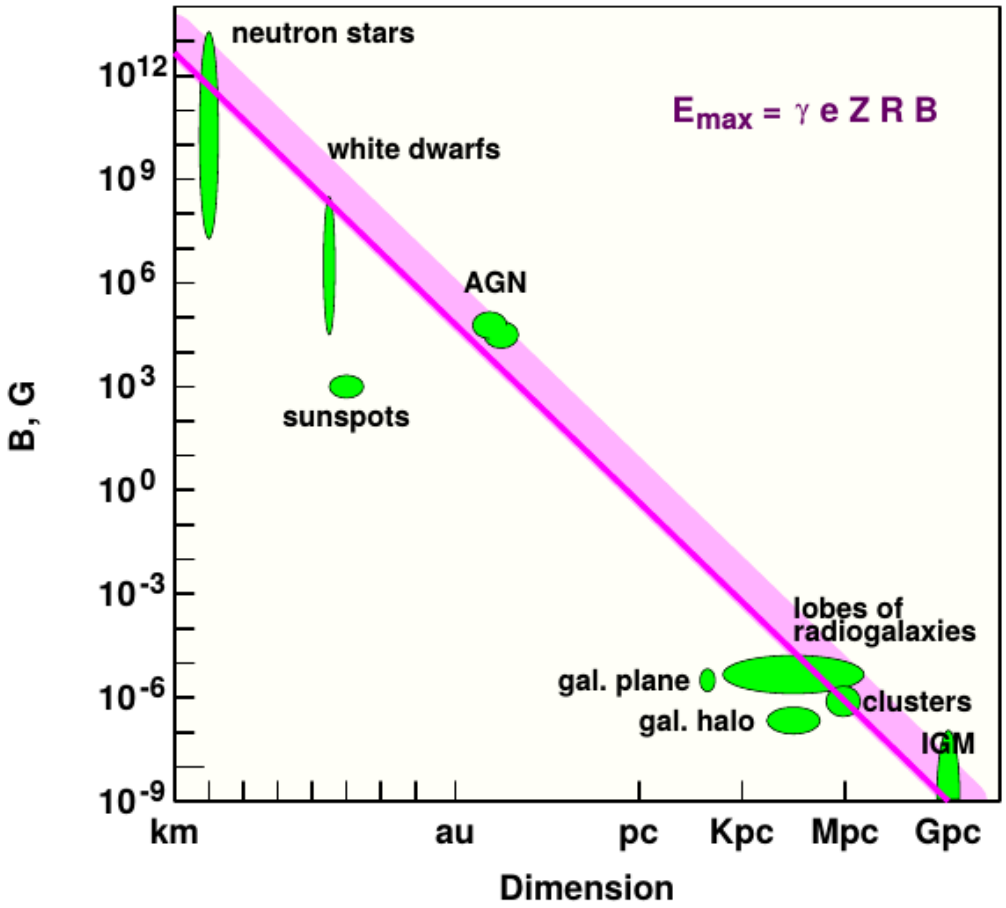

Figure 1.5: The Hillas diagram (after Hillas [17]) illustrates possible accelerating regions based on their magnetic field strengths (vertical axis) and size (horizontal axis). The lower edge of the shaded pink area represents the minimum requirements for the acceleration of iron nuclei to energies in excess of 10^{20} eV. The upper edge is for proton nuclei [18].

1.3 Cosmic Ray Sources

Although individual astrophysical sources of UHECR have yet to be identified, several acceleration models have been proposed for specific astrophysical objects. A brief description of several of these objects will be given in this Section. A more in depth discussion can be found in [19].

- **Active Galactic Nuclei (AGN):** are the brightest sources in the Universe and stand as the most likely candidates to have magnetic fields of sufficient strength and size to accelerate particles to ultra high energies. Particle acceleration is believed to occur at the jets of AGN, highly relativistic particles emanating perpendicular to the plane of the accretion disk, where concentrated and turbulent fields provide strong shocks ideal for acceleration [20].

- **Gamma Ray Bursts (GRBs):** are extremely energetic outbursts of gamma rays in distant galaxies and are considered to be the most luminous electromagnetic events to occur. Different models have been proposed [21, 22], each based on the acceleration of particles at the sites of the GRB shocks through 1^{st} order Fermi acceleration.

- **Galaxy Clusters:** the accretion shocks which are predicted to form in large galaxy clusters could provide a suitable environment for the production of UHECR. These shocks can have scale-lengths in the order of 500 kpc with magnetic fields of several μG, potentially accelerating cosmic rays up to energies of $\sim 10^{20}$ eV. Lower energy cosmic rays would be confined by the magnetic fields, with only the highest energy particles having the ability to escape [23].

- **Starburst Galaxies:** are galaxies exhibiting large-scale star formation, typically in regions located towards the galactic centre. The increased rate of activity (from supernova explosions and massive stellar winds) associated with these regions can generate galactic-scale superwinds leading to the formation of cavities of hot gas, whose cooling time is much greater than the expansion time scale. Winds of sufficient power can expel the ISM of the galaxy, generating a strong shock front upon contact with the surrounding cool ISM. The shock front reach speeds of several thousands of kilometres per second, creating an environment for the acceleration of nuclei up to ultra-high energies [24]. Prime candidates for this scenario include M82 and NGC 253.

- **Giant Radio Galaxies:** extended, luminous radio sources with hotspots in their lobes have been proposed as a point of origin for cosmic rays with energies above 1 EeV [25]. The hotspots are localised regions of intense synchrotron emission, believed to be the endpoints of powerful jets and form an attractive region for the acceleration of particles through diffusive shock acceleration. Potential candidates include Centaurus A and M87.

- **Pulsars:** are high magnetised rotating neutron stars which can have surface magnetic fields in the $10^{12} - 10^{14}$ G range, which can potentially accelerate iron nuclei to energies exceeding 10^{20} eV. In contrast to diffusive shock acceleration, which is a stochastic process, the acceleration process for a pulsar is magnetohydrodynamic. Interestingly, the cosmic ray energy spectrum predicted through such a scenario is proportional to $1/E$ [26].

Chapter 2

Extensive Air Showers and Cosmic Ray Detection Methods

The particle flux for cosmic rays of energy below 10^{14} eV is sufficiently large such that direct detection methods are a viable option. The design of modern detection instruments has changed significantly since early experiments and now typically consist of satellite-borne multi-layered particle detectors. Such detectors have the ability to measure the necessary parameters required for the successful reconstruction of particle energy, mass and charge [27].

At energies above 10^{14} eV the rapidly decreasing arrival rate of cosmic rays renders the direct detection of cosmic rays an impractical method. This is especially true for ultra high energy cosmic rays (UHECR), with only a handful arriving per year, per km^2 over the entire sky. Fortunately, cosmic rays at such energies initiate particle cascades of sufficiently large sizes (often referred to as an extensive air shower), providing a large footprint of observable secondary particles extending over many square kilometres at ground level. For example, an extensive air shower (EAS) initiated by a cosmic ray of energy 10^{19} eV can produce a ground level footprint extending over 25 km^2 [28].

In this Chapter we will introduce the concept of an EAS and simple models used to explain their properties, followed by a discussion of the methods used to detect them. Finally, we will briefly overview several notable past and current cosmic ray experiments.

2.1 Extensive Air Showers

An EAS is a complicated combination of electromagnetic and hadronic particle showers, or cascades, initiated at the top of the Earth's atmosphere following the collision of an incoming cosmic ray with an atmospheric air nucleus. The discovery of EAS can be attributed to French physicist Pierre Victor Auger who, in the 1930s, conducted several experiments in which he noted timing coincidences between several separated detectors in response to arriving cosmic ray particles.

Auger eventually concluded that these observations were in fact due to secondary particles originating from a common source [29].

The collision between a cosmic ray and an atmospheric air nucleus (usually an oxygen or nitrogen nucleus) will typically occur a few tens of kilometres above the surface of the Earth. Particles generated in this initial reaction will go on to interact with other nuclei, resulting in a large cascade of secondary particles that propagate towards the Earth's surface. The leading edge of the cascade, referred to as the shower front, is a thin disk-like structure travelling at close to the speed of light that increases in lateral width following particle interactions and Coulomb scattering. The size of the shower, which is characterised by the number of generated particles, increases rapidly following the initial interaction, eventually reaching some maximum number before decreasing following energy losses to the surrounding environment.

An important quantity, the atmospheric depth or slant depth (X), that is frequently used in the discussion of cosmic ray detection experiments will be defined here. X refers to the amount of matter between some altitude of interest (h) and the top of the atmosphere along the axis of shower propagation. X is expressed by the following integral

$$X = \int_h^\infty \rho(l) dl \tag{2.1}$$

where ρ is the density of the atmosphere. X is most commonly expressed in units of $\mathrm{g\,cm^{-2}}$.

An EAS has three components:

- **Electromagnetic component** - consists of electrons, positrons and γ-rays produced in a series of electromagnetic particle interactions in the atmosphere. The electromagnetic component is the largest of the three EAS components.
- **Hadronic component** - consists of protons, neutrons, charged pions and kaons.
- **Muonic component** - consists of muons and neutrinos produced in the decay of charged pions and kaons.

2.2 Heitler's Model for Electromagnetic Showers

A simple toy model for describing electromagnetic showers was proposed by Heitler and serves as a useful tool for understanding the basic concepts and properties of complex particle showers [30]. The model assumes that the energy of an incident particle is divided equally among secondary particles and that interactions in the atmosphere only occur once a fixed atmospheric depth (denoted as d,

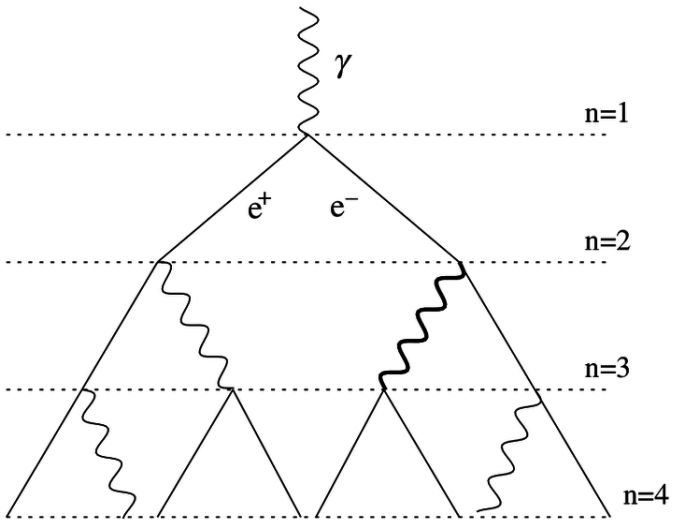

Figure 2.1: Schematic view of an electromagnetic cascade. Note that this image is not drawn to scale [31].

where $d = \lambda_r \ln 2$ where λ_r is the radiation length in the medium) has been traversed. In this model, a γ-ray of energy E_0 interacts with an atmospheric nucleus (N) resulting in the pair-production of an electron-positron pair

$$\gamma + N \rightarrow N + e^- + e^+ \tag{2.2}$$

The electron and positron produced in such an interaction each carry away half the energy of the incident γ-ray, $E_0/2$. After traversing a further distance equal to d, these particles lose energy through Bremsstrahlung radiation, with the new particles inheriting half the energy of the interacting particle

$$e^{\pm} + N \rightarrow N + e^{\pm} + \gamma \tag{2.3}$$

and these γ-rays go on to produce further electron-positron pairs. The production of secondary particles ceases when the energies of the particles drop below a critical energy (E_c), at which point the average energy loss due to collisional processes exceeds radiative losses. As a reference $E_c = 85\,\text{MeV}$ for air [31]. A basic schematic of the model is illustrated in Figure 2.1. A particle shower that develops in this way will contain 2^n particles after traversing an atmospheric depth of $d \times n$, with the energy of each shower particle given by

$$E(n) = \frac{E_0}{2^n} \tag{2.4}$$

The shower reaches its maximum size (in terms of particle number) when individual particles have an energy equal to E_c. For a shower initiated by a particle of energy E_0 the maximum number of shower particles N_{max} is given by

$$N_{max} = \frac{E_0}{E_c} \tag{2.5}$$

The penetration depth at which an electromagnetic shower reaches its maximum size, before the energy of individual particles drops below the threshold energy required for further production of new particles, is denoted by X_{max} and is given by

$$X^{\gamma}_{max} = \lambda_r \ln\left(\frac{E_0}{E_c}\right) \tag{2.6}$$

where γ indicates that this is the case for an electromagnetic shower. From Equation 2.6 the elongation rate, which defines the change in the depth of shower maximum per decade of energy, for the case of an electromagnetic shower can be can be derived to be $\Lambda^{\gamma} = 85\mathrm{g\,cm^{-2}}$ per decade [31].

Despite the simplistic nature of the model, it correctly describes two basic features of electromagnetic shower development which have been confirmed by detailed simulations and experimental data. In particular the model predicts that $N_{max} \propto E_0$ and $X_{max} \propto \ln(E_0)$ [31].

2.3 Hadronic Air Showers

The Heitler model (Section 2.2) can be extended to the case of an air shower initiated by the interaction of a hadron (a proton or heavier nuclei) with an atmospheric nucleus [31]. The atmosphere in this case is modelled as several layers of equal thickness $\lambda_I \times \ln 2$ where λ_I is the interaction length of strongly interacting particles. For energies below 10^5 GeV, the interaction lengths for a hadron and a pion are approximately 85 and $120\,\mathrm{g\,cm^{-2}}$, respectively [27, 31].

The first interaction takes place in the upper atmosphere and involves the collision of the primary hadron (p) and an atmospheric nucleus (N) (Equation 2.7). This interaction produces charged and neutral pions at a ratio of approximately 2:1 [27].

$$p + N \rightarrow p^{'} + N^{'} + \pi^0, \pi^+, \pi^- + ... \tag{2.7}$$

The primary hadron in this case will transfer approximately half of its energy to the secondary mesons, with the remaining energy being retained by the secondary hadron ($p^{'}$). The secondary hadron will then interact with another atmospheric nucleus, after traversing a further distance equal to one interaction length, to create another generation of shower particles. Neutral pions (π^0) have an extremely short half-life and will decay almost immediately into a pair of photons

$$\pi^0 \rightarrow \gamma + \gamma \tag{2.8}$$

These photons will go on to generate their own electromagnetic showers (Section 2.2), feeding the electromagnetic component of the EAS. This component can be thought of as the superposition of several electromagnetic showers initiated at different heights in the atmosphere.

Charged pions ($\pi^{\pm}$) have a much longer half-life compared to their neutral counterparts and can either decay or interact, with the two processes competing

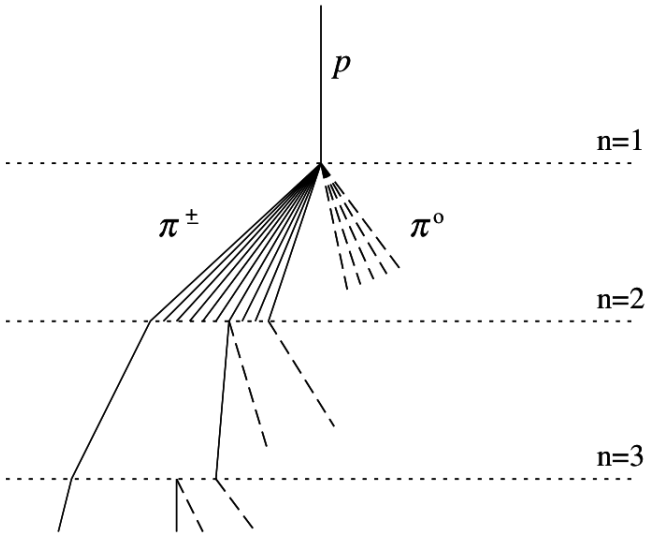

Figure 2.2: Schematic view of an air shower initiated by a hadron. Not all pion lines are drawn after the second interaction. The angles drawn here have been exaggerated and are not drawn to scale [31].

against each other during the development of an EAS. Charged pions of higher energy are more time dilated (giving them a longer lifetime) and are more likely to interact in the atmosphere, producing more charged and neutral pions. Lower energy charged pions will decay via the weak interaction to produce muons and neutrinos, forming the muonic shower component

$$\pi^- \rightarrow \mu^- + \overline{\nu}_\mu \tag{2.9}$$

$$\pi^+ \rightarrow \mu^+ + \nu_\mu \tag{2.10}$$

This process continues until the energy of the charged pions drops below a critical energy (E_c^π), at which point charged pions will almost exclusively decay into the muonic component. The hadronic shower can be thought of as a dense hadronic shower core surrounded by overlapping electromagnetic sub-showers produced through π^0 decays. These two components are accompanied by a muonic component generated from $\pi^\pm$ decays [27]. Figure 2.2 illustrates a basic schematic of a hadron initiated air shower.

This model can be used to determine the depth of shower maximum, X_{max}. Due to the complex evolution of the shower's electromagnetic component through continuous π^0 decays, it is simpler to consider only the first generation of electromagnetic showers to form an estimation of X_{max}. The depth of shower maximum for a proton (of primary energy E_0 and interaction length λ_I) initiated shower can be expressed as

$$X_{max}^p = X_0 + \lambda_r \ln\left(\frac{E_0}{3N_{ch}E_c^e}\right) \tag{2.11}$$

where X_0 is the atmospheric depth of the first interaction, λ_r is the radiation length of the medium and N_{ch} defines the multiplicity of charged particles produced in hadron interactions[1].

Equation 2.11 can be compared to the equivalent expression for an electromagnetic shower (Equation 2.6) and simplified to

$$X^p_{max} = X^\gamma_{max} + X_0 - \lambda_r \ln(3N_{ch}) \tag{2.12}$$

from which the elongation rate for a pure proton shower can be estimated to be $\Lambda^p \approx 58\,\mathrm{g\,cm^{-2}}$ per decade, a result compatible with sophisticated shower simulations [31, 32].

2.4 Detection Methods

The indirect detection of cosmic rays is possible through the study of various EAS observables at ground level, from which some characteristics of the particle that initiated the shower can be inferred. This section will discuss two well established and widely used EAS detection methods - ground arrays and atmospheric fluorescence telescopes.

2.4.1 Ground Arrays

Ground arrays employ a network of regularly spaced particle detectors designed to sample secondary EAS particles at ground level. It is not uncommon for such arrays to cover significantly large areas (several $\mathrm{km^2}$) to allow for the collection of a sufficient number of particles over a reasonable period of time. Air shower candidates are identified through timing coincidences between neighbouring detectors. Information provided by the density of signals measured at ground level and the relative time delay between different detectors is used to infer the energy and arrival direction of the primary cosmic ray [33]. There are two types of ground array detectors in common use: water-Cherenkov detectors and scintillation detectors.

Water-Cherenkov detectors consist of tanks filled with highly purified water, providing a dielectric medium for charged particles, much like the relativistic secondary particles produced in an EAS, to pass through. The interaction of the electric field of a charged particle, moving at speed v, with water molecules will induce an electric field within the medium. For $v << c$, the induced electric field is symmetric. As v approaches c, a net dipole is established, and destructively interfering electromagnetic pulses are emitted along the track of the particle. If $v > c/n$, where c/n is the local speed of light within a medium with refractive index n, the emitted electromagnetic pulses can constructively interfere, leading to the emission of Cherenkov radiation. These scenarios are illustrated in Figure 2.3.

[1] In the model presented by Matthews, $N_{ch} = 10$ [31].

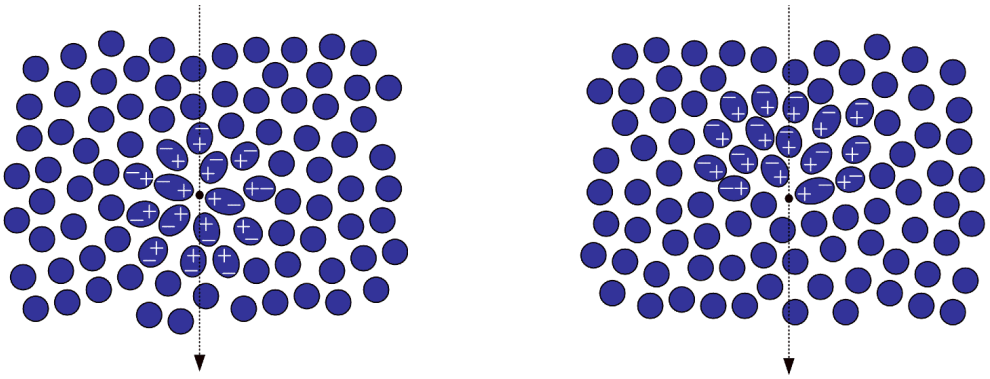

Figure 2.3: Illustration of the polarisation caused by a charged particle moving through a dielectric medium. Left: Charged particle moving at $v << c$, inducing a symmetric electric field. Right: Charged particle moving at $v > c/n$. In this scenario, emitted electromagnetic pulses can constructively interfere resulting in the emission of Cherenkov radiation.

The quick flash of bluish Cherenkov light is observed by sensitive photomultiplier tubes and converted to an electrical pulse through on-board electronics.

Scintillation detectors use a scintillating material to convert a fraction of ionisation losses, from the passage of charged particles, into visible light. The emitted light pulses can be observed by nearby photomultiplier tubes and converted to an electrical pulse.

Ground arrays are advantageous in the sense that they have a 100% duty cycle, enabling the collection of large data sets. However, such detectors do not have the ability to observe the direct development of a shower but instead must infer such information from reconstruction parameters and interaction models.

2.4.2 Fluorescence Detectors

While ground arrays sample EAS particles over a large area at a fixed altitude, the fluorescence technique employs specially designed detectors to measure the nitrogen emission induced by EAS as they evolve through the atmosphere. Charged particles created in an EAS will excite atmospheric nitrogen molecules which, upon de-excitation, will isotropically emit fluorescence light with wavelengths in the $\sim 300 - 430\,\text{nm}$ range. The nitrogen fluorescence spectrum is illustrated in Figure 2.4. The number of fluorescence photons (fluorescence yield) produced for a given air shower is proportional to the energy deposited in the atmosphere as a result of ionisation losses by charged particles [34]. In that sense, the observed fluorescence light profile can be used to estimate the calorimetric energy of an EAS and hence the energy of the primary particle. Due to practical requirements fluorescence detectors require cloudless, moonless nights for effective operation resulting in a duty cycle less than that of ground arrays ($\sim$ 15%). Despite the

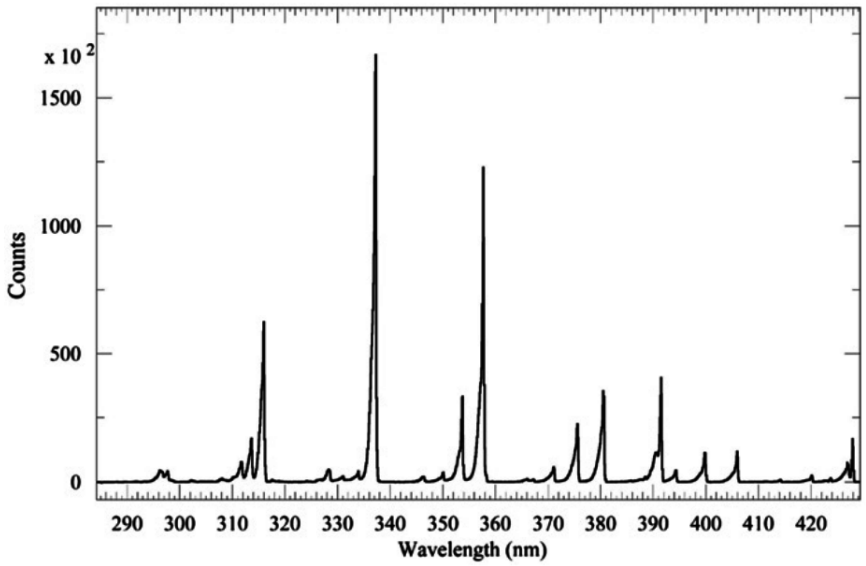

Figure 2.4: Fluorescence spectrum in dry air at 800 hPa and 293 K [34].

smaller duty cycle, fluorescence detectors offer the ability to study the longitudinal development of an EAS through a range of shower ages, providing unique benefits for various cosmic ray studies.

Standard fluorescence detectors image atmospheric nitrogen emission using a camera constructed from several pixels, each viewing a separate region of the sky. In practice these pixels are typically PMTs arranged on a grid, upon which fluorescence light emitted from an EAS is focussed towards. Fluorescence light from an EAS will appear as a small spot of light on the camera, which moves across the camera face in conjunction with the evolution of the shower. A description of how fluorescence detectors reconstruct an EAS is provided in Section 3.2.3.

2.5 Past and Current Experiments

Since Hess' discovery of cosmic rays in the early 20$^{\text{th}}$ century, numerous efforts have been made to construct detectors with the purpose of studying the cosmic ray flux at Earth. This section will briefly discuss several notable experiments, including surface, fluorescence and hybrid type detectors.

2.5.1 Volcano Ranch

The first giant shower array detector was constructed at Volcano Ranch, near Albuquerque, New Mexico, by a group led by Bruno Rossi from the Massachusetts Institute of Technology [1, 35]. The array operated between 1959 and 1978 and consisted of 19 3.3 m^2 plastic scintillation detectors initially arranged on a triangular grid with spacing 442 m (covering an area of 2 km^2) which was later extended to 884 m (8 km^2) [36, 37].

Being the first of its kind, the data recorded by Volcano Ranch yielded some pioneering results in the field of cosmic ray physics, including the earliest suggestion of a flattening of the cosmic ray spectrum above 10^{18} eV - possible evidence for the existence of the ankle [38]. Volcano Ranch data was also used in early anisotropy studies, with the results suggesting that UHECR did not appear to arrive from a preferred region of the sky. The most energetic event recorded was initially assigned an energy of 10^{20} eV (later revised to 1.4×10^{20} eV) and to this day, remains as one of the highest energy events ever detected [39].

2.5.2 Haverah Park

Following the efforts of the Volcano Ranch experiment was the construction of the Haverah Park array, near Leeds in northern England. Operating from 1967 to 1987, the array consisted of several water-Cherenkov detectors deployed over an area of 12 km^2. Land restrictions prevented the construction of a uniformly spaced array, with the adopted configuration being a central four detector array with 500 m spacing complemented by 6 sub arrays with detector spacings of 50 m and 150 m located 2 km from the centre [40].

The successful long term operation of the Haverah Park array demonstrated the merits of water-Cherenkov detectors (as opposed to scintillation detectors), a significant achievement as the Pierre Auger Observatory would later adopt similar technology for its ground array. In fact, the quality of the water used in the experiment was still suitable for human consumption, even after 20 years of exposure to billions of shower particles and surrounding environment [1].

2.5.3 Sydney University Giant Air-shower Recorder (SUGAR)

The Sydney University Giant Air-shower Recorder (SUGAR) was the first giant array to be constructed in the Southern hemisphere. The project was led by a group from the University of Sydney, and operated from 1968 to 1979 near the town of Narribri, New South Wales, Australia, at an altitude close to sea level. The array contained 54 pairs of 6 m^2 scintillators deployed over an area of 60 km^2. The detectors were buried 1.7 m underground, resulting in the preferential detection of muons [41]. Consequently, SUGAR's sensitivity to the electromagnetic shower component suffered, resulting in relatively poor energy resolution compared to that of other arrays. SUGAR's main contribution to the field were in arrival direction studies [42].

2.5.4 Yakutsk

The Yakutsk array is located in Oktyomsty near Yakutsk, Russia and operates at 100 m above sea level. The array began data collection in 1970 and has remained in operation to this day. During its lifetime, the array has undergone several reconfigurations with the current design consisting of 58 ground-based scintillation

detector stations (with an additional 6 underground stations) to sample charged air shower particles. These stations are complemented with 48 detectors (housed PMTs) designed to detect atmospheric Cherenkov light. At its largest, the array covered $\sim$ 17 km^2 (1990) but has since been contracted to $\sim$ 10 km^2. A more detailed description of the array's previous configurations can be found in [37]. The Yakutsk array has successfully detected over 10^6 showers of primary energy above 100 TeV, with the highest energy events exceeding 10^{20} eV [43].

2.5.5 Fly's Eye

The Fly's Eye experiment was located at Dugway Proving Grounds, approximately 160 km south-west of Salt Lake City, Utah, USA. The site was chosen because of its clear atmosphere and minimal light pollution, which provided an ideal environment for the detection of fluorescence emission. The original detector, referred to as Fly's Eye I (FE I), consisted of 67 spherical mirrors, each with a diameter of 1.6 m. Imaging of air showers was performed via a collection of PMTs (12-14) placed at the focus of each mirror. Each PMT viewed a 5.5° hexagonal diameter region of the sky. In total, 880 PMTs were used to successfully capture nitrogen fluorescence emission over the entire sky, with full operation beginning in 1981. In 1986 a second detector (Fly's Eye II or FE II) of a similar design was constructed 3.4 km from the original detector. FE II was comprised of 36 spherical mirrors and 464 PMTs, and only viewed half the sky in the direction of FE I. FE II was capable of operating as a standalone detector or in combination with FE I, providing a more accurate stereo analysis of air showers. The experiment remained in this configuration until operations ceased in 1992. The highest energy event was observed in October 1991, and was assigned an energy of 3×10^{20} eV (Figure 2.5), making it the most energetic event ever recorded [44–46].

The Fly's Eye experiment was considered to be the first successful air fluorescence based cosmic ray detector, demonstrating the merits offered by such a detection method, in particular in the areas of energy and composition resolution. This achievement would be deemed significant as future cosmic ray observatories, most notably the Pierre Auger Observatory and the Telescope Array, would go on to incorporate the technique as part of their hybrid designs.

2.5.6 Akeno Giant Air Shower Array (AGASA)

The Akeno Giant Air Shower Array (AGASA) was once the world's largest cosmic ray detector, covering an area of 100 km^2. Located in Akeno, 200 km west of Tokyo, Japan, AGASA consisted of 111 2.2 m^2 scintillation detectors, arranged on a grid with detector spacing of approximately 1 km [48]. The detector's sensitivity to the muonic component of EAS was later improved following the installation of 29 muon detectors of varying sizes (2.4-10 m^2). AGASA originally operated as 4 individual branches, which were not unified until December 1995 [49].

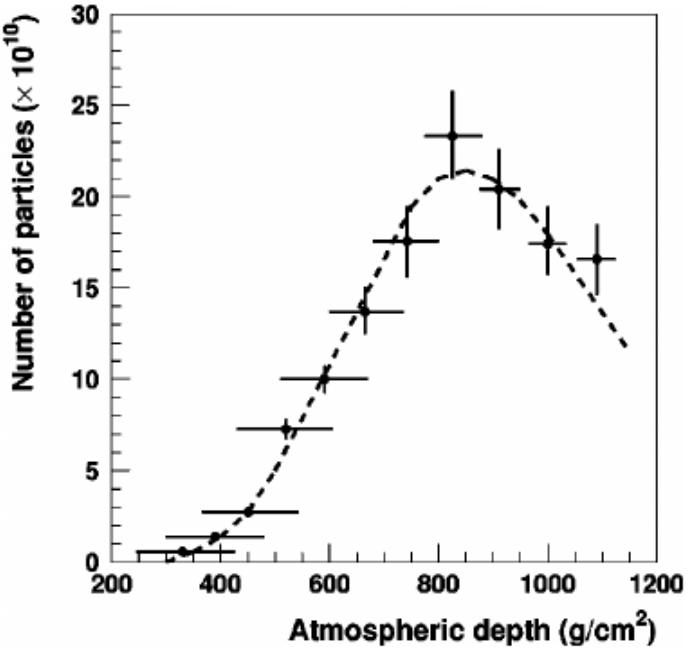

Figure 2.5: The longitudinal profile for the 3×10^{20} eV event recorded by the Fly's Eye detector [47].

In 1998 the AGASA collaboration published a result that indicated a continuation of the cosmic ray energy spectrum beyond an energy of 10^{20} eV [50]. AGASA reportedly observed 6 events above this energy, an observation inconsistent with a GZK cut-off from a uniform source distribution, which predicts an expectation of less than one event above 10^{20} eV. This analysis was later revisited, with the results being published in 2004 (Figure 2.6). Even after accounting for an 18% downward shift in cosmic ray energies (within the range of reported systematic errors), the 6 highest energy events will still remain above 10^{20} eV, with the data still $\sim 2.7\sigma$ away from the predicted one event [51].

2.5.7 HiRes

The Fly's Eye experiment (Section 2.5.5) was succeeded by the High Resolution Fly's Eye observatory (HiRes) experiment. HiRes consisted of two air fluorescence detectors (HiRes I and HiRes II) spaced 12.6 km apart, also located in the Dugway Proving Grounds in Utah. HiRes began operation as a 2-mirror prototype in 1991 located at the site of the original Fly's Eye detector. The first of the two detectors, HiRes I, was completed in 1997. In its final configuration HiRes I consisted of 22 telescope modules, with each module consisting of a mirror (with an effective area of 3.7 m^2) viewed by a 256 PMT camera placed at the focal plane. HiRes II was completed in 1999 and consisted of 42 of the same modules. In combination, the two detectors offered a field of view which covered nearly the entire sky in

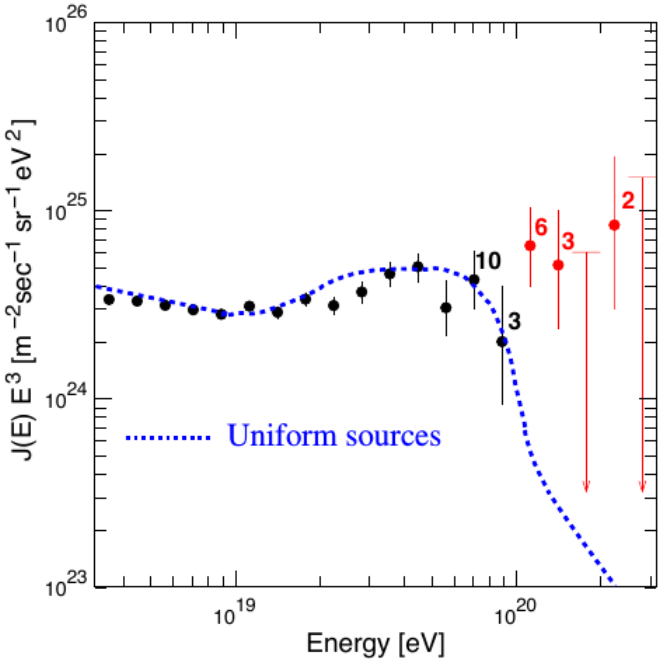

Figure 2.6: The cosmic ray spectrum measured by AGASA. The dashed blue line represents the flux predicted by the GZK hypothesis for a uniform source distribution. The red data points indicate a continuation of the cosmic ray spectrum above the predicted GZK cut-off [51].

azimuth, and 3°-17° (HiRes I) and 3°-31° (HiRes II) in elevation. Both detectors operated until 2006, collecting substantial data sets in both monocular and stereo configurations [52–54].

In 2008 the HiRes collaboration reported on the suppression of the cosmic ray flux at the highest energies, possibly attributed to the GZK effect [54]. The result was in contrast to previously reported results from AGASA, which had claimed a continuation of the flux at the highest energies (Section 2.5.6). The spectra measured by HiRes and AGASA are displayed in Figure 2.7. It should be noted that during its operation, HiRes collected a cumulative exposure more than twice that of AGASA for energies above the GZK threshold.

2.5.8 The Telescope Array Experiment (TA)

Located in the Millard County, 200 km south-west of Salt Lake City, Utah, USA, is the Telescope Array Experiment (TA) [55]. It is the largest cosmic ray detector in the Northern hemisphere. TA is a hybrid observatory, employing a surface detector array overlooked by a surrounding fluorescence detector. The surface array consists of 507 3 m^2 double-layered scintillation counters arranged on a square grid with 1.2 km detector spacing. The total area covered by the array

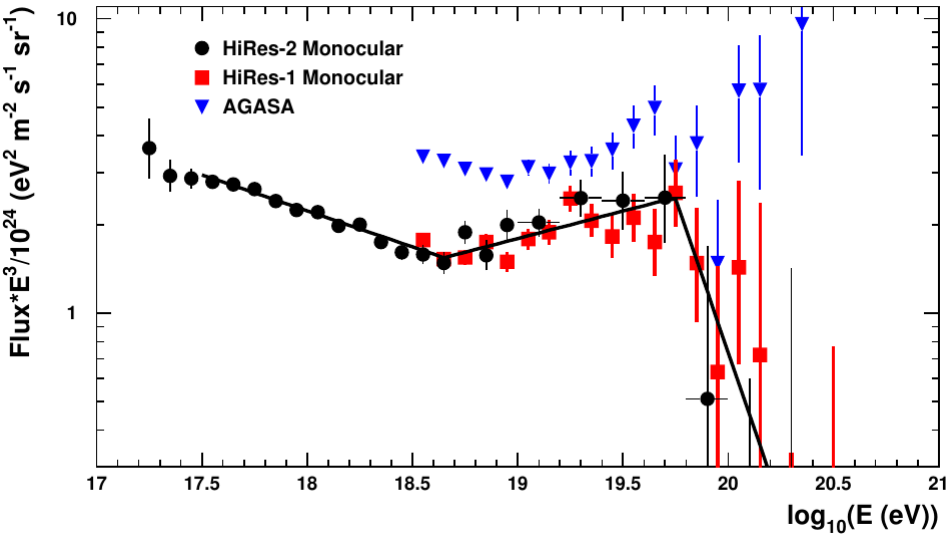

Figure 2.7: The cosmic ray energy spectrum measured by the HiRes detector. The spectra for both HiRes-I and HiRes-II are shown in red and black, respectively, and both indicate a suppression of the flux at the highest energies. The unbroken spectrum measured by AGASA is also displayed for reference [54].

is $\sim 700\,\mathrm{km}^2$. Overlooking the surface array are 38 fluorescence telescopes installed in three sites along the perimeter of the observatory. The three sites are Black Rock Mesa (BR), Middle Drum (MD) and Long Ridge (LR) which are located on the south-eastern, north-western and south-western corners of the array, respectively. The layout of the observatory is illustrated in Figure 2.8. Construction of the observatory began in 2003, with full hybrid operation commencing in March, 2008 [56]. A discussion of recent results presented by the TA collaboration can be found in Chapter 4.

The 24 telescopes housed at the BR and LR sites were newly developed for the observatory, while the 14 MD telescopes consist of refurbished telescopes, electronics and mirrors taken from the HiRes experiment. Each fluorescence telescope contains a camera constructed from 256 pixels arranged on a 16×16 grid, with each pixel viewing a $\sim 1^\circ$ region of the sky. The field of view of each telescope is 18° in azimuth and 15° in elevation, with the field of view of each detector covering up to 30° in elevation [55, 57, 58]. Measures have been taken to enhance the experiment's sensitivity to cosmic rays of lower energy through the Telescope Array Low Energy Extension (TALE). TALE consists of additional fluorescence telescopes installed at the MD fluorescence detector site, positioned to view elevation angles between 31° and 59°, along with an infill array of surface detector stations (arranged on grids of 400 m and 600 m detector spacing). These enhancements allow the minimum energy threshold to be lowered to $10^{16.5}$ eV [59].

The TA collaboration will expand the existing detectors in the coming years with the TA$\times$4 upgrade [60]. As part of the upgrade, the surface array will be ex-

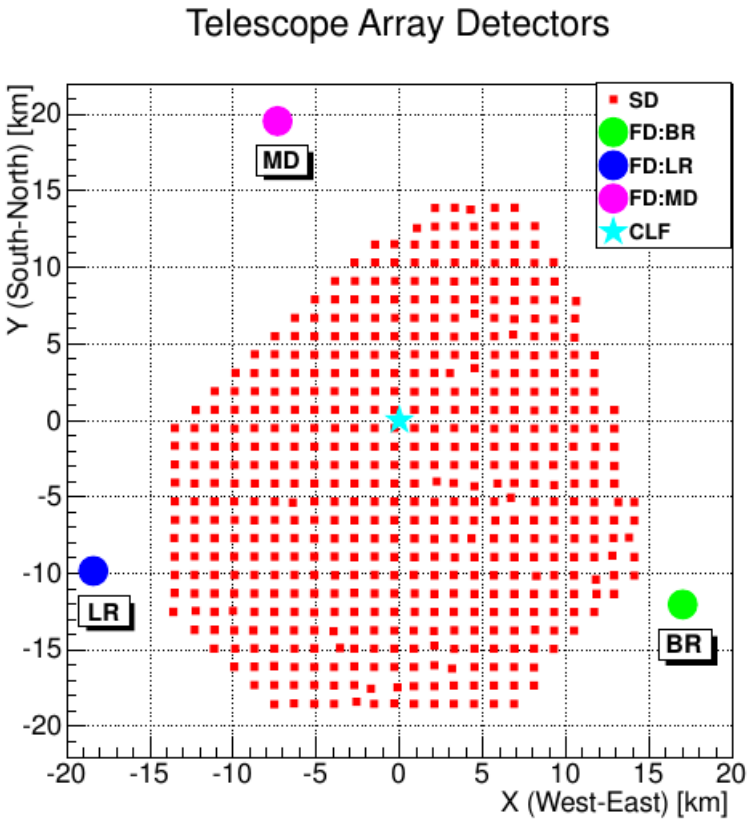

Figure 2.8: Layout of the TA observatory [55].

panded with 500 additional surface detectors arranged on a square grid of 2.08 km spacing, increasing the total area covered by the surface array to $\sim 3000\,\mathrm{km}^2$. This will allow for a quadrupling of the acceptance of the existing surface array. An additional 2 FD stations, to be installed at the MD and BRM sites, have also been proposed as part of the upgrade to complement the expansion of the surface array. The TA collaboration aims to achieve a number of scientific goals with the upgraded detector including: the further clarification of the significance and origin of the reported excess of cosmic rays in the northern sky (see Section 4.3), the search for point sources of the highest-energy cosmic rays and the determination of the mass composition of cosmic rays around the flux suppression. The layout of the TA$\times$4 upgrade is shown in Figure 2.9.

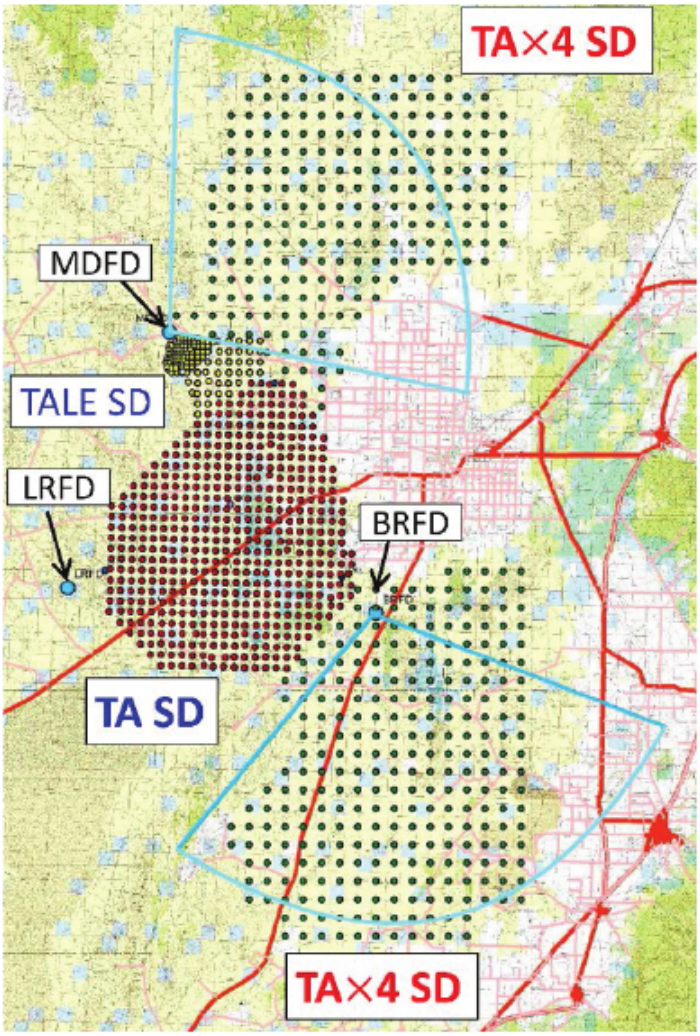

Figure 2.9: TA×4: The existing 507 surface detectors are denoted by red filled circles. The TALE surface detectors are shown as yellow filled circles and are located north of the existing array. The expansion of the surface array will see additional detectors (green filled circles) deployed in two sub-arrays to the east of the existing array. The blue fans indicate the field of view of the new telescopes to be installed at the MD and BRM sites [60].

Chapter 3

The Pierre Auger Observatory

At the forefront of cosmic ray physics is the Pierre Auger Observatory located in the Pampa Amarilla plains near Malargüe, Argentina. The idea of the observatory was first conceived in 1991 by physicists James Cronin and Alan Watson. In the following years, extensive design workshops were held in Paris (1992), Adelaide (1993) and Fermilab (1995). Construction of the Observatory began in 2001 with the deployment of an engineering array, and it reached completion in 2008. Originally called the Giant Air shower Project, the Observatory was later renamed in honour of the discoverer of extensive air showers, Pierre Auger [28, 61, 62].

The arrival flux of UHECR is low (Section 1.1), presenting a significant experimental challenge as extremely large collecting areas are required in order to observe a sufficient number of the most interesting events. The Pierre Auger Observatory boasts a collecting area of $3000\,\mathrm{km}^2$, making it the world's largest cosmic ray detector [28]. Such an immense collecting area allows for the accumulation of a large number of UHECR events, from which statistically significant conclusions can be drawn.

The Pierre Auger Observatory is a hybrid detector and employs two independent and well established detections methods to observe and study large particle showers initiated by cosmic rays. The surface detector (SD) is a large array of 1660 water-Cherenkov stations designed to sample air shower particles at ground level, $\sim 1400\,\mathrm{m}$ above sea level. The fluorescence detector (FD) is comprised of 27 fluorescence telescopes designed to detect atmospheric nitrogen emission produced during extensive air showers. In combination, these two detectors form a powerful instrument for the detection of cosmic rays, successfully detecting thousands of cosmic ray air shower events since operation began in 2004. The layout of the Observatory is shown in Figure 3.1.

3.1 Surface Detector

The surface detector is comprised of 1660 self-contained, water-Cherenkov stations (chosen for their robustness and low cost) arranged on a triangular based grid with station spacing of 1.5 km. An additional sub-array of shorter station

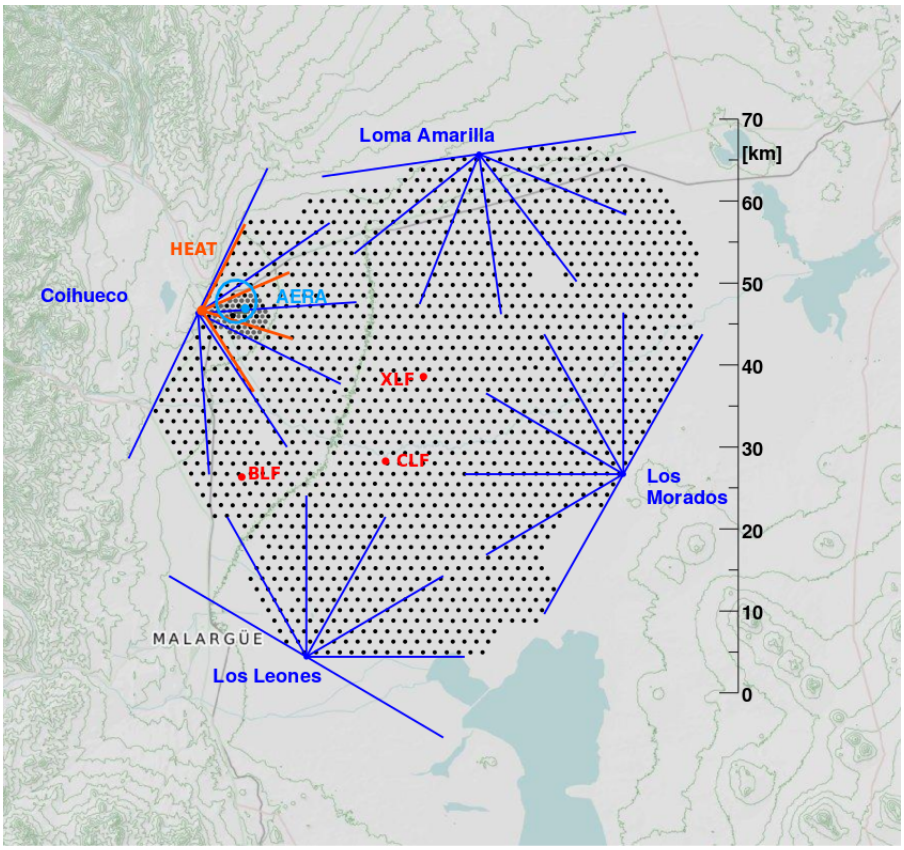

Figure 3.1: Map of the Pierre Auger Observatory. The black dots indicate the positions of individual water-Cherenkov stations. The four main fluorescence detectors are positioned along the perimeter of the Observatory, overlooking the atmosphere above the ground array.

spacing (750 m) is nested within the standard array, and forms the low energy extension of the SD (Section 3.5.2). A station spacing of 1.5 km was chosen as a compromise between cost considerations and the need to sufficiently sample EAS particles away from the shower core. The array covers an impressive 3000 km^2, with an aperture of 7350 km^2 sr for zenith angles less than 60°, and has a detection efficiency of 100% for energies above 3×10^{18} eV. This configuration allows approximately 10 stations to trigger for a vertical shower of energy 10^{20} eV, and can exceed 20 stations with increasingly inclined showers [63, 64].

3.1.1 Station Design

A single water-Cherenkov station consists of a 1.2 m high, 3.6 m diameter polyethylene cylindrical tank. Within the tank is a sealed liner with a reflective inner surface that stores 12,000 L of ultra-pure water. Cherenkov light produced by the passage of relativistic charged particles is captured by three 9" downward pointing PMTs symmetrically positioned on the surface of the liner, 1.2 m from

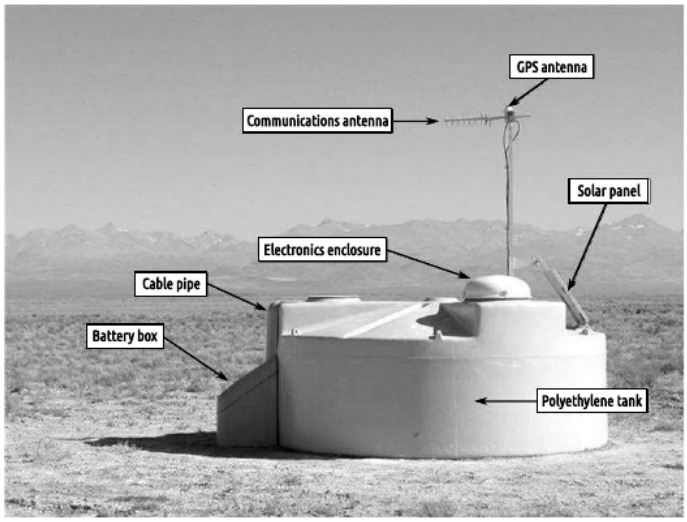

Figure 3.2: Schematic view of a water-Cherenkov station and its main components. Batteries are housed in an attached polyethylene container positioned on the shaded side of the station to prolong battery life [28].

the centre of the station. Each station is self-contained with a solar power system providing power to the PMTs and local electronics (consisting of a processor, GPS and radio receivers and power controller). Cherenkov signals recorded by the PMTs are digitised through on board processors and transmitted to the central data acquisition system (CDAS). The position and altitude of each station is known within an uncertainty of 1 m [64]. A schematic of a water-Cherenkov station is shown in Figure 3.2.

3.1.2 Station Calibration

Due to the remoteness and immense scale of the SD, it is important that the detector calibration procedure be robust and self-automated. During shower reconstruction, Cherenkov signals recorded by a station's PMTs are quantified in terms of the signal produced from a muon which vertically traverses the station (also known as a vertical and central through (VCT) going muon). The unit of interest here is referred to as the vertical-equivalent muon or VEM. The conversion to VEM units provides a common reference level amongst the SD stations, and allows calibration against Monte Carlo simulation studies. The calibration of the SD aims to obtain a conversion between the PMT signal into VEM units (more specifically, the value of 1 VEM in electronic units), and provides a stable and uniform trigger for the SD [65].

Calibration of each station involved in an EAS event is performed using data recorded immediately prior to an event trigger. The process begins with the identification of the signal corresponding to a VCT muon, achieved through the continuous monitoring of signals produced by the atmospheric muon flux [65].

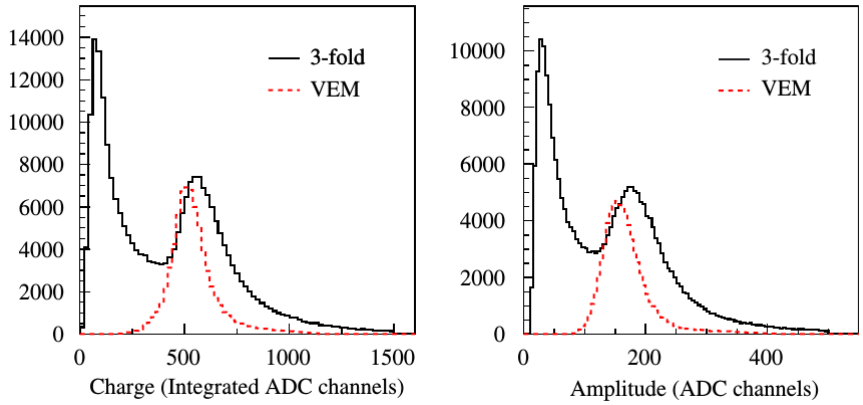

Figure 3.3: Examples of charge (left) and pulse height (right) distributions transmitted to CDAS by an SD station. The dashed red distribution in both plots is produced through an independent experiment by an external muon telescope, providing the trigger to select VCT muons. The solid black distribution represents the summed contributions for the 3 PMTs of this station. The rightmost peak in both black distributions can be attributed to the signal from a VCT muon [65].

Charge and pulse height distributions produced from atmospheric muons are recorded by an SD station's PMTs (in the minute preceding an event trigger) and are transmitted to CDAS along with relevant event data. Example charge and pulse height distributions produced by an SD station are shown Figure 3.3. Through an independent experiment, the position of the peak in the charge distribution (see left hand plot fo Figure 3.3), denoted as Q_{VEM}^{peak}, is known to correspond to a value of 1.09 VEM. A polynomial fit is used to find the position of Q_{VEM}^{peak} during data analysis, and its corresponding value is used to convert measured signals to VEM accordingly [65].

Data provided from the atmospheric muon flux is also used to establish the triggering levels of the SD. Triggering thresholds are set with respect to a value obtained from the current produced by the PMT from the atmospheric muon flux. The reference unit of interest in this case is the value of the peak of the pulse height distribution (I_{VEM}^{peak}) measured by the station. This is illustrated in the right hand plot of Figure 3.3. Details of the SD triggering system are provided in [66].

3.1.3 Energy Reconstruction

Signal strength and timing information from individual stations is used to reconstruct an EAS following the identification of a successful trigger. Shower properties such as the shower geometry, the arrival direction of the shower and shower size (a proxy for shower energy) can be derived by sampling this information from triggered stations. This section will focus primarily on the reconstruction

of the shower size. Details regarding the SD's reconstruction of shower geometry and arrival direction are provided in [28].

EAS energies are estimated by the SD through the fitting of a lateral distribution function (LDF) to the signals recorded by the relevant stations involved in the event. The LDF describes the shower particle density as a function of the perpendicular distance to the shower axis (Figure 3.4) and has the functional form given by a modified Nishimura-Kamata-Greisen function:

$$S(r) = S(r_{opt}) \left(\frac{r}{r_{opt}}\right)^{\beta} \left(\frac{r + r_1}{r_{opt} + r_1}\right)^{\beta+\gamma} \tag{3.1}$$

where $r_1 = 700\,\text{m}$, β and γ are zenith angle (θ) dependant slope parameters, r_{opt} is the optimum distance (determined empirically to be 1000 m) and $S(r_{opt})$ is the signal at the optimum distance [67]. From this the shower energy can be estimated by the calculation of S(1000); the signal that would have been produced in a station located 1000 m from the core. The uncertainty in S(1000) has contributions from three sources:

1. The statistical uncertainty in the finite number of shower particles that produce a signal in a given SD station coupled with the limited dynamic range of the signal detection.

2. Systematic uncertainties related to the assumptions made in the shape of the LDF.

3. Shower to shower fluctuations.

The third term has a contribution of $\sim$ 10% while the first two terms contribute between 6% (at the highest energies) and 20% (at low energies) to the total uncertainty in S(1000) [28, 68].

The value of S(1000) depends on two main factors, the energy of the primary cosmic ray as well as its arrival direction. The latter is characterised by the zenith angle (θ) of the primary cosmic ray, and acts as a proxy for the amount of atmosphere through which the event has traversed and subsequently, the degree to which the shower size has been attenuated by atmospheric effects. To adjust for the zenith-angle dependence of the signal, S(1000) is converted to S_{38}, which is the S(1000) that the shower would have produced had it arrived at a median observed zenith angle of 38°. This conversion is performed using the Constant Intensity Cut method [69]. The attenuation curve $f_{CIC}(\theta)$ is fitted with a third degree polynomial:

$$f_{CIC}(\theta) = 1 + ax + bx^2 + cx^3 \tag{3.2}$$

where $a = 0.980 \pm 0.004$, $b = -1.68 \pm 0.01$, $c = -1.30 \pm 0.45$ and $x = \cos^2(\theta) - \cos^2(38^\circ)$ [70]. S_{38} can then be calculated using S(1000) and θ with the following equation:

$$S_{38} = \frac{S(1000)}{f_{CIC}(\theta)} \tag{3.3}$$

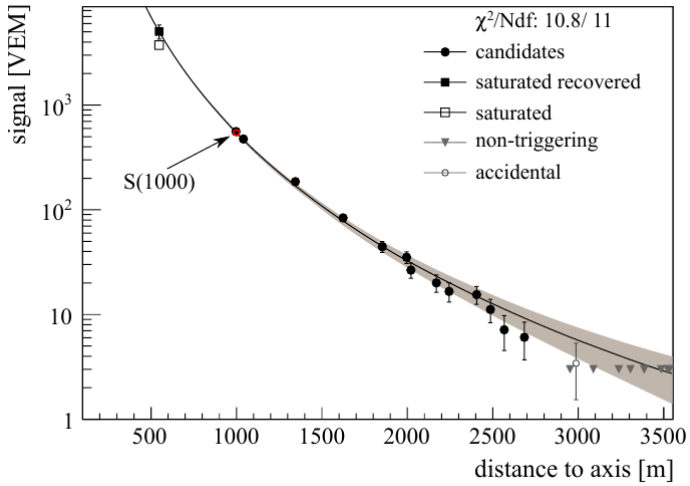

Figure 3.4: Dependence on the signal size as a function of perpendicular distance from the shower core [28].

3.2 Fluorescence Detector

The 24 individual telescopes of the FD are arranged in 4 sites along the perimeter of the Observatory, overlooking the atmosphere above the SD. An additional 3 telescopes combine to form HEAT, the low energy extension of the FD (Section 3.5.1). Each telescope has a field of view of 28.1° in elevation and 30° in azimuth, providing each site an azimuthal field of view of 180°. This arrangement allows for both a 100% FD triggering efficiency for energies above 10^{19} eV over the entire SD array, as well as full coverage of the SD with minimal wasteful overlap. Additionally, this configuration also allows for stereo and higher multiplicity events, although this was not a design prerequisite as in previous non-hybrid experiments due to the excellent shower geometry reconstruction provided by hybrid detectors [34]. The four sites are named Los Leones, Los Morados, Loma Amarilla and Coihueco and are located along the southern, eastern, northern and western boundaries of the observatory, respectively. It should be noted that each of the fluorescence detectors are located $\sim$ 1400 m above sea level, with the exception of Coihueco and HEAT, both of which are located in the Andes foothills at $\sim$ 1700 m above sea level.

The FD telescopes are housed in four specially designed buildings. Retractable shutters cover the windows to each telescope bay, providing protection from the elements and only open when the FD is being operated. The internal temperature of each building is carefully controlled to minimise the effects of temperature variations on the system. Under standard operation the FD requires clear nights with minimal moonlight contamination, giving an average duty cycle of approximately 13% [34].

3.2.1 Telescope Design

The fluorescence telescopes use a modified Schmidt optical design that was designed to confine the optical spot size to an angular spread of 0.5° [34][1].An optical filter placed at the entrance window is designed to only transmit UV photons of wavelengths between 290 nm and 410 nm. The presence of the filter allows for the transmission of nitrogen fluorescence photons which would otherwise be lost amongst the noise of visible photons. An annular corrector ring is used to provide a larger effective aperture for the telescopes, while correcting spherical aberration and largely eliminating coma aberration.

The mirror viewed by the camera is segmented, and follows one of two designs due to the use of two different manufacturers. The mirrors located at the Los Leones and Los Morados sites are comprised of 36 rectangular anodised aluminium mirror segments, while the Coihueco and Loma Amarilla mirrors are each made of 60 hexagonal glass segments layered with a reflective aluminium coating. Lasers are used to accurately align the mirror segments so that the correct spherical shape is achieved, with the centre of curvature aligned with the optical axis of the camera [34].

The camera is comprised of 440 hexagonal PMT pixels, each viewing a 1.5° diameter region of sky arranged on a 20 $\times$ 22 grid. Surrounding each PMT are 6 light collectors referred to as *Mercedes stars* designed to complement the light collection of the PMTs, maximising efficiency across the camera. When averaged over the entire camera, the light collection efficiency is 94%, compared to a value of 70% when the Mercedes stars are not in place. Accurate pixel alignment (within 0.1°) is achieved through the use of laser shots and the tracking of bright stars across the camera's field of view [34]. The layout of an FD telescope is illustrated in Figure 3.5.

3.2.2 Telescope Calibration

The reconstruction of the energy of the primary cosmic ray relies on the ability to accurately convert the signal measured by the FD cameras (in ADC counts) to a flux of photons at the aperture of the telescope. Both absolute and relative calibration procedures are performed at the Pierre Auger Observatory, allowing for the efficient tracking of both the short and long term calibration performance of the optical system.

3.2.2.1 Absolute Calibration

Absolute calibration is achieved through the attachment of a large, portable, calibrated light source at the aperture of each telescope, designed to uniformly illuminate the entire camera. This calibration is often referred to as the *drum calibration*

[1]Physical measurements indicate that the angular spread of the optical spot extends beyond 0.5° (see Section 7.3.1)

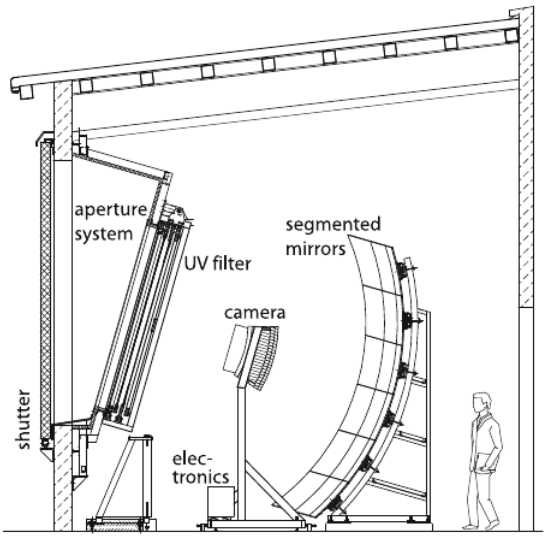

Figure 3.5: Schematic of the fluorescence telescope optical system [34].

in reference to the design and shape of the light source. This procedure provides a complete end-to-end calibration, encompassing all effects from both the optics and electronics and removing the need to study telescope components individually.

The drum itself is constructed from a lightweight aluminium frame 2.5 m in diameter and 1.4 m deep with the interior being lined with Tyvek - a diffusely reflective material in the UV. The front face of the drum is covered by a 0.38 mm thick Teflon sheet, providing diffuse illumination to the telescope optical system [71]. The response of each camera is compared to the incoming flux of photons from the drum (it having been calibrated beforehand), giving a pixel-by-pixel calibration. Measurements are made at several wavelengths[2], providing a spectral response curve which has been normalised to the absolute calibration. The average response of the FD is approximately 5 photons/ADC, with an uncertainty of 9% in the pixel response [34]. Due to the time consuming nature of this process (approximately 3 days for each FD site) absolute calibration is performed irregularly, approximately once per year. An illustration of the absolute calibration procedure is shown in Figure 3.6.

3.2.2.2 Relative Calibration

The relative calibration procedure is used to monitor the short and long term stability of the optical system between absolute calibration campaigns. Relative calibration is performed through the illumination of the telescope optical system from three different positions A, B and C (referred to as cal A, cal B and cal C respectively), each with the purpose of monitoring different groups of optical com-

[2] 320, 337, 355, 380 and 405 nm [34]

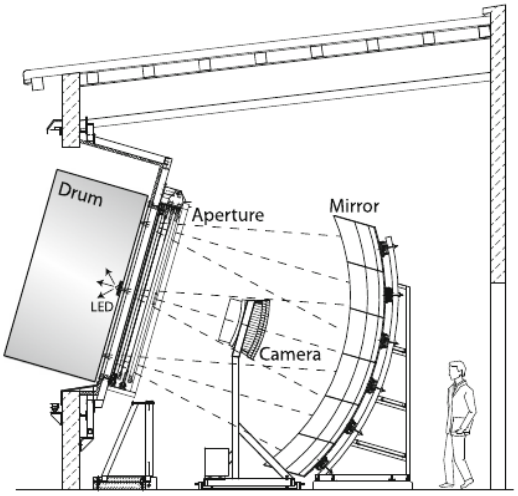

Figure 3.6: Schematic showing the positioning of the drum-shaped light source at the aperture of a fluorescence telescope [34].

ponents. Light used for the calibration is distributed to each telescope through optical fibres, from permanently installed sources housed towards the rear of each FD building. In contrast to the drum calibration, the relative calibration does not require the manual attachment of a light source to individual telescopes, allowing it to be executed remotely. Relative calibration is performed on a regular schedule for each telescope, typically occurring before and after each night of data acquisition. The three different relative calibration positions are illustrated in Figure 3.7.

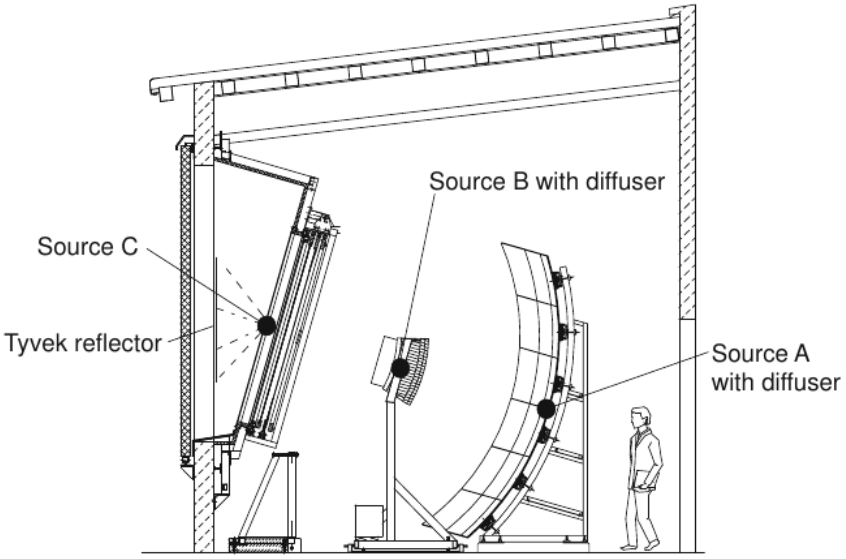

Figure 3.7: Schematic showing locations of the three light sources used in the relative calibration [34].

The light source for cal A is a 470 nm LED which is distributed into 1 mm thick Teflon diffusers located a the centre of each mirror. The FD camera is directly illuminated by a sequence of 50 rectangular light pulses (57 μs) produced at a rate of 1/3 Hz [72]. This calibration monitors the stability and linearity of the camera system. A detailed discussion of how cal A is used to monitor the gain of the FD pixels is provided in Section 5.1. Both cal B and cal C use Xenon flash lamps as their light source. Light from position B is directed towards the mirror, through a 1 mm thick Teflon diffuser placed on the side of each FD camera, which then reflects into the camera. The purpose of this calibration is to monitor both the reflectivity of the mirror as well as the gain of the camera. Cal C illuminates diffusely reflective Tyvek targets on the inside of the telescope shutters. This light will pass through the aperture, to the mirror and on to the camera. This calibration monitors the end-to-end performance of the telescopes.

3.2.3 Event Reconstruction

Event reconstruction with the FD begins with establishing the shower geometry using the sequence of pulse times from triggered camera pixels. The standard method for this begins with the calculation of the shower-detector plane (SDP), defined as the plane that contains the location of the telescope observing the event and the axis of shower propagation. This is achieved by fitting the pointing directions of each triggered pixel, weighted by the size of that signal [73]. Having established the SDP, timing information provided by individual pixels is used to define the shower axis within the SDP, which can be characterised by two parameters χ_0 and R_p. The former defines the angle between the shower axis and the ground plane while the latter is the impact parameter (or distance of closest approach) of the shower to the telescope. The various shower geometry parameters are illustrated in Figure 3.8.

The arrival time of light in the i^{th} pixel is given by:

$$t_i = t_0 + \frac{R_p}{c} \tan\left(\frac{\chi_0 - \chi_i}{2}\right) \tag{3.4}$$

where c is the speed of light, χ_i is the pointing elevation of the i^{th} pixel within the SDP and t_0 is the time at which the shower front passes the point of closest approach to the camera. For an EAS detected by a single fluorescence detector (a monocular reconstruction), the reliability of the fitted shower parameters is dependent on the measured angular speed ($\frac{d\chi}{dt}$) over the length of the track. For instances where $\frac{d\chi}{dt}$ changes very little over the observed track, which is typical for shorter tracks, a fit degeneracy between R_p and χ_0 is introduced, leading to an increase in uncertainties on the various shower parameters. It is possible to break this degeneracy if the shower reconstruction is performed in a hybrid sense - where timing information provided from the SD is used in combination with a fluorescence telescope [74].

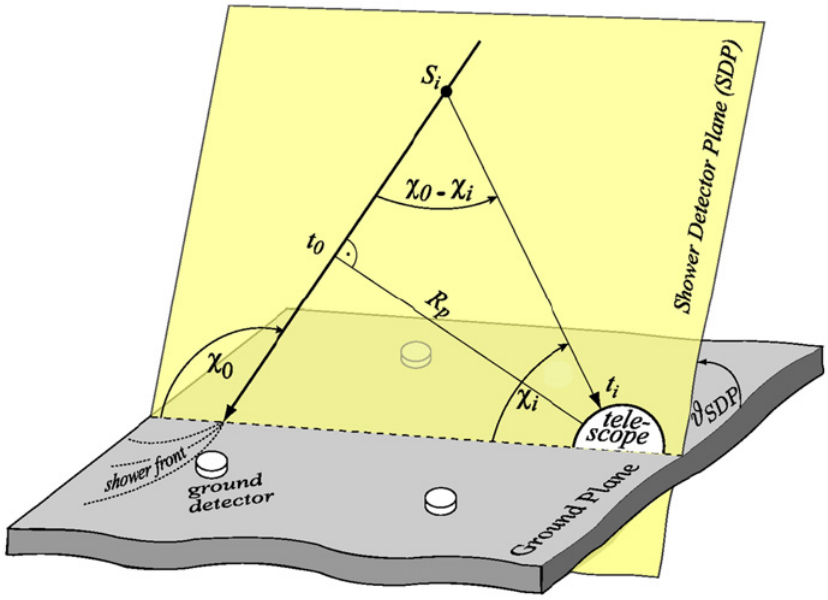

Figure 3.8: Geometrical reconstruction of an EAS by a fluorescence detector begins with the definition of the SDP. This figure illustrates the position of the SDP and shower axis relative to the fluorescence telescope that observed the shower [34].

Following the establishment of the shower geometry, the shower energy can then be reconstructed. This step requires the conversion of the signal recorded by the detector's PMTs to an energy deposit profile at the shower as a function of atmospheric slant depth (X). A Gaisser-Hillas function (Equation 3.5) is then fitted to the profile and integrated with respect to X to give an estimation of the calorimetric energy, E_{FD}.

$$f_{GH}(X) = \left(\frac{dE}{dX}\right)_{max} \left(\frac{X - X_0}{X_{max} - X_0}\right)^{\frac{X_{max}-X_0}{\lambda}} exp\left(\frac{X_{max} - X}{\lambda}\right) \tag{3.5}$$

While a straightforward concept, the conversion of PMT signals to an energy deposit profile is complicated by a variety of factors which, if not accounted for correctly, can lead to systematic errors in fitted shower parameters. As the atmosphere plays a key role in the fluorescence technique, knowledge of atmospheric conditions and their variations is vital for accurate EAS event reconstructions. Altitude profiles of atmospheric density, pressure, temperature and humidity should be known in detail as they are all factors that can affect fluorescence yield. The presence of atmospheric aerosols and cloud can obstruct the propagation of fluorescence photons as they propagate from the shower axis towards the detector's aperture and should be carefully monitored.

3.3 Atmospheric Monitoring

Extensive campaigns are in operation at the Pierre Auger Observatory to monitor atmospheric conditions. Figure 3.9 illustrates the locations of the various monitoring instruments across the Observatory. Data from a network of weather stations, balloon launches and satellite measurements provide detailed information regarding atmospheric temperature, pressure and density across the Observatory. Infra-red cameras installed at each FD site provide information about cloud coverage across the fields of view of individual fluorescence telescopes. Additional details for these instruments can be found in [28].

The abundance of atmospheric aerosols is characterised using measurements from regular laser shots observed from the various FD locations along the Obervatory's perimeter. Aerosols are capable of obstructing the propagation of fluorescence photons towards the FD and are also highly variable even on time scales of approximately one hour. For this reason, hourly vertical aerosol optical depth (VAOD) profiles are measured for each of the four FD sites using data provided through observations of the Central Laser Facility (CLF) and eXtreme Laser Facility (XLF), both of which are located towards the centre of the Observatory [75].

Both laser facilities use a frequency tripled Nd:YAG laser to provide pulsed laser shots at a wavelength of 355 nm - near the centre of the fluorescence spectrum. During data acquisition, the CLF and XLF fire 50 vertical shots at a fre-

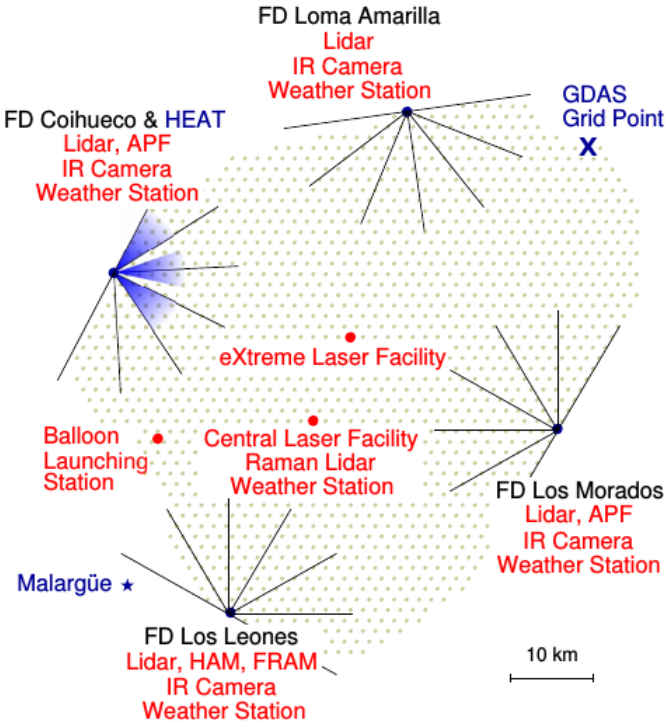

Figure 3.9: Map of the instruments used to monitor atmospheric conditions [28].

quency of 50 Hz every 15 minutes [75]. Laser light is scattered out of the beam and propagates through the atmosphere towards the FD. It is assumed that scattered laser light attenuates through the atmosphere in the same way as fluorescence light. Quarter hour light profiles are used to calculate hourly VAOD profiles in one of two methods [75]:

- Data Normalised Method - based on the comparison of measured laser profiles to a reference night (referred to as the Rayleigh night profile) for which light attenuation is dominated by molecular (Rayleigh) scattering.
- Laser Simulation Method - light profiles simulated in a variety of atmospheres are compared to measured laser profiles. A parametric model is then used to describe the aerosol attenuation.

A more extensive discussion of these two methods can be found in [76].

3.4 Hybrid Energy Calibration

The hybrid design of the Pierre Auger Observatory allows for the simultaneous detection of UHECR by both the SD and FD. The two independent detectors observe EAS in complementary ways, providing the opportunity for important cross-checks and inter-detector calibration.

The energy parameter provided by the SD (S_{38}) can be compared against the near-calorimetric measurements of the shower energy provided by the FD (E_{FD}) to determine the SD energy, E_{SD}. Empirically calibrating the energy scale avoids the need to use shower simulations which have uncertainties related to hardonic interaction models [77]. A calibration curve can be obtained using a subset of high quality hybrid data with measured FD energies above the SD full efficiency threshold. The relationship between reconstructed values of E_{FD} and S_{38} being described by the following power law:

$$E_{FD} = A \times S_{38}^{B} = E_{SD} \tag{3.6}$$

The most recent calibration curves presented by the Pierre Auger Collaboration are shown in Figure 3.10. The grey central data set corresponds to 2661 hybrid events reconstructed between January 2004 and December 2016 for showers with E_{FD} above 3×10^{18} eV and zenith angles below 60°. This data set yields the calibration parameters $A = (1.78 \pm 0.03) \times 10^{17}$ eV and $B = 1.042 \pm 0.005$ and an energy resolution of 15% [78].

The blue left-most data were derived from 1276 hybrid events detected by the 750 m spaced SD array (see Section 3.5.2) for the period beginning August 2008 through to December 2016. It should be noted that the energy parameter provided by the SD for the 750 m array is S_{35}. The events used in this set have a minimum energy of 3×10^{17} eV and a maximum zenith angle of 55°. The corresponding

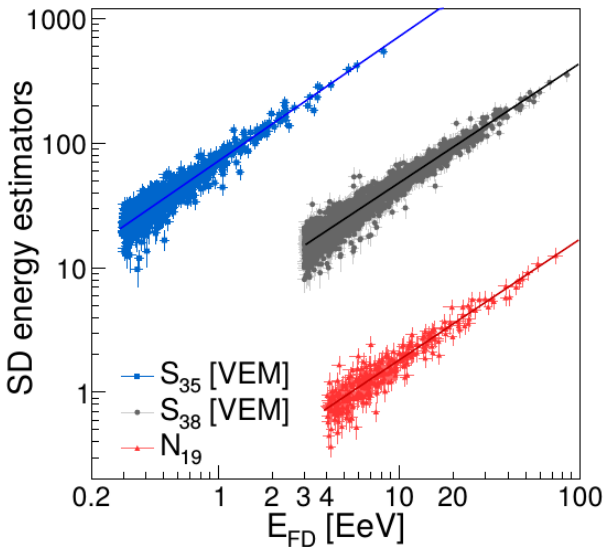

Figure 3.10: Calibration curves presented at the 35th International Cosmic Ray Conference. The vertical axis represents the energy estimator provided by the SD [80].

calibration parameters are $A = (1.4 \pm 0.04) \times 10^{16}$ eV and $B = 1.000 \pm 0.008$ and an energy resolution of 13% [78].

The remaining data set corresponds to 312 hybrid inclined showers (zenith angle ranging from 60-80°) observed by the 1500 m array with a minimum reconstructed energy of 4×10^{18} eV. Reconstruction for these showers relies on the estimation of the relative muon content (denoted as N_{19}) with respect to a simulated proton shower with energy 10^{19} eV [79]. The energy of the shower is then inferred from N_{19}. The fitted calibration parameters are $A = (5.445 \pm 0.075) \times 10^{18}$ eV and $B = 1.030 \pm 0.018$ and an energy resolution of 17% [78].

3.5 Auger Enhancements

Several enhancements have been made to the Observatory since the successful completion of the two main detectors. Of particular interest was the lowering of the Pierre Auger Observatory's minimum energy threshold, to improve sensitivity to showers in the knee-to-ankle region of the energy spectrum (E $\sim 10^{17}$ eV) - an interesting energy range, where the transition from galactic to extragalactic cosmic rays is believed to occur [28, 81]. This section will discuss a number of the notable enhancements, as well as future upgrade plans for the Observatory.

3.5.1 HEAT

The High Elevation Auger Telescopes (HEAT) is comprised of 3 tiltable telescopes and acts as the low energy extension of the FD (Figure 3.11). HEAT is situated

near the Coihueco FD eye, ~ 180 m north-east of the Coihueco building [82].

The design of the HEAT telescopes is similar to that of the standard FD, with each telescope providing a field of view 30° in azimuth and $\sim 30°$ in elevation. In contrast to the standard FD telescopes (which are fixed in position and housed in large concrete buildings) the HEAT telescopes are capable of operating in two configurations - a downward and upward tilting mode, the latter of which enhances the FD's ability to observe showers initiated by cosmic rays of lower energies. An EAS initiated by a cosmic ray of energy less than 10^{18} eV will emit fewer fluorescence photons compared to those of higher energies, and can be detected at only short distances from an FD telescope. Sensitivity to showers initiated by lower energy cosmic rays can be improved by extending the field of view of the FD to higher elevations. When operating in upward mode, the HEAT telescopes offer a field of view between 30° and 60° in elevation above the horizon, allowing for the capture of lower energy showers which would otherwise be unseen by the standard FD. In downward mode, the field of view of the HEAT telescopes overlap with those of Coihueco (in both azimuth and elevation), allowing for useful cross-calibration and shower reconstruction studies [81]. Figure 3.12 illustrates HEAT in both configuration modes.

The HEAT telescopes use an improved version of the data acquisition electronics found in the standard FD, incorporating larger and faster modernised FPGAs. The sampling rate was also increased from 10 MHz to 20 MHz for the HEAT telescopes. From a data acquisition standpoint, HEAT is able to function as a fifth fluorescence detector, or in combination with the Coihueco fluorescence detector[3], providing a high quality data set used in energy spectrum and mass composition studies. The first measurements with a single HEAT telescope began in January 2009, with all 3 telescopes commencing data acquisition in September 2009 [82].

Figure 3.11: Photo of the HEAT telescopes in titled mode [81].

[3]Forming a sixth eye referred to as HeCo.

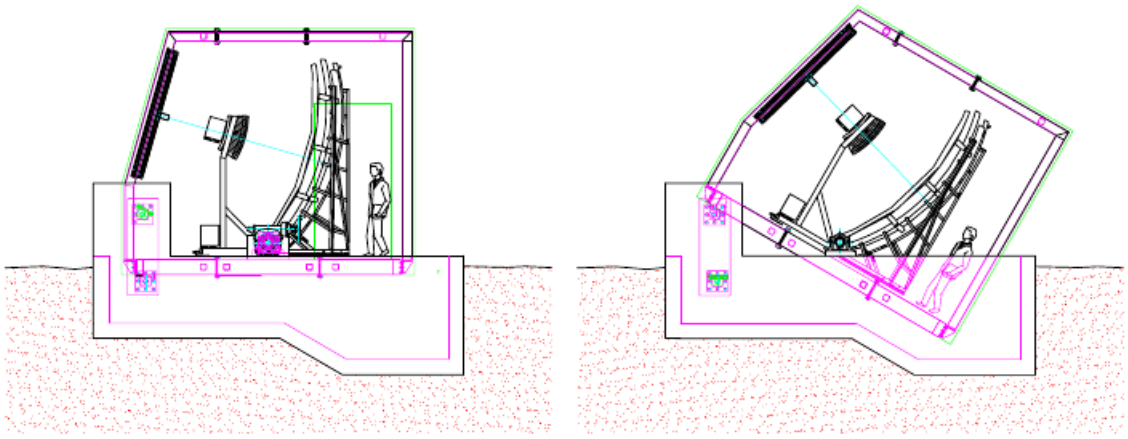

Figure 3.12: Left: Downward mode for service and calibration studies. Right: An electrical hydraulic system is used to tilt each telescope 29° upward for data acquisition [28].

3.5.2 AMIGA

The Auger Muon and Infill for the Ground Array (AMIGA) detector is the low energy extension of the SD. Similar to its FD counterpart, AMIGA was designed with the purpose of lowering the energy threshold of the SD, improving sensitivity to cosmic ray events with energies below 3×10^{18} eV. The AMIGA detector covers an area of 23.5 km^2 and is nested within the existing SD array approximately 6 km from the Coihueco FD site [28]. The AMIGA design consists of 61 water-Cherenkov stations arranged on a triangular grid with a station spacing of 750 m, lowering the minimum energy threshold for full detection efficiency to 3×10^{17} eV. The 750 m array was completed in September 2011 [83]. Alongside each water-Cherenkov station will be a buried 30 m^2 scintillation detector, designed to directly measure the penetrating muon component of an EAS. The buried detectors will provide valuable composition sensitive information for cosmic rays within this lower energy regime. A Unitary Cell consisting of seven water-Cherenkov stations and their accompanying scintillation detectors (arranged in a hexagonal layout) has been in operation since February 2015 [84]. The layout of the AMIGA detector is shown in Figure 3.13.

3.5.3 AERA

The Auger Engineering Radio Array (AERA) is the radio extension of the Pierre Auger Observatory. AERA was designed to detect the radio emission of charged air shower particles in the 30-80 MHz frequency band. In its current configuration, AERA consists of 153 autonomously operating radio detector stations deployed over 17 km^2 and is embedded within the SD array, in the field of view of the

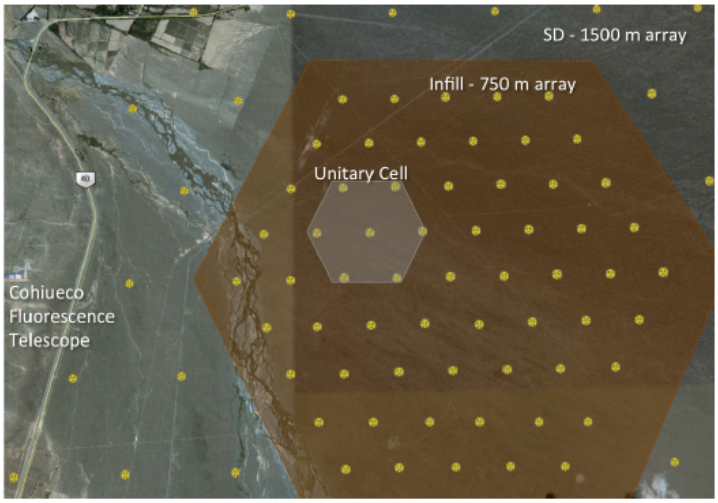

Figure 3.13: The AMIGA detector spans an area of 23.5 km^2 within the existing SD array. Scintillation detectors will be buried underground, beneath $\sim$ 540 g cm^{-2} of vertical mass [85].

Coihueco and HEAT FD sites [86]. The layout of AERA is illustrated in Figure 3.14.

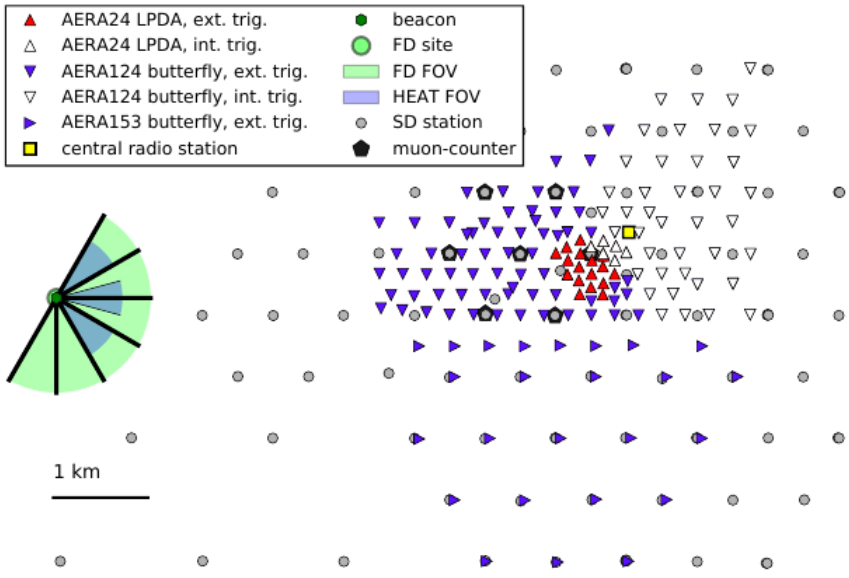

Figure 3.14: The AERA array: The first 24 detectors (equipped with log-periodic dipole antennas) were installed in 2011 on a triangular grid with detector spacing of 144 m. An additional 129 stations were installed in 2013 (100 stations arranged on 250 m and 375 m grids) and 2015 (29 stations arranged on a 750 m grid). All detectors installed post-2011 were equipped with Butterfly antennas [86].

3.5.4 AugerPrime

The Pierre Auger Observatory is currently undertaking an extensive upgrade of its detectors, with construction underway on the Observatory's latest enhancement, AugerPrime. The underlying motivation of AugerPrime is to enhance the Pierre Auger Observatory's ability to clarify the mass composition of cosmic rays at the highest energies [87].

A significant component of AugerPrime is the installation of new $4\,\mathrm{m}^2$ plastic scintillators above the existing water-Cherenkov stations (Figure 3.15). The combination of the Surface Scintillator Detectors (SSD) and the existing water-Cherenkov stations will enhance the ability of the SD to discriminate between the muon and electromagnetic components of an EAS. Accompanying this will be an overhaul of the electronics system used to process both SSD and water-Cherenkov station data, which aims to improve data quality, local triggering and processing capabilities, along with station calibration and monitoring performance.

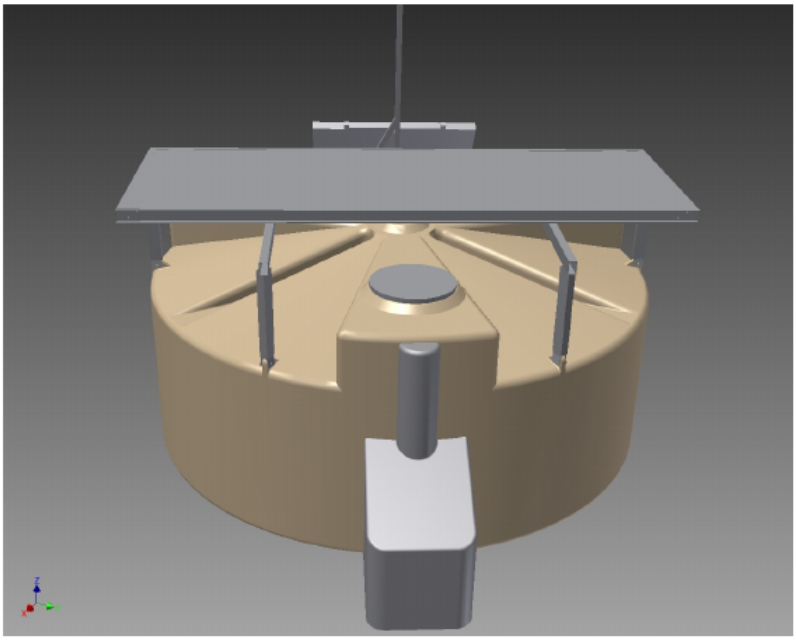

Figure 3.15: A 3D view of a new plastic scintillator unit mounted above a water-Cherenkov station. This design was chosen (after detailed Monte Carlo simulations) for its simple design, with minimal intrusion on the existing detectors, and ease of deployment [87].

In parallel with the SD array upgrade, the operation of the FD will be modified to extend its operation under increased night sky background. At present, the FD duty cycle is $\sim 13\%$, to prolong the life of the FD PMTs by limiting their exposure to periods of higher night sky background. To operate under increased night sky background, the high voltage driving the FD PMTs will be carefully lowered, such

that the increased night sky background exposure does not significantly accelerate their ageing. This will allow an increase of $\sim 50\%$ in the current duty cycle [87].

The upgrade procedure will not greatly affect the current data acquisition of the existing detectors and is expected to reach completion by the end of 2018. The upgraded detectors will continue to operate until the end of 2024, by which time the Pierre Auger Observatory will have collected an impressive data set containing additional composition-sensitive information. Such high quality data promises to provide new and exciting results for cosmic ray astrophysics.

Chapter 4

Recent Results From Cosmic Ray Experiments

Numerous advances have been made in the field of cosmic ray astrophysics in the past two decades following the successful development and operation of very large cosmic ray detectors, most notably the Pierre Auger Observatory (Chapter 3) and the Telescope Array experiment (Section 2.5.8). Improvements in data collection and analysis techniques have been instrumental in this process, aiding in the discovery of several notable results. This Chapter will highlight recent results from both experiments concerning the cosmic ray energy spectrum, mass composition and anisotropy studies.

4.1 Energy Spectrum Studies

The cosmic ray energy spectrum (Section 1.1) displays several defining features at the highest energies which are inherently tied to the origin, composition and propagation of cosmic rays. For this reason, the measurement and confirmation of these features has long been an experimental focal point for cosmic ray experiments.

The large areas covered by the surface detectors of the Pierre Auger Observatory and Telescope Array allow for the accumulation of sufficient cosmic ray statistics at the highest energies. The large collection areas, coupled with the ability to operate 24 hours a day, enable surface detectors to contribute the majority of exposure to energy spectrum studies. The energy scale is determined through the analysis of cosmic ray events reconstructed by both the surface and fluorescence detectors of the respective experiments. The Pierre Auger Observatory uses the fluorescence detector's near calorimetric reconstructed energy to calibrate the signal recorded by the surface detector (see Section 3.4). The Telescope Array estimates the relationship between the surface detector response and zenith angle through Monte Carlo simulations, from which the energy scale is then determined. The uncertainty in the energy scale of the Monte Carlo simulation is large (due to its reliance on hadronic interaction models) but can be constrained using

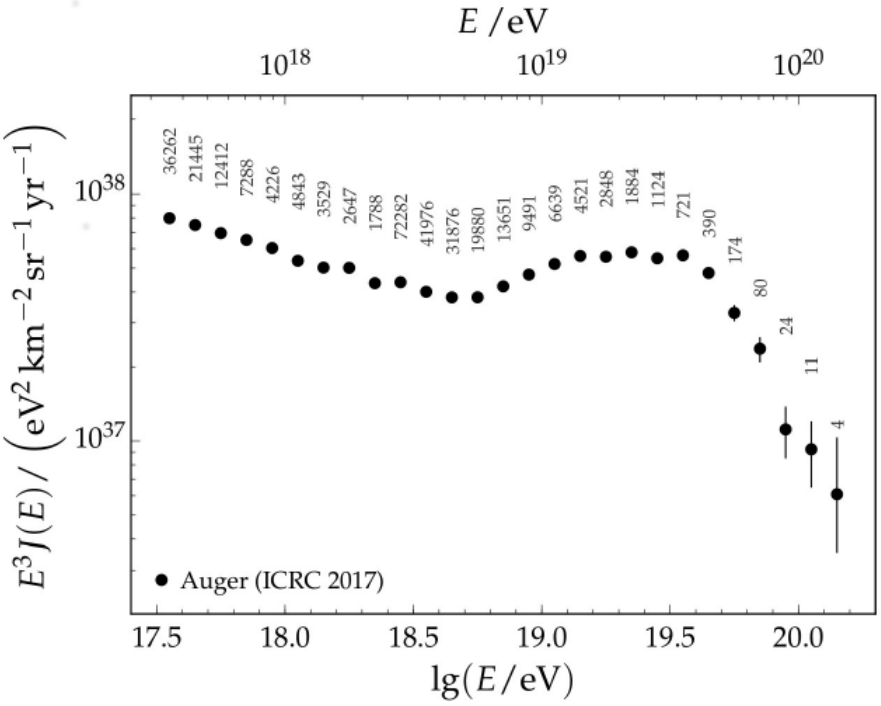

Figure 4.1: The combined energy spectrum presented by the Pierre Auger Collaboration at the 35th International Cosmic Ray Conference in 2017. The number of events within each energy bin is labelled above the corresponding data points [78].

the calorimetric energy obtained by the FD for hybrid events [88]. At present, the systematic uncertainty in the energy scale is 14% for the Pierre Auger Observatory and 21% for the Telescope Array [89, 90].

Figure 4.1 shows the most recent cosmic ray energy spectrum published by the Pierre Auger Collaboration. The spectrum combines data obtained from the 750 m (with zenith angle $\theta < 55°$) and 1500 m ($\theta < 80°$) SD arrays as well as the FD in hybrid mode, and spans over 12 years of operation with a total exposure exceeding 50,000 km^2 sr yr. It should be noted that showers are classified as either *vertical* ($\theta < 60°$) or *inclined* ($60° < \theta < 80°$), the latter category being dominated by muons requiring a separate reconstruction method [79]. The combined spectrum of Figure 4.1 clearly shows a flattening of the spectrum above an energy of $(5.08 \pm 0.06 \pm 0.8) \times 10^{18}$ eV[1] corresponding to the *ankle* of the spectrum (Section 1.1). Another notable spectral feature is the suppression of the cosmic ray flux, clearly observable at $E_s = (3.9 \pm 0.2 \pm 0.8) \times 10^{19}$ eV [78].

In 2015 the Telescope Array Collaboration presented spectra spanning 4.5 decades of energy using data obtained from the surface detector, the Black Rock Mesa and Long Ridge fluorescence detectors, and the experiment's low energy

[1]Statistical and systematic uncertainties quoted.

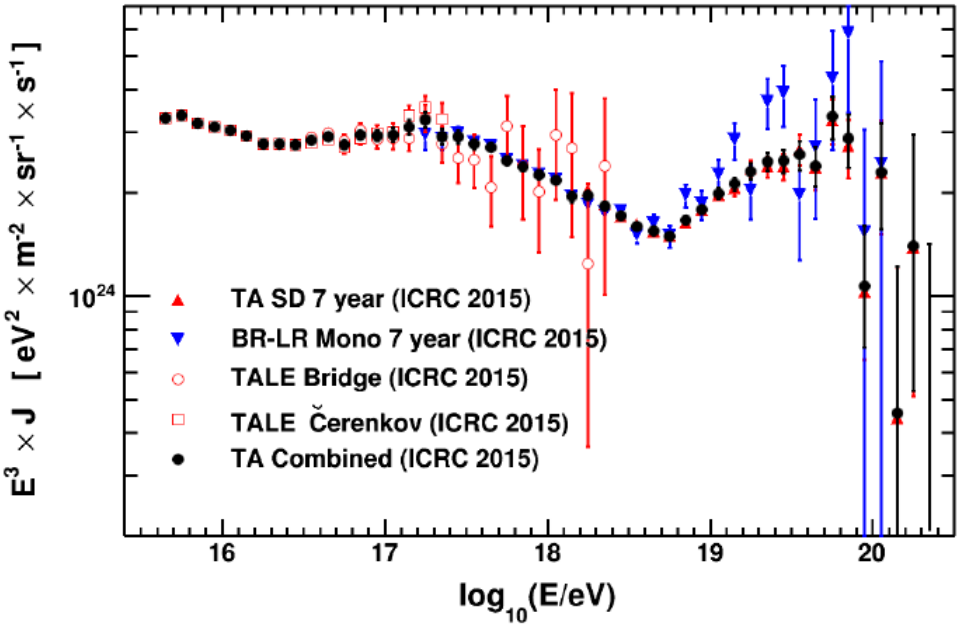

Figure 4.2: The energy spectra presented by the Telescope Array Collaboration at the 34th International Cosmic Ray Conference in 2015. The combined spectrum is shown as black circles [91].

extension, TALE. The individual spectra along with a combined spectrum are shown in Figure 4.2. Key spectral features (which are also observed in the spectrum measured by the Pierre Auger Observatory) are identified at $10^{18.70\pm0.02}$ eV and $10^{19.78\pm0.06}$ eV corresponding to the ankle and onset of the flux suppression, respectively [91].

Combined energy spectra measured by the Pierre Auger Observatory and Telescope Array are compared in Figure 4.3. A clear discrepancy in the absolute scale of the two spectra can be seen in the left hand plot of Figure 4.3, which may be attributed to differences in fluorescence yield calculation models and invisible energy[2] corrections. The spectra can be brought into better agreement following a shift ($+5.2\%$ for Auger and -5.2% for TA) in the energy scales of the two experiments. The shifts are within the reported systematic uncertainties of the respective experiments and aim to bring consistency in the measured spectra for energies below $\sim 10^{19.5}$ eV. The shifted spectra are illustrated in the right hand plot of Figure 4.3.

The effect of scaling the respective energy scales fails to address the discrepancy between the two measured spectra for energies beyond $\sim 10^{19.5}$ eV. Such a disagreement could be explained by an energy dependent systematic effect or, since the exposure of the two experiments cover different regions of the sky, could

[2]Energy carried by high energy muons and neutrinos that remain undetected by the fluorescence detectors.

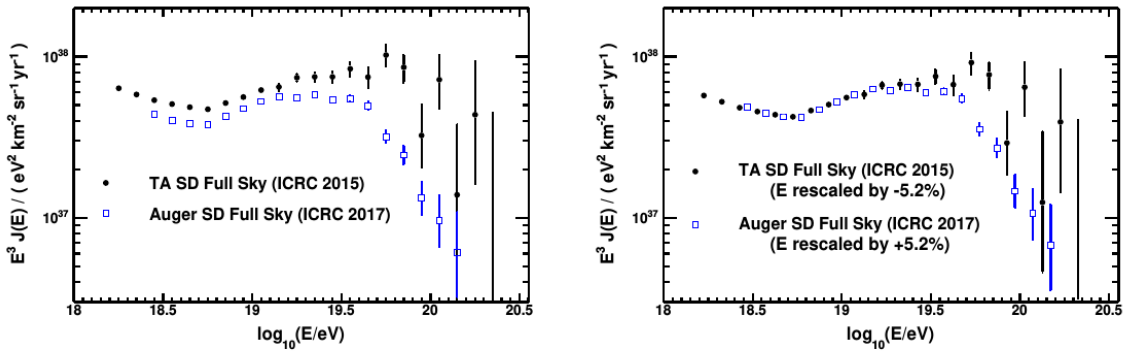

Figure 4.3: Left: Comparison of the energy spectra presented by the Pierre Auger and Telescope Array collaborations across the overlapping energy range. Right: The result after scaling the respective energy scales of the two experiments. Note that in both plots the fluxes have been multiplied by E^3 [92].

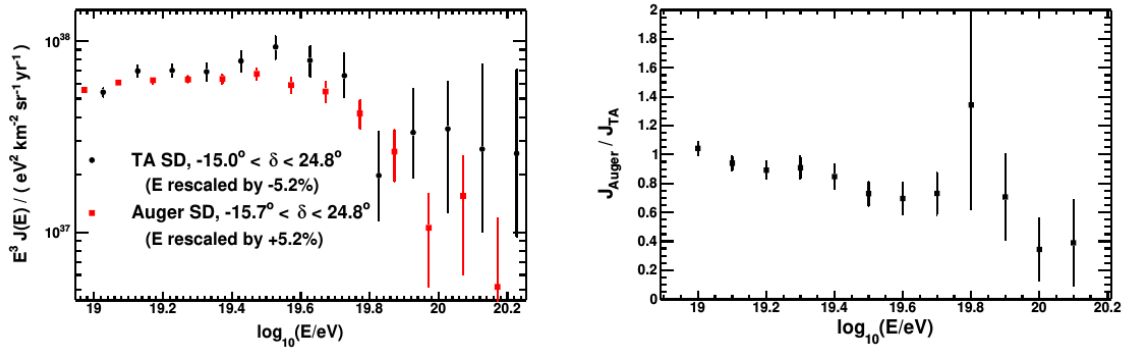

Figure 4.4: Left: Comparison of the energy spectra at the highest energies (after rescaling the respective energy scales) for both experiments in the common declination band. Right: The ratio of the two energy spectra in the common declination band. The two spectra are not in agreement within statistical uncertainties [92].

be an indication of an anisotropy in cosmic ray arrival directions at the highest energies. A study of the spectrum measured by each experiment in an overlapping declination band is shown in Figure 4.4 and indicates a disagreement in the measured spectra at the highest energies. This topic is subject to ongoing efforts from both collaborations [92].

4.2 Mass Composition Studies

Cosmic ray composition studies aim to determine the type and relative abundance of different cosmic ray species as a function of energy. Such studies play a vital role in assisting to understand the origins of cosmic rays of the highest energies, as they allow constraints to be placed on possible acceleration and propagation

scenarios. This Section will highlight recent mass composition results presented by the Pierre Auger and Telescope Array collaborations.

The fluorescence technique offers the unique benefit of studying the development of a cosmic ray induced EAS through a variety of shower ages, allowing for the measurement of shower observables useful to mass composition studies. The primary shower observable used to extract composition information is X_{max} (defined in Section 2.2). The longitudinal development of cosmic rays will vary as a function of primary mass, resulting in different distributions of X_{max}. Statistical fluctuations in the interaction of a cosmic ray of a specific mass and the atmosphere prevents the determination of the mass composition on an event by event basis. Instead, mass composition information can be inferred through the study of distributions of X_{max} as a function of energy.

Prior to discussion of recent X_{max} results, it should be noted that direct comparisons between published X_{max} data between the two experiments is not a trivial task, as biases introduced by detection and analysis methods must be taken into consideration. For example, the Pierre Auger Observatory enforces strict cuts on the geometry of reconstructed events to minimise any bias introduced from the limited field of view of the Observatory's FD[3]. These cuts, referred to as fiducial field of view cuts, limit the data to showers which enter the upper field of view of the FD at low atmospheric slants depths and develop along an axis directed towards the detector [93]. The fiducial field of view cuts allow for comparisons between the 'true' measured X_{max} distributions (at the expense of shower statistics) and theoretical predictions based on hadronic interaction models [61]. The Telescope Array experiment approaches this problem with a different philosophy. In an effort to maximise shower statistics, cuts applied to reconstructed showers focus on data quality and do not account for potential detection biases [94]. Any biases or detector resolution effects are incorporated into expectation distributions calculated using hadronic interaction models, against which measured X_{max} distributions are then compared. It is possible that the different approaches adopted by each experiment has led to discrepancies in mass composition results, some of which are highlighted below.

The latest mass composition results presented by the Pierre Auger Collaboration are summarised in Figure 4.5 and show the mean ($\langle X_{max} \rangle$) and RMS of X_{max} ($\sigma(X_{max})$) for the energy range between $10^{17.2}$ to $10^{19.6}$ eV. X_{max} results are often interpreted with reference to the elongation rate, which defines the rate of change of $\langle X_{max} \rangle$ per decade of energy. For energies between $10^{17.2}$ and $10^{18.33}$ eV the elongation rate is $(79 \pm 1)\,\mathrm{g\,cm^{-2}}$ per decade of energy, an observation that is larger than that expected for a composition unchanging in mass ($\sim 60\,\mathrm{g\,cm^{-2}}$ per decade of energy) and indicates the mean primary mass becoming lighter with increasing energy (Figure 4.5, left). Above an energy of $10^{18.33}$ eV, the elongation rate flattens out to $\sim 26\,\mathrm{g\,cm^{-2}}$ per decade of energy, which can be interpreted as the mean primary mass trending towards heavier nuclei. Similarly, $\sigma(X_{max})$ (Figure

[3]These are made in addition to cuts on data quality.

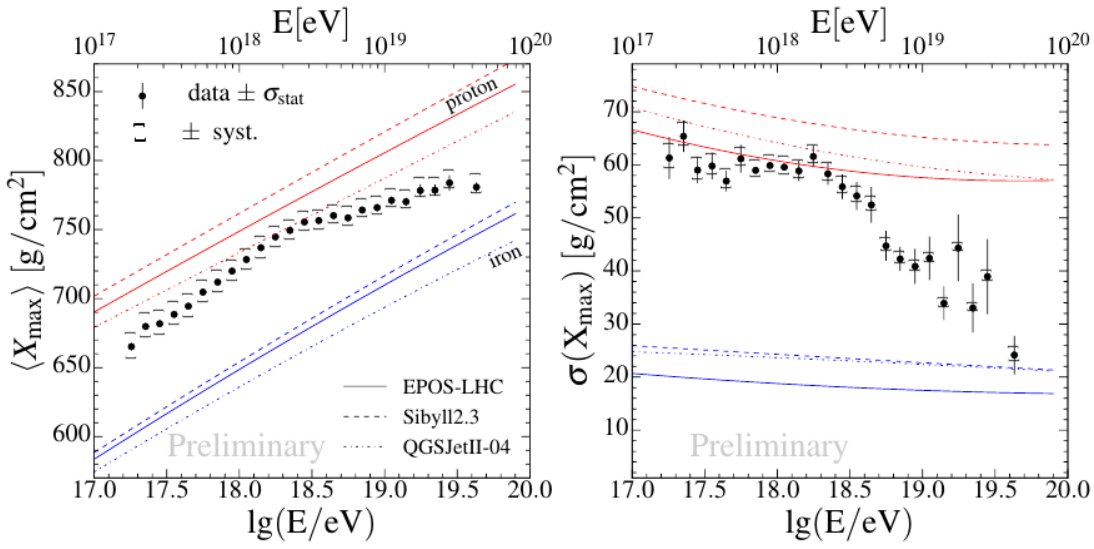

Figure 4.5: Mean X_{max} (left) and the RMS in X_{max} (right) measured by the Pierre Auger Observatory. The inclusion of data collected using HEAT (Section 3.5.1) decreases the minimum energy threshold to $10^{17.2}$ eV. Results are compared to pure proton and iron expectations calculated using the EPOS-LHC, QGSJetII-04 and Sibyll 2.3 hadronic interaction models [95].

4.5, right) appears to be approximately constant for energies up to $10^{18.33}$ eV, above which the fluctuations in X_{max} decrease, indicating a divergence from lighter elements [95].

The Telescope Array Collaboration presented its most recent mass composition results at the 35th International Cosmic Ray Conference in 2017. These results are summarised in Figure 4.6, in which a comparison is made between four different measurements of X_{max} using data obtained from the experiment. The Figure illustrates $\langle X_{max} \rangle$ measurements obtained through the hybrid operation of the Black Rock Mesa and Long Ridge fluorescence detectors, hybrid measurements using the Middle Drum fluorescence detector, as well results produced through a stereo analysis (of two or more fluorescence detectors). The different methods agree in $\langle X_{max} \rangle$ within the respective systematic uncertainties. In contrast to the results obtained by the Pierre Auger Observatory, which are inconsistent with a mass composition constant with energy, the Telescope Array reports on a mass composition that favours light (mostly proton) nuclei [96].

In recent years the Pierre Auger and Telescope Array collaborations have undertaken a joint effort to reconcile differences observed in the respective mass composition results [97, 98]. Of particular interest is establishing whether observed discrepancies are related to experimental factors or result from different interpretations of hadronic interaction models. Both collaborations reported on this work in [99], in which a composition (obtained from air shower simulations from different primary nuclei) which best described the measured composition

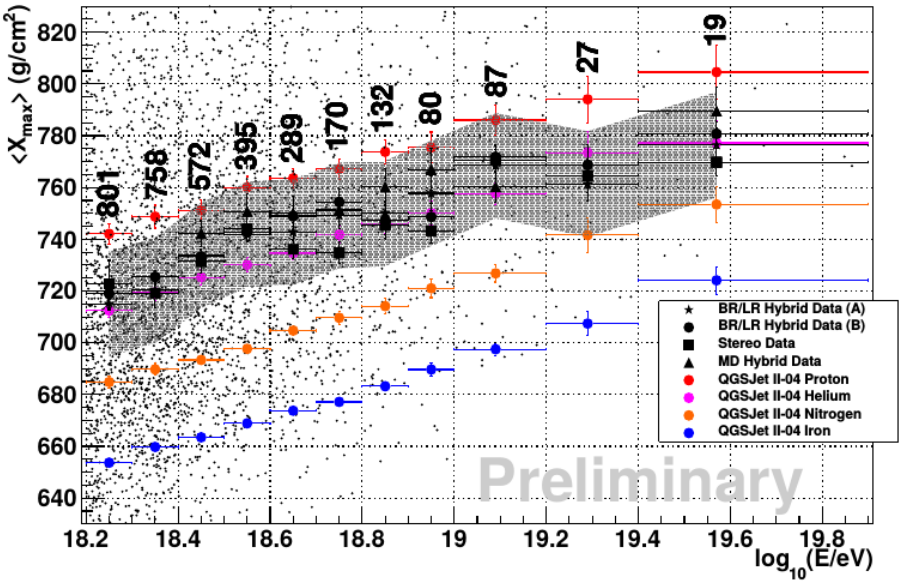

Figure 4.6: Mean X_{max} measured by the Telescope Array. The A and B labels for the Black Rock Mesa and Long Ridge hybrid results refer to two different analysis authors. Results are compared to pure proton, helium, nitrogen and iron expectations calculated using the QGSJetII-04 hadronic interaction model. The gray shaded region indicates the systematic uncertainty in the Black Rock Mesa and Long Ridge hybrid data (20.3 g cm^{-2}) [96].

presented by the Pierre Auger Collaboration was simulated through the Telescope Array's analysis chain, producing X_{max} distributions of the Auger composition. The simulated X_{max} distributions, which included all detector resolution effects and biases associated with the Telescope Array's analysis chain, were directly compared to Telescope Array mass composition measurements. The results of this study indicated that X_{max} data measured by the Telescope Array is compatible (within systematic and statistical errors) with a mixed composition which best describes X_{max} data measured by the Pierre Auger Observatory [99].

4.3 Anisotropy Studies

Anisotropy studies aim to assist in the current understanding of the processes through which cosmic rays are created, as results allow constraints to be placed on possible origin scenarios.

Cosmic rays are charged particles and will consequently suffer from deflections due to the presence of galactic and extragalactic magnetic fields as they propagate through the universe. This complicates anisotropy studies as most cosmic rays will lose all information pertaining to their points of origin upon arrival at Earth. A useful metric that can aid in understanding this phenomenon is the Larmor radius (r_L), which defines the radius of the helical motion of a charged

particle in the presence of a uniform magnetic field. For a particle of charge Z moving through a magnetic field of strength B, this can be expressed as

$$r_L = \frac{p_\perp}{Zq_eB} \tag{4.1}$$

where $p_\perp$ is the particle's momentum perpendicular to the magnetic field and q_e is the charge of an electron. For a proton of energy 10^{20} eV in the presence of the magnetic field of the Milky Way Galaxy (a microgauss-scale magnetic field), Equation 4.1 returns a gyroradius in the order of 100 kpc. For comparison, the radius of the Milky Way Galaxy is approximately 20 kpc. For cosmic rays of sufficiently large energies (above a few tens of EeV), deflections due to the presence of magnetic fields may be small enough such that information of their points of origin may be contained within their arrival directions [100].

The Pierre Auger Collaboration has recently reported on the observation of a broad-scale anisotropy in the arrival directions of cosmic rays, offering valuable insight into the origins of cosmic rays of energies above a few EeV [101]. The analysis used cosmic ray data measured during the period beginning in January 2004 through to August 2016 (with a total collected exposure of $\sim$76 800 km^2 sr yr) with energies above 4 EeV. Zenith angles ranged up to 80°, allowing for coverage of 85% of the sky. To remain consistent with previous anisotropy analyses [102–104], the data was separated into two energy ranges 4 EeV < E < 8 EeV and E $\geq$ 8 EeV.

Large-scale anisotropy studies are traditionally performed through a classical harmonic search for non-uniformities in the distribution of cosmic ray arrival directions as a function of right ascension (α). For a data set totalling N events, the first-harmonic Fourier components are given by

$$a_\alpha = \frac{2}{\eta}\sum_{i=1}^{N}\omega_i\cos\alpha_i \quad \text{and} \quad b_\alpha = \frac{2}{\eta}\sum_{i=1}^{N}\omega_i\sin\alpha_i \tag{4.2}$$

where each event is weighted by a factor ω_i accounting for non-uniformities in the SD's exposure as a function of α_i, and η is a normalisation factor given by the sum of all ω_i's. The amplitude (r_α) and phase (ϕ_α) of the first harmonic can be expressed as

$$r_\alpha = \sqrt{a_\alpha^2 + b_\alpha^2} \quad \text{and} \quad \phi_\alpha = \cot\left(\frac{b_\alpha}{a_\alpha}\right) \tag{4.3}$$

The distribution of the normalised rate of events above 8 EeV as a function of α is illustrated in Figure 4.7. The results indicate that for cosmic rays with energies above 8 EeV, the chance probability of the observed amplitude being due to statistical fluctuations in an isotropic cosmic ray distribution is 2.6×10^{-8}, corresponding to a post-trial significance of $5.2\,\sigma$. The anisotropy of these events can be well described by a dipole harmonic of amplitude $6.5^{+1.3}_{-0.9}{}^\circ$ in the direction of right ascension $\alpha = 100 \pm 10^\circ$ and declination $\delta = -24^{+12}_{-13}{}^\circ$. Figure 4.8

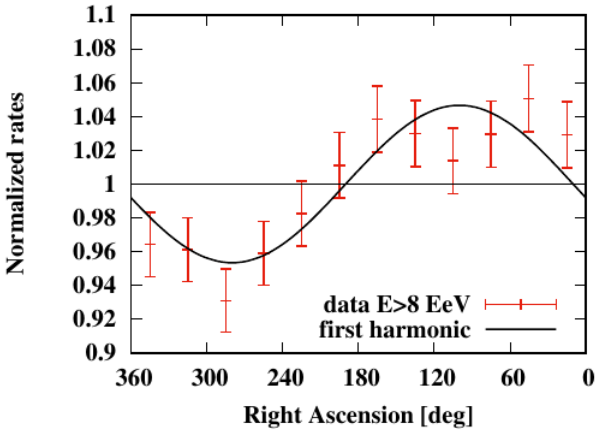

Figure 4.7: The normalised rate of events as a function of right ascension for cosmic rays with energies above 8 EeV. The solid line represents the first harmonic curve and has a reduced $\chi^2 = 10.5/10$ [101].

illustrates a sky map of the distribution of cosmic ray events with energies above 8 EeV. Interesting observations can be drawn between the observed cosmic ray dipole and the distribution of infrared-detected galaxies in the 2 Micron All-Sky Redshift Survey (2MRS) catalogue [105]. In the Galactic coordinate system, the cosmic ray dipole and the flux-weighted dipole of the distribution of galaxies are separated by approximately 55°, a discrepancy which can be improved once cosmic ray deflections due to galactic magnetic fields are taken into consideration. This is indicated by the arrows in Figure 4.8.

The results of this analysis favour an extragalactic origin for cosmic rays with energies above 8 EeV, which is in contrast to several origin models which propose a Galactic origin for cosmic rays of the highest energies [106, 107]. While the scientific consensus has long been that cosmic rays of the highest energies are extragalactic in their origins, this analysis is the first statistically significant confirmation of such a scenario.

In addition to the broad-scale dipole analysis, the Pierre Auger Collaboration has recently published results indicating a possible anisotropy in the arrival directions of cosmic rays of the highest energies from extragalactic gamma-ray sources [108]. The analysis used 5514 events with energies exceeding 20 EeV detected by the Observatory between the 1st of January 2004 and the 30th of April 2017 for a zenith angle range up to 80°. In this energy regime, cosmic ray deflections due to galactic and extragalactic magnetic fields are sufficiently small, allowing for small-to-medium scale arrival direction studies. Two source population sky models were formulated for active galactic nuclei (AGNs) and starburst galaxies. A sample of 17 radio-loud AGNs were selected from the Second Catalog of Hard *Fermi*-LAT sources (2FHL) [109] to form the AGN model. Twenty-three of the brightest starburst galaxies, as observed by *Fermi*-LAT, were selected as the basis

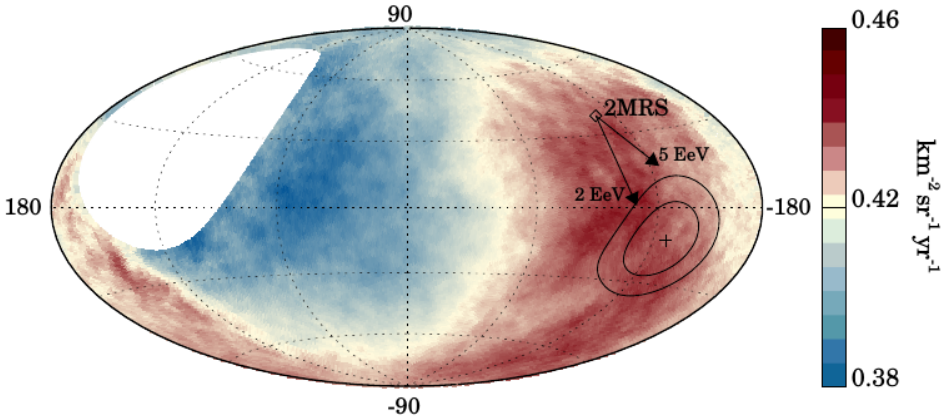

Figure 4.8: Sky map for the cosmic ray events with energies above 8 EeV. The results are displayed in terms of the galactic coordinate system, which has the Galactic centre positioned at the origin. The direction of the measured dipole is marked by the cross with the contours representing the 68% and 95% confidence level regions. The direction of the dipole in the 2MRS galaxy distribution is indicated by the diamond. The arrow heads represent the expected arrival directions of cosmic rays at Earth, assuming common values of $E/Z = 5$ EeV or 2 EeV where Z is the atomic number [101].

of the starburst galaxy model. All objects selected for both models were required to lie within a radius of 250 Mpc.

The selected events were used in an unbinned maximum-likelihood analysis to measure the strength of each model (AGN or starburst galaxies) against the null hypothesis of an isotropic cosmic ray distribution. A test statistic (TS) representing the deviation away from isotropy was calculated for each model scenario over a range of minimum energy thresholds, beginning at 20 EeV and increasing in 1 EeV steps[4]. Figure 4.9 illustrates the TS as a function of threshold energy for different population models. The effect of accounting for the attenuation of UHECR is minimal for the starburst galaxy source model, especially for threshold energies above 39 EeV. In comparison, the TS for the AGN model appears to suffer greatly when attenuation is included in the analysis.

Figure 4.10 shows the 2-dimensional profile for the TS for both source population models. The strongest deviation from isotropy is found in the starburst galaxy model scenario for energies above 39 EeV. This deviation, significant to the 4σ level, is found at an angular scale of $12.9^{+4.0}_{-3.0}{}^{\circ}$ and corresponds to an anisotropy fraction of $9.7^{+4.0}_{-3.8}$%. In other words, the results indicate the possibility that $\sim$ 10% of observed cosmic rays above 39 EeV originate from a handful of

[4]The minimum p-value calculated in each case was penalised for the energy scan. The penalisation factor was estimated using Monte Carlo simulations.

starburst galaxies. For comparison, the strongest deviation for the AGN model was a 2.7 σ excess for the energies above 60 EeV.

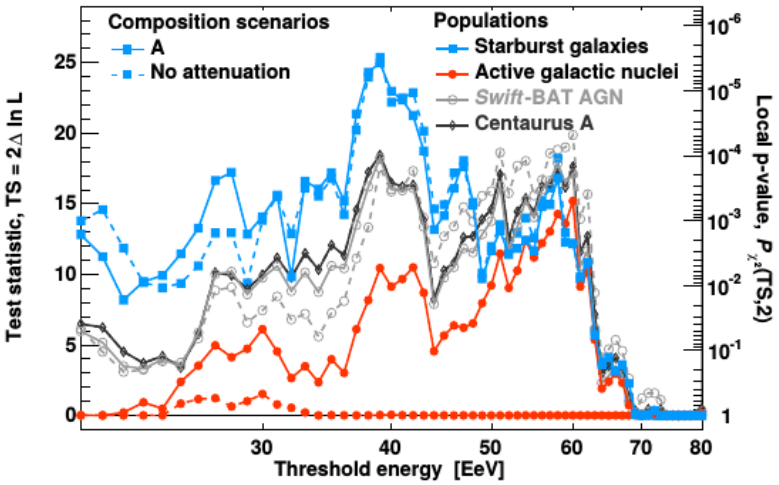

Figure 4.9: TS as a function of threshold energy. Different composition scenarios account for the attenuation of UHECR (originating from distant objects) through interactions with the cosmic microwave background and were modelled to reproduce composition and spectral constraints set by the Pierre Auger Observatory. The model labelled as 'A' was determined to best describe the observed data and assumes a hard injection index of $\gamma = 1$ for homogeneously distributed sources through the local Universe [108].

As noted in [108], the starburst model was not an *a priori* hypothesis and consequently, the results should be treated carefully. Numerous anisotropy searches have been performed from within and beyond the Pierre Auger Collaboration, presenting a sizeable challenge as there is no reliable way to account for all previous and hidden trials. The post-trial significance of 4 σ accounts for the search of the optimal search radius and anisotropic fraction, and also includes a statistical penalty for a scan in energy.

In 2014 the Telescope Array Collaboration reported evidence of an excess of cosmic ray events with energies above 57 EeV (referred to as the *hotspot*) in the northern sky, $\sim 19^\circ$ off the super-galactic plane [110]. The data used in the analysis was collected over a 5 year period between May 2008 and May 2013. A total of 72 events were found to have met the following conditions

1. At least four surface detector stations were included in the event.

2. The reconstructed zenith angle of arrival of the event was less than 55°.

3. The reconstructed energy of the event exceeded 57 EeV - a threshold determined from AGN correlation analysis performed by the Pierre Auger Observatory [111].

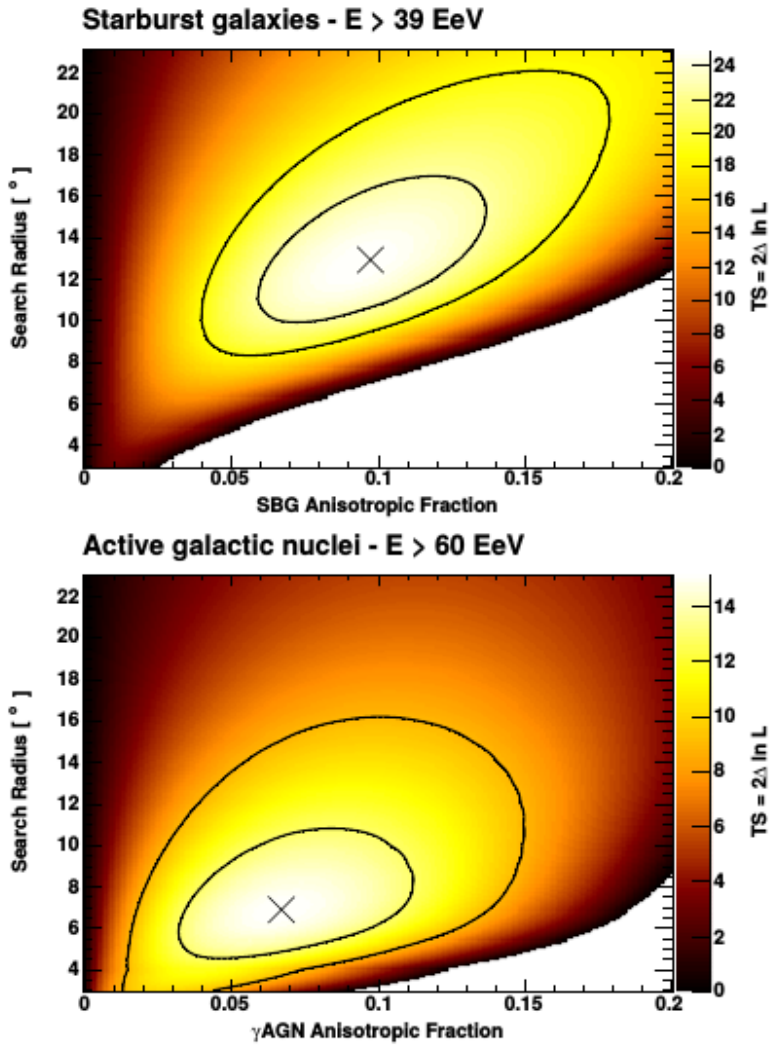

Figure 4.10: The best fit search radius and anisotropic fraction for the starburst galaxy (top) and AGN (bottom) source population models. The solid lines indicate the 1 and 2 σ confidence contours [108].

When projected onto a sky map, it was observed that a cluster of events appeared to be centred at a right ascension $\alpha \simeq 150^\circ$ and declination $\delta \simeq 40^\circ$, within a diameter of $\sim 30^\circ$ - 40°. The significance of this observation was tested by oversampling using 20° radius circles - a method based on elements from the AGASA collaboration's search for large-scale anisotropy [112]. The integral number of cosmic ray events was calculated across a 20° radius circle at each point along a $0.1^\circ \times 0.1^\circ$ grid over the field of view of the Telescope Array (0° to 360° in α, -10° to 90° in δ). The maximum number of observed events was determined to be 19 within an integration region centred at $\alpha = 146.7^\circ$ and $\delta = 43.2^\circ$. A Monte Carlo simulation was used to show that, within the same region as the hotspot, only 4.49 events with energy above 57 EeV were expected for an isotropic cosmic ray

flux. The excess of observed events in the hotspot corresponded to a 5.1 σ significance, later revised to a post-trial significance of 3.4 σ. The analysis was revisited following a further two years of exposure and showed an additional 5 events (a total of 24 events) with a background expectation of 6.88 within the hotspot. No change in the post-trial significance of 3.4 σ was observed [113]. A sky map of the hotspot from the original analysis is shown in Figure 4.11.

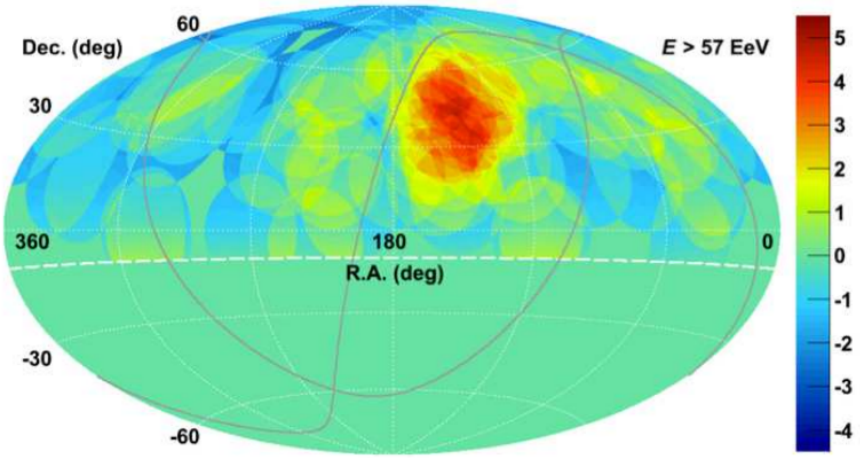

Figure 4.11: A sky map (in equatorial coordinates) of the hotspot observed by the Telescope Array. The hotspot is centred at $\alpha = 146.7^{\circ}$ and $\delta = 43.2^{\circ}$. The field of view of the Telescope Array is defined as the region above the dashed line at $\delta = -10\,\text{deg}$. The colour scale represents the excess in units of standard deviation, σ [110].

Chapter 5

Monitoring the Energy Scale of the Pierre Auger Observatory

Thousands of cosmic ray air shower events have been successfully detected by the Pierre Auger Observatory since operation commenced in 2004. A subset of these events meet the requirements to be detected and reconstructed by both of the Observatory's two independent detectors, the SD and FD. As discussed in Section 3.2.3, the Pierre Auger Observatory's FD utilises the fluorescence technique to obtain a near-calorimetric measurement of the energy of the primary cosmic ray, E_{FD}. Not only is this key measurable quantity important in all cosmic ray analyses, it is also used to calibrate the SD energy scale (see Section 3.4) through comparisons with S_{38}, the zenith angle-corrected shower size measured by the SD.

This Chapter will begin with a discussion of how the existing FD calibration procedures are used to monitor both the short and long term stability of the fluorescence telescopes. This will be followed by an extensive analysis of the long term stability of the Pierre Auger Observatory's energy scale.

5.1 Calibration Constants

The fluorescence technique aims to estimate the energy of the primary cosmic ray by using the atmosphere as a calorimeter. An important detail of this technique is the proportionality of the fluorescence yield to the energy deposited in the atmosphere. The FD calibration aims to provide a reliable conversion between the electronic signal recorded by the FD telescopes (in units of ADC counts) to a photon flux at the telescope's aperture, which can be converted to an energy deposit as a function of atmospheric slant depth. The process outlined in this Section is discussed in [72].

For a given FD camera pixel, the signal measured in a given ADC time bin directly corresponds to the fluorescence light emitted at a particular segment of

atmospheric depth (ΔX) along the axis of the shower. The conversion from ADC counts (denoted by N_{ADC}) for the i^{th} pixel can be expressed as

$$N_{ADC,i} = \frac{dE}{dX} \times Y_\gamma \times \Delta X \times T \times \frac{A}{4\pi r^2} \times C_i^{abs} \tag{5.1}$$

where dE/dX is the energy deposit specific to that part of the track, Y_γ is the fluorescence photon yield per unit of energy deposit and T characterises the transmission of fluorescence photons through the atmosphere along a light path r towards a telescope of aperture A. The final term, C_i^{abs}, represents the absolute calibration factor for the pixel and is dependent on several factors including: the optical efficiency of the telescope, the quantum efficiency, collection efficiency and gain of the pixel and the electronics used to convert the measured current into a digital quantity. C_i^{abs} has units of photons per ADC count.

The determination of C^{abs} on a pixel by pixel basis is achieved through the absolute calibration of the FD telescopes (Section 3.2.2.1). Performed one telescope at a time, the calibrated light source is tuned to uniformly illuminate the entire optical system at a wavelength of 375 nm. The absolute calibration measurements have a quoted uncertainty of 9% [89], although efforts have been made to reduce this to the order of 5% [114].

In conjunction with the absolute FD calibration, a relative FD calibration (consisting of three separate calibration procedures) is performed on a nightly basis to track the daily performance and time stability of the entire telescopic system between consecutive absolute calibration campaigns (see Section 3.2.2.2). Of most importance is cal A, which monitors the response of the FD cameras through direct illumination from fixed light sources[1]. For each measurement of cal A, 50 rectangular shaped LED pulses illuminate each FD camera at a frequency of 1/3 Hz. An example cal A calibration pulse is shown in Figure 5.1.

For a given telescope, the raw cal A data is processed to determine the mean integral charge (denoted as $< Q^{cal\ A} >$) for the i^{th} pixel over N_{LED} pulses. For the k^{th} calibration measurement this can be expressed as

$$< Q^{cal\ A} >_{i,k} = \sum_{n}^{N_{LED}=50} \frac{Q_{n,i,k}^{cal\ A}}{N_{LED}} \tag{5.2}$$

where

$$Q_{n,i,k}^{cal\ A} = \left(\sum_{l=t_{start}}^{l=t_{stop}} n_{ADC_l} \right)_{n,i,k} \tag{5.3}$$

is the integral signal in ADC counts for the n^{th} calibration pulse beginning and ending in the t_{start} and t_{end} time bins, respectively, and l is a single 100 ns ADC time bin.

[1]It should be noted that this measurement is made when the FD shutters are closed.

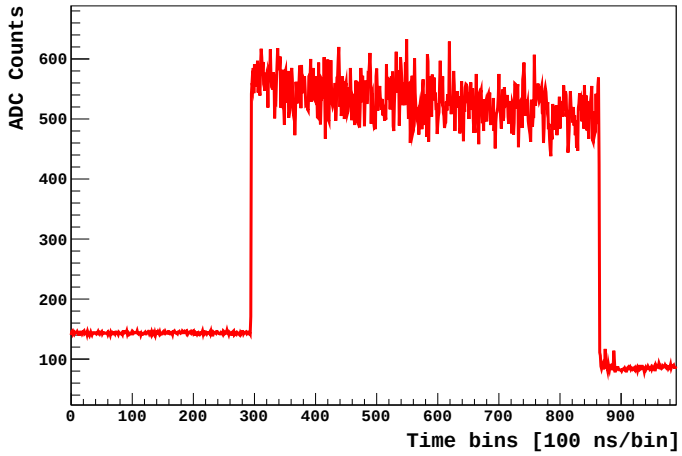

Figure 5.1: An example light pulse emitted during the cal A relative calibration. The rectangular light pulses have a typical width of 57µs. The decay of the pulse (as well as the discrepancy between the pedestal before and after the pulse) is due to the AC coupling of the PMT to the FD electronics. The decay of the signal, as well as the underlying pedestal are corrected during data processing.

For each cal A measurement, a relative calibration constant for the i^{th} pixel (denoted as C_i^{rel}) is calculated by normalising Equation 5.2 with respect to a reference value $< Q^{cal\,A} >_i^{ref}$ - defined as the same measurement as Equation 5.2 taken within one hour following the absolute FD calibration. For the k^{th} calibration run, this can be expressed as

$$C_{i,k}^{rel} = \frac{< Q^{cal\,A} >_{i,k}}{< Q^{cal\,A} >_i^{ref}} \tag{5.4}$$

giving the relative change in the absolute gain of the pixel of interest. Further processing leads to the calculation of absolute calibration constants (from here on we will simply refer to these as the calibration constants), denoted by C_{FD}, which monitor any deviations from the absolute calibration factor of the reference calibration[2]. In other words, the calibration constants are free to take on any value to compensate for short and long term variations in the response of individual pixels. For the i^{th} pixel at the time of the k^{th} calibration measurement this is expressed as

$$[C_{FD}]_{i,k} \propto \frac{C_i^{abs}}{C_{i,k}^{rel}} = \frac{< Q^{cal\,A} >_i^{ref}}{< Q^{cal\,A} >_{i,k}} \times C_i^{abs} \tag{5.5}$$

Further corrections are made to account for other factors, including the stability of the LED light source used in cal A measurements. This light source is housed towards the rear of each FD site building and is monitored by the LED Calibration Unit (LCU), a photodiode [115]. The calibration constants are calculated as

[2]Calibration constants can be thought of as an *inverse gain*.

follows

$$[C_{FD}]_{i,k} = \frac{< Q^{cal\ A} >_i^{ref}}{< Q^{cal\ A} >_{i,k}} \times C_i^{abs} \times \frac{LCU_k}{LCU^{ref}} \times LCU_{corr} \times Halo \tag{5.6}$$

where LCU_k and LCU_{ref} are the values of the LCU at the time of the k^{th} and reference calibration measurements, respectively. LCU_{corr} accounts for the stability of the LED itself and $Halo$ is a factor (determined through simulations) which accounts for the reflections of 'drum' photons off the surface of the camera (discussed in greater detail in Appendix D). Calibration constants are measured with an uncertainty of the order of 2% [89].

As cal A is typically performed before and after data acquisition, it is possible to calculate two calibration constants for each pixel on a nightly basis. The nightly calibration constant databases are produced using measurements acquired following the conclusion of data acquisition as the response of the FD system is typically more stable (compared to before data acquisition) [72]. The possible implications of this choice are discussed in Section 5.2.

Finally, an important yet subtle detail regarding the calibration of the FD is that the procedure provides a conversion for the number of 375 nm-equivalent photons at the aperture, owing to the operational wavelength of the light source used during the absolute calibration.

5.1.1 Monitor for Camera Performance

The calibration constants monitor the stability of the pixel performance with respect to the reference calibration measurements, providing a convenient measure of the telescope's stability over various time scales. Figure 5.2 illustrates the calibration constants for a single pixel from Coihueco Telescope 4 across 12 years of operation. A clear seasonal variation can be seen in the calculated values, most likely a consequence of temperature effects on the PMT gains revealed by the nightly relative calibration [72]. The most striking feature is the large discontinuity observed at the beginning of 2010, which can be attributed to a re-calibration (or *flat fielding*) of this particular telescope during the 2010 absolute calibration campaign [116].

When studied across shorter time scales (Figure 5.3) it can be seen that the calibration constants behave in a peculiar way. For example, the initial calibration constant acquired for a given observational shift is noticeably greater than all subsequent measurements belonging to that shift. This measurement is followed by continuously decreasing values of the calibration constants, which eventually reach some minimum value before appearing to recover towards the conclusion of the shift. The same pattern is observed in all 3 observational shifts displayed in Figure 5.3. Laboratory experiments indicate that this behaviour is induced by the exposure of the FD pixels to the night sky background, with a greater effect for the first night of each observational shift after a dark *recovery* period of $\sim$ 2 weeks [117, 118].

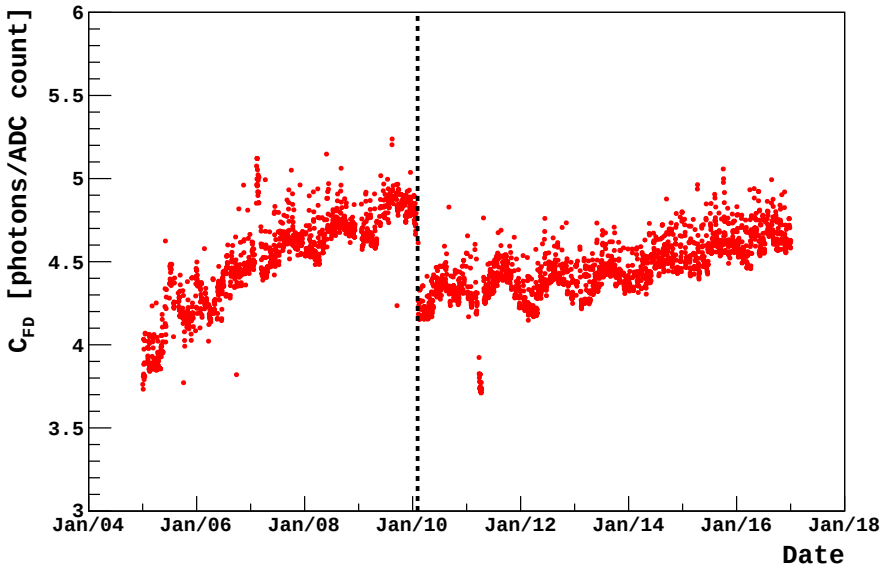

Figure 5.2: Calibration constants for pixel 210 of Coihueco Telescope 4 since January 2005. The date of the 2010 absolute calibration campaign is marked by the dashed line.

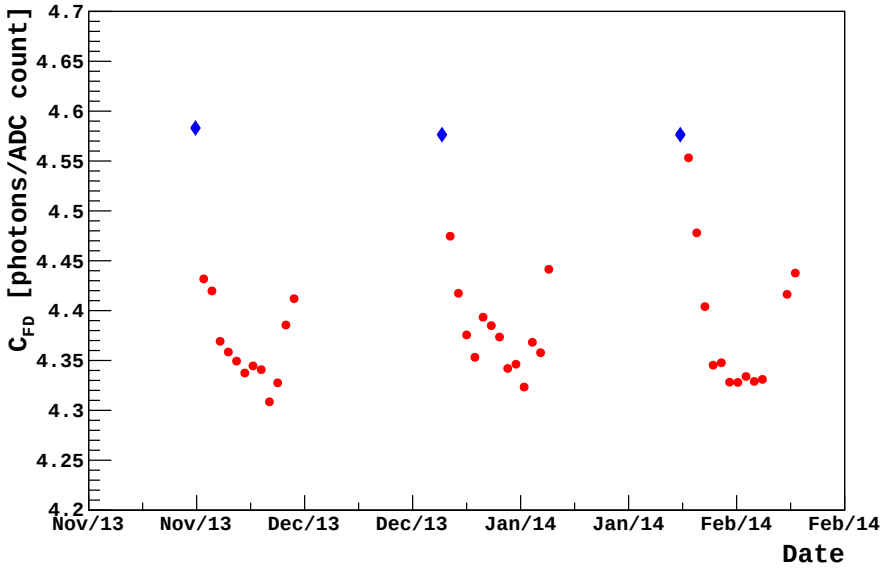

Figure 5.3: Calibration constants for pixel 210 of Coihueco Telescope 4 over a period of approximately 3 months (corresponding to 3 observational shifts). The calibration constant measured following the first night of data acquisition for each shift is marked by the blue diamond. Calibration constants are a measure of the inverse gain.

5.2 Running Cal A Measurements

In 2014 the relative calibration procedure was modified to introduce a running cal A measurement, performed during data acquisition for each operating FD telescope [119, 120]. In contrast to the regular relative calibration, which requires manual operation from human *shifters*, the running cal A is performed automatically every 30 minutes during data acquisition, with minimal impact on the standard operation of the FD[3].

The results of the running cal A offer valuable insight into the stability of individual FD telescopes over very short time scales i.e. over the course of a single night of data acquisition. An example of the average performance of individual telescopes is illustrated in Figure 5.4, where a proxy for the pixel gain is plotted as a function of time. For comparison, the results from the regular cal A measurement are displayed and indicate a small discrepancy, on the order of $\sim 2\%$ (depending on the telescope), between the relative calibration performed after and prior to data acquisition. This is consistent with the previously reported stability of the relative calibration $(2-3\%)$ [72].

An interesting observation is the sudden gain decrease immediately following the commencement of data acquisition, indicated by the first running cal A measurement recorded by each telescope. This is followed by a steady increase in the gain through the course of the night. Previous studies detailed in [118] indicate that the sudden exposure of the FD pixels to the night sky background induces a rapid gain reduction of the order of a few percent, presumably caused by charging processes within the PMT structure. This is followed by a gradual recovery phase with a time constant of comparable duration to the observation night, behaviour which is consistent with the results presented in Figure 5.2.

There exists a modest discrepancy between the measurement used to produce the nightly FD calibration database (acquired following the conclusion of data acquisition) and the 'true' gain throughout the night. This difference can be as large as $\sim 4\%$, although this varies between telescopes as well as the time of night, and has obvious implications on the cosmic ray energy, E_{FD}. Figure 5.4 indicates a maximum discrepancy immediately following the commencement of data acquisition, a feature that is likely to be consequence of the FD pixels taking time to reach a stable state. Another complicating factor is that the gain discrepancy may have a seasonal dependence, as the brightness of the night sky background (which is correlated with the background stars) can fluctuate throughout the year.

[3]The FD shutters do not close for the running cal A.

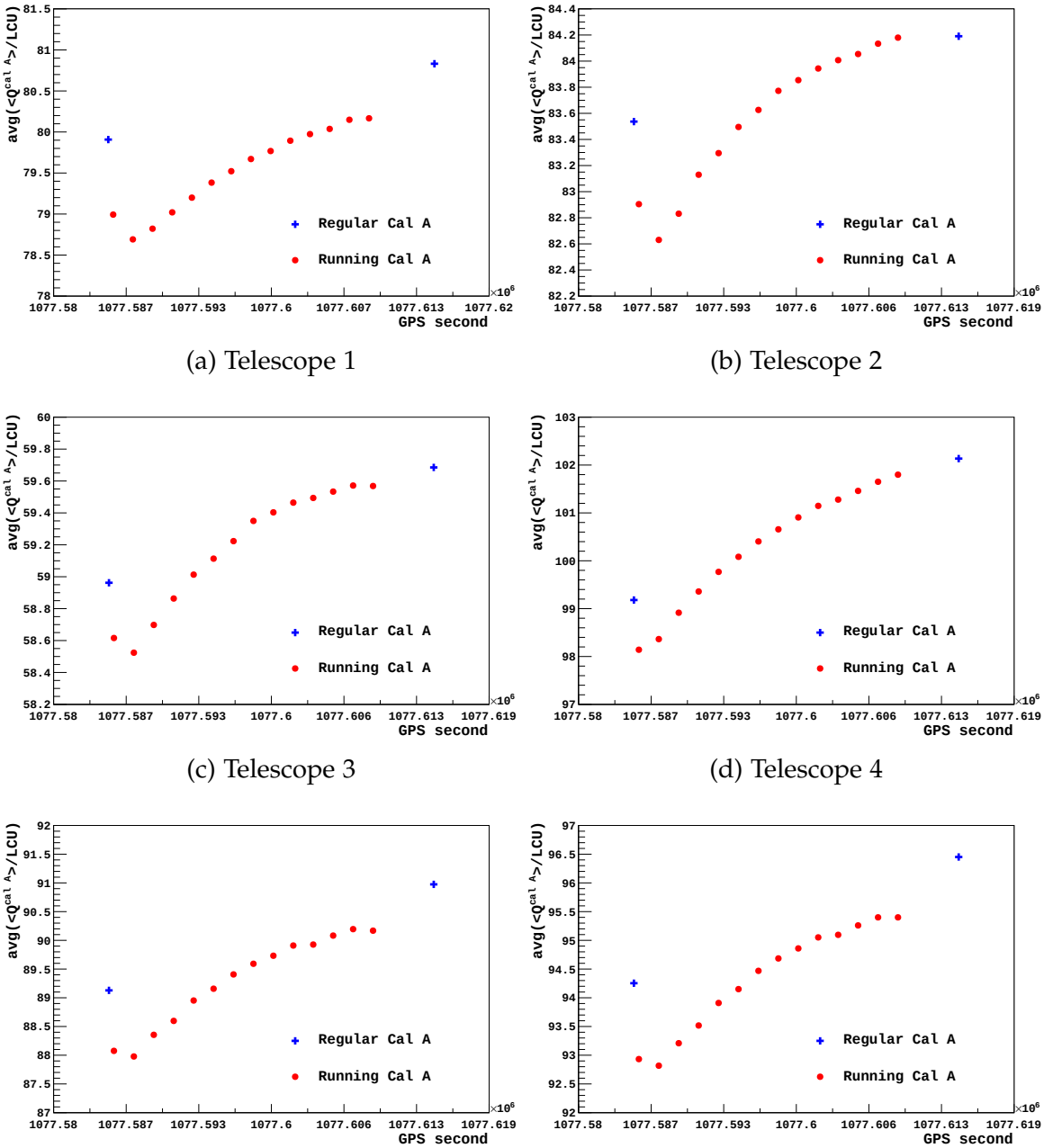

(a) Telescope 1

(b) Telescope 2

(c) Telescope 3

(d) Telescope 4

(e) Telescope 5

(f) Telescope 6

Figure 5.4: Cal A results for all Coihueco telescopes measured across a single night during the February 2014 observation shift. The vertical axis (a proxy for the pixel gain) is the ratio of the integrated cal A pulse and the LCU, averaged across all pixels for a given telescope. The blue crosses indicate the results acquired from the standard cal A, measured before and after data acquisition. The red points, separated in time by 30 minutes, indicate the running cal A measurements.

5.3 Calibration Constant Temperature Dependence

The FD telescopes are housed within climate-controlled buildings designed to minimise any temperature dependent effects on the gain of the FD pixels (the temperature gain coefficient of the FD pixel is quoted by the manufacturer to be $-0.2\%\,\text{per}\,^{\circ}\text{C}$ [115]). The climate within the FD buildings is controlled by an air-conditioning unit and is monitored at several locations:

- **TemperatureCam_A:** measured by a sensor located at the side of the aluminium camera body.
- **TemperatureCam_B:** measurement of the air temperature above the camera, above the electronics boards.
- **TemperatureCalib:** measured inside the calibration room which is situated towards the rear of each FD building.
- **TemperatureOutside:** measured outside the FD building. It should be noted that these sensors are exposed to sunshine at times.
- **TemperatureBays:** measured inside the bay, above the central door close to the air-conditioning outlet.

All temperature measurements are available from the monitoring database with regular measurements (made every minute) dating back to November 2010 with the exception of TemperatureBays, for which measurements exist since May 2007. Of particular interest here are the measurements of TemperatureCam_A, which can be used as an indicator for the average FD pixel temperature. The alternative camera temperature measurement (TemperatureCam_B) will be systematically larger (relative to TemperatureCam_A) due to heat emitted from the electronics boards. The result is a small discrepancy between the two measurements (of the order of $\sim 2-3^{\circ}\text{C}$), as illustrated in Figure 5.5.

It is important to stress that TemperatureCam_A only provides an estimate for the temperature of an individual FD pixel, as the sensor is placed on the side of the aluminium casing which houses the FD pixels. Due to the positioning of the sensor on the side of the camera body, it is possible that a lag exists between the true temperature of a pixel (on the opposite side of the camera to that of the sensor) and the value recorded by the sensor. Consequently, the results presented in this Section only provide a general indicator of the temperature dependence of the FD pixel gain.

Figure 5.5 suggests that the camera temperature (monitored through TemperatureCam_A) has a seasonal modulation of amplitude $\sim 3^{\circ}\text{C}$. Using the manufacturer's quoted temperature gain coefficient of $-0.2\%\,\text{per}\,^{\circ}\text{C}$, we estimate that the FD pixel gain (in the extreme scenario where the gain of the FD pixels are not monitored regularly) may vary seasonally by as much as $\sim 0.6\%$. It is unlikely

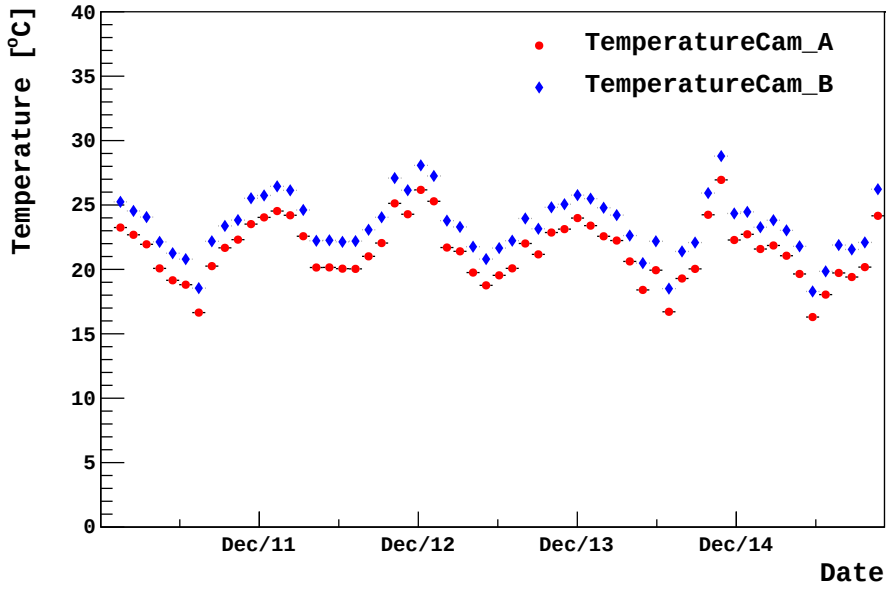

Figure 5.5: Camera temperature for Coihueco Telescope 2 measured during observational shifts beginning in January 2011 through to December 2015. Each data point represents the average camera temperature for a single FD observing shift. Measurements of TemperatureCam_B (blue diamonds) return slightly larger values compared to TemperatureCam_A (red circles), most likely due the warming of the air above the camera from the FD electronics board. A clear seasonal variation in the temperature is observed which peaks during the Southern hemisphere's summer months, as expected.

that such an extreme modulation in the FD pixel gains is not already accounted for at some level, as the nightly calculation of the FD calibration constants should compensate for effects induced by short term temperature variations.

5.4 Calibration Constant Background Light Dependence

In Section 5.1.1 it was mentioned that the exposure of the FD pixels to the night sky background can induce some unexpected behaviour, particularly with regards to the gains of the FD pixels. In this Section we use results obtained through the running cal A measurements to study any correlation between the night sky background exposure and changes in the pixel gain. Details regarding how the FD telescopes monitor the night sky background are provided in Chapter 6.

The top plot of Figure 5.6 illustrates the average running calibration constants for Coihueco Telescope 2 for a single night of data acquisition. The observed trend is consistent with the behaviour shown in Figure 5.4, recalling that the calibration constants are a measure of the inverse gain, in that the average value of the calibration constant has a steady downwards drift throughout the night.

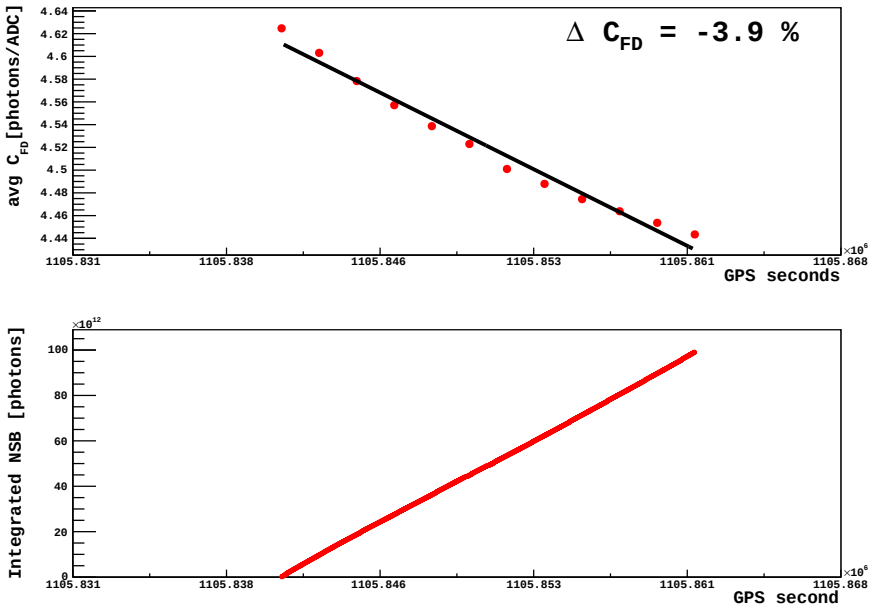

Figure 5.6: The running calibration constants averaged over all pixels for Coihueco Telescope 2 measured during a single night in January 2015 (top). It should be noted that only the calibration constants derived from the running cal A measurements are shown here. The bottom figure illustrates the integrated night sky background photon flux(across the same time period) for this particular telescope. In contrast to the running calibration constants, which are measured every 30 minutes, the night sky background is sampled every 30 seconds during data acquisition. It should be noted that this particular night remained free of any disruptions to data acquisition (such as the FD shutters closing) as the integrated night sky background only increases with time and never unexpectedly plateaus.

The nightly change in the average calibration constants (ΔC_{FD}) can be estimated by a fitted linear function, as illustrated in the figure. The bottom plot of Figure 5.6 shows the integrated night sky background photon flux observed by the same telescope over the same period of time.

From Figure 5.6 it can be seen that a decrease in the calibration constants correlates with increasing night sky background exposure, at least over the time period concerned in this particular example. This exercise is repeated for all data acquisition nights during which running calibration constants were measured, with results summarised in Figure 5.7. The non-zero slope of the fitted function implies that the nightly changes in the gains of the FD pixels are not completely independent on the pixels' exposure to background light. Furthermore, the negative slope suggests that the greater a pixel's exposure to the night sky background, the more negative (positive) the change in the calibration constant (gain).

Figure 5.8 illustrates ΔC_{FD} as a function of time for Coihueco Telescope 2 for which a small seasonal modulation of amplitude $\sim 0.7\%$ is observed. This is an

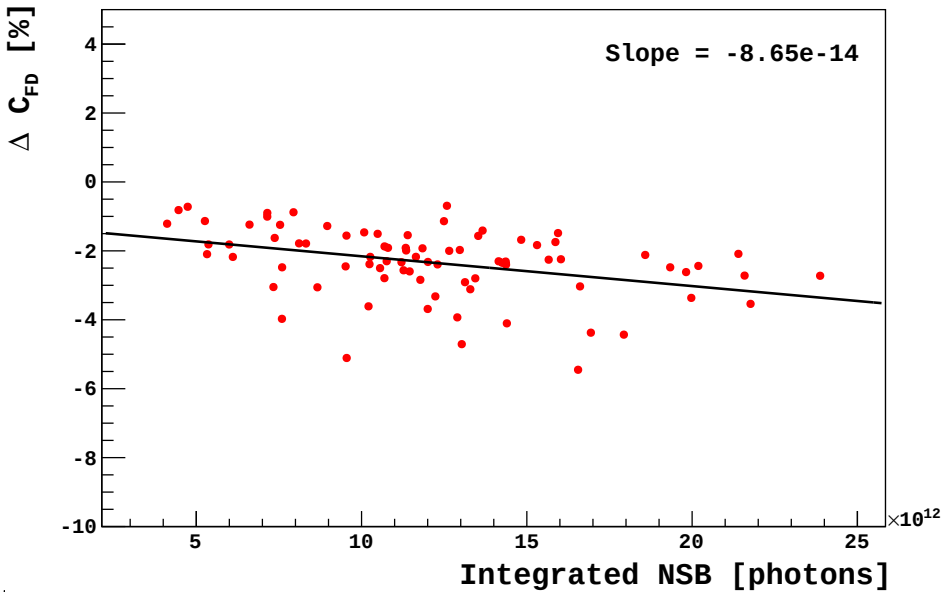

Figure 5.7: The change in the nightly calibration constants as a function of the integrated night sky background for Coihueco Telescope 2. It is important to note that the horizontal axis is dependent on both the intrinsic brightness of the night sky background as well as the duration of exposure.

interesting observation which suggests that the change in the calibration constants is greatest towards the beginning (or end) of the year. Before trying to study how this modulation is correlated with the night sky background exposure, it is important to decouple the two components which determine the total observed night sky background. These two components are the brightness of the night sky background itself as well as the duration for which the FD pixels are exposed. The seasonal dependence of these two components are shown in Figure 5.9.

From the left hand plot of Figure 5.9 it can be seen that this telescope's exposure to the night sky background is at its shortest (in duration) towards the beginning (and end) of the year. This is an expected result as the FD observational shifts are typically longer during the winter months. Having said that, it might be expected that due to their increased exposure during the winter months, the change in the nightly calibration constants (Figure 5.8) would also be at their greatest (most-negative) during this time. However, the average exposure time should be coupled with the intrinsic brightness of the night sky background (right hand plot of Figure 5.9), which appears to be approaching a minimum during the winter months. The fact that the night sky background is at its dimmest seems to negate the effect of the increased exposure, which is reflected in the relatively small (compared to the beginning and end of the year) change in the nightly calibration constants. Conversely, the periods of brighter night sky background

appear to coincide (despite the shorter exposure periods) with the times at which the change in the nightly calibration constants are at their greatest.

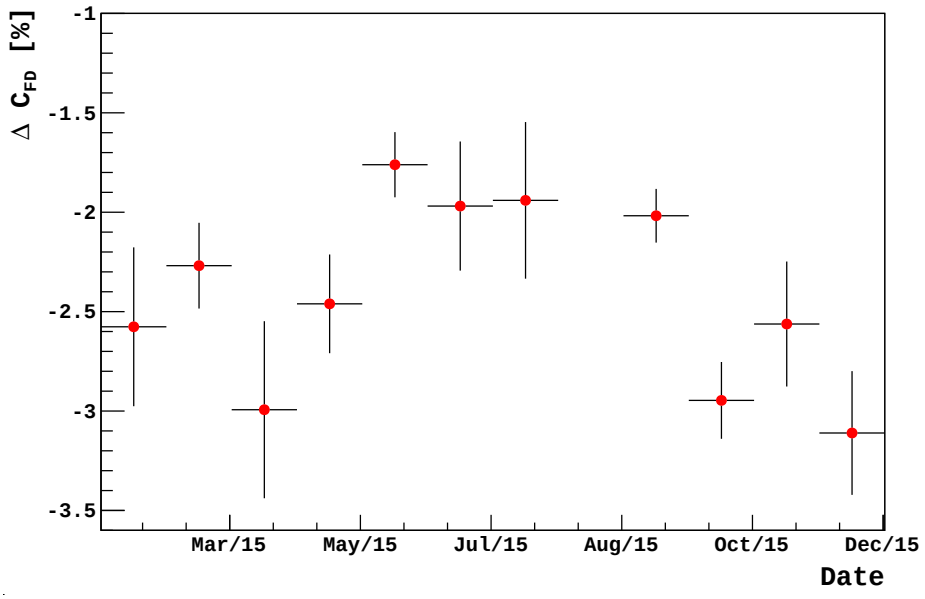

Figure 5.8: The nightly change in the calibration constants (for Coihueco Telescope 2) as a function of time. The shape of the profile suggests a small seasonal modulation. The horizontal bin has width equal to approximately 1 month.

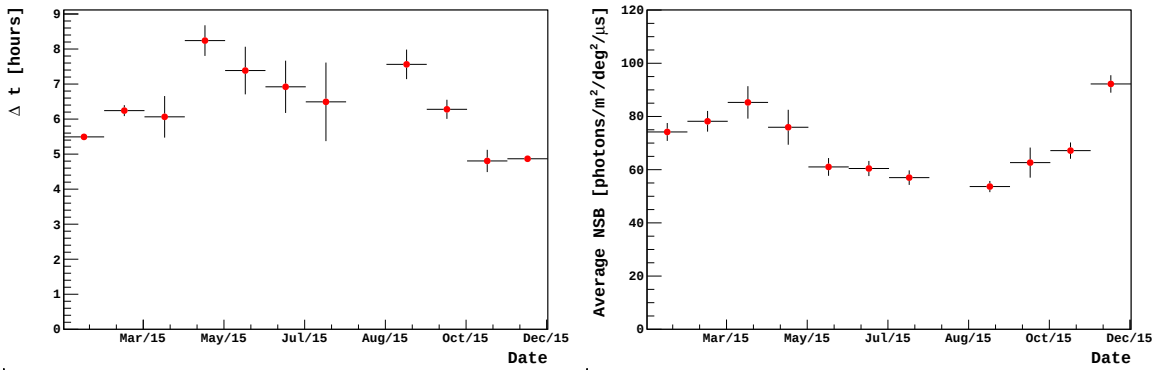

Figure 5.9: Left: The vertical axis represents the average time over which running calibrations are measured for Coihueco Telescope 2 in 2015 and is an indicator for the duration of the telescope's exposure to the night sky background. Right: The average night sky background photon flux observed by Coihueco Telescope 2 as a function of time. The horizontal bin width in both plots is equal to approximately 1 month.

The results presented here suggest that a correlation exists between the gain fluctuations of an FD pixel and its exposure to the night sky background. The

physical mechanisms driving this phenomenon is a topic which requires further work to completely understand. It is hypothesised that sudden changes in the illumination of the FD pixels introduces a *space-charge* effect within the PMT structure. For example, when the shutters are first opened at the commencement of data acquisition, the FD pixels are suddenly exposed to a sudden increase in illumination. The increased background signal creates a space-charge which acts to inhibit the passage of photoelectrons from the pixel's photocathode to its first dynode, as well as the passage of electrons between subsequent dynodes thereafter. Such a phenomenon could introduce a sudden drop in the pixel's gain following the commencement of data acquisition, as observed in Figure 5.4. As the night evolves, the effectiveness of the space-charge begins to leak away, allowing the gain to steadily recover. This is further complicated by the continual exposure of the pixel to background light, which presumably continues to feed the space-charge at a steady rate, inhibiting the rate at which the pixel's gain can recover.

5.5 Long Term Stability of the Observatory's Energy Scale

The hybrid design of the Pierre Auger Observatory allows for the measurement of two independent energy estimates (or in the case of the SD, a quantity that is representative of the size of the particle shower from which the energy can be inferred) of the primary cosmic ray. These parameters have been introduced earlier as E_{FD} and S_{38} for the FD and SD, respectively. In this Section we investigate the long term stability of the Observatory's energy scale. The data used in the following analysis comprises of 8895 high quality vertical (i.e. $\theta < 60^{\circ}$) hybrid showers with a minimum reconstructed FD energy of 3 EeV (above which the SD is 100% efficient), observed during the period spanning January 2005 through to December 2015. A complete list of quality cuts is provided in Appendix A.

This Section will begin with an analysis of the long term stability of the Observatory's energy scale during which notable features will be highlighted. This will be followed by an investigation into recent cosmic ray reconstruction and analysis improvements, and the effect of these improvements on the energy scale's stability.

5.5.1 Functional Fit to the Long Term Energy Scale

The stability of the Observatory's energy scale can be monitored through the ratio of E_{FD} and S_{38} (hereinafter the energy scale ratio or ESR) as a function of time. As the ESR is defined to be the ratio of two independent energy estimates, then it is expected to be equal to a constant value[4]. The long term behaviour of the ESR is illustrated Figure 5.10. It is obvious that the ESR is not constant as a function of time, as a clear seasonal modulation which appears to peak during the Southern

[4]Not necessarily equal to 1. This would be the case if the ESR were defined to be E_{FD}/E_{SD}.

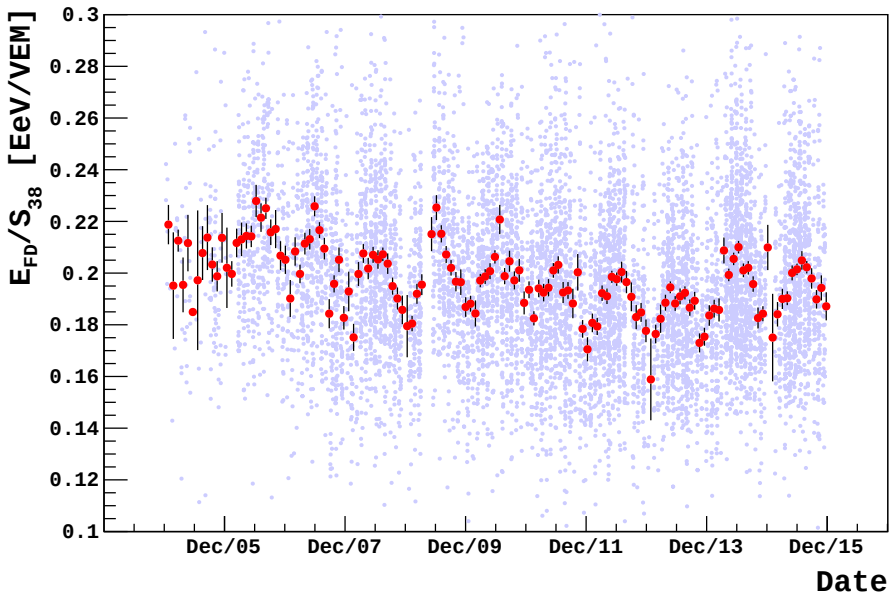

Figure 5.10: The ESR spanning 11 years of hybrid data collection. A red profile plot (red circles) of horizontal bin width equal to 1 synodic month (29.53 days) is overlaid on a scatter plot (blue dots). Statistical uncertainties are indicated by the error bars. Cosmic ray shower data were reconstructed using a modified version of the *v3r3* Offline branch.

hemisphere's winter months, along with a downward long term drift are observed in its evolution.

The exact origins of the ESR's seasonal modulation and long term drift may be solely associated with the SD, FD or (most likely) a combination of factors from both detectors. The Observatory's hybrid design allows for a variety of cross-checks to be made between cosmic ray energy measurements. As a first guess, the ESR is parametrised by a sum of a linear and sinusoid function:

$$\frac{E_{FD}}{S_{38}}(t) = B + m\left(\frac{t-t_s}{T}\right) + A\sin\left(\phi + 2\pi \times \left(\frac{t-t_s}{T}\right)\right) \tag{5.7}$$

where T is the period fixed to one year (in seconds), ϕ is the phase and t is the time in seconds since t_s (chosen to be the 1st of January 2006), and the fit parameters m and A are proportional to the drift and amplitude of the seasonal modulation, respectively. The fit result is displayed in Figure 5.11 and indicate a drift in the ESR of $\sim$ 0.9% per year and a seasonal modulation of amplitude $\sim$ 5.6% (half peak-to-peak).

The goodness-of-fit of the function can be inferred from the reduced χ^2, which is estimated to be $\sim$ 3.5, indicating that this particular functional fit is not completely representative of the underlying data. The lack of compatibility may be

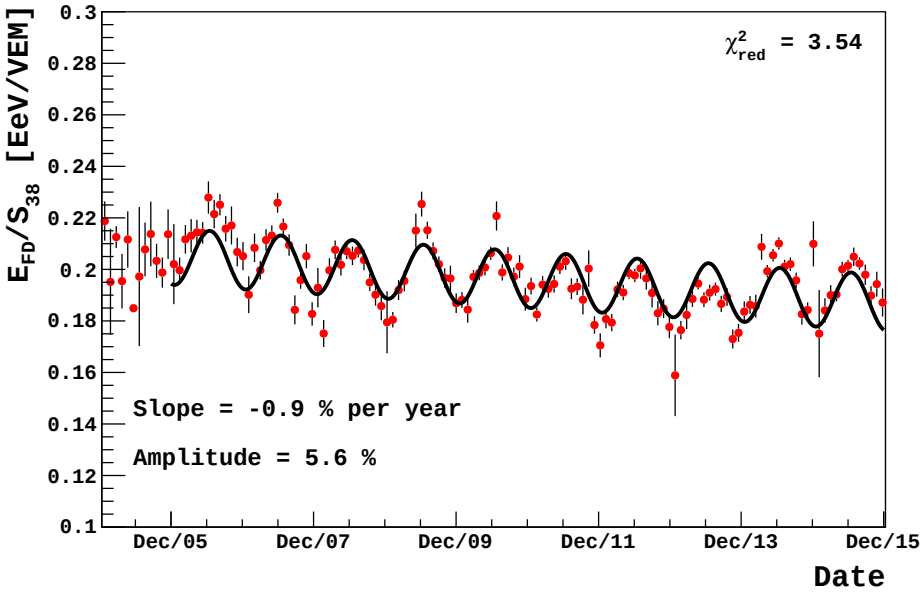

Figure 5.11: Fitting Equation 5.7 to the ESR as a function of time. Data prior to 2005 have been omitted from the fit as the relative FD calibration was quite unstable during the early years of the Observatory's operation.

due to the assumed functional form of the ESR, which can not be accurately represented through a single fit across a period spanning 10 years of hybrid operation. Any changes introduced to the Observatory, whether they be related to the data acquisition or the detectors themselves, since 2006 may induce anomalous features (such as sudden discontinuities or steps) in the ESR. An equation of the form of Equation 5.7 does not have the flexibility to account for such features if fitted across such a long time scale. For this reason, it may be worthwhile analysing the stability of the energy scale during different epochs of the Observatory's lifetime, which will be the focus of the following section.

5.5.2 Broken Fits to the Energy Scale Ratio

The first notable change to the operation of the Observatory which will be considered here was introduced in late 2006, and is related to the brightness of the night sky background. Prior to this change, the FD continued to operate through periods of increased night sky background, in particular during times where the background light included significant contributions from moonlight. In Section 5.2 it was noted that the performance of the FD pixels, in particular with regards to their gain, is dependent on their exposure to background light. Consequently, the exposure of the FD pixels to increased background light during the early years of the operation may have affected their performance. In $\sim$ 2007 the Collaboration adopted more stringent operational conditions for the FD to address these

concerns [121], the effect of which is clearly noticeable when the night sky background (as observed by the FD) is analysed as a function of time, as shown in Figure 5.12.

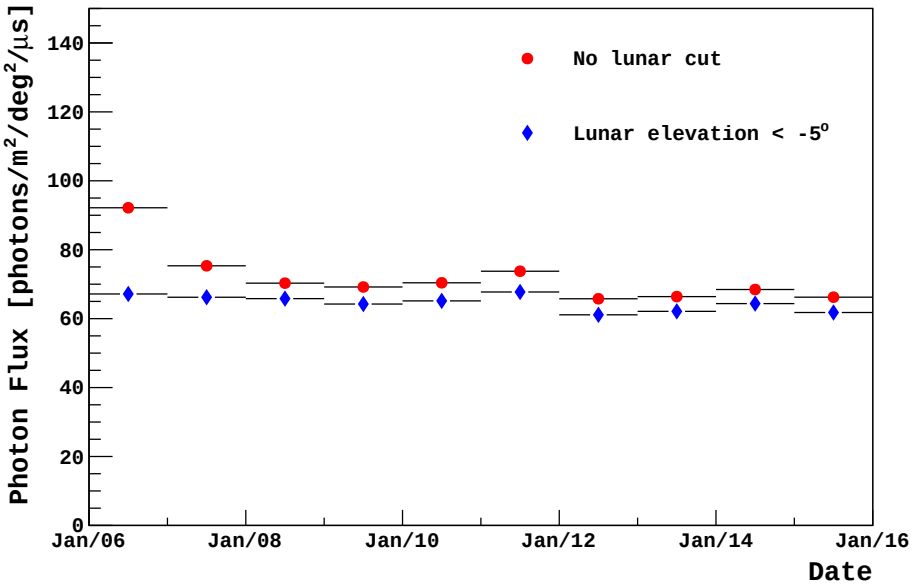

Figure 5.12: The average yearly night sky background photon flux measured by Los Leones telescope 4 from 2006 to 2015. The two profiles represent the signal before (red circles) and after (blue diamonds) cuts are placed on the moon's elevation. The large discrepancy between the signal measured during 2006 compared to subsequent years is a function of less stringent operational conditions during the Observatory's early years of operation. The discrepancy is removed once cuts are placed on the position of the moon. Actual operating conditions are between these two profiles, as the FD still continues to operate under some moonlight.

The second significant change is chosen to be the time at which the fully completed FD (not including the low energy extension, HEAT) began the acquisition of hybrid data. The last of the four main FD sites to be constructed was the northernmost site Loma Amarilla, for which the first hybrid event (from those used in this particular analysis) was detected on the 25th of February 2007. As this date is relatively close in time with the implementation of more stringent background conditions (within the span of a few months of operation) we will combine the two changes into a single date (or *breakpoint* in the ESR), chosen to be the beginning of March 2007.

A second breakpoint is chosen to occur in mid-2008, corresponding to the completion of the SD array.

The functional form adopted for the broken fit is given by

$$\frac{E_{FD}}{S_{38}}(t) = \begin{cases} B_1 + m_1\left(\frac{t-t_s}{T}\right) + A_1 \sin\left(\phi + 2\pi \times \left(\frac{t-t_s}{T}\right)\right), & t < t_1 \\ B_2 + m_2\left(\frac{t-t_s}{T}\right) + A_2 \sin\left(\phi + 2\pi \times \left(\frac{t-t_s}{T}\right)\right), & t_1 \leq t < t_2 \\ B_3 + m_3\left(\frac{t-t_s}{T}\right) + A_3 \sin\left(\phi + 2\pi \times \left(\frac{t-t_s}{T}\right)\right), & t \geq t_2 \end{cases} \tag{5.8}$$

where t_1 and t_2 correspond to the time of the completion of the FD and SD, respectively. The phase (given by ϕ) is required to be the same for all epochs, as the periodicity of the seasonal modulations is not expected to have changed at these times. Furthermore, Equation 5.8 makes no requirements on the normalisation of the fitted equations as any real discontinuities in the ESR should be reflected in the broken fits. Figure 5.13 shows the application of the broken fit to the ESR since 2006. The reduced χ^2 suggests that the performance of the broken fit is slightly improved compared to the single fit (Figure 5.11) but there still exists scope for improvement.

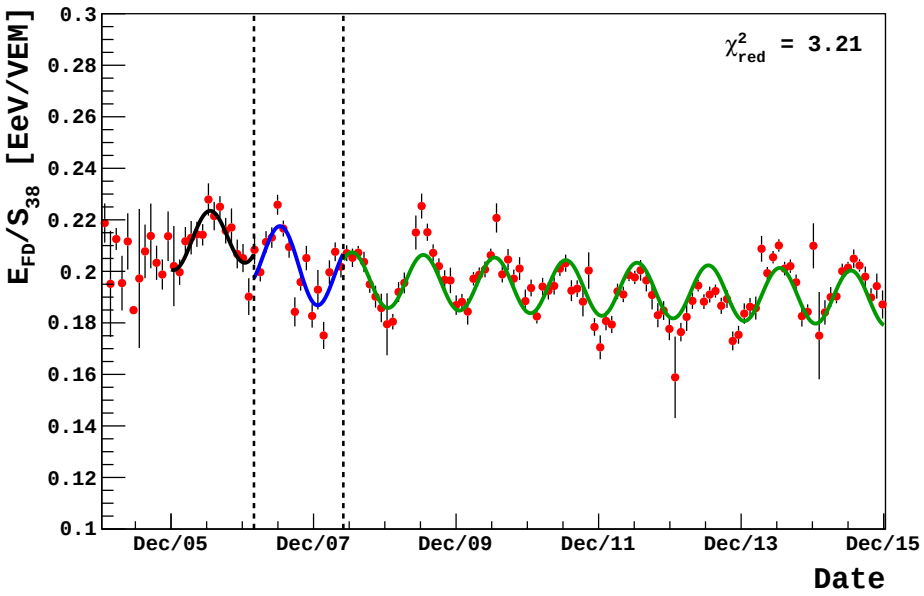

Figure 5.13: Fitting the ESR with a function of 2 breakpoints. The breakpoints in the function (indicated by the different colours and vertical rails) were chosen to occur at times corresponding to notable changes to the Observatory. The reduced χ^2 is slightly improved from the single functional fit to the entire data set ($\chi^2 \sim 3.5$) but is still moderately large.

The performance of the broken fit could be further improved if the breakpoints are selected based on significant changes to the Observatory's operation as well as empirically, through inspection of the ESR profile itself. An obvious example of an empirically selected breakpoint would be at the beginning of 2014, where a step-like feature (of $5-10\%$) is observed in the ESR. This feature poses a problem

to any functional fit as the data would force the fit to be skewed upwards. This could potentially cause an underestimation of the underlying drift in the ESR, in particular for the data prior to 2014 and an overall poor fit which will be reflected in a large reduced χ^2. The result of introducing the third, empirically selected breakpoint to the broken functional fit is displayed in Figure 5.14. By inspection it can be seen that the third fit (green) no longer underestimates the drift of the profile prior to 2014, and that the fit appears to better represent the long term behaviour of the ESR. This observation is supported by the modest improvement in the reduced χ^2 (2.20 c.f 3.21).

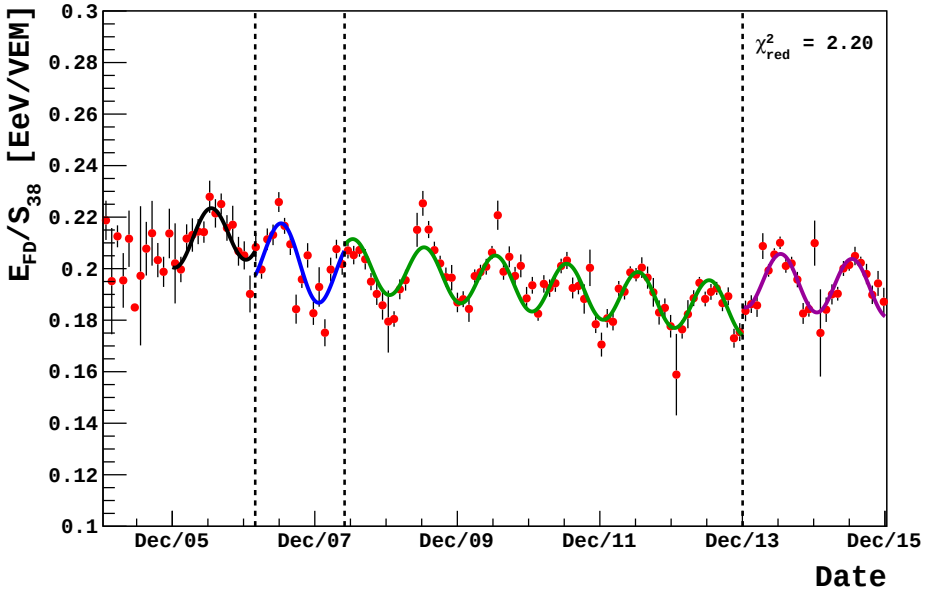

Figure 5.14: Fitting the ESR with a function of 3 breakpoints. The first two breakpoints (from the left) are those used in Figure 5.13. The third breakpoint at the beginning of 2014 was chosen empirically, as a noticeable discontinuity in the data is observed at that time. Fitting for an additional step has further improved the reduced χ^2.

It may be worthwhile to investigate the benefits of including numerous breakpoints. In Figure 5.15 the first breakpoint (corresponding to the completion of the FD) was omitted from the fit, which appears to have had a small effect on the reduced χ^2 (compared to Figure 5.14). This result suggests that the completion of the FD has not introduced any significant systematic effects on the energy scale.

This analysis can be taken one step further with the omission of data prior to the completion of the Observatory (recalling that the SD array reached completion in mid-2008) from the fit all together. This particular scenario is shown in Figure 5.16. The fit to the completed Observatory prior to 2014 (labelled as the dark green function in Figure 5.16) is extrapolated on either side of the fitted range. The left hand side appears to describe the underlying data reasonably well,

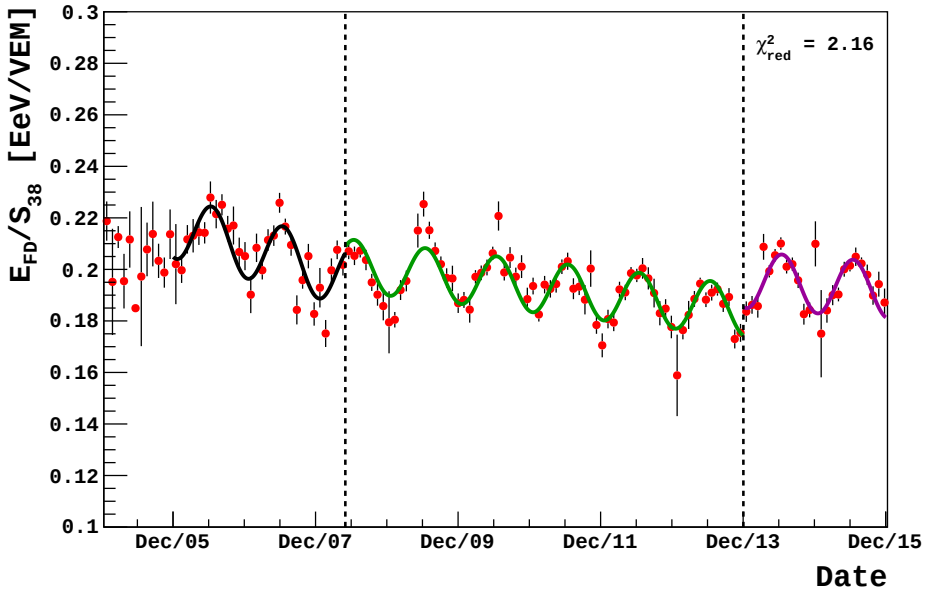

Figure 5.15: Fitting the ESR with a function consisting of 2 breakpoints. The first breakpoint is set at the completion of the SD and the second at the beginning of 2014.

suggesting that the ESR prior to the completion of the SD was quite stable with respect to its behaviour post completion. This is in contrast to the period after 2014, where a significant discrepancy is observed between the extrapolated function and the underlying data. If only data beyond the breakpoint is considered, then a reduced χ^2 of 1.78 is returned for the fitted (magenta) function. In contrast, calculating a goodness-of-fit using the extrapolated function for the same period returns a reduced χ^2 of 21.26, providing further justification for the addition of a breakpoint at the beginning of 2014. Interestingly, the overall fit returns a reduced χ^2 of 1.93 suggesting that, of all the fitting scenarios tested, the long term and seasonal trends of the ESR are best described by broken functional fit to a completed Observatory with a single breakpoint positioned at the beginning of 2014.

From Figure 5.16 the ESR is estimated to have a drift of -1.6% per year for the period before 2014, after which the drift appears to flatten out to -1.0% per year. At first these values may seem small but are magnified if considered over a sufficiently long period (e.g. 10 years of operation). The seasonal modulation is estimated to be 5.1% and 5.5% before and after the break, respectively. As this particular casting of the broken fit returns the best goodness-of-fit of those tested, it will be adopted as the optimal functional form of the ESR and will be used in all subsequent analyses presented in this Chapter.

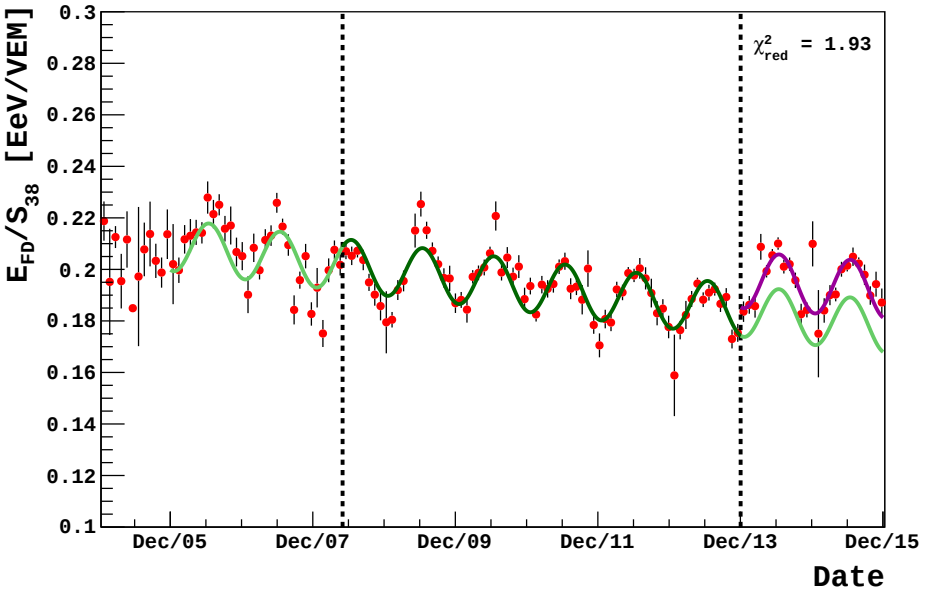

Figure 5.16: Fitting the ESR from the completed Observatory with a function consisting of one empirically defined breakpoint. The fit function from mid-2008 through to 2014 is extrapolated on either side of the vertical rails.

5.5.3 Estimating Uncertainties

All attempts of parametrising the evolution of the ESR thus far have been met with varying results. Through visual inspection it is obvious that a singular fit spanning the entirety of the ESR fails to adequately describe the underlying data set, most likely due to the discontinuity observed at the beginning of 2014. This is reflected by the relatively large reduced χ^2. The goodness-of-fit can be improved by introducing an empirically determined breakpoint within the function, as shown in Figure 5.16. In this Section we will present a method which can be used to estimate the uncertainties on the fitted parameters.

Estimated uncertainties for the fitted parameters are only meaningful if the reduced χ^2 returned by the fit is ~ 1. For instances where this is not the case, such as those examples presented within this Chapter, it is possible to scale the error bars of the data points by a factor S such that a reduced χ^2 of 1 is returned. It should be noted that the error bars in question represent statistical uncertainties, whereas the process of scaling errors is typically done if the systematic uncertainties have been underestimated (and in certain cases where statistical uncertainties are difficult to estimate). This can be justified by the necessity to account for the uncertainty in the assumed functional form of the ESR, which is defined to be a combination of a linear and sinusoidal function. If the true form of the ESR can not be completely represented by such a function then it may lead to an artificially large reduced χ^2.

The reduced χ^2 for a data set of N points is given by

$$\begin{aligned} \chi^2_{red} &= \frac{\chi^2}{NDF} \\ &= \frac{1}{NDF}\sum_{i=1}^{N}\left(\frac{O_i - E_i}{\sigma_i}\right)^2 \end{aligned} \tag{5.9}$$

where O_i and E_i are the observed and expected values for the i^{th} data point, respectively, with an uncertainty of σ_i. The number of degrees of freedom is given by NDF. The scaling factor S is incorporated into the goodness-of-fit as follows

$$\chi^2_{red} = \frac{1}{NDF}\sum_{i=1}^{N}\left(\frac{O_i - E_i}{S\sigma_i}\right)^2 \tag{5.10}$$

Rearranging Equation 5.10 gives

$$S^2 = \frac{1}{\chi^2_{red}} \times \frac{1}{NDF}\sum_{i=1}^{N}\left(\frac{O_i - E_i}{\sigma_i}\right)^2 \tag{5.11}$$

To achieve a reduced χ^2 equal to 1, Equation 5.11 can then be simplified to

$$S = \left(\frac{\chi^2}{NDF}\right)^{\frac{1}{2}} \tag{5.12}$$

Applying this error scaling factor to the fit in Figure 5.16 we find that the ESR changes at a rate of $-1.6 \pm 0.2\%$ per year prior to 2014, after which the drift improves to a rate of $-1.0 \pm 0.8\%$ per year. These results imply that the ESR has a real drift (a slope which is inconsistent with zero) followed by an apparent stabilisation during which the slope appears to be consistent with being flat[5]. The amplitude of the seasonal modulation is consistent (within uncertainties) across the entire time period and is estimated to be $5.1 \pm 0.4\%$ and $5.5 \pm 0.7\%$ before and after the breakpoint, respectively.

5.6 Improvements to the Aerosol Database

Atmospheric aerosols can scatter fluorescence photons beyond the field of view of an FD telescope weakening both the detected signal and consequently, the reconstructed shower energy. It is therefore imperative that the atmosphere's aerosol content be well understood and accurately measured so that the appropriate corrections can be made. In Section 3.3 the two existing methods used by the Observatory to quantify atmospheric aerosols were introduced. This Section will begin

[5]Additional statistics are required to conclusively comment on the energy scale's stability following 2014.

with a discussion of the ESR's dependence on atmospheric aerosols, followed by a brief overview of recent improvements made to the methods used to measure atmospheric aerosols and how these improvements affect the ESR.

The ESR's dependence on the aerosol transmission from the point of shower maximum and the observing FD telescope is shown in Figure 5.17. The non-zero slope of the fitted function indicates that the ESR (more specifically, E_{FD}) is not completely independent of the aerosol content (which would be the case if the fitted slope was consistent with a flat line). For any EAS observed by the FD, the reconstructed energy is proportional to the amount of light emitted by the shower. Each event requires an additional correction to account for fluorescence photons which have been scattered (by aerosols) beyond the FD's field of view. The positive slope in Figure 5.17 implies an under-correction of E_{FD} during periods of higher aerosol concentration. In other words, the existing aerosol analysis methods are incorrectly quantifying the atmosphere's true aerosol content, leading to a systematic underestimation of E_{FD}.

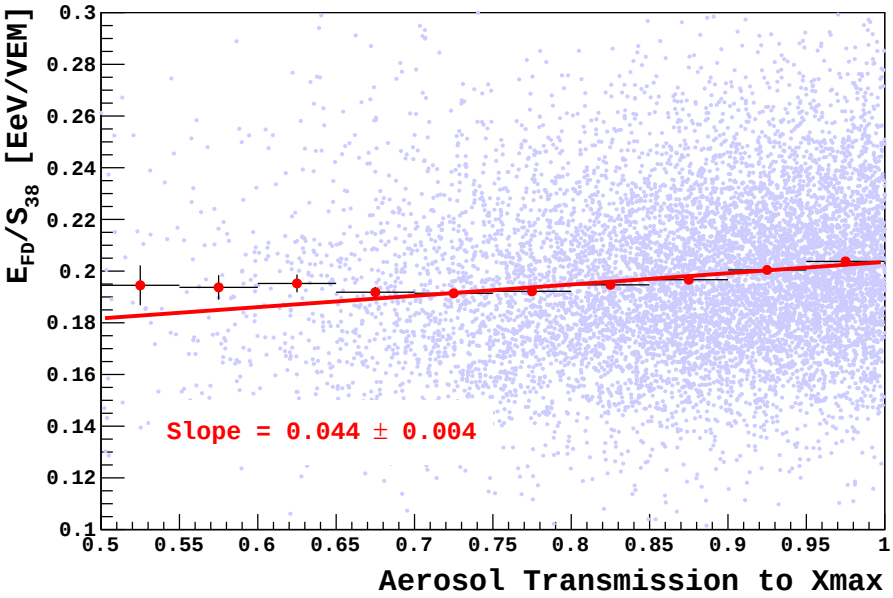

Figure 5.17: The ESR as a function of the aerosol transmission from the observing FD telescope and X_{max}.

In recent years, the Collaboration has strived to gain a better understanding of the existing aerosol measurement methods to clarify any induced systematic effects on reconstructed shower energies and depths of shower maximum. The most significant improvements include accounting for the shape of the aerosol phase function and the inclusion of multiple scattered light from the laser beam, both of which lead to a modest increase in VAOD measurements. These corrections result in an increase in reconstructed shower energies of (on average) 1.5% at $10^{17.5}$ eV, up to 3% at an energy of $10^{19.5}$ eV, as well as an increase in the average

depth of shower maximum of $2\,\mathrm{g\,cm^{-2}}$ at $10^{17.5}\,\mathrm{eV}$, up to $5\,\mathrm{g\,cm^{-2}}$ at an energy of $10^{19.5}\,\mathrm{eV}$ [122]. Both shifts are within current aerosol related systematic uncertainties published in [89] and [93], and improve the non-zero slope observed in Figure 5.17, as shown in Figure 5.18.

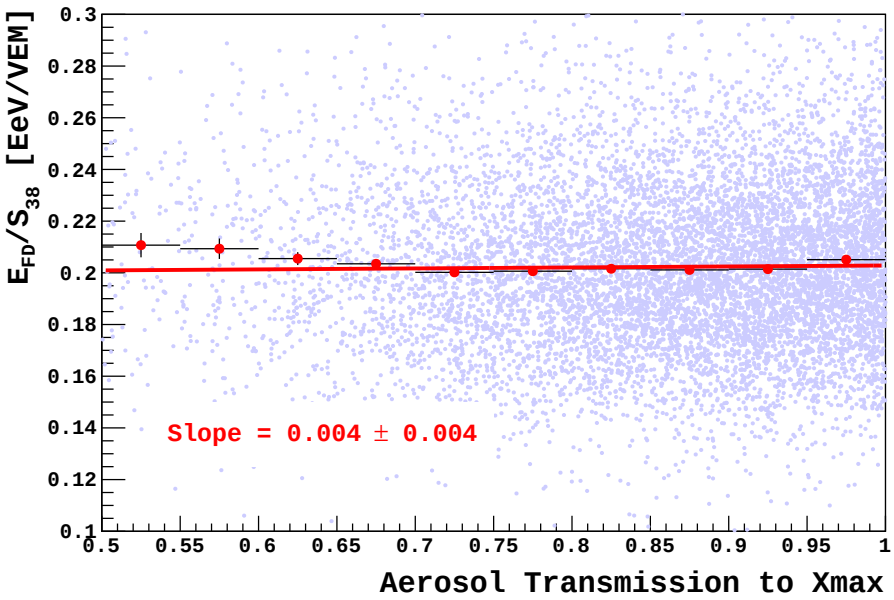

Figure 5.18: The ESR as a function of the aerosol transmission following the improvements to the aerosol database. The slope of the fitted function (which is compatible with that of a flat line) suggests that the underestimation of atmospheric aerosols has been remedied.

The improvements were applied on a shower-by-shower basis through a modified Offline reconstruction[6] of the same set of hybrid events outlined in Section 5.5. The resulting ESR profile is shown in Figure 5.19. Compared to previous versions, Figure 5.19 displays an increase in the average value of the ESR, an expected result as the aerosol improvements act to increase E_{FD}. From the fitted function the long term drift is estimated to be $-1.7 \pm 0.2\%$ per year before the breakpoint and $-0.6 \pm 0.9\%$ per year after, a result which is consistent with the ESR's behaviour prior to the aerosol database changes. Improvements are observed with regards to the amplitude of the seasonal modulations, which reduce to $4.3 \pm 0.4\%$ and $4.0 \pm 0.7\%$ before and after the breakpoint, respectively (summarised in Table 5.2). This is perhaps an expected result, as the corrections are correlated with the atmospheric aerosol content which varies seasonally.

[6]Using the aerosol database *Atm_Aerosol_1_A* with software version *CSM_NAP_v2.0*.

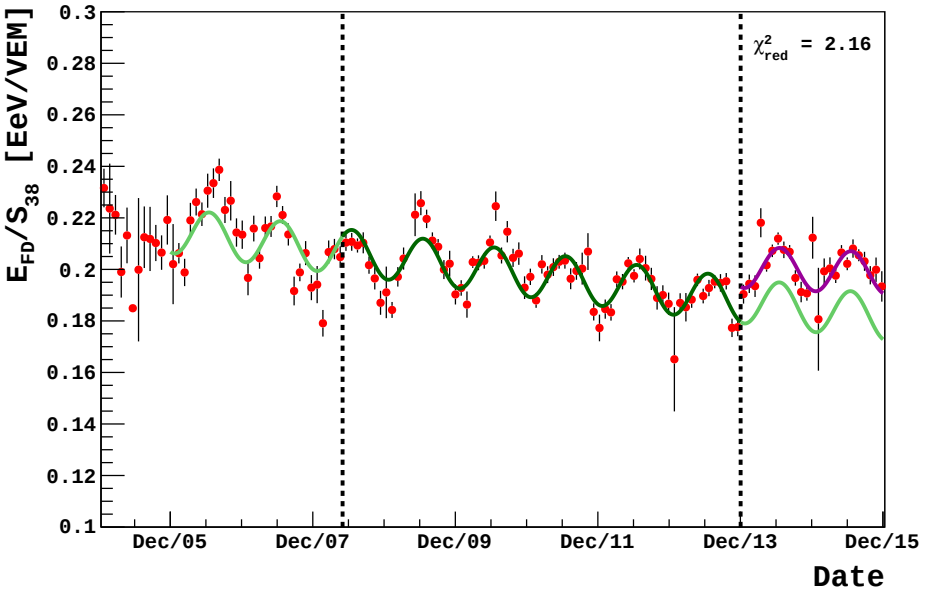

Figure 5.19: The long term behaviour of the ESR following improvements to the aerosol database. The effect of the improvements is an increase in the average value of E_{FD} and consequently an upwards shift in the ESR (compared to Figure 5.16.

5.7 Surface Detector Weather Correction

Fluctuations in atmospheric pressure and density can impact the evolution of the electromagnetic and muonic components of an EAS, directly affecting the signal measured by the SD. An SD weather correction has been formulated with the purpose of correcting for any weather dependent signal variations. The first form of this correction was published in 2009 in [123] and later revisited in 2017 following improvements to its methodology and the accumulation of a significantly larger data set [124]. In this Section, we will briefly introduce the latest form of the surface detector weather correction before applying it to the ESR defined in Section 5.5, making note of any significant effects. More detailed discussions of the weather correction are provided in references [123] and [124].

Atmospheric pressure (P) provides a measure of the vertical air column mass above ground level with an increase (decrease) in pressure corresponding to an increase (decrease) in matter overburden. Variations in pressure act to affect the attenuation of the shower's longitudinal development beyond the shower maximum [123]. In terms of the signal measured by the SD, an EAS developing through an atmosphere of greater pressure will arrive at ground level in a more advanced stage of its evolution compared to an atmosphere of lower pressure.

As the SD is sensitive to both the electromagnetic and muonic components of an EAS, it is useful to consider the effect of pressure variations on the two

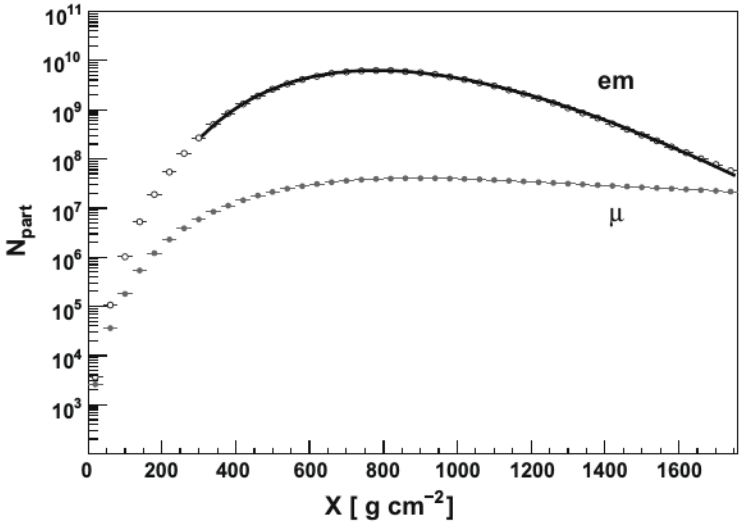

Figure 5.20: Average longitudinal profiles for the electromagnetic and muonic components of 300 proton initiated showers simulated with CORSIKA-QGSJETII. The longitudinal development of the muonic component is ∼flat compared to that of the electromagnetic component [123].

components separately. Simulated longitudinal profiles for the electromagnetic and muonic components are illustrated in Figure 5.20. In contrast to the electromagnetic component, the number of particles in the shower as a function of slant depth for the muonic component is quite stable and as a result, no significant correction for the muonic component is required due to pressure variations.

Fluctuations in atmospheric density (ρ) affect the Molière radius of an EAS, a quantity that describes the transverse dimension of the shower's electromagnetic component as a result of multiple Coulomb scattering interactions. Changes in ρ are met with changes in the shower's signal, directly affecting its lateral distribution and thus S(1000) [123].

The signal sampled by the SD is dominated by shower particles produced in the last two radiation lengths above the detector [125], making variations in atmospheric conditions at these altitudes (typically $500 - 1000\,\mathrm{m}$ above ground level) the most important. The correction published in [124] (see Equation 5.13) accounts for density variations in two separate terms. The first term accounts for variations of the daily averaged density, denoted by ρ_d, which are similar at both ground level as well as the relevant altitudes of interest. The second term is proportional to departures of the density measured at a given time of interest ($\widetilde{\rho}$) from the daily averaged density. An important note is that $\widetilde{\rho}$ is the density measured at ground level 2 hours prior to the event. This accounts for the delay between density variations at the relevant altitudes with respect to ground measurements.

The correction can be applied on an event by event basis and takes the following form:

$$S(1000) = S_0 \left[1 + \alpha_P(P - P_0) + \alpha_\rho(\rho_d - \rho_0) + \beta_\rho(\widetilde{\rho} - \rho_d)\right] \tag{5.13}$$

where $P_0 = 862\,\mathrm{hPa}$ and $\rho_0 = 1.06\,\mathrm{kg\,m^{-3}}$ are reference values for pressure and density corresponding to average values obtained at the Pierre Auger Observatory site, S_0 is the equivalent SD signal obtained under the reference atmosphere and P is the pressure at ground level at the time of the event. In other words, S_0 is the size of the shower having corrected for atmospheric effects.

A maximum likelihood fit is performed on the SD event rate to determine the fit coefficients α_P, α_ρ and β_ρ (hereinafter the atmospheric coefficients), recognising that modulations in the atmosphere, if uncorrected for, can affect the rate at which cosmic ray events above a threshold signal (or apparent energy) are detected by the SD. Modulations in the shower size can result in showers migrating above and below the threshold signal, manifesting in a seasonal variation in the event rate which is expected to remain constant[7].

For the correction formulated in [124] the SD event rate is defined as the number of detected events (within one hour time bins) normalised by the area of the SD array, given by the number of hexagons of active SD stations during that particular time bin. Performing this fit allows for the determination of the rate coefficients (a_P, a_ρ and b_ρ, see below) through the maximisation of the following likelihood function

$$L = \prod \frac{\mu_i^{n_i}}{n_i!} e^{-\mu_i} \tag{5.14}$$

which assumes that for the i^{th} time bin, the number of events (n_i) follows a Poisson distribution of mean μ_i. The mean number of events is given by

$$\mu_i = R_0 \times A_i \times C_i \tag{5.15}$$

where R_0 is the average rate of events per unit area observed under the reference atmosphere, A_i is the effective area of the array in the i^{th} time bin and

$$C_i = 1 + a_P(P - P_0) + a_\rho(\rho_d - \rho_0) + b_\rho(\widetilde{\rho} - \rho_d) \tag{5.16}$$

is the rate correction term.

The rate coefficients can be used to calculate the atmospheric coefficients as follows

$$a_{P,\rho} = B(\gamma - 1)\alpha_{P,\rho} \simeq 2.3\alpha_{P,\rho} \tag{5.17}$$

$$b_\rho = B(\gamma - 1)\beta_{P,\rho} \simeq 2.3\beta_\rho \tag{5.18}$$

where the spectral index in the energy range of interest is determined to be $\gamma = 3.29$ [126] and B is derived from the energy calibration (see Section 3.4).

[7] This is assuming that the intrinsic event rate above the threshold signal is constant with time, and that any modulations in the observed rate are due to external (detector) effects.

Any zenith angle dependencies in the weather correction are accounted for by repeating the analysis across several data subsets of equal width in $\sin^2\theta$ (equal solid angle), with new rate coefficients fitted for each subset. The results are summarised in Figure 5.21, where a fitted polynomial (Equation 5.19) is used to describe the dependence of each coefficient as a function of $\sin^2\theta$. The polynomial coefficients are listed in Table 5.1 for the 1500 m SD array. Results for the 750 m array can be found in [124].

$$f(\sin^2\theta) = c_0 + c_1(\sin^2\theta) + c_2(\sin^2\theta)^2 \tag{5.19}$$

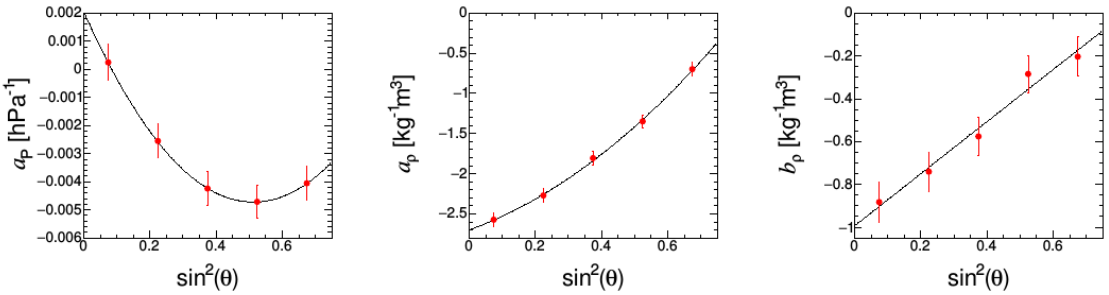

Figure 5.21: The rate coefficients as a function of $\sin^2\theta$. The polynomial used to describe the dependence of each coefficient as a function of $\sin^2\theta$ is also shown [124].

Coefficient	c_0	c_1	c_2
a_P [hPa^{-1}]	$(2.1 \pm 0.9) \times 10^{-3}$	$(-2.6 \pm 0.6) \times 10^{-2}$	$(2.6 \pm 0.7) \times 10^{-2}$
a_ρ [kg^{-1}m^3]	-2.7 ± 0.1	1.5 ± 0.8	2.2 ± 1.0
b_ρ [kg^{-1}m^3]	-1.0 ± 0.1	1.2 ± 0.8	0.0 ± 1.1

Table 5.1: Fitted polynomial coefficients used to describe the dependence of each rate coefficient as a function of $\sin^2\theta$ [124].

5.7.1 Surface Detector Event Rate

As previously discussed, the rate at which events above a threshold energy (E_{th}) are detected by the SD can act as a proxy for the stability of the energy measurement of the SD. The relationship between the SD event rate and the SD energy scale can be derived by considering the differential energy spectrum for cosmic rays, dN/dE (Section 1.1), which can be expressed as

$$\frac{dN}{dE} \propto E^{-\gamma} = kE^{-3} \quad \text{m}^{-2}\text{s}^{-1}\text{sr}^{-1}\text{eV}^{-1} \tag{5.20}$$

for some normalisation constant k. As this analysis is focussed on UHECR, the spectral index γ is chosen to have a single value of 3 to reflect the 'flatter' part of the energy spectrum. The event rate is given by integrating Equation 5.20 with respect to E above E_{th} as follows

$$Event\ Rate\ (E > E_{th}) = \int_{E_{th}}^{\infty} \frac{dN}{dE} dE \tag{5.21}$$

Substituting Equation 5.20 into Equation 5.21, the above expression can be simplified to

$$Event\ Rate = \int_{E_{th}}^{\infty} kE^{-3} dE = k \int_{E_{th}}^{\infty} E^{-3} dE = \left[-\frac{k}{2E^2} \right]_{E_{th}}^{\infty} = \frac{k}{2E_{th}^2} \tag{5.22}$$

Equation 5.22 can be used to determine how the event rate changes with changing E_{th}

$$\frac{d(Event\ Rate)}{dE_{th}} = -kE_{th}^{-3} \tag{5.23}$$

which can be rearranged to give

$$d(Event\ Rate) = -kE_{th}^{-3} \times dE_{th} \tag{5.24}$$

Finally, dividing Equation 5.24 by Equation 5.22 gives

$$\frac{d(Event\ Rate)}{Event\ Rate} = \frac{-kE_{th}^{-3} dE_{th}}{(k/2)E_{th}^{-2}} = -2\frac{dE_{th}}{E_{th}} \tag{5.25}$$

Equation 5.25 shows how a drift in E_{th} causes a drift in the SD event rate (if a spectral index of $\gamma = 3$ is assumed). For example, if the threshold energy were to increase by 10% (i.e. $dE_{th}/E_{th} = 0.1$) then the event rate would decrease by 20%, as fewer events would meet the minimum energy requirements to satisfy E_{th}. Alternatively, if we consider the scenario of a fixed E_{th}, then Equation 5.25 can be modified to indicate how a drift in the reconstructed shower energy (or S_{38}) can correspond to a change in the SD event rate above E_{th}

$$\frac{d(Event\ Rate)}{Event\ Rate} = -2 \times \frac{dS_{38}}{S_{38}} \tag{5.26}$$

The effect of the SD weather correction is demonstrated in Figure 5.22 for which the SD event rate above 2 EeV is illustrated before and after weather corrections. From the bottom profile in Figure 5.22 it is evident that the seasonal modulations of the event rate (above a threshold energy) have been removed, as seasonal atmospheric dependencies in shower sizes measured by the SD have been taken into account.

A similar analysis to that shown in Figure 5.22 can be repeated for a threshold SD energy of 3 EeV, to remain consistent with the minimum energy requirement

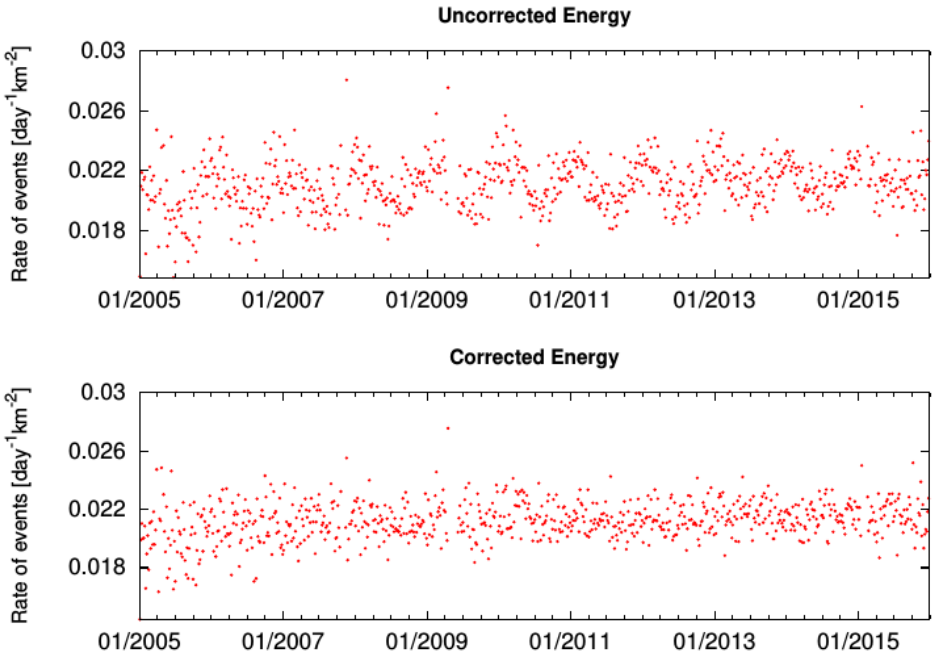

Figure 5.22: Daily SD event rate (for the 1500 m array) above a threshold energy of 2 EeV before (top) and after (bottom) correcting for the modulations in atmospheric pressure and density [124].

for the hybrid showers used in this Chapter's work. The event rate is calculated by the ratio of the number of detected showers[8] and the effective area of the detector across a given time period. The number of live hexagonal SD station cells (defined as a hexagonal grouping of 7 working SD stations) is monitored every minute, and is representative of the SD's effective area at any point during the Observatory's lifetime. The SD event rate above an energy of 3 EeV as a function of time is shown in Figure 5.23.

From Figure 5.23 we estimate that the SD event rate increases by 0.56% per year. For a fixed E_{th}, an increasing event rate implies that showers are being reconstructed with larger energies (or S_{38}), allowing an increasing number of showers to migrate above the threshold with time. This behaviour is consistent with a negative drift in the ESR, recalling that the SD's contribution to the ESR is on the denominator. Using Equation 5.26 we estimate the SD's contribution to the ESR to be -0.3% per year.

It should be noted that no significant discontinuity is observed in the SD event rate at the beginning of 2014. This observation suggests that the step-like feature observed in the ESR is related to a change to the FD.

[8] Vertical showers with minimum reconstructed SD energies of 3 EeV.

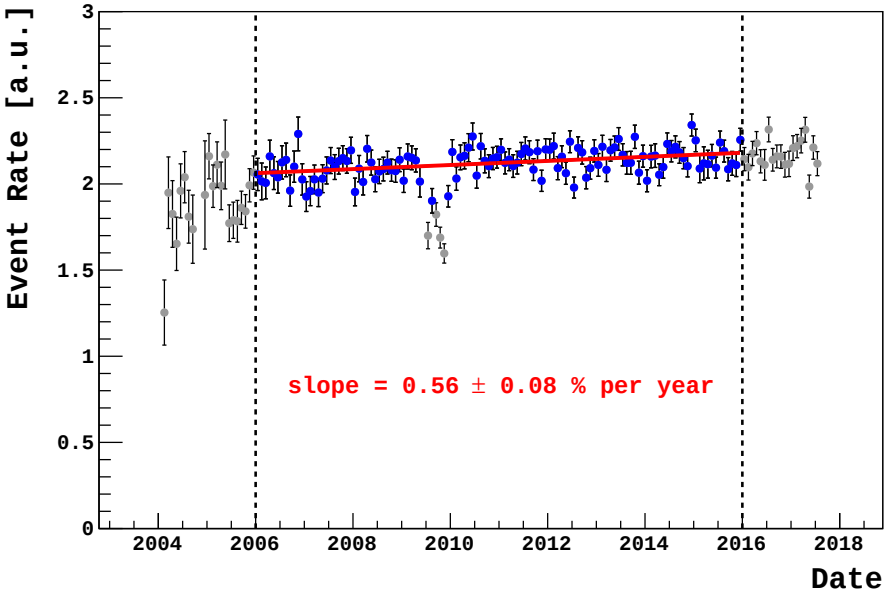

Figure 5.23: The monthly SD event rate (arbitrary units) for a threshold energy of 3 EeV post-SD weather correction. The events used here were taken from the Observer reconstruction. The linear function (red) is fitted across the same time period (blue profile) as the data set defined earlier in this Chapter.

5.7.2 Application to the Energy Scale Ratio

The SD weather correction is performed on a shower-by-shower basis using Equation 5.13. At the time of this analysis, the correction existed as an $\overline{\text{Off}}\underline{\text{line}}$ algorithm applied post-reconstruction. The majority of the temperature and pressure data used as part of the correction were recorded by the weather station located at the Observatory's CLF, with missing periods supplemented with data from weather stations positioned at the FD sites [124]. The effect of the SD weather correction on the ESR is shown in Figure 5.24, in which a clear reduction of the seasonal modulations is observed. This is further supported from the fitted function, which estimates the amplitude to the seasonal modulations to be $2.7 \pm 0.4\%$ and $3.4 \pm 0.7\%$ before and after the breakpoint, respectively. Interestingly, the SD weather correction has not resulted in a significant change in the ESR's long term drift.

5.8 Combining Corrections

In this Section we combine both the improvements to the aerosol database analysis as well as the SD weather correction to the ESR. In addition to these two corrections a third correction accounting for the azimuthal modulation of estimated cosmic ray energies due to the geomagnetic field is included for completeness.

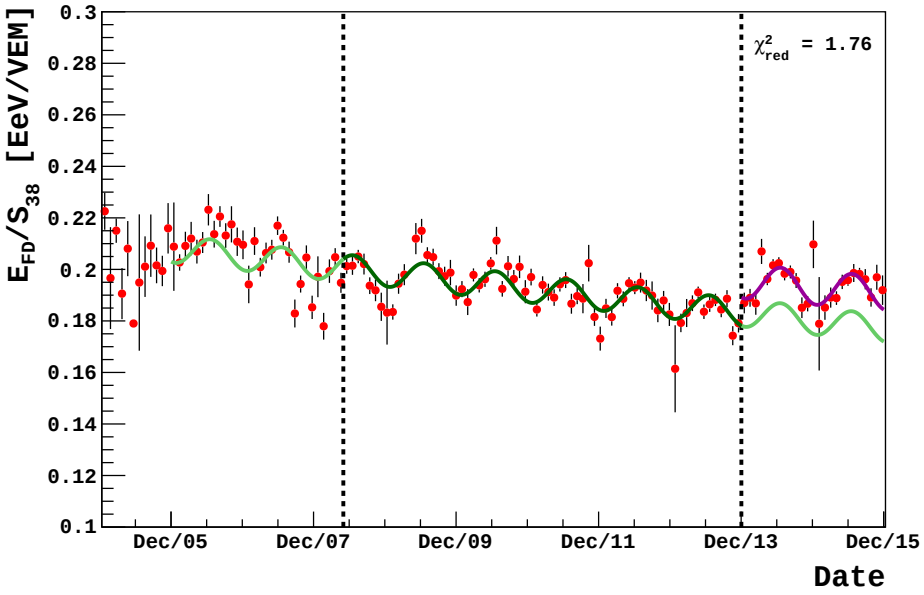

Figure 5.24: The ESR following the application of the SD weather correction to which the optimal broken function is fitted. It should be noted that no improvements to the aerosol database were included in this reconstruction.

Additional details regarding the geomagnetic correction can be found in [127]. The resultant ESR profile following the aforementioned corrections to the FD and SD analyses is illustrated in Figure 5.25. The seasonal modulations have improved significantly following the corrections and are estimated to be $2.0 \pm 0.4\%$ and $1.7 \pm 0.7\%$ before and after the breakpoint, respectively. In comparison to the ESR prior to any correction, it can be seen that modulations have decreased by $\sim 3\%$ in both epochs. In contrast, the long term drift has not been met with a noticeable improvement, and remains consistent with the ESR prior to any corrections.

The effect of the individual corrections on the long term drift and seasonal modulation are summarised in Table 5.2. The listed fit parameter uncertainties were estimated using the method described in Section 5.5.3.

	χ^2_{red}	Drift [% per year] (pre 2014)	Modulation [%] (pre 2014)	Drift [% per year] (post 2014)	Modulation [%] (post 2014)
Nominal Energy Scale	1.93	-1.6 ± 0.2	5.1 ± 0.4	-1.0 ± 0.8	5.5 ± 0.7
+ Aero. DB	2.16	-1.7 ± 0.2	4.3 ± 0.4	-0.6 ± 0.9	4.0 ± 0.7
+ SD WC (old aero. DB)	1.76	-1.6 ± 0.2	2.7 ± 0.4	-1.2 ± 0.8	3.4 ± 0.7
+ Aero. DB + SD WC + Geo.	2.04	-1.6 ± 0.2	2.0 ± 0.4	-0.7 ± 0.9	1.7 ± 0.7

Table 5.2: Summary of the optimal broken fit parameters for different SD and FD corrections.

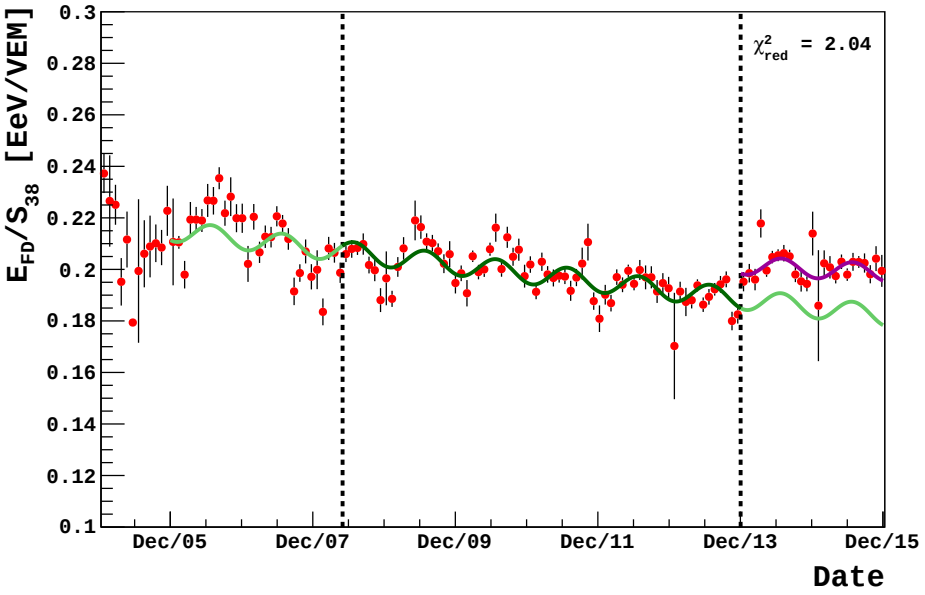

Figure 5.25: The ESR profile following the improvements to the aerosol database, the SD weather correction on the shower size and (for completeness) a geomagnetic shower size correction.

5.8.1 Discussion of Residual Features

The analyses improvements applied to both the FD and SD reconstructions have been shown to improve the stability of the ESR. In particular, a significant reduction is observed with regards to the seasonal modulations which are of the order of $\sim 2\%$ post-improvements. The same improvements appear to have had a negligible effect on the ESR's long term drift, which is estimated to be $\sim -1.6\%$ post-improvements, indicating that the drift may originate from a factor beyond those already accounted for in this Chapter. It should be noted that statistics are limited beyond 2014, and that the drift appears to be consistent (within estimated uncertainties) with both a stable ESR and a drift of -1.6% per year.

The residual non-zero amplitude observed in the seasonal modulation may be related to the calibration of the FD. In Section 5.1.1, the FD calibration constants (C_{FD}) were introduced as a monitor for the gain of the FD pixels. It was noted that the FD calibration constants have the freedom to fluctuate such that they appropriately account for any short and long term FD pixel gain variations, including those which vary seasonally (see Figure 5.2). This includes seasonal gain fluctuations as a function of temperature (Section 5.3) which we estimate, in the most extreme scenario, to be as much as $\sim 0.6\%$. Even in the most extreme case, the seasonal modulations introduced from temperature dependent gain variations are not sufficiently large enough to account for the entirety of the residual modulation of the ESR ($\sim 2\%$), implying that another, more dominating effect should be

considered. In reality it is likely that the temperature dependent modulation on the FD pixel gains is less than $\sim 0.6\%$, considering the regularity at which the pixel gains are monitored.

Further complicating this is the decision to derive the nightly FD calibration constants from the relative calibration performed following the conclusion of data acquisition. Results obtained using the running cal A procedure (Section 5.2) indicate that the gain of the FD pixels during the night can be as much as $\sim 4\%$ different compared to the gain measured following data acquisition. In Section 5.4 it was shown that the gain of an FD pixel is correlated with its exposure to the night sky background, with an increased exposure to background light resulting in a greater change in the gain. As the night sky background changes seasonally it is strongly suspected that the residual seasonal modulations observed in the ESR are related to night sky background induced FD pixel gain variations.

A possible solution to this problem would be to employ the FD calibration constants calculated using the running cal A measurements in place of those calculated in the nominal procedure. In theory, the running calibration constants should provide a more accurate estimate of E_{FD}. The results of this reconstruction are summarised in Figure 5.26 using only those events observed during 2015, as running cal A measurements were not readily available for the period prior to 2015. Furthermore, running calibration constants were not recorded for Los Leones in the particular database used in this analysis[9], and so Figure 5.26 only includes hybrid events observed from the three remaining FD sites.

The improvements to the FD and SD analyses act to reduce the amplitude of the seasonal modulation (at least for 2015) to a level that is consistent with that of a stable ESR. This result, while in itself a positive indicator for the effectiveness of the analyses improvements, unfortunately provides little clarity regarding the effect of the running calibration constants, in particular on the seasonal modulations (the amplitudes of the corrected profiles are consistent with one another). The running calibration constants do however increase the average value of E_{FD}, an expected result as the FD calibration constants measured during data acquisition are (on average) larger compared to that measured at the night's conclusion[10]. Due to insufficient statistics it is difficult to draw any significant conclusions with regards to the effect of the running calibration constants on the ESR's seasonal modulations. Additional years of running calibration constants are required for further investigation.

The ESR's discontinuity at the beginning of 2014 is an interesting feature. As noted in Section 5.7.1, there are no obvious indications that the discontinuity is related to the SD. The discontinuity is investigated in further detail in Section 7.5.2.

[9]The database *FD_ Calib_ 1_ ARunning* existed as a test database at the time of this analysis.

[10]See Figure 5.4, recalling that the calibration constants (which are proportional to E_{FD}) can be thought of as an inverse gain.

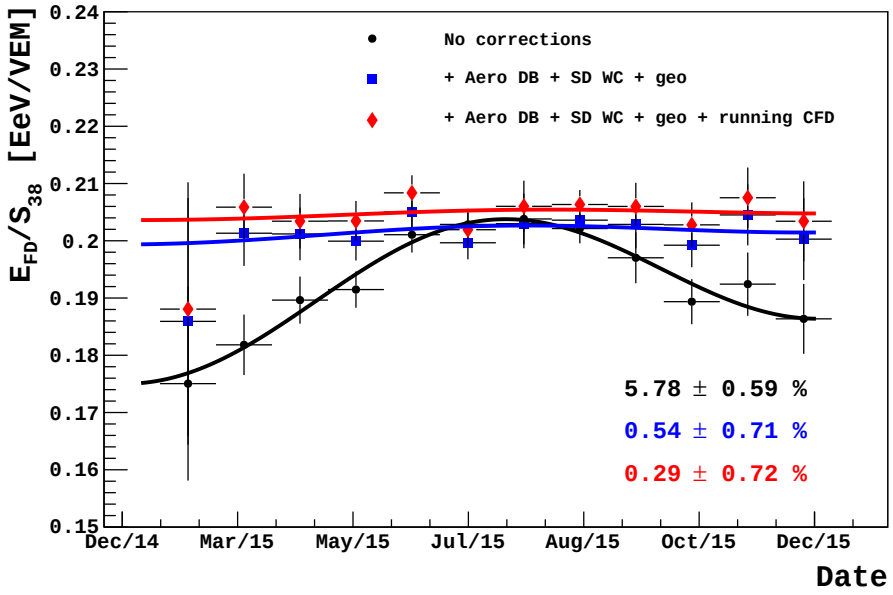

Figure 5.26: The ESR for three different Offline reconstructions of hybrid data measured during 2015. The black circles represent the ESR prior to any analyses improvements. The blue squares represent the ESR following improvements to the aerosol database and the inclusion of the SD weather and geomagnetic corrections. The red diamonds indicate the ESR following the aforementioned analyses improvements reconstructed using the running calibration constants. Each profile is fitted with a function of the form given in Equation 5.7 and the amplitude of the seasonal modulation listed in the bottom right hand corner.

None of the improvements tested in this Chapter have had a noticeable effect on the ESR's long term drift, which remains of the order of $\sim -1.6\%$ per year. The lack of significant improvement could be an indication that the long term drift originates from a source not related to the corrections covered in this Chapter. It was estimated that the SD's contribution to the drift is small (approximately -0.3% per year), indicating that the residual ESR drift is dominated by the FD. The long term drift will be revisited later in Section 7.5.1.

5.9 Conclusions

We have presented an analysis of the long term stability of the Pierre Auger Observatory's energy scale using high quality cosmic ray data collected from 10 years of hybrid operation. To aid in this we studied the evolution of the ratio of E_{FD} and S_{38}, a quantity labelled as the ESR. Three unexpected features were noted in the evolution of the ESR, these being a seasonal modulation which reaches its maximum during the Southern hemisphere's winter months, a long term drift in a downwards direction and a discontinuity appearing to begin in 2014. Using a

modified version of the *v3r3* $\overline{\text{Off}}\underline{\text{line}}$ branch reconstruction, it was illustrated that the ESR decreased at a rate of $\sim 1.6\%$ per year with a seasonal modulation of amplitude $\sim 5.2\%$. The magnitude of the discontinuity is of the order of $5 - 10\%$.

Several improvements have been implemented within the respective reconstruction chains of the SD and FD in recent years. Two corrections, namely the improvements to the methods employed by the Observatory to characterise the atmospheric aerosol content and atmospheric effects on the shower size reconstructed by the SD, were highlighted and applied separately to the ESR. In both instances significant reductions (but not complete removal) of the seasonal modulation's amplitude were observed, which were only magnified upon combining the corrections ($\sim 2\%$ amplitude post-improvements). As noted in the Chapter, none of the corrections appear to have had a significant effect on the long term drift, which remains of the order of $\sim -1.6\%$ per year, or the discontinuity.

The residual modulations and long term drift following the analyses improvements are intriguing, and are believed to be related to factors beyond those accounted for within the corrections presented in this Chapter. For example, the calibration of the FD is monitored through the calculation of nightly FD calibration constants, which provide a means of tracking the FD's gain stability with respect to a reference calibration. A possible remedy for any systematic introduced as a result of incorrect FD calibration constants could be employed through the running calibration constants, designed to monitor the FD gain every 30 minutes during data acquisition. The long term drift could be related to the ageing of the FD pixels, which can be studied through the monitoring of a carefully chosen light source. If the flux from the light source is assumed to be constant with time, then any deviations from a constant value (as observed by the FD) can be attributed to the detector's response. The ESR's long term drift and discontinuity are investigated in further detail in Chapter 7.

Chapter 6

A Cross Check of the Fluorescence Detector Relative Calibration Using the Night Sky Background

The Pierre Auger Observatory's FD uses a well established detection method to study the longitudinal development of large particle cascades initiated by the interaction of cosmic rays with atmospheric nuclei in the upper atmosphere (Section 2.4.2). Part of the FD's ability to accurately estimate the energy of a primary cosmic ray relies on its ability to convert electronic signals into a fluorescence light flux. To aid in this, extensive FD calibration campaigns have been developed to maintain accurate telescope calibrations. Individual FD telescopes are absolutely calibrated in a complete end-to-end check through the deployment of a large, drum-shaped light source. This rather time consuming effort is complemented with a relative calibration, performed before and after each night of data acquisition, which is designed to monitor the stability of the FD calibration in the periods between absolute calibration campaigns (Section 3.2.2).

In addition to capturing nitrogen fluorescence emission from air showers, the FD also monitors the night sky background (NSB) during data acquisition, providing important information used to monitor FD background signals as well as FD operational conditions. This Chapter will begin with an introduction of the NSB and how it is measured by the FD telescopes, followed by a discussion of how the electronic signal recorded by individual FD pixels can be converted into a flux of photons. We will then discuss how the flux of NSB photons can be used as a cross checking tool for the relative FD calibration of neighbouring telescopes using NSB data dating back to 2007.

6.1 The Night Sky Background

The largely isolated Pampa Amarilla plains of western Argentina provide an ideal environment for the Pierre Auger Observatory's FD. Limited sources of man-made light pollution allow for the successful operation of the FD telescopes,

which rely on the detection of faint atmospheric nitrogen fluorescence light emitted during a cosmic ray induced particle shower. UV filters placed at the aperture of each FD telescope greatly limits the degree to which unwanted light pollution, in particular from bands outside of the fluorescence spectrum, pass through to the remaining telescope components. Despite the presence of the UV filters, signals recorded by the FD still have significant contributions from various background sources, within the $\sim 300 - 400\,\text{nm}$ wavelength range, which can be attributed to night sky emissions from within and beyond the Earth's atmosphere. The typical contributions from these sources are summarised in Table 6.1.

Initially we had intended to use the NSB as a whole, treating it as a constant light source to monitor the long term calibration stability of individual telescopes. This was motivated by the drift ($\sim -1.6\%$ per year) observed in the evolution of the Observatory's energy scale (see Section 5.5), a significant fraction of which is most likely associated with the long term stability of the FD. Unfortunately the various components comprising the NSB are subject to large uncertainties and can often fluctuate over short and long time scales, making the NSB unsuitable as a constant light source. A compromise was found in the form of star tracks - discussed in greater detail in Chapter 7. Despite this, the NSB can still be used to study the stability of the relative FD calibration between adjacent FD telescopes at any point in time.

The NSB is sampled for individual PMTs every 30 seconds during data acquisition. Due to the AC coupling of the PMT signal to the analogue front-end electronics, it is not possible to directly measure the DC component of the signal which is proportional to the NSB. Fortunately, we can take advantage of the random nature of incoming NSB photons, recognising that the received NSB photons obey Poisson statistics. In other words, the signal variance recorded by individual PMTs ($[\sigma^2_{ADC}]$) is proportional to the incoming NSB photon flux (the mean signal) [34]. The variance is calculated from 100 ns integration samples taken over 6.5 ms.

Source	**Relative Brightness [%]**
Airglow	~ 60
Zodiacal Light	~ 30
Starlight scattered by interstellar dust	4
Light Pollution	< 4
Unresolvable faint stars	~ 2
Extragalactic light	< 1
Aurorae	0

Table 6.1: Values listed here apply to V-band magnitude and are representative of emissions in the U-band [128]. The largest contribution can be attributed to airglow - the nightly recombination of upper atmospheric atoms and molecules following their ionisation from solar radiation during the day [129].

Every 30 seconds, the average[1] and variance of these 65 thousand samples is calculated and stored in the background files [130]. The signal variance has units of ADC counts^2.

The total ADC signal variance has an additional contribution from electronic noise (Equation 6.1), which must first be subtracted (in quadrature) if precise NSB measurements are to be estimated.

$$[\sigma^2_{ADC}]^{total} = [\sigma^2_{ADC}]^{NSB} + [\sigma^2_{ADC}]^{ele} \tag{6.1}$$

Estimating $[\sigma^2_{ADC}]^{ele}$ is achieved by tracking the value of $[\sigma^2_{ADC}]^{total}$ during data acquisition periods where the FD shutters have been closed. For each observation night, the FD data acquisition will typically begin and conclude with the shutters of each telescope in a closed state. When in such a configuration, $[\sigma^2_{ADC}]^{NSB}$ in Equation 6.1 becomes zero, leaving electronic noise as the only contribution to the measured variance. Additionally, the shutters of a given FD telescope may close during data acquisition if any of the following conditional flags are triggered:

- Wind speeds (local to an FD site) in excess of $50\,\mathrm{km\,h^{-1}}$. Wind speeds are monitored by weather stations located at each FD site.
- The detection of rainfall at the site of the FD (on site weather station).
- The average variance of an individual camera exceeds 100 ADC counts^2.
- The number of individual pixels with a variance above 200 ADC counts^2 exceeds a maximum threshold.

The final two conditions are designed to minimise the effect of excessive NSB exposure on the ageing of the FD pixels.

We recognise that the electronic noise component may change both as a function of time as well as between individual FD pixels. To cope with this we dynamically update the value of $[\sigma^2_{ADC}]^{ele}$ for each pixel in accordance to the most recent shutter closing which had occurred at that time. For a typical night, data acquisition begins with the FD shutters in a closed position, providing the first value for $[\sigma^2_{ADC}]^{ele}$ which can then be subtracted from the total variance by rearranging Equation 6.1. The same value for $[\sigma^2_{ADC}]^{ele}$ will continue to be subtracted from subsequent background measurements and will only be updated once the shutters enter a closed position, which may not occur until the night's conclusion, at which a new value for $[\sigma^2_{ADC}]^{ele}$ becomes available. Repeating this for all pixels allows for the dynamic correction of the electronic noise on a pixel by pixel basis. An example of the electronic noise correction is illustrated in Figures 6.1 and 6.2.

[1]The average should be zero, except for an electronics related offset.

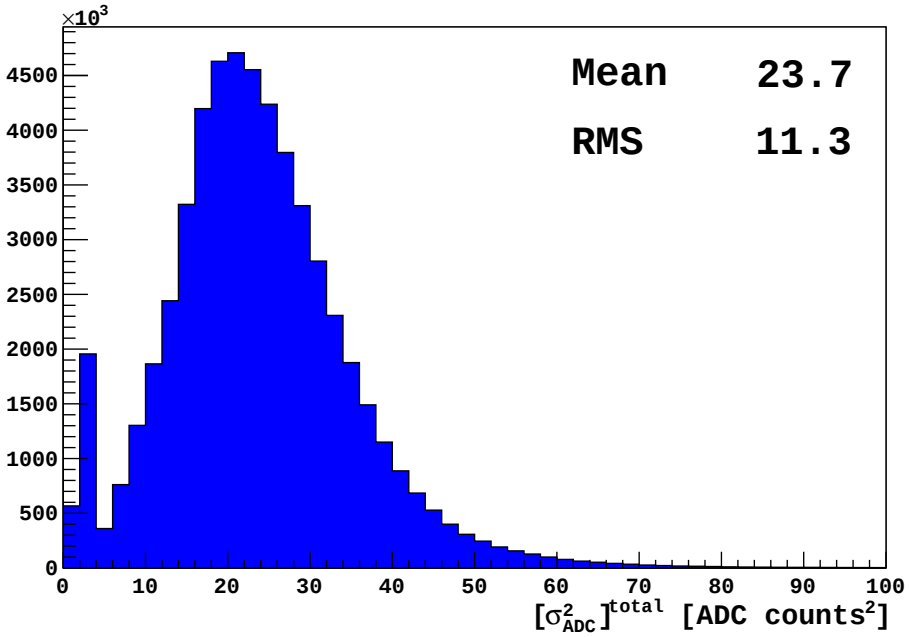

Figure 6.1: Distribution of $[\sigma^2_{ADC}]^{total}$ for all pixels of Loma Amarilla Telescope 4 for the whole of 2015 before correcting for the electronic noise component. The small distribution below $\sim$ 5 ADC counts^2 can be attributed to measurements made while the shutters are closed.

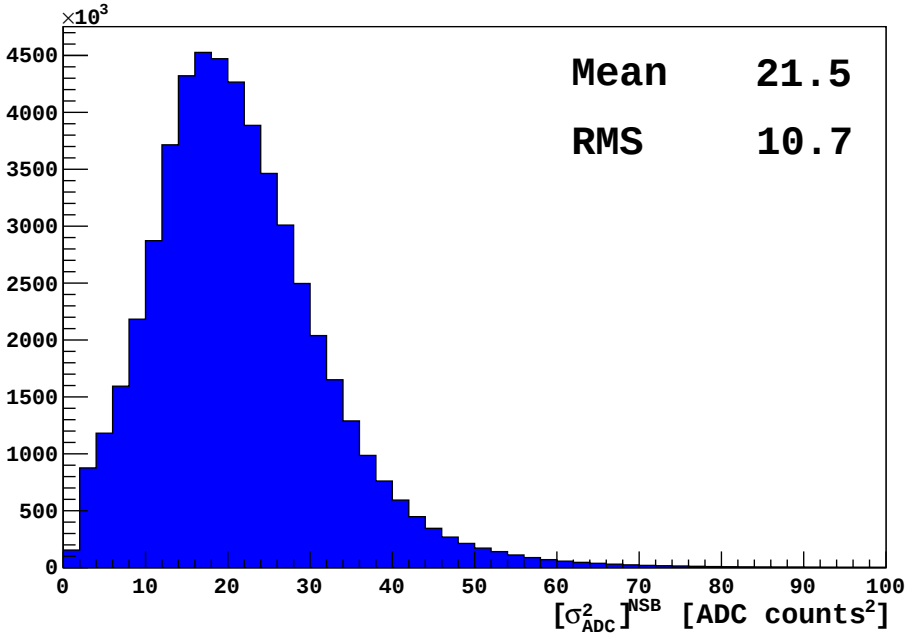

Figure 6.2: Distribution of $[\sigma^2_{ADC}]^{NSB}$ after applying the electronic noise correction. The effect of the correction is a shift of the entire distribution to the left.

6.2 Calculating the Night Sky Background Photon Flux

The FD quantifies the NSB variance in units of ADC counts^2, which is not a particularly meaningful measurement of the true NSB brightness as the gain of the FD has yet to be taken into account. For this reason, the NSB variance is converted to a photon flux at the telescope's aperture, providing a more precise measure of the NSB signal. This conversion can be approached through two methods:

1) **Identical Pixel method** - a method which makes the simplifying assumption that all FD pixels are (mostly) identical in their optical response.

2) **$\mathbf{K_v}$ method** - a method which accounts for the unique response of individual FD pixels through the definition of a variance scaling factor K_v.

While different in their respective approaches, both methods serve the same purpose and provide a means for converting the NSB variance into a photon flux with units of (375 nm equivalent) photons/m^2/deg^2/μs. Descriptions of the two methods are given below.

6.2.1 Identical Pixel Method

The Identical Pixel method is adapted from the the method outlined in [131]. The conversion from a NSB variance to a photon flux is as follows:

1. Convert the NSB variance in terms of ADC counts^2 to a variance in terms of photoelectrons

$$\sigma^2_{phe} = \frac{[\sigma^2_{ADC}]^{NSB}}{A^2_G} \tag{6.2}$$

where

$$A_G = \frac{1}{C_{FD} \times f \times Q} \tag{6.3}$$

is defined as the absolute gain with units of ADC counts per photoelectron. Definitions of f,Q and C_{FD} are given below.

2. Convert the variance of photoelectrons to a number of photoelectrons

$$n_{phe} = \frac{\sigma^2_{phe}}{1 + V_G} \tag{6.4}$$

3. Convert the number of photoelectrons to a photon flux

$$\Phi_\gamma = \frac{n_{phe}}{Q \times f \times A \times \Delta t} \tag{6.5}$$

4. Finally, combining Equations 6.2, 6.3, 6.4 and 6.5

$$\Phi_\gamma = \frac{C_{FD}^2 \times f \times Q \times [\sigma_{ADC}^2]^{NSB}}{(1+V_G) \times A \times \Delta t} \qquad [\text{photons/m}^2/\text{deg}^2/\mu\text{s}] \tag{6.6}$$

we obtain an expression for the conversion of the NSB variance into a photon flux. A discussion of how the uncertainty in the photon flux is calculated is provided in Appendix B.

Definitions of constants and parameters are as follows

- C_{FD} is the calibration constant and can be thought of as the *inverse gain* of the pixel of interest (see Section 5.1). C_{FD} values are available through the FD Calibration database.
- f is the optical factor = 0.494 (filter transmission at 370 nm $\times$ corrector ring transmission at 370 nm $\times$ mirror reflectivity at 370 nm $\times$ camera shadow factor $\times$ mercedes collection efficiency).
- Q it the PMT quantum efficiency at 337 nm = 0.29.
- $[\sigma_{ADC}^2]^{NSB}$ is the variance of the background signal following the removal of electronic noise.
- V_G is the gain variance factor = 0.41. The extra non-Poissonian width of a photoelectron distribution (measured by a single PMT) can be attributed to the variance in the gain of the PMT.

  If N_{pe} photoelectrons are emitted from the photocathode then, for a PMT gain of G_{PMT}, this would correspond to $G_{PMT} \times N_{pe}$ electrons at the PMT's anode. If only Poisson fluctuations in N_{pe} are considered, then

$$\sigma_{anode} = G_{PMT} \times \sqrt{N_{pe}} = G_{PMT} \times \sigma_{pe} \tag{6.7}$$

  and

$$\sigma_{anode}^2 = G_{PMT}^2 \times \sigma_{pe}^2 \tag{6.8}$$

  gives the variance in the number of electrons at the anode. To account for the fluctuations in the gain of individual dynodes, and the imperfect collection efficiency between the cathode and first dynode, an additional factor V_G is required

$$\sigma_{anode}^2 = G_{PMT}^2 (1+V_G) \sigma_{pe}^2 \tag{6.9}$$

  where V_G is non-zero.

- A is the pixel aperture = 7.68 $\text{m}^2\,\text{deg}^2$ (the telescope aperture multiplied by the square of an FD pixel's angular size).
- Δt is chosen to be 100 ns.

The simplifying assumption is made that certain parameters, in particular f, V_G and Q, are uniform across all FD pixels for all times, an assumption which is unlikely to hold true. The parameter f encompasses the efficiencies from several optical components, which are all subject to degradation over the Observatory's lifetime. The segmented mirrors for example, despite being housed within closed, climate-controlled environments, may accumulate significant dust layers over time, having an obvious effect on their reflective properties. The UV filters are positioned at the aperture of each telescope and are regularly exposed to the dry and dusty environment of the Pampa Amarilla plains. The accumulation of dirt and potential damage resulting from this exposure could affect the UV filters' transmission[2].

The value of V_G for a given FD pixel is dependent on the gain variations of individual dynodes which comprise the pixel, in particular at the very first dynode where the photoelectron statistics are within the regime where Poisson fluctuations become important. The collection efficiency of photoelectrons emitted from the photocathode at the first dynode also causes variation on the value of V_G, which is unlikely to be constant across all FD pixels.

Finally, the quantum efficiency of the FD pixels is likely to vary from pixel to pixel, and may even degrade with time.

6.2.2 K_v Method

The K_v method reduces the reliance on some of the simplifying assumptions outlined in Section 6.2.1, providing a more reliable (on an individual pixel basis) conversion for the measured NSB variance into a photon flux. The following method was adapted from references [132–134].

Firstly, the variance scaling factor K_v is defined as follows

$$K_v = \frac{I_{ADC}}{\sigma^2_{ADC}} \tag{6.10}$$

which is the ratio of the mean I_{ADC} and variance σ^2_{ADC} of an ADC trace. The nightly calibration pulses used as part of the cal A procedure of the relative FD calibration (Section 5.1) provide a convenient (and regular) ADC trace from which K_v can be derived on a pixel by pixel basis. It can be shown that an alternative expression for Equation 6.10 is

$$K_v = \frac{10}{2 \times G \times (1 + V_G) \times F} \tag{6.11}$$

where G is the PMT gain (ADC counts per photoelectron), V_G is the aforementioned PMT gain variance and F is the noise equivalent bandwidth (MHz) from

[2]There are plans to perform regular filter cleaning campaigns.

the complete analogue signal chain [132]. Using information provided by K_v, the photon flux is given by

$$\Phi_\gamma = \frac{[\sigma^2_{ADC}]^{NSB} \times K_v \times C_{FD}}{A \times \Delta t} \qquad [\text{photons}/\text{m}^2/\text{deg}^2/\mu\text{s}] \tag{6.12}$$

where definitions of $[\sigma^2_{ADC}]^{NSB}$, C_{FD}, A and Δt were provided in Section 6.2.1.

For this analysis we have chosen to calculate K_v using a slightly modified form of Equation 6.11. Several calibration related parameters (such as G and F) can be obtained through the monitoring database and are recorded for all pixels for each cal A measurement. This includes the cal A performed before and after data acquisition. To remain consistent with the measurements of C_{FD} (for which we use the value calculated after data acquisition), the values of K_v will be derived using calibration results obtained at the end of the shift.

The software used to analyse the cal A data (and produce the relevant calibration parameters to be uploaded to the monitoring database) contains the following equation:

$$G = \frac{\sigma^2_{ADC}}{I_{ADC}} \Big/ F \times Sphe_{res} \Big/ 5 \Big/ range_{coeff} \tag{6.13}$$

where $Sphe_{res}$ and $range_{coeff}$ are predefined constants with values of 1.4 and 0.99893, respectively. By substituting in Equation 6.10, this can be rewritten as

$$G = \frac{1}{K_v} \Big/ F \times Sphe_{res} \Big/ 5 \Big/ Range_{coeff} \tag{6.14}$$

which can be rearranged to give

$$K_v = \frac{5}{G \times F \times Sphe_{res} \times range_{coeff}} \tag{6.15}$$

The results yielded from both the Identical Pixel and K_v methods will be compared later in this Chapter.

6.3 Cross Check Method

A single FD site is comprised of six fluorescence telescopes, each with a field of view of 30° in azimuth and 28° in elevation, arranged side by side to provide a total azimuthal field of view of 180°. The standard convention for labelling telescopes will be adopted in this analysis, with the right most telescope (with respect to an observer standing at the centre of an FD building, looking inwards towards the SD array) being labelled as telescope 1. The telescope to the immediate left of telescope 1 is labelled as telescope 2 and so forth.

Individual telescopes are equipped with a camera comprised of 440 hexagonally shaped PMTs (or pixels) arranged on a 22 × 20 grid (see Section 3.2.1). The projection of the camera face onto the hemisphere of the sky results in a *fanning*

out effect of the pixels, as illustrated in the left hand plot of Figure 6.3. Due to this effect, the fields of view of two telescopes placed side by side will share an overlapping region. In particular the pixels within a small azimuthal range along the boundary of the two telescopes will share a common field of view, as illustrated in the right hand plot of Figure 6.3. If the sky is imagined to be a sphere, then the sphere's circumference (in degrees) at any zenith angle θ is given by $\sin\theta \times 360^{\circ}$. The sphere's circumference in this scenario can be thought of as the true azimuth range for a particular value of θ. As an example, consider the case for which n pixels (each of equal solid angle, as is the case of the FD pixels) are required to cover 360° in azimuth along the horizon. As θ decreases, fewer pixels are required to cover the available azimuth range and, since the number of pixels in a camera row is fixed, the fields of view of the pixels will eventually overlap with one another.

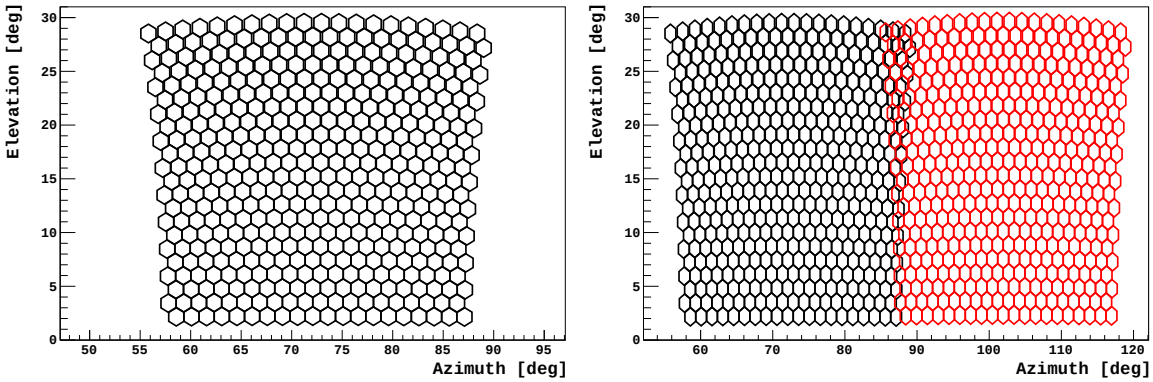

Figure 6.3: Left: The pixel arrangement of a typical FD telescope. Most telescopes share the same arrangement with the exception of telescopes 1 and 6 of Los Leones, both of which are missing columns of pixels (used in HEAT). Right: The field of view of an adjacent telescope is shown in red. The fields of view of the two cameras begin to overlap with increasing elevation.

The relative FD calibration stability between adjacent telescopes can be studied by calculating the ratio of the NSB photon flux observed by FD pixels sharing a common field of view. For simplicity the overlapping region is defined to be the two neighbouring FD pixel columns along the edges of the respective FD cameras of interest, across which the NSB is assumed to be azimuthally homogeneous. From Figure 6.3 it is evident that the FD pixels within this region do not completely overlap, which complicates the possibility of a direct pixel to pixel comparison of the NSB signal. For this reason we have chosen to compare the average NSB photon flux for the FD pixel columns of interest. For a perfectly calibrated detector the ratio of the NSB photon flux within the overlapping region is expected to be ~ 1. The convention adopted for calculating the NSB photon flux ratios is illustrated in Figure 6.4.

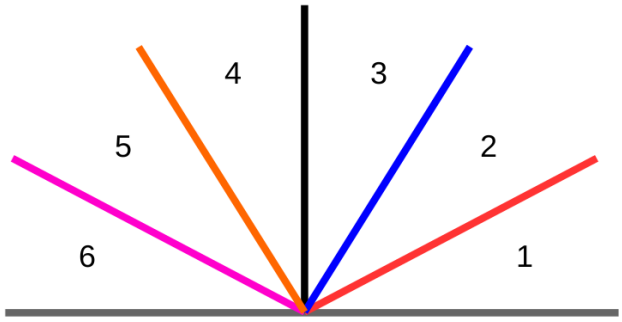

Figure 6.4: The arrangement of a typical FD site where telescopes are numbered from 1 through to 6. The coloured lines indicate the telescope boundaries along which the NSB ratio will be calculated. For this analysis the numerator of each ratio will always correspond to the telescope of the greater number i.e. telescope 2/telescope 1, telescope 3/telescope 2 and so on.

6.4 Results and Discussion

NSB variance data measured during the period beginning in January 2007 through to December 2016 are converted to a photon fluxes using the two methods outlined in Section 6.2. For the period prior to 2007, the information required (from the monitoring database) to calculate the factor K_v was lacking, and so data from this period was omitted from the analysis. The NSB variance is converted to a photon flux every 30 seconds if the following conditions are met:

- The moon is below an elevation of -5°.
- The sun is below an elevation of -18° (astronomical twilight).
- $\left[\sigma^2_{\mathrm{ADC}}\right]^{\mathrm{NSB}}$ greater than 0.
- FD calibration constant for the pixel of interest greater than 0.

Owing to the significantly large data set used in this analysis, recalling that the NSB variance is typically sampled every 30 seconds by each FD pixel throughout data acquisition, it may be convenient if the NSB photon flux is averaged over an extended period of time. As this analysis aims to evaluate the stability of the relative calibration of the 24 main fluorescence telescopes, a calibration which is performed on a nightly basis, it seems appropriate to average the NSB photon flux (for each FD pixel) over the same period of time. An example of the NSB photon flux averaged over a single night of observation is shown in Figure 6.5. It should be noted that the night displayed in Figure 6.5 was not chosen for any particular reason, and that the NSB photon flux is dependent on a number of factors including the time of year (which will determine which background stars are visible during data acquisition), atmospheric attenuation and cloud coverage.

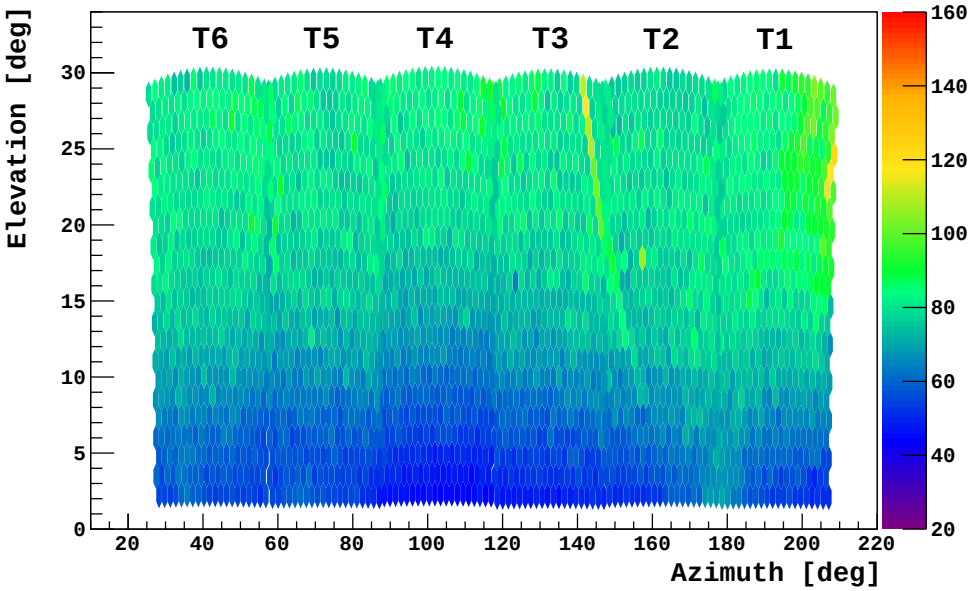

Figure 6.5: The average NSB photon flux observed by the six telescopes (labelled) of the Coihueco fluorescence detector during a single night. The colour scale represents the photon flux in units of 375 nm-equivalent photons/m^2/deg^2/μs. FD pixels pointing towards higher elevations will, on average, observe a greater NSB signal relative to those directed towards lower elevations. This may be attributed to the reduction in atmospheric extinction of NSB photons as a function of decreasing zenith angle. The track of bright pixels observed in telescopes 2 and 3 can be attributed to a star (with a bright U-band magnitude) crossing the fields of view of these two telescopes.

Using the cross check method outlined in Section 6.3, profiles of the NSB photon flux ratio as a function of time are constructed. These profiles provide a useful means of visualising the stability of the relative calibration for all telescopes within a given FD site. NSB photon flux ratio profiles calculated using the Identical Pixel method for Coihueco are shown in Figure 6.6. For this analysis we have chosen to study the quantity $\sqrt{\text{Photon Flux Ratio}}$ as we aim to clarify the stability of the relative calibration of the FD, which is proportional to the calibration constant C_{FD}, whereas the photon flux (Equation 6.6) is proportional to $[C_{FD}]^2$. The equivalent results obtained using the K_v method are shown in Figure 6.7. In comparison to Figure 6.6, ratio profiles obtained through the K_v method appear to be more consistent with a value of 1, with less spread about the central values. This is an expected result as the K_v method, by construction, allows for a more precise conversion between the NSB variance to a photon flux on a pixel by pixel basis. Additional figures for the Los Leones, Los Morados and Loma Amarilla fluorescence detectors are provided in Appendix C and show a similar trend between the two methods.

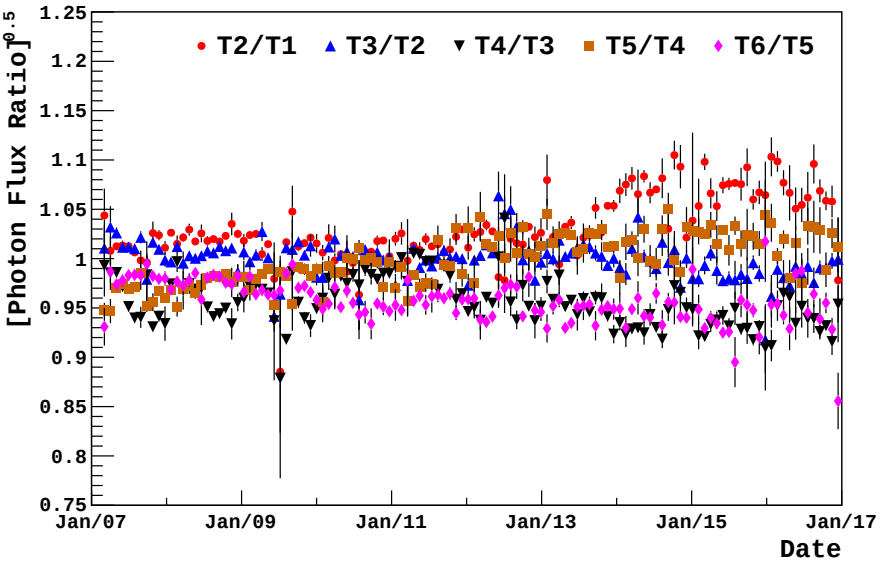

Figure 6.6: Results for Coihueco for the years 2007 to 2016 calculated using the Identical Pixel method. To reduce clutter, the horizontal axis has a bin width equal to 1 synodic month rather than 1 night.

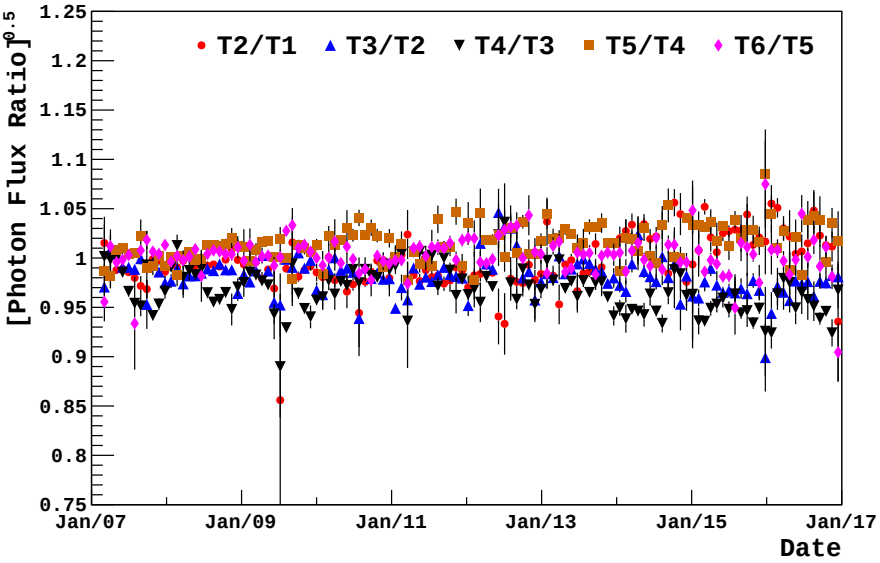

Figure 6.7: Results for Coihueco using the K_v Method for calculating the photon flux. The vertical axis is given in terms of $\sqrt{\text{Photon Flux Ratio}}$ - to allow for direct comparison with results obtained from the Identical Pixel Method. An interesting note is the increased spread beyond $\sim$ 2014, which is perhaps due to the lack of absolute calibration campaigns in recent years (the most recent occurring in April of 2013 [135]).

The long term stability of the relative calibration between a pair of adjacent telescopes can be inferred from the slope of a linear function fitted to the ratio profile. A slope compatible with a flat line would be an indication of a stable relative calibration. Fitted slopes for individual ratio profiles are summarised in Tables 6.2 and 6.3 for the Identical Pixel and K_v methods, respectively, and indicate only a handful of telescope pairings with fitted slopes which are consistent with zero. The average slopes for the two methods are compared for each FD site in Table 6.4. For the case of the Los Leones and Los Morados FD sites, the K_v method indicates a relative calibration that is more stable with time than that estimated using the Identical Pixel method. For Loma Amarilla and Coihueco, the average slope of both methods are consistent with one another.

	T2/T1	**T3/T2**	**T4/T3**	**T5/T4**	**T6/T5**
Los Leones	1.12 ± 0.09	0.78 ± 0.04	0.39 ± 0.04	-0.30 ± 0.05	0.08 ± 0.02
Los Morados	0.56 ± 0.07	0.00 ± 0.07	-0.23 ± 0.04	0.83 ± 0.06	0.32 ± 0.02
Loma Amarilla	0.30 ± 0.05	0.06 ± 0.04	0.00 ± 0.03	-0.63 ± 0.06	0.35 ± 0.04
Coihueco	0.46 ± 0.04	-0.17 ± 0.03	-0.38 ± 0.09	0.77 ± 0.03	-0.68 ± 0.08

Table 6.2: Listed here are the fitted slopes (in % per year) to each $\sqrt{\text{Photon Flux Ratio}}$ profile. The uncertainties were estimated by scaling the error bars such that a reduced χ^2 of 1 is returned (see Section 5.5.3).

	T2/T1	**T3/T2**	**T4/T3**	**T5/T4**	**T6/T5**
Los Leones	0.70 ± 0.08	0.28 ± 0.03	-0.13 ± 0.03	0.12 ± 0.04	-0.01 ± 0.02
Los Morados	0.07 ± 0.05	0.04 ± 0.07	-0.14 ± 0.03	0.08 ± 0.04	0.03 ± 0.02
Loma Amarilla	-0.13 ± 0.04	0.11 ± 0.02	0.07 ± 0.03	-0.63 ± 0.06	0.12 ± 0.03
Coihueco	0.43 ± 0.01	-0.16 ± 0.03	-0.34 ± 0.07	0.43 ± 0.04	-0.08 ± 0.10

Table 6.3: Fitted slopes (in % per year) using the K_v method.

	Identical Pixel Method	**K_v Method**
Los Leones	0.41 ± 0.05	0.19 ± 0.04
Los Morados	0.29 ± 0.06	0.01 ± 0.05
Loma Amarilla	-0.01 ± 0.05	-0.09 ± 0.04
Coihueco	0.00 ± 0.06	0.06 ± 0.06

Table 6.4: Average fitted slopes (across all adjacent telescope pairs) for each FD station.

It is important to recognise that this particular analysis only provides a measure of the relative difference between the calibration of two telescopes and offers

no information regarding any absolute differences in the calibration. An an example, if the absolute calibration of a single telescope (call this T_1) was known to be perfectly stable with time, then the ratio of T_1 and a second telescope T_2 would be a measure of the absolute difference of the calibration stability for T_2. Unfortunately, this particular analysis is not capable of determining the stability of the absolute calibration of a single telescope, and so results should be treated in a relative sense. Due to this limitation, it is difficult to directly compare any drift inferred from these results to the $\sim -1.6\%$ per year drift in the Observatory's energy scale, which itself is an absolute drift. From Table 6.4 the average calibration drift between two telescopes is small ($\sim 0.2\%$ per year), a possible indication that the drift in the stability of the energy scale is dominated by an effect common to all mirrors which can not be detected through this specific analysis. This is discussed later in Section 7.4.4, where we use stellar photometry to compare the evolution of the FD calibration between individual telescopes belonging to the same FD site.

The uncertainty (or stability) of the relative FD calibration between a pair of adjacent telescopes at any point in time can be estimated from the width of the distribution formed from $\sqrt{\text{Photon Flux Ratio}}$. More specifically, the uncertainty is given by $\sigma/\sqrt{2}$, where σ is estimated using a fitted Gaussian function. The results for all telescope pairings across the FD are summarised in Tables 6.5 and 6.6 for the Identical Pixel and K_v methods, respectively. Distributions for individual telescope pairs are provided in Appendix C.

		T2/T1	T3/T2	T4/T3	T5/T4	T6/T5
Los Leones	**mean**	1.03	1.04	0.97	1.01	1.03
	$\sigma/\sqrt{2}$	0.04	0.02	0.01	0.01	0.01
Los Morados	**mean**	1.00	1.05	0.96	1.02	1.04
	$\sigma/\sqrt{2}$	0.04	0.01	0.01	0.02	0.01
Loma Amarilla	**mean**	0.95	1.01	0.99	0.96	0.95
	$\sigma/\sqrt{2}$	0.01	0.01	0.01	0.01	0.02
Coihueco	**mean**	1.03	1.00	0.96	1.00	0.96
	$\sigma/\sqrt{2}$	0.03	0.01	0.02	0.02	0.02

Table 6.5: Summarised here are the means and σ for each $\sqrt{\text{Photon Flux Ratio}}$ distribution using results calculated from the Identical Pixel method.

An overall estimate of the uncertainty in the relative FD calibration at any point in time can be inferred from a combined distribution, incorporating results from all possible telescope pairings. The combined distributions for the two methods are illustrated in Figure 6.8. From the left hand plot of Figure 6.8, the uncertainty in the relative FD calibration (calculated using the Identical Pixel method) is estimated to be 3.3%. It should be noted that this particular method made several simplifying assumptions (discussed in Section 6.2.1) regarding the

		T2/T1	T3/T2	T4/T3	T5/T4	T6/T5
Los Leones	**mean**	1.00	1.02	1.01	1.00	1.03
	$\sigma/\sqrt{2}$	0.02	0.01	0.01	0.01	0.01
Los Morados	**mean**	1.00	1.03	0.99	1.00	1.01
	$\sigma/\sqrt{2}$	0.02	0.01	0.01	0.01	0.01
Loma Amarilla	**mean**	0.99	1.00	0.99	0.99	1.00
	$\sigma/\sqrt{2}$	0.01	0.01	0.01	0.01	0.01
Coihueco	**mean**	1.00	0.98	0.97	1.02	1.00
	$\sigma/\sqrt{2}$	0.02	0.01	0.02	0.02	0.01

Table 6.6: Summary mean and width of distributions using the K_v method for calculating the photon flux. The results suggest that the uncertainty in the relative FD calibration is of the order of $\sim 1-2\%$.

characteristics of individual FD pixels. The estimated uncertainty of 3.3% must include the fact that these assumptions are unlikely to be realistic, implying that the natural variation in the FD pixel gains must be smaller than 3.3%. In other words, 3.3% is likely to be an overestimation of the relative FD calibration uncertainty.

In contrast to the Identical Pixel method, the K_v method accounts for variations in the characteristics of individual FD pixels, allowing for a more precise estimation of the NSB photon flux. This is reflected in the results yielded using the K_v method (right hand plot of Figure 6.8) which estimates an uncertainty in the relative FD calibration of 1.8%. This result is consistent with the earlier statement that the 3.3% uncertainty estimated through the Identical Pixel method is

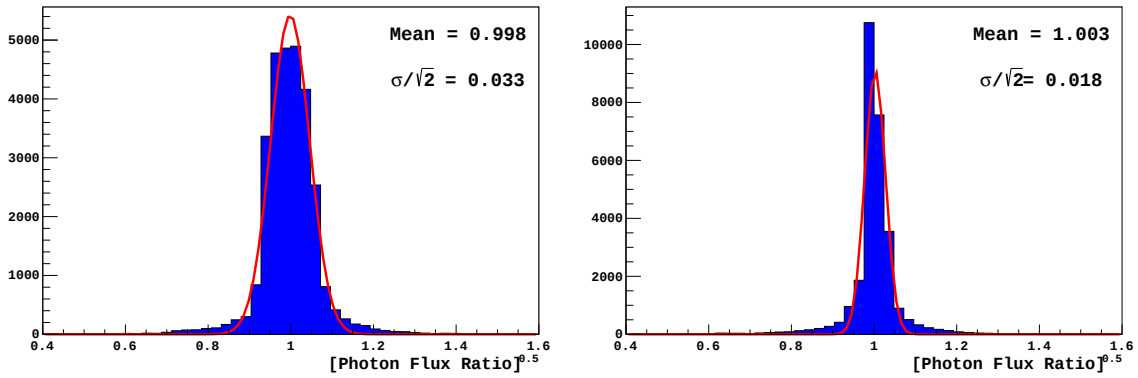

Figure 6.8: Left: Combined distribution of $\sqrt{\text{Photon Flux Ratio}}$ using the Identical Pixel method for the period between January 2007 through to December 2016. Right: Combined distribution using the K_v method. The width of the distribution formed through the K_v method is significantly narrower compared to that of the Identical Pixel method. A single entry in each distribution corresponds to a single value of $\sqrt{\text{Photon Flux Ratio}}$ (calculated nightly) for a single telescope pairing.

Systematic Uncertainties	
Fluorescence Yield	3.6%
Atmosphere	$(3.4 - 6.2)\%$
FD Calibration	9.9%
FD Profile Reconstruction	$(6.5 - 5.6)\%$
Invisible Energy	$(3 - 1.5)\%$
Time Stability	5%
Total	14%

Table 6.7: Table of systematic uncertainties presented at 33$^{\text{rd}}$ International Cosmic Ray Conference. Of particular interest here is the uncertainty for the FD calibration (9.9%) which combines both the relative and absolute FD calibration uncertainties [89].

likely to be an overestimate.

A sizeable discrepancy is observed between these results and the quoted FD calibration systematic uncertainty of 9.9% (Table 6.7), which could exist for a variety of reasons. The 9.9% combines the uncertainties from both the absolute and relative FD calibrations, whereas the analysis performed in this Chapter only measures contributions from the relative FD calibration. By subtracting (in quadrature) the contribution from the absolute FD calibration, estimated to be between $5 - 9\%$ [89, 114], we expect the relative FD calibration to have an uncertainty of the order of $\sim 4.1 - 8.5\%$, the lower end of which is comparable with the results obtained in this analysis. Any remaining difference could be due to a limitation in this particular analysis, which only compares the calibration stability at an instant in time and is blind to any long term calibration drifts which may be common to all telescopes. Interestingly, if a calibration drift does indeed exist, the results presented here suggest that the apparent sensitivity of all FD pixels appear to change at a similar rate, within the estimates listed in Tables 6.2 and 6.3.

6.5 Conclusions

In this Chapter we have used the NSB to study the stability of the FD relative calibration between adjacent FD telescopes. To achieve this, a cross check method was developed to compare the NSB photon flux (calculated though two different methods) observed by neighbouring FD pixel columns of adjacent FD telescopes. It was assumed that the FD pixels within these columns share a common field of view when projected onto the hemisphere of the sky. By comparing the observed NSB photon flux on a nightly basis we conclude the following:

- By using nightly averaged NSB photon flux data measured since 2007, we were able to analyse the long term stability of the relative calibration between adjacent telescopes (belonging to the same FD site) across 10 years

of operation. Having repeated this for all possible telescope pairings from the four main FD sites, we concluded that the relative calibration drift between two telescopes is small and that the observed $\sim -1.6\%$ per year drift reported in the stability of the Observatory's energy scale (Section 5.8) is likely to be dominated by an effect common to all telescopes.

- It was demonstrated that results obtained using the K_v method for converting the NSB variance into a photon flux indicated a more stable calibration as a function of time. This is an expected result as the K_v method reduces the reliance on several simplifying assumptions regarding the performance of individual FD pixels, allowing for a more precise conversion on a pixel by pixel basis.

- We estimate an uncertainty of 1.8% in the relative FD calibration between adjacent FD telescopes at any point in time. It was noted that this estimate combines results from all FD telescopes, and should therefore be considered as an overall estimate across the entire FD. We find that the results are well within the quoted total FD calibration systematic uncertainty of 9.9% ($4.1 - 8.5\%$ after removing the contribution from the absolute FD calibration).

At the beginning of this Chapter it was mentioned that the original intention of studying the NSB photon flux was to treat it as a constant light source to track the long term absolute gain stability of the FD pixels. In Chapter 7 we will investigate the feasibility of using signals associated with bright stars as they traverse the fields of view of individual FD telescopes to monitor the absolute FD calibration stability.

Chapter 7

A Cross Check of the Fluorescence Detector Absolute Calibration Using Stellar Photometry

In Chapter 5 the long term stability of the Pierre Auger Observatory's energy scale was monitored. To aid in this, we defined the energy scale ratio (ESR) as the ratio of the reconstructed energy of the primary cosmic ray by the FD, E_{FD}, and the zenith angle-corrected shower size estimated by the SD, S_{38}. Several unexpected features were noted in the time evolution of the ESR most notably a downwards drift of $\sim 1.6\%$ per year, a seasonal modulation of amplitude $\sim 2\%$ and a discontinuity of $\sim 5-10\%$ beginning in 2014. In Section 5.7.1 it was concluded that a small fraction of the drift ($\sim 0.3\%$) can be associated with the SD event rate. It is suspected that the residual drift in the ESR is related to the long term performance of the FD. The following Chapter will investigate the hypothesis that the FD's contribution to the ESR drift is associated with the long term calibration stability of the FD telescopes, more specifically the PMTs which form the FD cameras. The long term calibration stability can be monitored through the study of a constant light source as observed by the FD. To achieve this, a search is performed on the FD background files for signals associated with specific stars moving across the fields of view of individual FD cameras.

In this Chapter we present a method developed to monitor the absolute calibration stability of the Pierre Auger Observatory's FD using stellar photometry. The Chapter will begin with a review of the selection criteria for suitable star candidates, followed by how the signals associated with these stars can be extracted from the FD night sky background (NSB) files. Following this will be a discussion of the method developed to use star signals to monitor the FD's absolute calibration and an extensive analysis of the systematic uncertainties of the method. Finally, long term star calibration measurements obtained for a number of FD telescopes are compared to the evolution of the ESR.

The concept of using stellar photometry to monitor the absolute calibration of the Observatory's FD is based on work by Alberto Segreto, the details of which

are documented in reference [132]. The method presented in this Chapter is a more complete analysis of this early work.

7.1 Choosing a Constant Light Source

The performance of the absolute calibration stability of the FD telescopes can be monitored by studying their response to a light source of known absolute brightness. If the absolute brightness of the light source is known to be stable with time, then any changes in the response of the FD can be attributed to the detector itself. A possible candidate light source would be either of the Observatory's two laser facilities, the CLF and XLF (Section 3.3), both of which provide regular laser shots observable from several locations across the FD. The effect of atmospheric attenuation on the laser signal must be known precisely (on any given night) in order to determine the expected brightness of the laser signal. This is a difficult task which, when coupled with the long term reliability of the laser facilities, unfortunately make them unsuitable for our purposes. Moving away from man-made light sources, the NSB as a whole could be considered as a constant light source when averaged over a long enough time period. However, the uncertainty and time variability of the various contributing sources (see Table 6.1) would have complicated this task. Finally, a compromise was found in the form of signals generated by bright stars crossing through the fields of view of individual FD telescopes. Stars which satisfy the following criterion are deemed suitable for this purpose:

- Star of interest is sufficiently bright in the operational bandpass of the FD, limiting candidates to those with bright U-band magnitudes.
- A star with a well known spectral type and preferably measured stellar spectrum. In cases where the stellar spectrum is not well known the method can still be used to monitor the calibration stability in a relative sense (this is an important detail which will be revisited later in this Chapter).
- Star of interest is observable by at least one FD telescope. Ideally the star should cover a large range of zenith angles within the field of view of a single FD telescope, providing a sufficient lever arm in air mass (see Section 7.1.1 for a definition of air mass).

One star for which these conditions are satisfied is Sirius, a binary star system comprised of a main sequence star of spectral type A1V (Sirius A) accompanied by a faint white dwarf of spectral type DA2 (Sirius B) [136]. It is the main sequence star which is of relevance in this study and will be referred to as Sirius hereinafter. Sirius has a U-band magnitude of -1.51 [137], and is significantly brighter than any other star in the night sky allowing for its relatively straightforward detection amongst the underlying NSB signal. Sirius is observable from four individual FD

telescopes across the standard FD, as well as an additional telescope in HEAT. During the months spanning August to November of each year, Sirius can be observed rising in the East from Coihueco telescope 4, Los Leones telescope 1 and Loma Amarilla telescope 6 (CO 4, LL 1 and LA 6, respectively). Earlier in the year (from February to June) Sirius can be seen setting in the West from Los Morados telescope 5 (LM 5). The path of Sirius across the fields of view of these telescopes is illustrated in Figure 7.1.

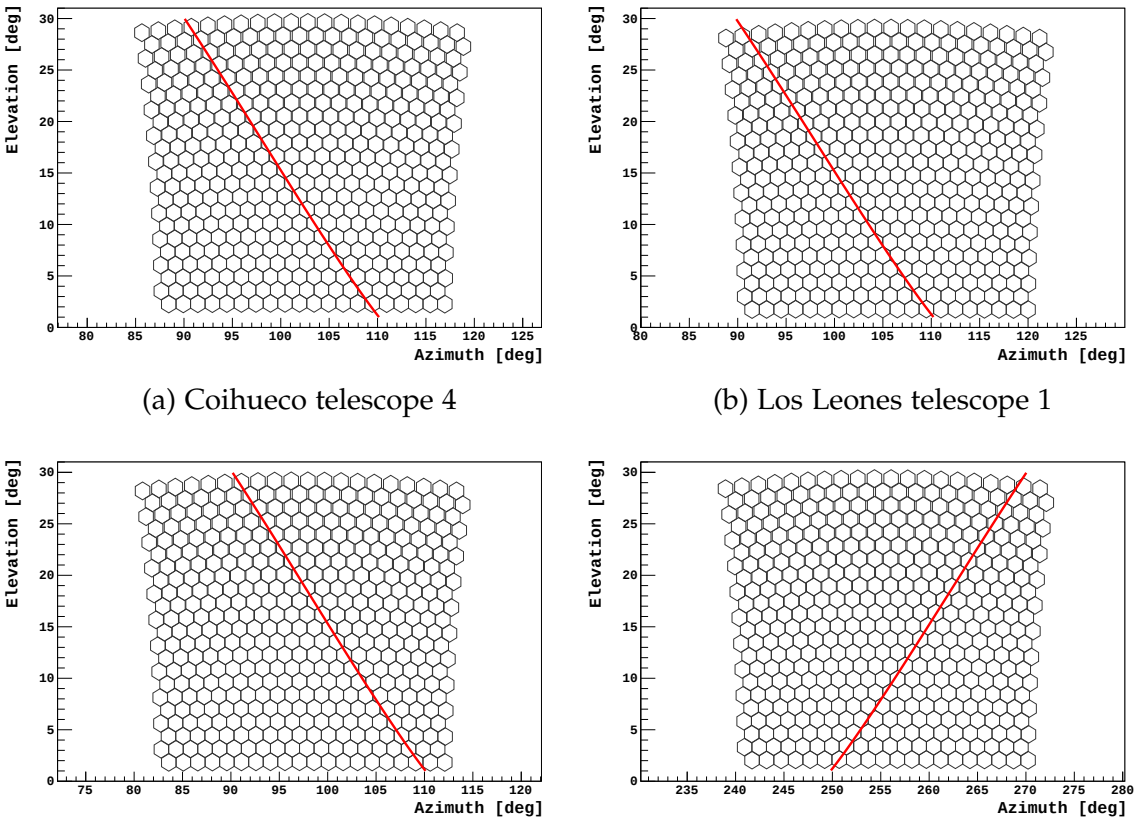

(a) Coihueco telescope 4

(b) Los Leones telescope 1

(c) Loma Amarilla telescope 6

(d) Los Morados telescope 5

Figure 7.1: Theoretical paths calculated using the Python package PyEphem are overlaid in red. Sirius covers the entire field of view in elevation ($\sim 30°$) for each of these telescopes, although the effective track length is subject to observational conditions on any given night. The duration of these transits takes approximately 2 hours to complete.

It should be noted that Sirius (and any other star for that matter) will cross the sky along the same path each night, with the only difference being the time at which Sirius reaches a particular position in the sky[1]. The analysis method presented in the following sections was developed for Sirius as it crosses the

[1]The star will appear at a given position $\sim$ 4 minutes earlier compared to the previous night.

field of view of CO 4 but is applicable to any star for which the previously listed conditions are satisfied.

7.1.1 Identifying Star Signals from FD Night Sky Background Files

On clear (cloudless) nights, Sirius will appear as a bright spot moving across the field of view of the telescope. Quantitatively, this signal will manifest itself as significantly large measurements of the NSB variance. The transit of Sirius can be visualised by converting the NSB into an average photon flux (using the method discussed in Section 6.2.2), as shown in Figure 7.2.

The NSB is sampled every 30 seconds during data acquisition, allowing the signal from Sirius to be calculated with the same regularity. The method is outlined as follows:

1. The first step is to recognise that NSB variance measurements (σ^2_{total}) stored in the FD background files have contributions from the star of interest (σ^2_{star})

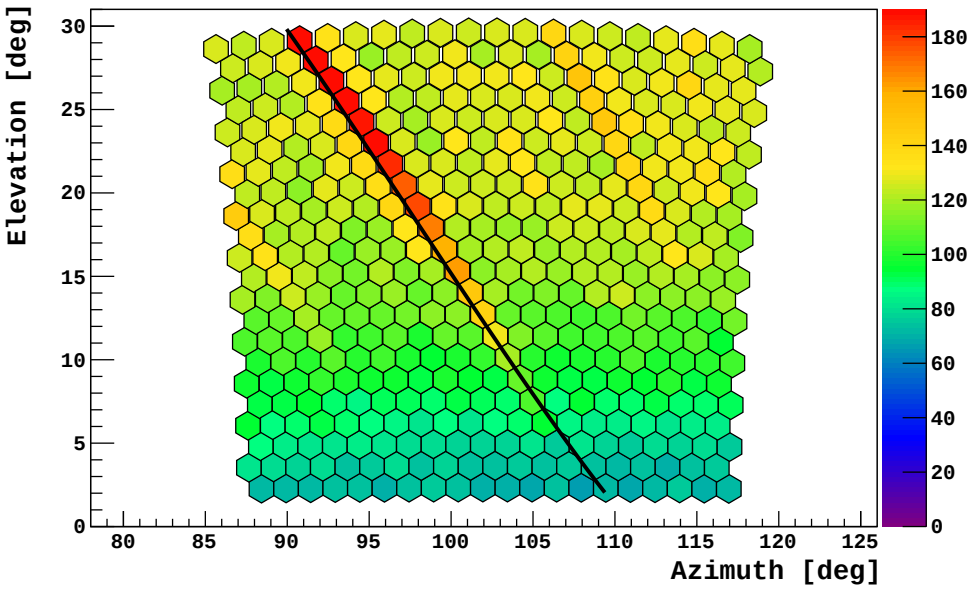

Figure 7.2: The NSB photon flux observed by the pixels of CO 4 averaged over a period of less than 2 hours. The colour scale here indicates the average photon flux in units of 375 nm-equivalent photons/$m^2/\mu s$. The track of bright PMTs can be attributed to the transit of Sirius (which begins at an elevation of $\sim 10^\circ$ for the time period considered here). The expected path of Sirius is overlaid in black. It should be noted that the brightness of the star (and the NSB) increases with elevation. NSB photons viewed at higher elevations propagate through less atmosphere, suffering from less atmospheric attenuation on their paths towards the detector.

as well as the underlying NSB (σ^2_{NSB}), the latter of which must be removed.

$$\sigma^2_{total} = \sigma^2_{star} + \sigma^2_{NSB} \text{ ADC counts}^2 \tag{7.1}$$

To correct for the underlying NSB, a linear function (not necessarily flat) is fitted to the trace of σ^2_{total} as a function of time, ignoring any significant features (most likely to be associated with other bright NSB objects). An example of this is shown in Figure 7.3. Using the fitted linear function, the contribution of σ^2_{NSB} can be subtracted (in quadrature) from σ^2_{total} as a function of time. This step is repeated for all pixels in the camera.

2. Identify the position of Sirius on the camera of interest at a given time. To aid in this process, the Python package PyEphem is used to calculate the position of the star in both azimuth (ϕ_{star}) and elevation (θ_{star}).

3. Identify the pixel that is nearest to the position of Sirius (this will be referred to as PIX_{star}). Pointing directions of individual pixels are known to within 0.1°, making this calculation straightforward. The space angle ζ for the i^{th} pixel pointing in the $(\phi_{PIX_i}, \theta_{PIX_i})$ direction and the position of the star is given by:

$$\zeta_i = \arccos\left(\frac{\overrightarrow{P}_{PIX_i} \cdot \overrightarrow{P}_{star}}{|\overrightarrow{P}_{PIX_i}| \cdot |\overrightarrow{P}_{star}|}\right) \tag{7.2}$$

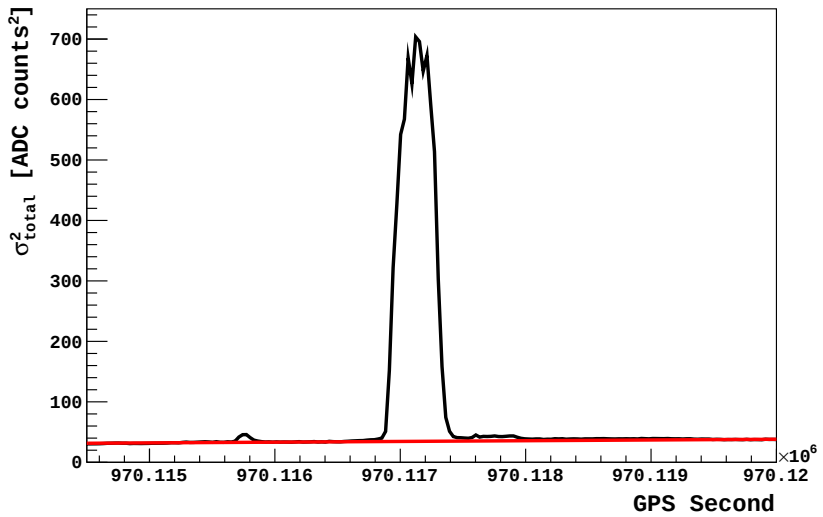

Figure 7.3: σ^2_{total} as a function of time for pixel 208 in CO 4 for a particular period of data acquisition. The large peak is due to the transit of Sirius through this pixel. The underlying NSB (σ^2_{NSB}) is estimated by a linear function (shown in red), which accounts for any gradient in the NSB throughout the night.

where $\overrightarrow{P}_{PIX_i} = (r, \phi_{PIX_i}, \theta_{PIX_i})$ and $\overrightarrow{P}_{star} = (r, \phi_{star}, \theta_{star})$. The choice of r is arbitrary and chosen to be 1. Minimising ζ over all camera pixels gives PIX_{star}, a first guess of the location of Sirius on the camera.

4. Search the area of the camera surrounding PIX_{star} for the pixel with the largest NSB signal (call this $PIX_{hottest}$). This is a precautionary step, and more often than not PIX_{star} and $PIX_{hottest}$ correspond to the same pixel.

5. Identify the six pixels surrounding $PIX_{hottest}$ (Figure 7.4). The total star signal will be integrated across this crown of pixels. This not only accounts for the uncertainty in the location of the optical spot of the star on the camera but also its size (the extent of the optical spot is discussed in greater detail in Section 7.3.1).

   The uncertainty in the location of the spot is partly due to the geometry of the transit of the star across the camera. For example, from Figure 7.2 it can be seen that the path of the star (indicated by the overlaid track) does not always pass through the centre of the field of view of individual pixels, particularly at higher elevations. During this particular segment of the track, it is possible that $PIX_{hottest}$ regularly alternates between neighbouring pixels. Integrating the signal across an extended region of the camera will minimise the amount of signal lost due to the choice of $PIX_{hottest}$. Due to the choice of integration area, the analysis does not compute the signal if the spot of the star is located along the border of the camera, as a complete crown can not be formed.

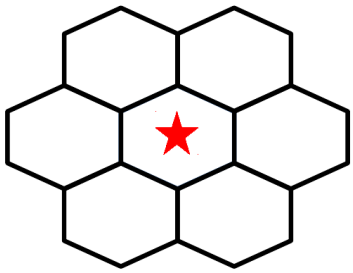

Figure 7.4: The hottest pixel (central) and its surrounding crown.

6. Convert σ^2_{star} to a photon flux. This step is repeated for each pixel in the crown of interest.

$$\Phi_\gamma = \frac{\sigma^2_{star} \times K_v \times C_{FD}}{A \times \Delta t} \quad [\text{photons/m}^2/\mu\text{s}] \tag{7.3}$$

   where definitions of K_v, C_{FD}, A and Δt were provided in Section 6.2. The total star signal at any point in time is then given by:

$$\Phi_{total} = \sum_i \Phi_{\gamma,i} \quad [\text{photons/m}^2/\mu\text{s}] \tag{7.4}$$

where i is a loop over all relevant crown pixels.

The star signal can be evaluated as a function of its elevation in the sky by repeating steps 2-7 for all time bins during which Sirius is in the field of view of CO 4. This is illustrated in Figure 7.5. It should be noted that the star signal is measured in terms of 375 nm-equivalent photons (see Section 5.1). Alternatively, the signal can be studied as a function of air mass (AM), a quantity which is representative of the amount of atmosphere between the observing telescope and the star of interest. For the purposes of this study, we will define air mass in a non-standard way where 1 air mass is the amount of atmosphere between an observer (on Earth) and an object located directly overhead, at the zenith[2]. This definition implies that a measurement made at an air mass of 0 corresponds to a measurement made beyond the Earth's atmosphere. A crude conversion for the elevation of the star (θ_{star}) into an air mass is as follows:

$$AM(\theta_{star}) \approx \sec(90 - \theta_{star}) \tag{7.5}$$

Equation 7.5 assumes that the Earth's atmosphere is a simple, single layer of uniform density lying plane parallel with the Earth's surface, and provides a valid approximation above elevations of 30°. At lower elevations, such as those considered in this analysis, these approximations begin to break down as the curvature of the Earth and the fact that the atmosphere is much more complex than a single, uniform layer become significant. For this reason, an alternative equation (adopted from [138]) which accounts for a more complex atmosphere as well as the Earth's curvature will be used for this analysis:

$$AM(z_t) \approx \frac{1.002432\ \cos^2 z_t\ +\ 0.148386\ \cos z_t\ +\ 0.0096467}{\cos^3 z_t\ +\ 0.149864\ \cos^2 z_t\ +\ 0.0102963\ \cos z_t\ +\ 0.000303978} \tag{7.6}$$

where $z_t = 90 - \theta_{star}$. It is important to note that the relationship between air mass and elevation angle is not a linear one. Air mass increases rapidly for an elevation angle approaching the horizon, and slowly for an elevation angle approaching the zenith. An example of the star signal as a function of air mass (which will be referred to as a *track*) is shown in Figure 7.6.

7.1.2 Functional Form of Star Tracks

Photons emitted from a star will propagate through the Earth's atmosphere towards the FD, a path along which they experience some level of atmospheric attenuation due to absorption and scattering. The transmittance (T) of a single wavelength (λ) light source through a medium can be described using the Beer-Lamber Law:

$$T = \frac{\Phi^t}{\Phi^r} \tag{7.7}$$

[2]The standard definition is for an observer located at sea-level.

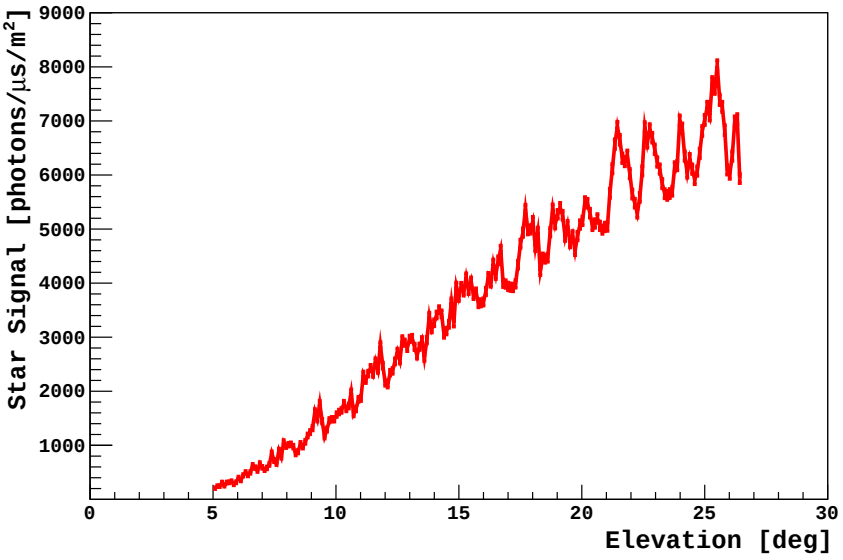

Figure 7.5: Example signal of Sirius viewed by CO 4 as a function of the elevation of the star. The almost periodic modulations arise because of the pixelated design of the FD camera. A minimum elevation angle of 5° has been applied to the track as the signal becomes increasingly difficult to observe at lower elevations. It should be noted that the vertical axis is actually in terms of 375 nm-equivalent photons/μs/m^2.

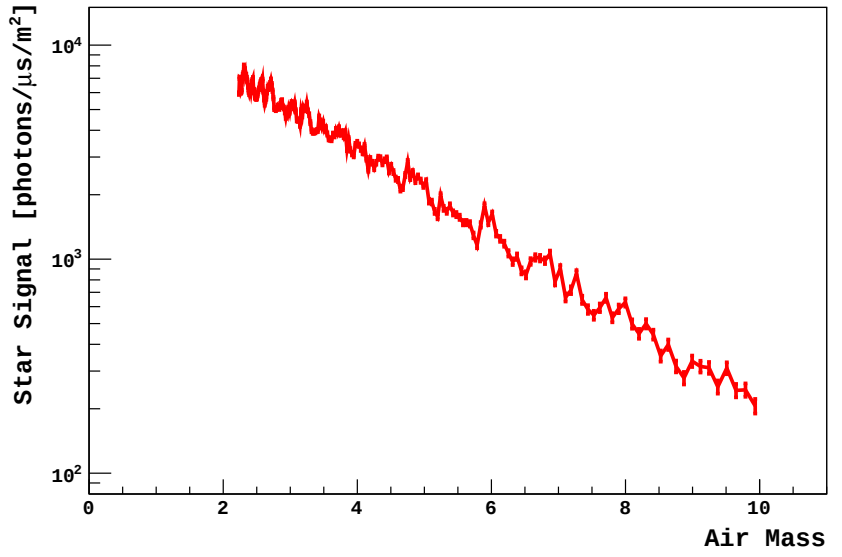

Figure 7.6: Signal from Figure 7.5 as a function of air mass. The fixed field of view of the FD telescopes limits star signal measurements to a minimum air mass of ~ 2.

where Φ^r is the radiant flux entering the medium and Φ^t is the flux which is emitted. An equivalent expression is a simple exponential function:

$$T = e^{-\tau} \tag{7.8}$$

where τ is the optical depth of the medium. For the scenario of star light propagating towards a telescope, the medium of interest is the Earth's atmosphere, for which we assign an optical depth denoted by τ_{total}^{atmos}. For a realistic atmosphere, τ_{total}^{atmos} has contributions from several sources, the most dominant of which are Rayleigh (or molecular) scattering, ozone absorption and Mie (or aerosol) scattering. Therefore, for an air mass of 1, this can be written as

$$\tau_{total}^{atmos} = \tau_{Rayleigh} + \tau_{O_3} + \tau_{aero} \tag{7.9}$$

An important note is that all 3 contributions have a wavelength dependence, so a more appropriate expression would be

$$\tau_{total}^{atmos}(\lambda) = \tau_{Rayleigh}(\lambda) + \tau_{O_3}(\lambda) + \tau_{aero}(\lambda) \tag{7.10}$$

Photons emitted from a star cover a broad wavelength range with the total signal (at ground level) being equal to the summation over all wavelengths. It should be noted that the sum of several exponential functions does not equate to an exponential function.

$$\begin{aligned} [Star\ Signal]_{Total}^{Ground}(AM) &= \sum_i F_0(\lambda_i) \times e^{-\tau_{total}^{atmos}(\lambda_i) \times AM} \\ &= \sum_i F_0(\lambda_i) \times e^{-\left(\tau_{Rayleigh}(\lambda_i) + \tau_{O_3}(\lambda_i) + \tau_{aero}(\lambda_i)\right) \times AM} \end{aligned} \tag{7.11}$$

where $F_0(\lambda_i)$ is the star flux at the top of the atmosphere. Finally, the total signal measured by the FD is given by folding Equation 7.11 with the optical response of the detector:

$$[Star\ Signal]_{Total}^{Telescope}(AM) = [Optics] \times [Star\ Signal]_{Total}^{Ground}(AM) \tag{7.12}$$

7.1.3 Characteristics of Star Tracks

The method outlined in Section 7.1 can be extended to all cloudless nights during which the star of interest is observable. Example tracks for Sirius observed by CO 4 during a selection of nights are shown in Figure 7.7. A number of interesting features are noted here.

Star tracks are sampled from a variety of atmospheric conditions throughout the year. From Equation 7.11 it can be seen that the exponential slope of each star track is proportional to the signal's attenuation through the atmosphere. This means that star tracks measured during nights of greater atmospheric attenuation will display characteristically steeper (exponential) slopes relative to those

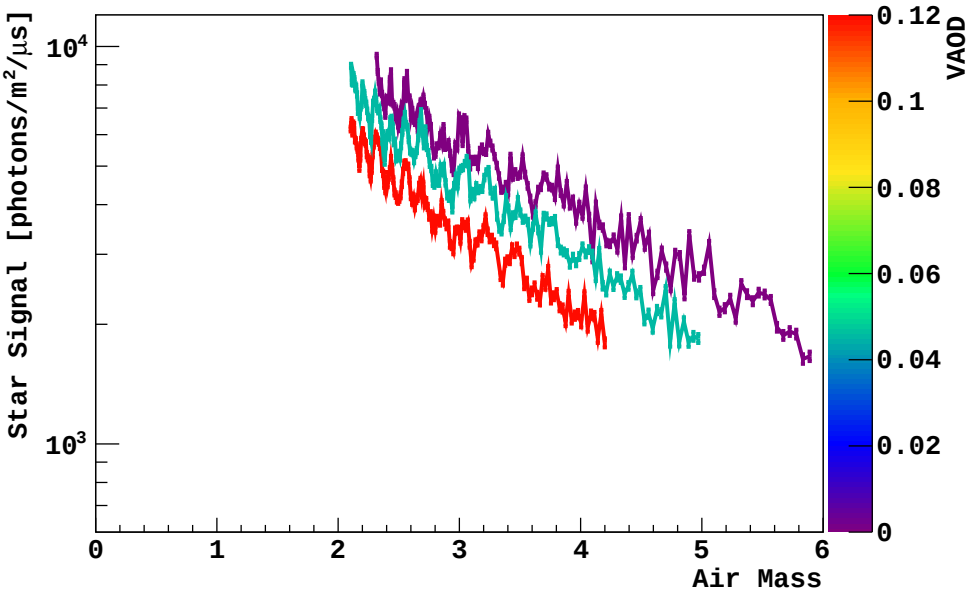

Figure 7.7: The star signal from Sirius observed by CO 4 over several nights. The colour scale here represents the average VAOD (up to a reference height of 4.5 km a.s.l) as measured by the CLF.

measured during nights of less attenuation. The colour scale of Figure 7.7 represents the average nightly VAOD measured using the CLF and is inversely proportional to the cleanliness of the atmosphere. Star tracks obtained from nights with larger measured VAODs are attenuated more rapidly as a function of increasing air mass. In theory, if all signals were measured with an equally calibrated instrument, each star track should converge to a single value at 0 air mass. The significance of this detail will become apparent later in the analysis.

The ability to measure high quality star tracks is strongly dependent on ideal observational conditions. The analysis requires cloudless nights during which FD data acquisition remains largely uninterrupted, especially during the transit of the star of interest. In a similar fashion to how varying atmospheres can affect the track's slope, observational conditions can alter the track length on different nights i.e. the effective range of air mass covered by the star of interest. A number of operational safety flags have been implemented in the FD system (see Section 6.1) that, when triggered, will block the telescope's view of the star resulting in an artificial shortening of the star track.

Modulations appear in each track as a consequence of the design of the FD camera. For a perfectly efficient camera surface, one would expect the logarithm of the star signal to be approximately linear as a function of air mass. However, due to its pixelated design, the FD camera surface is not uniformly efficient, resulting in almost periodic modulations in the star track. As previously mentioned, a given star will traverse the sky along the same path night to night, implying that

(for a given telescope) the same collection of pixels will be sampled during each transit. On average the modulations for individual tracks will be the same for a given star and telescope pairing.

7.2 Analysis Method

Having demonstrated a technique which can be used to extract relevant star tracks from the FD NSB files, we can now proceed to the next stage of the analysis - how star tracks can be used to monitor the absolute calibration of the FD. Once again, the method outlined here was developed for the case of Sirius passing through the field of view of CO 4 but is applicable to all other star and telescope pairings.

7.2.1 Correcting the Rayleigh Atmosphere

In Section 7.1.2 it was established that the exponential slope of each star track is proportional to its attenuation through the atmosphere, with the significant contributions coming from Rayleigh scattering, ozone absorption and aerosol scattering. The atmospheric attenuation of a given star track can be partially corrected using knowledge of the atmosphere's molecular and ozone content at the time of the transit of the star. A model, which will be referred to as the *Rayleigh Model*, of the expected star track in a model atmosphere is calculated and used to partially correct the attenuation of the measured track.

The model begins with the photon flux of the star at the top of the Earth's atmosphere (prior to its attenuation through the atmosphere) across the operational bandpass of the FD ($\sim 290 - 410\,\text{nm}$). This is provided using a stellar spectrum for the star of interest. Ideally this spectrum would have been measured using an instrument positioned beyond the Earth's atmosphere. The stellar spectrum for Sirius was measured using the Space Telescope Imaging Spectrograph (STIS), an instrument located on board the Hubble Space Telescope, and is shown in Figure 7.8 [139].

The spectrum is then weighted by the relative efficiency curve of the FD telescope of interest. This curve is the convolution of the transmission of the UV filter and corrector ring, the reflectivity of the segmented mirror and the quantum efficiency of the FD pixels. An example of one of these curves is illustrated in the left hand plot of Figure 7.9. It should be noted that the efficiency curve has slight variations between different FD telescopes due to the different combinations of materials used for individual optical components. Additional information regarding the FD's relative efficiency curves are outlined in reference [140]. The spectrum of Sirius weighted by the relative efficiency of the FD is shown in the right hand plot Figure 7.9.

The weighted spectrum is then attenuated as a function of air mass through a model atmosphere, taking into account the wavelength (λ) dependence of Rayleigh

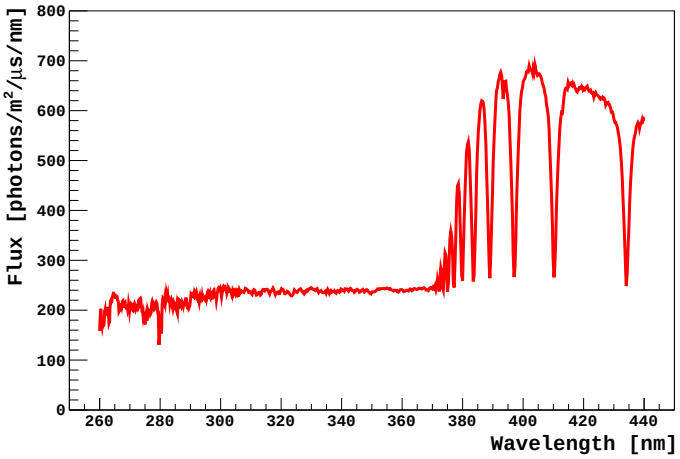

Figure 7.8: The spectrum of Sirius measured by the STIS. The large absorption features above a wavelength of $\sim 365\,\text{nm}$ correspond to the Balmer series.

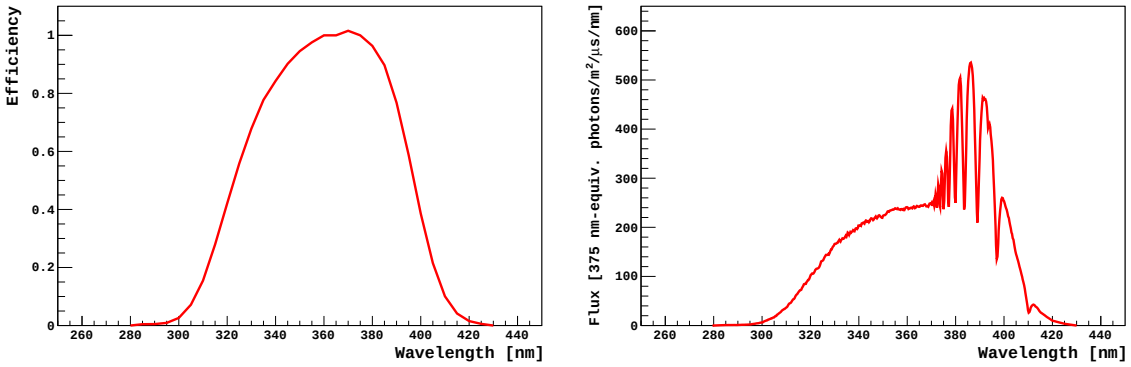

Figure 7.9: Left: Measured multi-wavelength efficiency curve for Coihueco telescope 4. All values are relative to 375 nm (the operational wavelength of the absolute calibration). The same curve is used for Coihueco telescopes 1, 5 and 6, along with all telescopes from Loma Amarilla and HEAT [141]. Right: Measured spectrum for Sirius folded with the efficiency of Coihueco telescope 4.

scattering ($\tau_{Rayleigh}$) and ozone absorption (τ_{O_3}). For a given value of λ the expected signal from Sirius is given by:

$$Rayleigh\,Model(AM,\lambda) = F_0'(\lambda) \times e^{-(\tau_{Rayleigh}(\lambda)+\tau_{O_3}(\lambda))\times AM} \tag{7.13}$$

where $F_0'(\lambda)$ is the weighted star spectrum evaluated at λ. Daily measurements for $\tau_{Rayleigh}$ and τ_{O_3} are provided through the Global Data Assimilation System (GDAS) and the Ozone Monitoring Instrument (OMI), respectively [142, 143][3].

[3] Accessed through a modified Offline tutorial module. Ozone data can be accessed through the URL provided in reference [143].

The total Rayleigh Model (Figure 7.10) is given by the summation of Equation 7.13 over all values of λ in the operational bandpass of the FD.

$$\begin{aligned} \textit{Rayleigh Model}(AM) &= \sum_i \textit{Rayleigh Model}(AM, \lambda_i) \\ &= \sum_i F_0'(\lambda_i) \times e^{-(\tau_{Rayleigh}(\lambda_i)+\tau_{O_3}(\lambda_i))\times AM} \end{aligned} \tag{7.14}$$

Equation 7.14 is not quite an exponential function given the broadband star signal and the strong wavelength dependence of Rayleigh scattering. The total atmospheric attenuation of the measured star track is partially corrected using the Rayleigh Model. This is achieved by calculating the ratio of the measured signal and the Rayleigh Model as a function of air mass:

$$\textit{Ratio}(AM) = \frac{[\textit{Star Signal}]^{Telescope}_{Total}(AM)}{\textit{Rayleigh Model}(AM)} \tag{7.15}$$

where $[\textit{Star Signal}]^{Telescope}_{Total}$ is the star signal measured by the detector (Equation 7.12) and $\textit{Rayleigh Model}(AM)$ is given by Equation 7.14. The ratio for a single example track is shown in Figure 7.11.

At this point of the analysis we will introduce the Angstrom coefficient (γ), a parameter which describes the wavelength dependence of τ_{aero}. Mathematically, this is expressed as

$$\frac{\tau_{aero,\lambda}}{\tau_{aero,\lambda_0}} = \left(\frac{\lambda}{\lambda_0}\right)^{\gamma} \tag{7.16}$$

where $\tau_{aero,\lambda}$ is the aerosol optical depth at a wavelength λ, and τ_{aero,λ_0} is the reference optical depth at a wavelength of λ_0. By assuming that γ is zero[4], Equation 7.15 can then be simplified to an exponential function:

$$\begin{aligned} \frac{[\textit{Star Signal}]^{Telescope}_{Total}(AM)}{\textit{Rayleigh Model}(AM)} &= \frac{[Optics] \times \left[F_0(\lambda_1) \times e^{-\tau_{aero}AM}\right] + ...}{F_0'(\lambda_1) + F_0'(\lambda_2) + ...} \\ &= \frac{[Optics] \times [F_0(\lambda_1) + F_0(\lambda_2) + ...] \times e^{-\tau_{aero}AM}}{F_0'(\lambda_1) + F_0'(\lambda_2) + ...} \\ &= [Optics] \times \frac{F_{0,Total}}{F'_{0,Total}} \times e^{-\tau_{aero}AM} \qquad \text{for } \gamma = 0 \end{aligned} \tag{7.17}$$

where $\frac{F_{0,Total}}{F'_{0,Total}}$ is the ratio of the measured and expected brightness of the star at the top of the atmosphere.

[4]The aerosol optical depth is the same at all wavelengths. The systematic effect introduced by this simplifying assumption is discussed in Section 7.3.3.1.

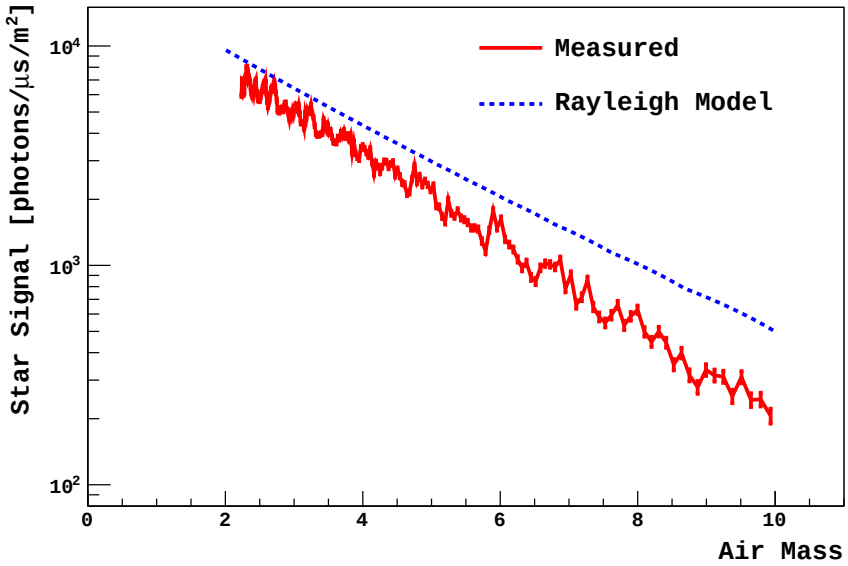

Figure 7.10: A comparison between the Rayleigh Model (dashed blue line) and measured signal (red) for an example Sirius track observed by CO 4. The Rayleigh Model is not a perfect exponential function. The discrepancy between the slopes of the two profiles is proportional to any atmospheric attenuation not accounted for as part of the Rayleigh Model (i.e. aerosol attenuation).

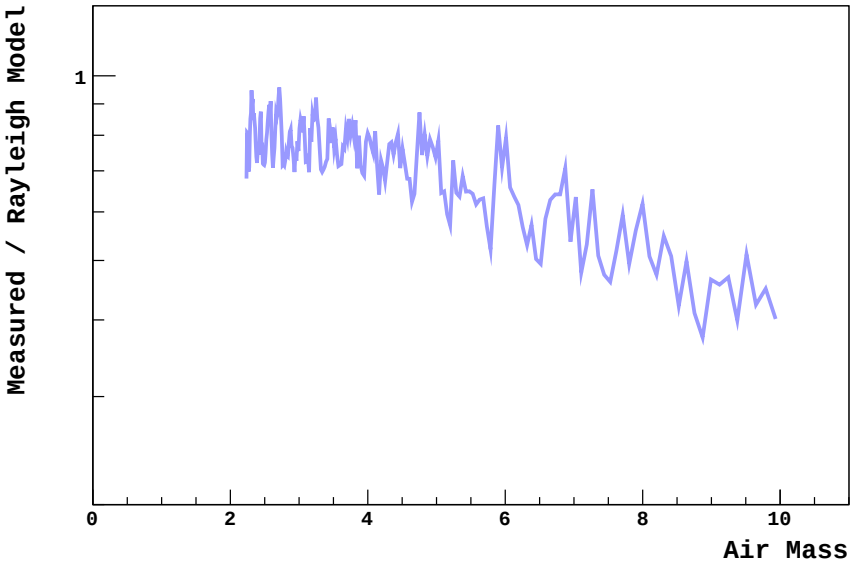

Figure 7.11: Ratio of the track of Sirius measured by CO 4 and the expected signal from a model Rayleigh atmosphere. The exponential slope of this profile is proportional to the attenuation of the signal due to atmospheric aerosols.

7.2.2 Correcting Track Modulations

Modulations due to camera inefficiencies are corrected using an elevation dependent function (which will be referred to as the *template*). This section will overview the various approaches that can be taken to calculate an appropriate template, outlining the advantages and disadvantages of each method and the compromise made with the final solution.

7.2.2.1 Simulated Template

A modified $\overline{\text{Off}}\underline{\text{line}}$ ray tracing module is used to simulate a beam of photons across the field of view of an FD telescope. The beam is positioned to mimic the path traversed by the star of interest during data acquisition. The beam is simulated to contain a fixed number of N photons across all time bins, where each time bin can be converted to an equivalent elevation bin. For each time bin, the ray tracing module calculates the total number of photons on the camera, taking into account any variations in the collection efficiency introduced by the camera's pixelated design.

The simulated template corresponding to the path taken by Sirius across the field of view of CO 4 is shown in Figure 7.12. The amplitude of the modulations in the simulated template depend on the distance between the spot of the star and the centre of the observing pixel. Peaks in the template correspond to instances where the spot of the star is approaching the centre of a pixel's photocathode, where collection efficiency is at its greatest. Troughs correspond to regions along the track where the spot of the star is approaching the less efficient regions of the camera (the spaces between neighbouring FD pixels which are filled with Mercedes stars light collectors, see Section 3.2.1).

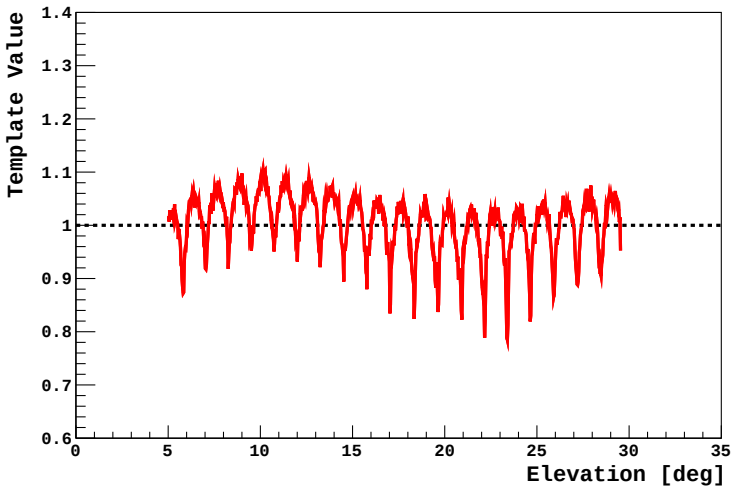

Figure 7.12: Simulated template for the path of Sirius across CO 4. The simulated template has been normalised to have a mean of 1.

While simple and straightforward to calculate for any star and telescope pairing, the simulated template is disadvantageous in that it assumes all pixels are identical in terms of collection efficiency. It is unlikely that such an assumption is true in reality, as the collection efficiency of individual pixels may vary with time as well as between pixels. For example, the Mercedes light collectors wedged between neighbouring pixels are coated in a reflective layer which may be subject to long term wear and tear; an effect that would degrade the camera's collection efficiency with time. Additionally, it is unlikely that the degradation of the Mercedes is uniform across the entire telescope. The Offline simulation module overlooks both of these factors.

The simulated template does however offer important information regarding the average behaviour of the template as a function of camera position. The average behaviour will be referred to as the *shape function*, and is defined by the average template value for each 'pixel'[5]. The shape function associated with the simulated template for the path of Sirius across CO 4 is shown in the left hand plot of Figure 7.13. When compared to the right hand plot of Figure 7.13, it can be seen that the shape function is correlated with the position of the star relative to the observing pixels. For example, the shape function appears to steadily increase between elevations of $\sim 5^\circ - 10^\circ$, corresponding to the spot of the star moving closer towards the centre of the photocathodes of the observing pixels. Similarly, the shape function begins to decrease at an elevation of $\sim 14^\circ$ at which point the spot of the star appears to move between pixels rather than through them. As the shape function appears to simply be a function of the path of the star across the observing camera, we believe it is a real (and important) feature that should be included in the template.

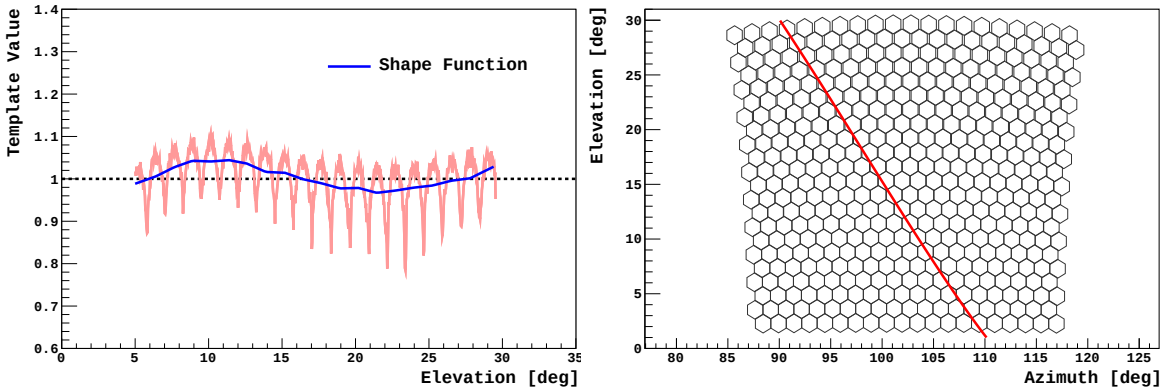

Figure 7.13: Left: The shape function (blue) overlaid on the simulated template. Right: For reference, the path of Sirius across CO 4.

[5]In the context of this Section a 'pixel' refers to each bump in the template. Individual pixels are identified by eye.

7.2.2.2 Empirical Template

An alternative to simulating a template is to empirically derive one from real star track measurements. The method is as follows:

1. The Rayleigh atmosphere is removed from each star track using the method outlined in Section 7.2.1.

2. An exponential function is fitted to the Rayleigh atmosphere corrected star track. This is achieved by minimising χ^2 where

$$\chi^2 = \sum_i^N \frac{(O(AM_i) - E(AM_i))^2}{\sigma(AM_i)^2} \tag{7.18}$$

   where $O(AM_i)$ is the value of the Rayleigh atmosphere corrected star track (from step 1) at an air mass of AM_i and $\sigma(AM_i)$ is the corresponding uncertainty. $E(AM_i)$ is the expected value (chosen to be an exponential function) and is given by

$$E(AM_i) = A \times e^{-b \times AM_i} \tag{7.19}$$

   where A and b are the fit parameters of the exponential function.

3. The ratio of the Rayleigh atmosphere corrected star track and the exponential fit (Equation 7.19) is calculated as a function of air mass. This is the empirical template for a single track.

4. Steps 1-3 are repeated for all valid star tracks measured across all years, from which an average empirical template is then calculated. An example empirical template is illustrated in Figure 7.14.

In contrast to the simulated template, the empirical template makes no assumption regarding the collection efficiency of individual pixels. In other words, empirically deriving a template from real data incorporates real collection efficiency information for each pixel, a detail that is overlooked by the simulated template. However, this method fails to account for the underlying shape function due to the chosen form of the fitted equation (a simple exponential function) in step 2.

7.2.2.3 Guided Template

Both the simulated and empirically derived templates are advantageous in their own way. The simulated method provides a shape function which is representative of the position of the optical spot relative to the surrounding pixels while the empirical template provides real collection efficiency information on a pixel by pixel basis. For these reasons, we have decided to use a template (referred to as a *guided template*) which takes advantage of both the simulated and empirical methods. The method for calculating this template is similar to that of the empirical

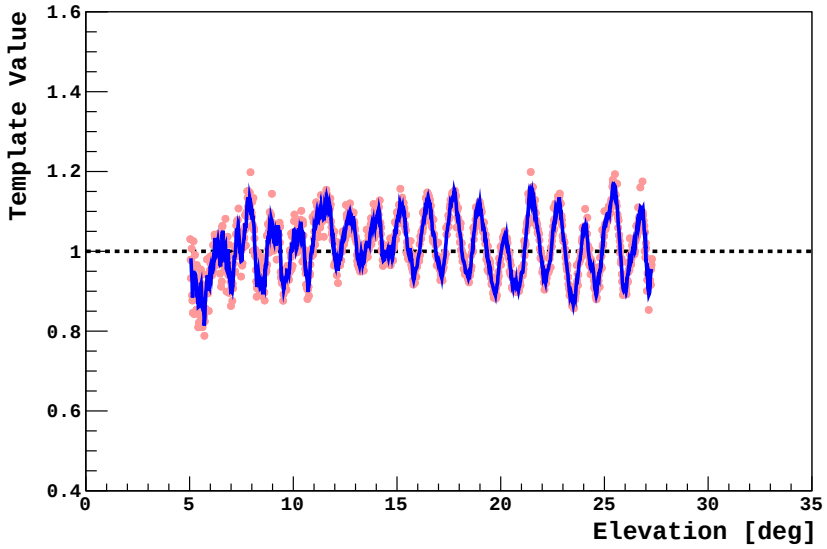

Figure 7.14: Empirical template for the path of Sirius across CO 4. The average template (faint red) was calculated using star tracks measured from 2007-2016. The overlaid profile (blue) is a box-car average of the underlying average template. Note that for illustrative purposes, the empirical template is shown as a function of elevation rather than air mass. In practice, the template is defined as a function of air mass.

method, only the exponential fit (Equation 7.19) to each star track is modulated by the shape function provided by the simulated template (see Equation 7.20). The guided template for Sirius CO 4 is shown in Figure 7.15.

$$E(AM) = [Shape\ Function(AM)] \times A \times e^{-b} \times AM \tag{7.20}$$

The template is chosen to fluctuate about a mean value of 1 rather than a peak value of 1 (the latter may seem like the obvious choice at first, given the peaks of the template correspond to the most efficient regions of the camera). The choice of this normalisation is a relic of the absolute FD calibration (Section 3.2.2.1). An important yet subtle detail of the absolute calibration is that the entire camera surface is illuminated by the drum shaped light source. This includes the efficient photocathodes of each pixel as well as their surrounding less efficient areas. Therefore, the calibration resulting from the absolute calibration is the average response of each pixel, encompassing regions of all efficiencies. In terms of this analysis, the normalisation implies that the fitted function lies along the $\sim$middle of the star track rather than its peaks. This is analogous to fitting a Gaisser-Hillas function through the middle of a shower profile of a cosmic ray event, an example of which is shown in Figure 7.16.

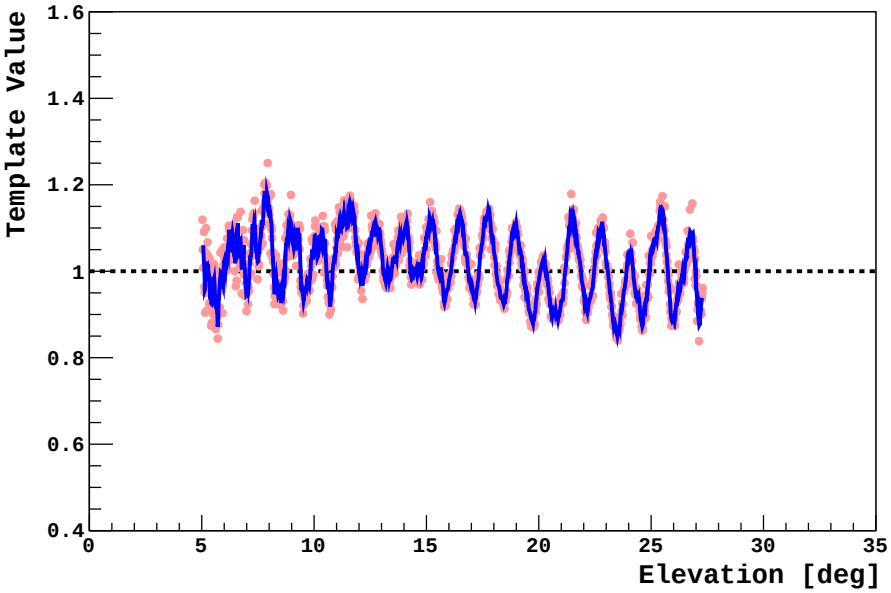

Figure 7.15: Guided template for Sirius CO 4. The overlaid blue profile is a box-car average of the underlying template. Once again the template is shown as a function of elevation only for illustrative purposes.

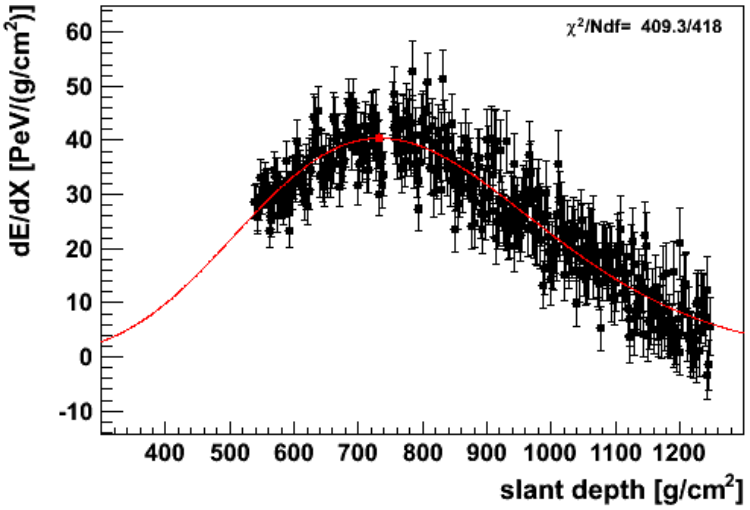

Figure 7.16: Example of a Gaisser-Hillas function (red) being fitted to the centre of a shower profile observed by the FD.

7.2.3 Fitting Algorithm

To assess the performance of an FD telescope's absolute calibration, measured star tracks are passed through the following analysis chain. For the following example consider a star track of N data points.

1. Partially correct the track's molecular attenuation by calculating the ratio between the observed star track and an expected signal (Section 7.2.1).

2. Minimise χ^2 where

$$\chi^2 = \sum_i^N \frac{(O(AM_i) - E(AM_i))^2}{\sigma(AM_i)^2} \tag{7.21}$$

where $O(AM_i)$ is the observed value of the corrected star track (from step 1) at an air mass of AM_i, $\sigma(AM_i)^2$ is the corresponding uncertainty, and the expected value $E(AM_i)$ is given by

$$E(AM_i) = [Guided\ Template(AM_i)] \times AC \times e^{-AOD \times AM_i} \tag{7.22}$$

Definitions of the Absolute Calibration (AC) and Aerosol Optical Depth (AOD) are given below.

3. Repeat for all measured star tracks to form a "star calibration profile (or measurement)" for the telescope of interest.

The absolute calibration (AC) corresponds to the value of Equation 7.22 extrapolated to an air mass of 0. This is a significant value as the act of extrapolation essentially corrects for the signal's attenuation through the atmosphere. The absolute calibration is therefore defined as the direct comparison between the measured star brightness (observed by the FD) and the brightness expected from the Rayleigh model at the top of the Earth's atmosphere. For a perfectly calibrated telescope, a value of 1 is expected for the absolute calibration. Values greater than 1 imply that the telescope is overestimating the true brightness of the star. Conversely, values of the absolute calibration below 1 imply that the brightness of the star has been underestimated.

In theory, a star track can be calculated for each night of data acquisition for which Sirius is visible from the FD telescope of interest. As previously mentioned, operational conditions can affect the characteristics of the measured track (i.e. the range of air mass covered) which can result in an artificial shortening of the track. Furthermore, atmospheric conditions such as the presence of clouds, can block the telescope's field of view of the star, with the resulting star track displaying abnormal features (such as uncharacteristically large troughs along the track). Such tracks would disrupt the calculation of the template function and should be removed from the analysis. The results presented in this Chapter only use star tracks which were observed during cloudless periods of data acquisition and are selected by eye. It should be noted that this strict but necessary condition will greatly reduce the year to year star track statistics.

A preliminary star calibration profile for CO 4 using Sirius is shown in Figure 7.17. For this particular profile, it is required that the length of an individual star track (in elevation) be at least 10°. The effect of requiring this condition is

discussed in Section 7.2.4. A further correction to the profile (not yet applied here) is required to account for the broadening of the telescope's point spread function, discussed in greater detail in Section 7.3.1.

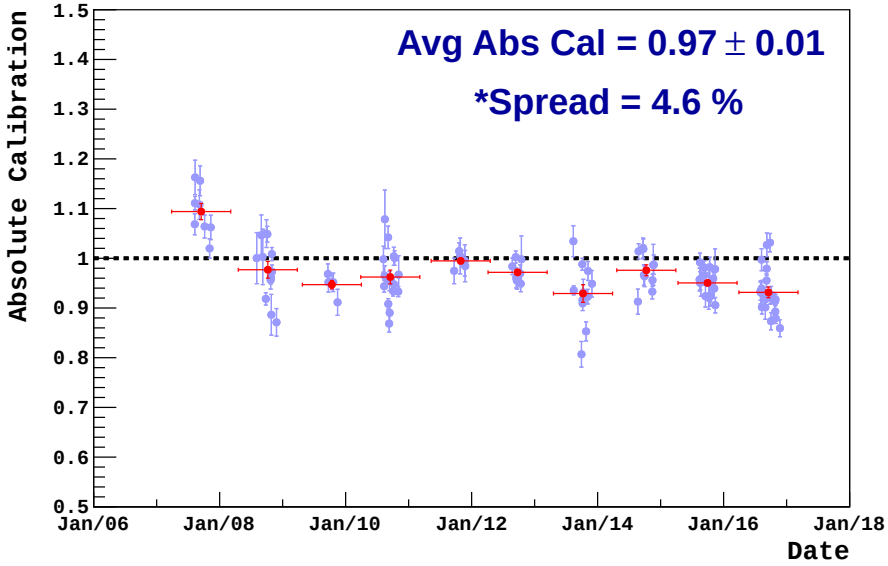

Figure 7.17: The fitted absolute calibration of CO 4 estimated with Sirius. The calibration constants for 2016 at the time of this analysis were sourced from the test database *FD_Calib_1_AV1All_11012017*. Individual star tracks are represented by the blue markers. The red overlaid profile is the nightly data binned yearly. The spread of 4.6 % is calculated with respect to the mean of each year rather than the mean of the entire profile (to account for any year to year discontinuities).

The second fit parameter is the aerosol optical depth and is defined as the exponential slope of the fit function. More specifically, AOD is the aerosol optical depth per unit air mass. For an air mass of 1, $(AOD \times AM)$ returns the aerosol optical depth through 1 atmosphere. In contrast to the VAOD (which at the Observatory is typically measured between ground and 4.5 km above sea level at a single wavelength of 355 nm), the AOD is measured between ground and infinity, and is averaged across the bandpass of the star coupled with the FD response. Due to these factors, it is not expected that AOD and VAOD be identical, although some correlation should exist. It should be noted that using star tracks to monitor the atmosphere's aerosol content was not the aim of this analysis. Despite this, the results are intriguing and offer an opportunity to cross-check measurements from monitoring campaigns currently employed at the Observatory.

7.2.4 Spread in the Fitted Absolute Calibration

From Figure 7.17 it can be seen that the nightly variation of the fitted absolute calibration is of the order of several percent. A fraction of this spread is inher-

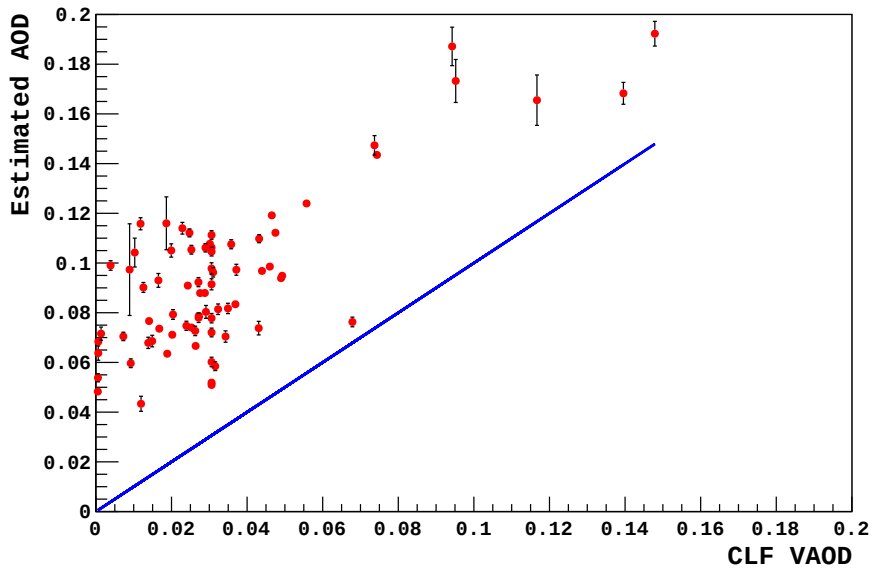

Figure 7.18: The fitted aerosol optical depth (*AOD*) as a function of the VAOD. A clear but expected discrepancy is observed between the two values. This discrepancy could be partly due to high level aerosols or cloud which only the *AOD* is sensitive to.

ent due to nightly variations in the calibration of the FD telescopes, which have previously been shown to have some correlation with their exposure to the NSB (Section 5.4). In this Section we investigate other factors which may contribute to the observed nightly variations.

It was previously mentioned (for Figure 7.17) that a requirement was made on the minimum track length for each star track. The effect of this condition is illustrated in Figure 7.19 for Sirius tracks observed by CO 4. From the left hand plot, a clear correlation between the spread in the fitted calibration and the minimum track length is observed. This is an expected result, as star tracks of longer length will provide increasingly longer lever arms for the fitting routine, reducing the variations in the value of the extrapolated function. This requirement is expectedly met with a reduction in the the number of star tracks (right hand plot), and a compromise between an improvement in the spread and a reduction in statistics must be made. For this particular example, a minimum track length of 10° is chosen, as the spread does not significantly improve beyond that point. The optimal minimum track length will vary depending on how the star in question crosses the field of view of the observing telescope (the star may not cover a full 30° in elevation).

Alternatively, a cut could be placed on the minimum track length in terms of air mass rather than elevation angle. This is illustrated in Figure 7.20. Much like in Figure 7.19, it can be seen that beyond a certain track length ($\sim$ 3.5 air mass) the spread does not improve significantly and remains of the order of $\sim$ 4%.

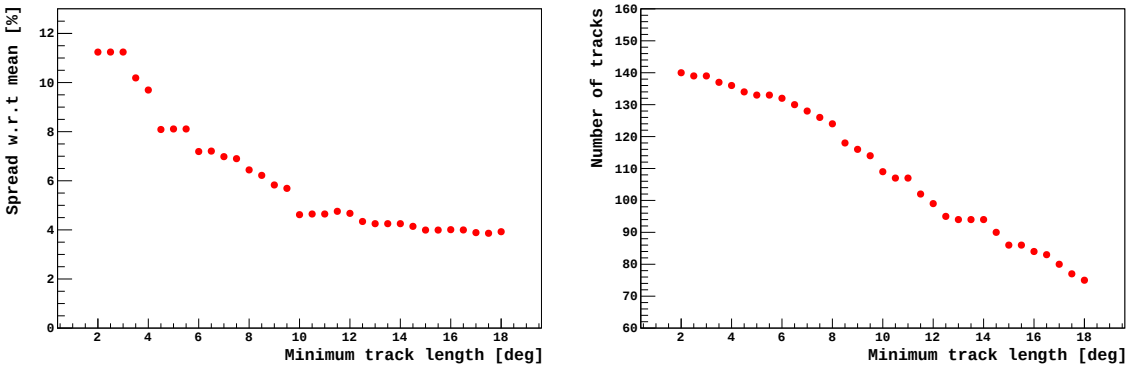

Figure 7.19: Left: For Sirius in CO 4 - the spread in the fitted absolute calibration with respect to the mean of each year as a function of the minimum track length. Right: The number of star tracks with length above a given minimum track length.

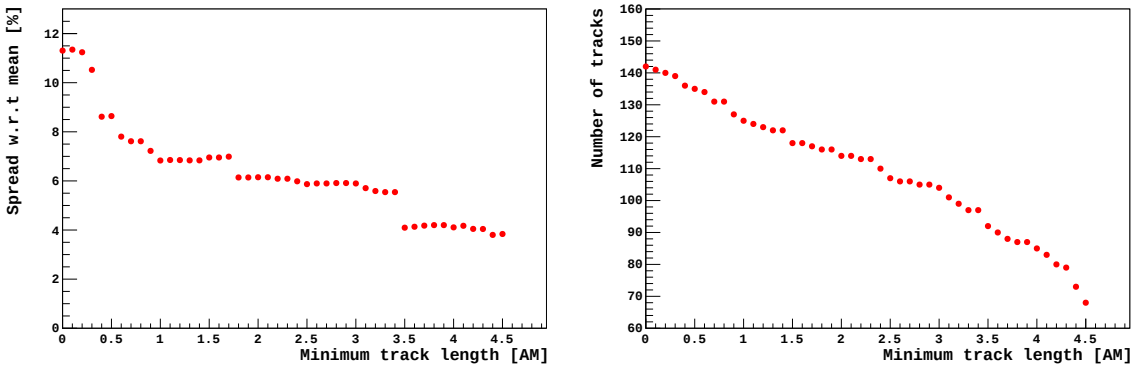

Figure 7.20: Left: The spread in the fitted absolute calibration with respect to the mean of each year as a function of the minimum air mass track length. Right: The number of star tracks above the minimum track length.

It has been demonstrated that the removal of shorter star tracks can significantly reduce the nightly variations in the fitted absolute calibration. Despite this improvement, there still exists some residual spread of the order of several percent. Part of this spread can be attributed to the positioning of the star track within the telescope's field of view. Due to the non linearity of air mass as a function of elevation angle, a track of a given length in elevation positioned towards lower elevations will cover a greater range of air mass compared to a track of the same length positioned at higher elevations. This not only affects the effective lever arm of the star track, but also the amount of extrapolation required to reach 0 air mass (recalling that the absolute calibration is defined as the value of the function extrapolated to 0 air mass). Requiring long tracks (greater than 10° in angular length) to terminate at low air masses can further improve night to night variations, although this is done at the further expense of track statistics (Figure 7.21). It should also be noted that enforcing this condition is not possible for all

star and telescope pairings, as the transit of particular stars may not reach the upper regions of the FD's field of view.

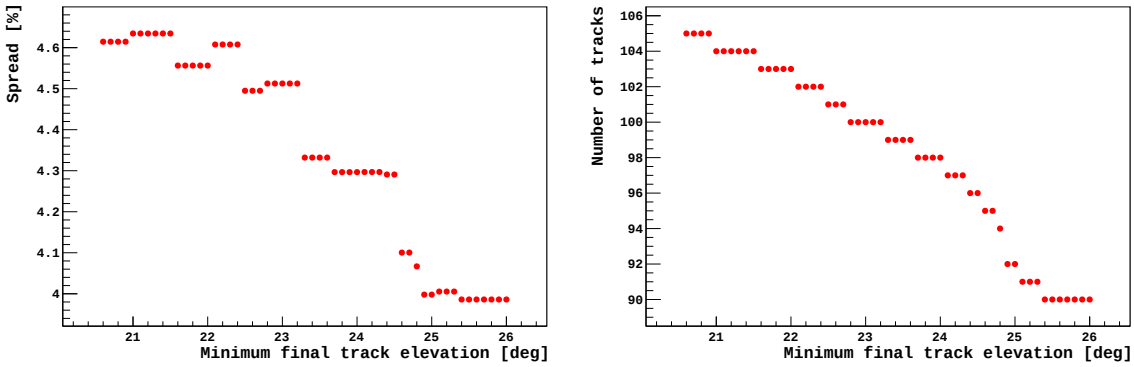

Figure 7.21: Left: The spread in the fitted absolute calibration using tracks which terminate above a minimum elevation angle. Right: The number of tracks which end above a certain elevation angle. Tracks used for this particular example were required to be of at least 10° in length.

7.3 Analysis of Systematic Errors

The following sections will discuss the various sources of systematic errors associated with various components of the analysis, and their contributions to the overall systematic uncertainty in the fitted results.

7.3.1 Broadening of the Point Spread Function

A key feature of the analysis method outlined in Section 7.1.1 was the integration of the star signal across a fixed area of the FD camera. More specifically, the assumption was made that the optical spot of the star was fully contained within a crown of FD pixels, centred on the pixel with the largest signal (see Figure 7.4). It is unlikely that this is a realistic assumption due to the known broadening of the point spread function (PSF) across the camera surface, believed to be related to the deposition of dust on the surface of the FD mirrors. The presence of dust acts to scatter incoming fluorescence photons, disrupting the normal specular reflection from the mirror surface resulting in a widening of the PSF (see references [144–146] for additional details). Such studies have provided valuable insight into the optical properties of the FD telescopes, allowing for a deeper understanding of systematic uncertainties of reconstructed shower properties.

In this Section, the additional light beyond the nominal camera integration area used in this analysis will be estimated. Using these results, a one sided correction will be estimated and applied to the fitted results. In the following

sections, the correction will be estimated for the case of Sirius observed by LL 1 and will be assumed to be applicable to all other FD telescopes.

7.3.1.1 Direct Measurement of the Point Spread Function

The PSF can be directly measured by taking a snapshot (in time) of the NSB across the camera and integrating the signal across an area of increasing size. For this exercise the integration area is defined to be all FD pixels with centres enclosed within a ring of radius ζ, centred on the pixel within which Sirius is contained. This is illustrated in Figure 7.22.

To minimise the effect of statistical fluctuations in NSB measurements, the snapshot of the NSB is defined to be the average NSB across a specific time window of interest. A single star will appear in the field of view of a given FD pixel for approximately 6 minutes, depending on the geometry of the transit of the star through that pixel. For the purpose of this exercise, we define the time window of interest to be the central 4 minutes[6] during which Sirius appears in the field of view of pixel 144 of LL1. An example of the signal trace captured by a single pixel is illustrated in Figure 7.23.

As the integration area expands with increasing ζ additional pixels will fall within the enclosed ring, contributing additional light to the integrated signal. ζ is chosen to increase with a step size of 1.5° (corresponding to the angular size of a single FD pixel), so that a new ring of pixels is included with each step. The number of pixels enclosed within different ζ rings is summarised in Table

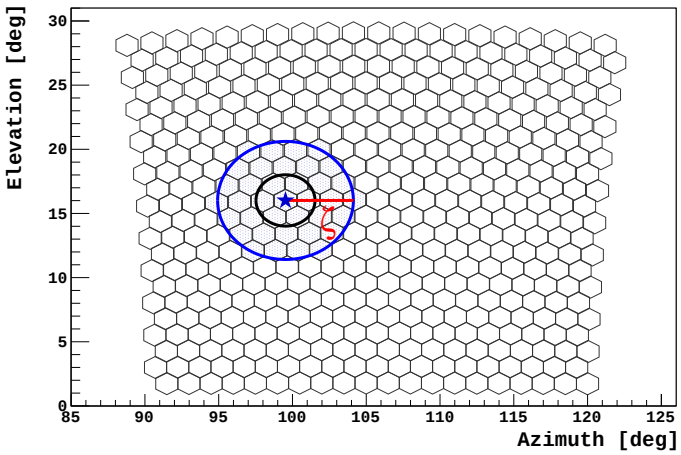

Figure 7.22: The integration area is defined by all pixels with centres enclosed within a ring of radius ζ. Also shown for reference is the standard integration area used in this analysis (inner ring).

[6]The window begins 1 minute after the star enters the field of view of the pixel and ends 4 minutes later.

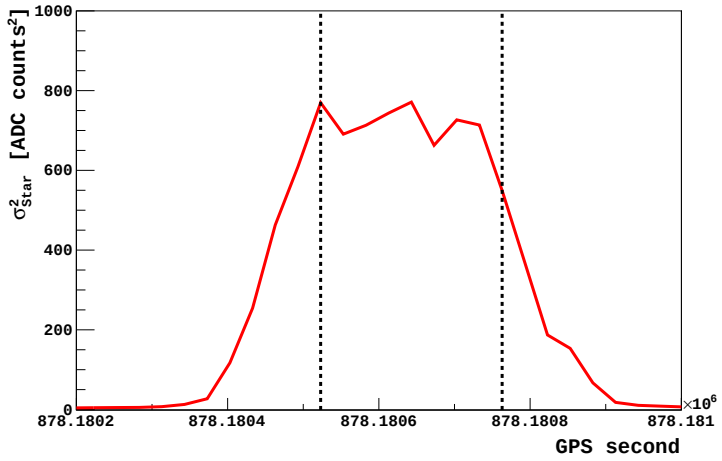

Figure 7.23: The NSB variance σ^2_{star} trace for pixel 144 of LL 1. The vertical rails indicate the 4 minute period over which the signal is averaged. Note that the contribution from the underlying NSB has been removed.

7.1. Figure 7.24 illustrates the σ^2_{star} traces for pixels belonging to the first crown and clearly demonstrates the broadening of the star's optical spot through the surrounding pixels. For a ring of radius ζ containing N pixels, the total integrated signal is given by

$$Total\ Signal(\zeta) = \sum_{i}^{N} Photon\ Flux_i \tag{7.23}$$

where $Photon\ Flux_i$ is the average NSB photon flux for the i^{th} pixel across the time window of interest.

Crown Number	ζ [°]	Number of Pixels
0	0	1
1	1.5	7
2	3.0	19
3	4.5	37
4	6.0	61

Table 7.1: Number of pixels with centres contained within integration areas of various sizes. An additional crown of pixels is included with each step in ζ.

The result of directly measuring the PSF is summarised in Figure 7.25. The total signal for each ζ is normalised with respect to the total signal in the first crown, recalling that the purpose of this exercise was to estimate the fraction of light beyond the nominal integration area of $\zeta = 1.5°$. As ζ increases, the total light collected within the integration area increases accordingly with each step in ζ contributing an additional $\sim 1-2\%$ of signal. The fractional light however

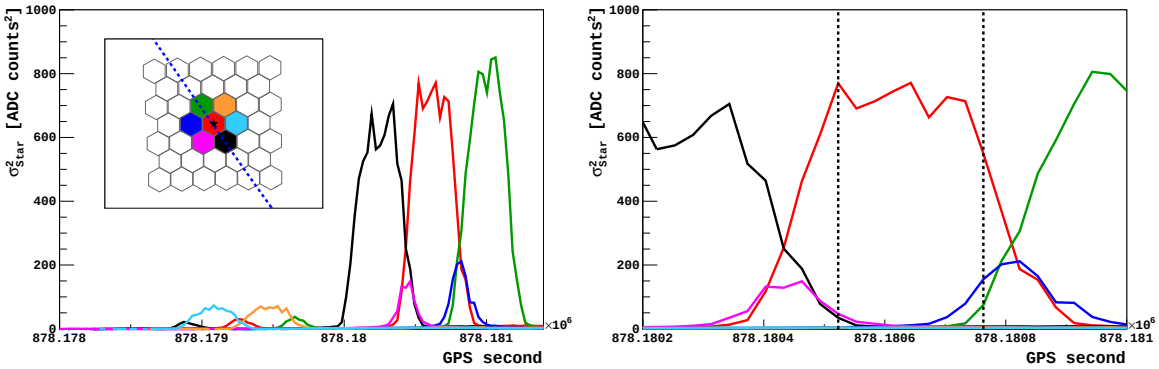

Figure 7.24: Left: σ^2_{star} for the 7 pixels contained within the first crown. The leading (smaller) bump can be attributed to the star Mirzam, a nearby star passing through the field of view of the telescope approximately 20 minutes before Sirius. Right: A closer look at the pixel traces. The signal of each pixel within the integration area is averaged over the same time window.

does not plateau to a steady value as one may have expected at large ζ. In fact, a substantial increase in the fractional light is observed at $\zeta = 6^\circ$ which can be attributed to the signal from a nearby star, Mirzam, being captured within the integration area (see Figure 7.26). Further complicating this is the fact that the optical spot of Mirzam overlaps with that of Sirius, suggesting that the result shown in Figure 7.25 is most likely an overestimation of the fractional light (from Sirius) beyond the nominal integration area.

To summarise, due to the contamination of the signal from nearby stars and the overlapping nature of their optical spots, it is not feasible to directly measure the PSF using NSB data and an alternative approach should be taken.

7.3.1.2 Verification of Previously Measured PSF

In Section 7.3.1.1 it was demonstrated that the presence of nearby star restricts the ability to directly measure the PSF using NSB data. Alternatively, the NSB data can be used to verify previous measurements of the broadening of the optical spot from which a correction can be derived. An example of such a measurement is illustrated in Figure 7.27. It should be noted that Figure 7.27 was measured for telescope 3 of Los Leones. For the purposes of this analysis, it will be assumed that all FD telescopes have a similar PSF.

Verification begins with the modelling of the expected light distribution for the relevant stars. For simplicity, the calculated PSF model will only include contributions from two stars (Sirius and Mirzam) and will be assumed to be radially symmetric. Furthermore, the shape of the spot is assumed to be the same everywhere on the camera. Models are calculated by scaling the light distribution from Figure 7.27 by the brightness of each star on a given night. An example of scaled

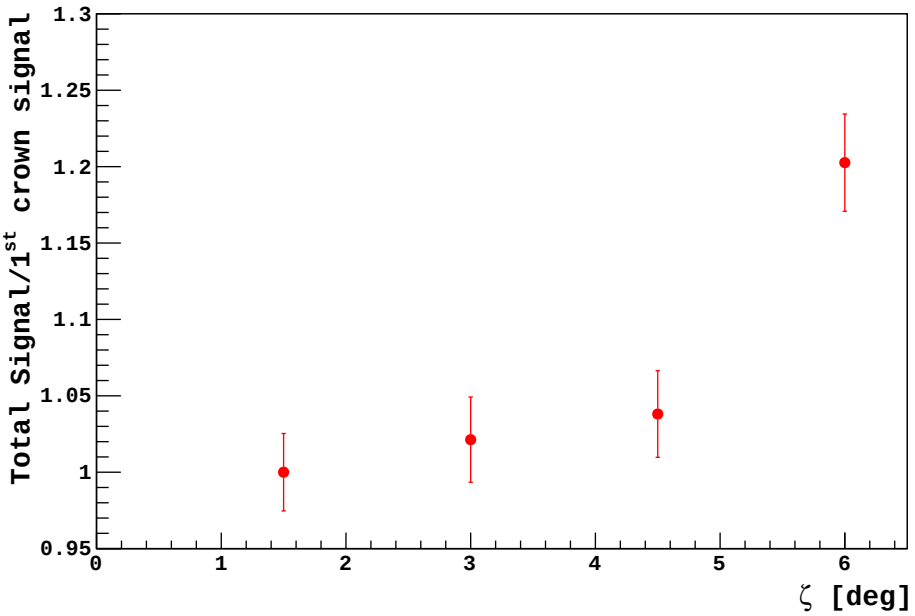

Figure 7.25: σ^2_{star} traces from 24 different tracks was used to calculate the average fractional star light beyond the nominal integration area of a single crown of pixels.

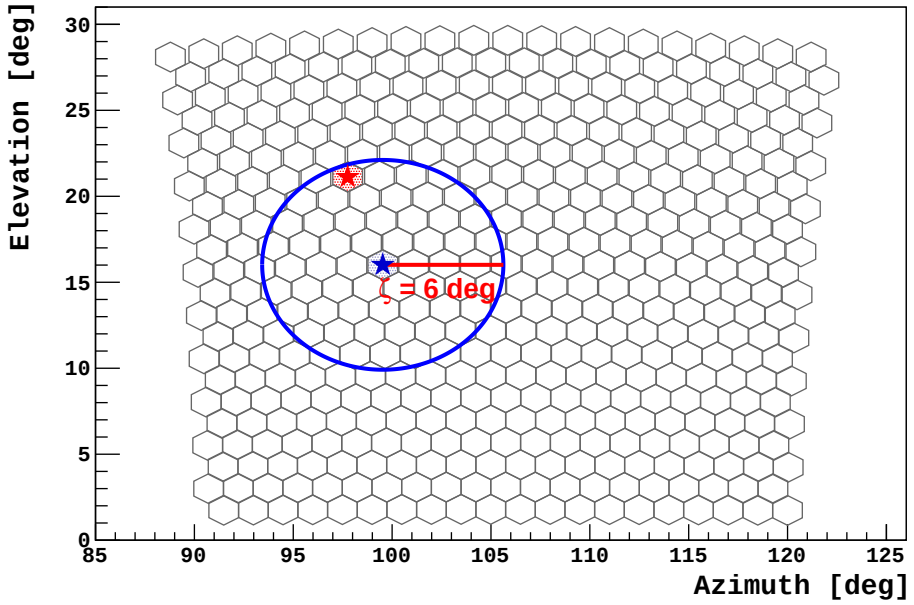

Figure 7.26: Relative camera positions of Sirius (blue) and Mirzam (red). For sufficiently large integration areas, e.g. $\zeta = 6°$, the signal from Mirzam will contribute to the integrated signal.

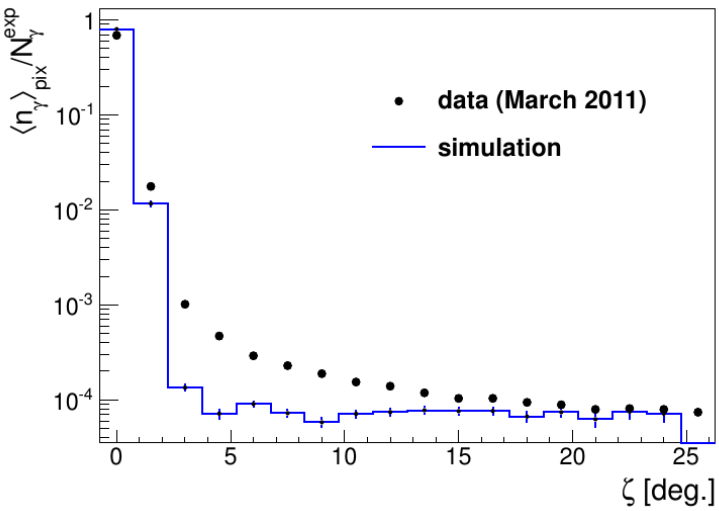

Figure 7.27: The differential light distribution for an FD camera (Los Leones telescope 3) measured using a point-like light source mounted on an octocopter. The vertical axis represents the average number of detected photons per pixel $\langle n_\gamma \rangle_{pix}$ divided by the expected number of photons N_γ^{exp}. Additional details are provided in [144].

light distributions for Sirius and Mirzam are shown in Figure 7.28. For a crown of N pixels enclosed within a ring of radius ζ the total signal predicted by the model is given by

$$Total\ Signal_{Model}(\zeta) = \sum_{i}^{N} \left(PSF_{Sirius}(\zeta_i) + PSF_{Mirzam}(\zeta_i^{'}) \right) \tag{7.24}$$

where ζ_i and $\zeta_i^{'}$ is the space angle between the i^{th} crown pixel and the pixel observing Sirius and Mirzam, respectively. As the model is assumed to be radially symmetric, all pixels belonging to the same crown will have an equal contribution to the integrated signal. A new model is calculated for each track belonging to the subset of tracks used in Figure 7.25.

A comparison between the measured average light beyond the nominal integration area and that predicted by this model is shown in Figure 7.29. The small discrepancy between the central values in each ζ bin is most likely due to the simplistic nature of the model, in that it only accounts for the light emitted from two stars. In reality it is possible that additional (fainter) stars are captured within the region of the sky covered by a given ζ ring, which are not accounted for in this simple model. Nonetheless, Figure 7.29 demonstrates excellent agreement between the two methods and implies that the PSF presented in Figure 7.27 can be used to estimate a reliable correction for this analysis.

It is important to understand the nature of the shape of the PSF, particularly at larger values of ζ. The measured differential light distribution shown in Figure

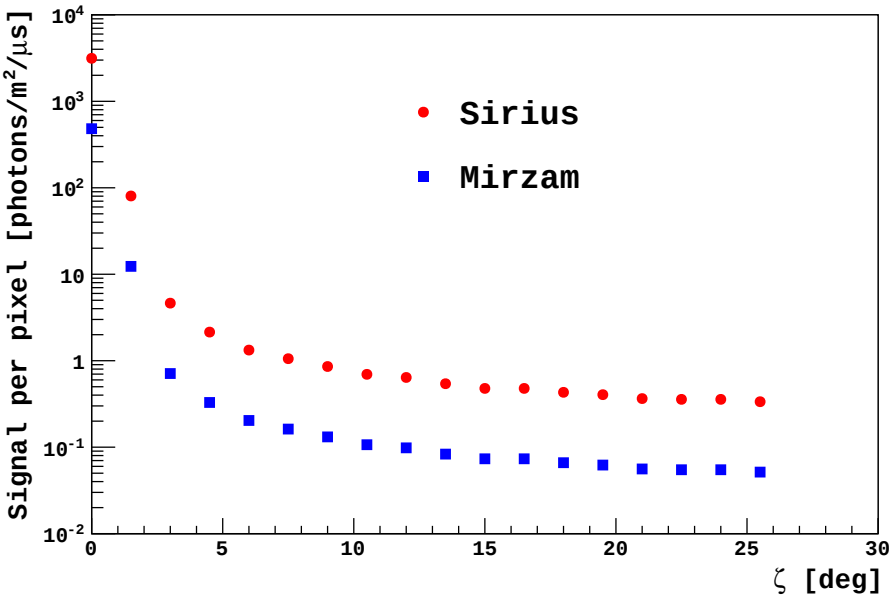

Figure 7.28: Rescaled differential light distributions (see Figure 7.27) for Sirius and Mirzam for an example track. The $\zeta = 0^\circ$ points are determined by the star signal averaged across a central time window (see Section 7.3.1.1) for the two FD pixels observing Sirius and Mirzam. All subsequent value are calculated relative to the $\zeta = 0^\circ$ signal.

7.27 has a long tail which extends well beyond $\zeta = 15^\circ$. It is hypothesised that a fraction of fluorescence photons will be reflected off the surface of the FD camera, resulting in an extended tail in the PSF [144]. It is reasonable then to only integrate the contributions from the measured differential light distribution between $\zeta = 1.5^\circ$ and $\zeta = 15^\circ$, which is estimated to be $\sim 7\%$ (with an uncertainty equal to half of the correction). Additional details regarding this choice of ζ can be found in Appendix D.

To simplify the correction it is assumed that the shape of the PSF, and consequently the magnitude of the correction, is independent of the position of the optical spot on the camera face. For any point along a measured star track, it is estimated that $\sim 7\%$ of the total light remains undetected due to the choice of integration area. This assumption allows individual tracks to be corrected by simply increasing the fitted absolute calibration by 7%. All subsequent results will include this correction. It should be noted that the AOD remains unchanged by this correction.

7.3.2 Rayleigh Model Systematic Uncertainties

In Section 7.2.1 the Rayleigh Model was introduced as the expected light flux arriving at the detector from the star of interest through a model atmosphere which

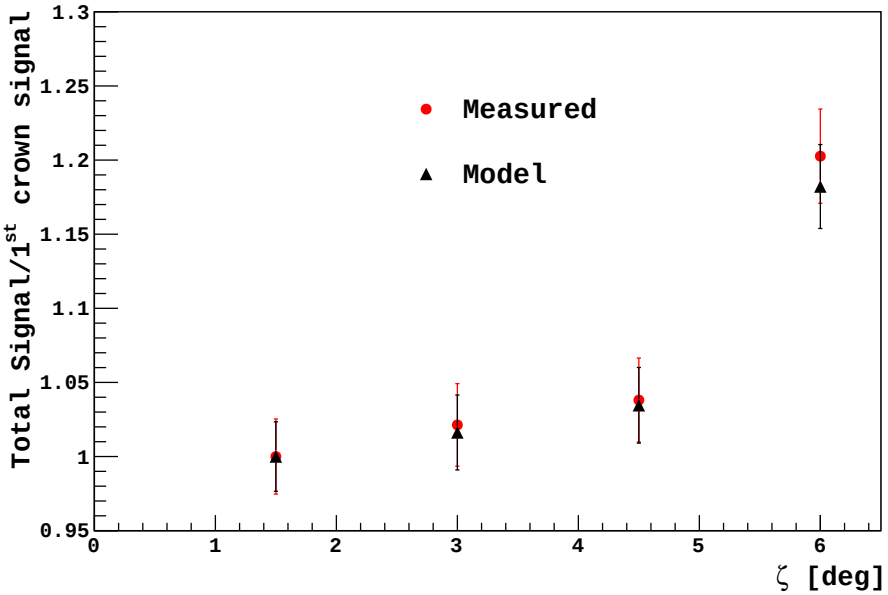

Figure 7.29: A comparison between the average fractional light beyond the indicated integration radius determined through a direct measurement (red circles) and a simple model (black triangles) based on previous PSF measurements.

is free of aerosols. The following Sections will discuss the systematic uncertainties associated with the various model components and their contribution to the uncertainty in the analysis.

7.3.2.1 Spectrum

The most important component of the Rayleigh Model is the spectrum of the star of interest. The spectrum defines the light flux of the star prior to any atmospheric attenuation and detector efficiency effects. Any uncertainty in the spectrum will propagate through to the rest of the Rayleigh Model, systematically affecting fitted parameters.

In an ideal scenario, all candidate stars used in this analysis will have stellar spectra obtained through direct measurements using instruments located on satellites (or at least a spectrum corrected for atmospheric attenuation). In such cases it would be possible to study the absolute calibration of the observing FD telescope, as the Rayleigh Model would be derived using the absolute brightness of the star. Unfortunately, directly measured spectra for potential candidate stars, especially those in the U-band, have proven to be difficult to obtain. Of all the stars which have been considered in this analysis, only Sirius has a measured spectrum (Figure 7.8) which is easily accessible. For other stars, the analysis relies on appropriately scaled 'library spectra' for a star belonging to the same (or in some cases, similar) spectral type. These library spectra are sourced from [147]

with additional information being provided in [148]. The method used to rescale library spectra is provided in Appendix E.

The result of scaling library spectra for a Sirius-like star[7] is demonstrated in Figure 7.30. Four spectra are shown in the figure, 3 of which are rescaled library spectra with the fourth (red) being the measured spectrum which has been included for reference. Unfortunately, and this has proven to be the case with many stars used in this analysis, none of the library spectra available from [147] match the spectral type of the star in question, a problem which only further increases the uncertainty on the absolute value of the Rayleigh model. For Sirius, there are two library spectra which lie either side of A1V, these being A0V (blue) and A2V (black). For the purposes of this demonstration we can calculate an average spectrum (magenta) using the A0V and A2V spectra to form a crude approximation of what an A1V spectrum might look like. It can be seen that the general features of the 3 library spectra match up well with the measured spectrum, with only the normalisation being the most significant difference. Interestingly, it is the spectrum corresponding to an A0V type star which best matches the measured spectrum, and not the *A1V* spectrum.

The star calibration profiles estimated using the 4 spectra are shown in Figure 7.31. The normalisation of each library spectra profile relative to the measured

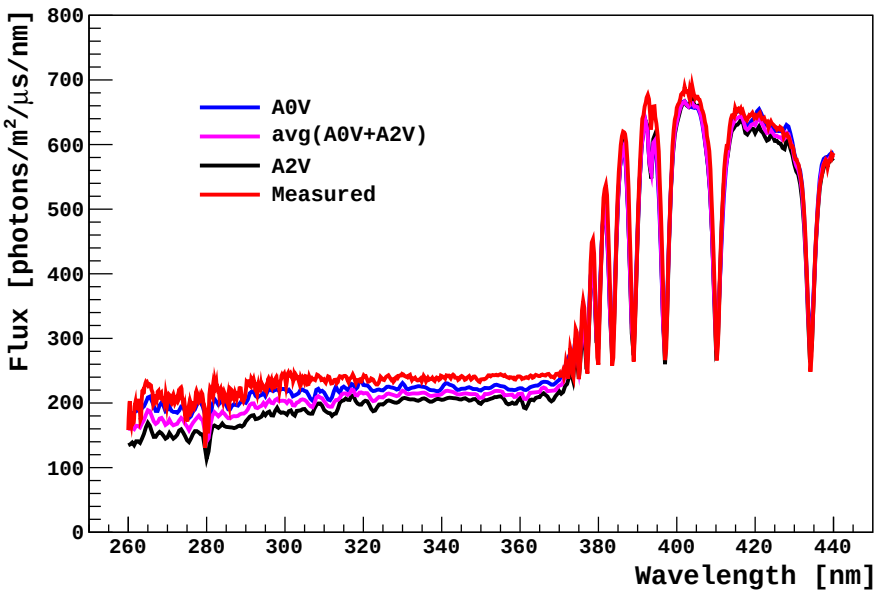

Figure 7.30: Scaled library spectra for stars of a similar spectral class to that of Sirius. As a library spectrum of the same type as Sirius (A1V) was not available, the two closest spectra either side of A1V (A0V and A2V) as well as their average are shown instead. The spectrum measured by the STIS is also shown for reference.

[7]Recalling the Sirius is classified as a type A1V star.

spectrum profile (red) is consistent with the normalisation of their respective spectra. The spectra shown in Figure 7.30 indicate that, for a given wavelength, the photon flux estimated from each of the library spectra appears dimmer compared to the measured spectrum. When propagated through the analysis chain, the library spectra predict that less light should be observed by the FD which leads to a larger value of the absolute calibration (given the earlier definition). The discrepancy in the absolute calibration estimated using the measured spectrum and the library spectra ranges from $\sim 3 - 10\%$.

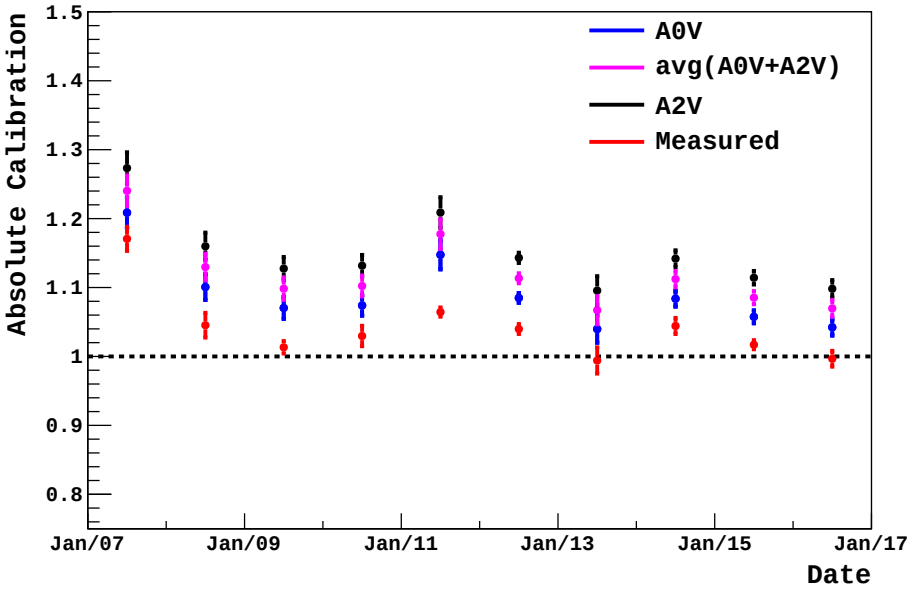

Figure 7.31: A comparison of the fitted absolute calibration using various spectra. The 7% correction associated with the broadening of the optical spot has been included here (Section 7.3.1.2).

For the case of Sirius, the contributing uncertainty from the choice of spectrum on the fitted absolute calibration is given by the uncertainty on the measurement of the spectrum by the STIS. From [149] it is estimated that this uncertainty is of the order of 5%. For other stars which require the use of library spectra, it is difficult to estimate the contribution of the selected spectrum on the uncertainty of the absolute calibration, as this would depend on how well the spectral type of the star is known and the reliability of the selected spectrum itself. Due to this limitation we have concluded that results calculated using library spectra can only be used to study the stability of the FD calibration in a relative sense and not an absolute sense.

7.3.2.2 Fluorescence Detector Efficiency

The spectral response of the FD is incorporated into the Rayleigh Model through the FD efficiency curves (introduced in Section 7.2.1). These relative efficiency curves were measured for multiple telescopes through a spectral calibration campaign [140]. The necessity to measure efficiency curves for multiple telescopes comes from the fact that not all telescopes were constructed using the same choice of materials. The 12 mirrors of Los Leones and Los Morados are comprised of rectangular aluminium segments, each with a 2 mm thick $AlMgSiO_5$ layer glued on to form the reflective surface. The mirrors of Coihueco and Loma Amarilla are constructed from hexagonal glass segments coated with a 90 nm thick Al layer followed by a 110 nm thick SiO_2 layer. The corrector rings are constructed from one of two materials, Borofloat 33 and a crown glass labelled P-BK7, with the UV transmission of both materials being different. In total, there exists four different mirror-corrector ring combinations which form the FD (additional details regarding these combinations can be found in reference [140]). In this Section we estimate the systematic uncertainty in the fitted absolute calibration associated with the uncertainty in the FD relative efficiency curves.

An example of an FD relative efficiency curve and its associated systematic uncertainties is shown in Figure 7.32a. The curve is normalised to 1 at 375 nm, the wavelength used in the absolute FD calibration. To estimate the effect of the uncertainty of the efficiency curve on the fitted absolute calibration, the nominal efficiency curve is fluctuated by its lower and upper error limits (Figure 7.32b) and propagated through the analysis chain. The blue (green) curve indicates the lower (upper) error limits for an FD telescope of this particular composition. A Rayleigh Model calculated using the blue curve will return a signal which appears dimmer relative to one calculated using the nominal efficiency curve. Conversely, the green curve will return a Rayleigh Model which appears brighter, as a higher fraction of photons are able to propagate through all components of the telescope chain.

Summarised in Table 7.2 are the average absolute calibrations for each of the four Sirius observing telescopes. Sirius is observed by at least 1 telescope from each FD site (see Figure 7.1), allowing this particular study to sample the effect of different telescope compositions. For each telescope the average absolute calibration is listed for Rayleigh Models calculated using the lower error limit, nominal and upper error limit efficiency curves. The results suggest that the systematic uncertainty introduced on the fitted absolute calibration from the FD efficiency curve is a telescope dependent value, of the order of $2 - 5\%$.

7.3.3 Fitting Algorithm

The reliability of the fitting algorithm outlined in Section 7.2.3 is evaluated using a simple toy simulation. To do so, 1000 mock tracks were generated and

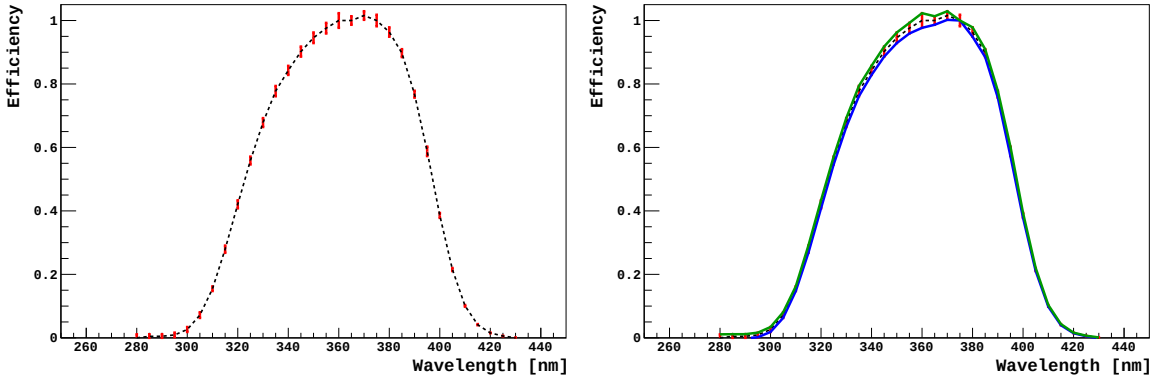

(a) (b)

Figure 7.32: Left: The efficiency curve measured for CO 4. The red markers indicate the wavelengths (spaced 5 nm apart) at which the telescope's relative efficiency was measured. The errors bars indicate the systematic uncertainty associated with each measurement. Right: The lower and upper error bound relative efficiency curves are shown in blue and green, respectively.

	Lower	Nominal	Upper
CO 4	1.05 ± 0.01	1.03 ± 0.01	1.02 ± 0.01
LL 1	1.08 ± 0.02	1.02 ± 0.02	0.97 ± 0.04
LA 6	1.05 ± 0.01	1.03 ± 0.01	1.01 ± 0.01
LM 5	0.98 ± 0.01	0.96 ± 0.01	0.95 ± 0.01

Table 7.2: Average fitted absolute calibrations for the four Sirius observing FD telescopes. The effect of varying the respective efficiency curves of each telescope is a change in the absolute calibration of $\sim$ 2% for the Cohiueco, Los Morados and Loma Amarilla telescopes and $\sim$ 5% for Los Leones. The relative efficiency curves for Los Leones have larger uncertainties compared to telescopes from other FD sites (additional details in [140]).

passed through the fitting procedure described in Section 7.2.3. Each track is defined by its exponential slope along with the positions in the sky at which the signal begins and terminates (either as a function of elevation or an equivalent air mass). For simplicity, each track is assumed to have an identical underlying Rayleigh atmosphere. The only track to track variations in the exponential slope stem from a change in the aerosol atmosphere (characterised by VAOD). Tracks are modulated by a function (similar to the simulated template shown in Figure 7.12) characterising the typical camera inefficiencies along the camera face. Furthermore, the amplitude of each 'pixel' along the modulating function is scaled by a factor sampled from a Gaussian distribution, which aims to mimic pixel gain

variations throughout the night[8], recalling that the amplitude of each pixel along the template is proportional to the gain of that pixel. In order to generate a subset of realistic tracks, track parameters are sampled from distributions based on real star track measurements. These distributions are shown in Figure 7.33.

The results of the simple toy simulation are summarised in the two distributions of Figure 7.34. The left hand distribution suggests that the systematic uncertainty in the absolute calibration introduced by the fitting algorithm is small (much less than 1%). The spread in the distribution is of the order of $\sim$ 3%, suggesting that the night to night variations in the fitted absolute calibration are partly due to the fitting algorithm. The difference in the fitted and true aerosol optical depth is of the order of 1%.

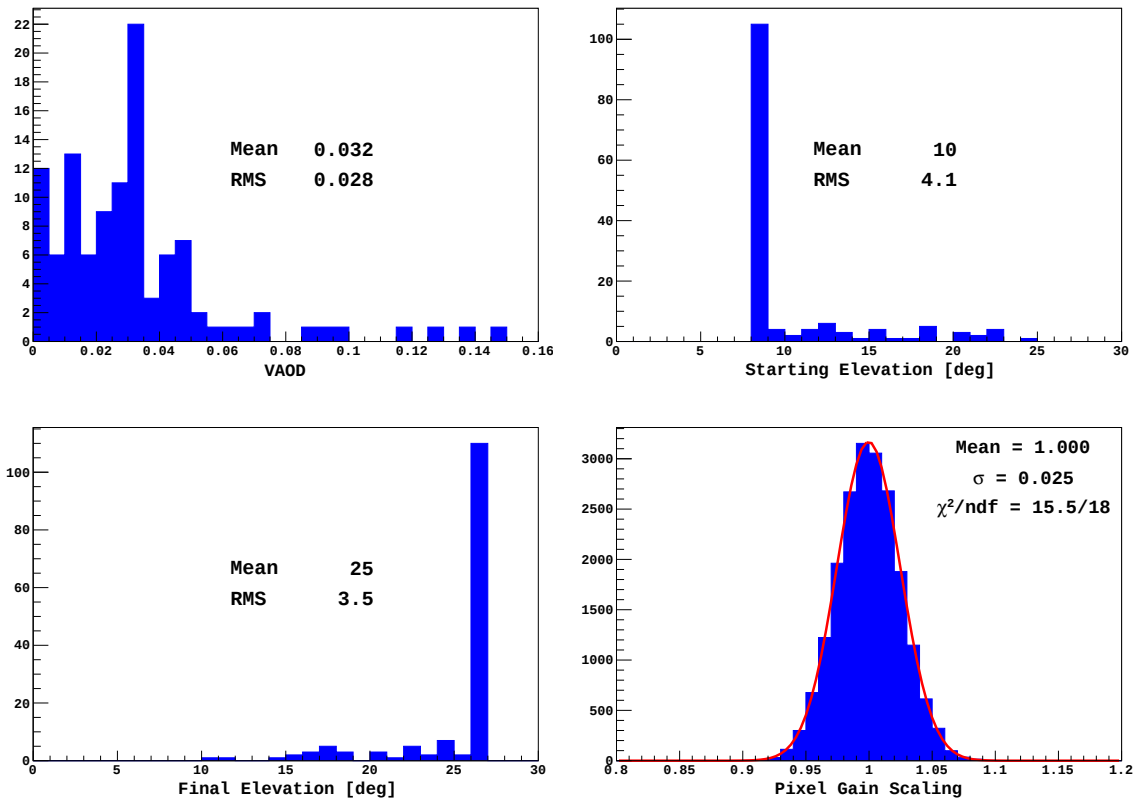

Figure 7.33: Shown here are the three track parameter (VAOD, starting and ending elevations) distributions used to generate realistic mock tracks. The values of VAOD are taken from the aerosol database. Also shown (bottom right) is the distribution from which the pixel gain variation factor is sampled.

[8]Running Cal A studies suggest this could be of the order of $\sim 2-3\%$. See Section 5.2.

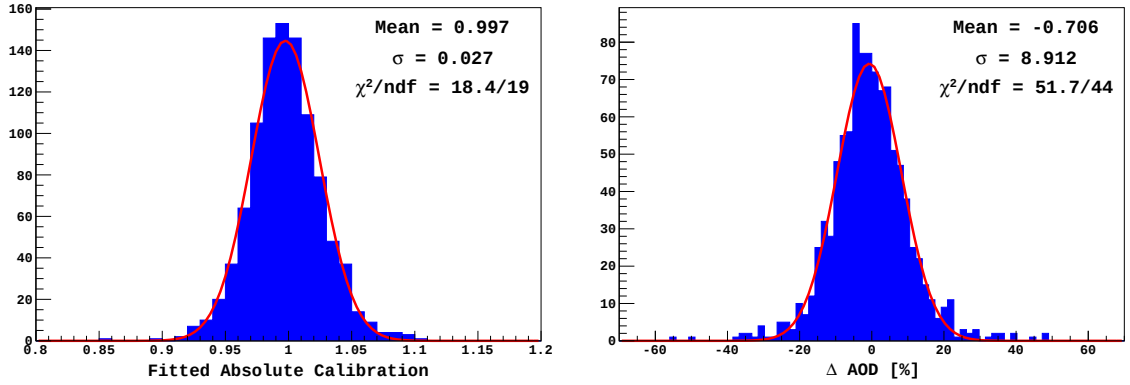

Figure 7.34: Left: Distribution of the fitted absolute calibration for the 1000 mock tracks (expected mean of 1 by construction). Right: Distribution of the difference between the fitted and true aerosol optical depth for the 1000 mock tracks.

7.3.3.1 Angstrom Coefficient

In Section 7.2.1 the assumption was made that the Angstrom coefficient γ, which characterises the wavelength dependence of the aerosol optical depth (τ_{aero}), was 0. This simplifying assumption enabled the corrected star track equation to be reduced to a simple exponential function (see Equation 7.17). In reality it is unlikely that this is the case, with measurements at the Observatory indicating a non-zero time varying value of γ (which can have a value as large as 2 in rare circumstances) [150]. The systematic effect on the fitted parameters due to this assumption are estimated here. It should be noted that the equivalent value for Rayleigh scattering is 4 (which is taken into account through the Rayleigh model), implying that aerosol scattering has a comparatively weaker wavelength dependence.

Firstly, recall the earlier definition of γ:

$$\frac{\tau_{aero,\lambda}}{\tau_{aero,\lambda_0}} = \left(\frac{\lambda}{\lambda_0}\right)^{\gamma} \tag{7.16}$$

where $\tau_{aero,\lambda}$ is the aerosol optical depth at a wavelength λ, and τ_{aero,λ_0} is the reference optical depth at a wavelength of λ_0. For this exercise, the value of τ_{aero,λ_0} is chosen to be 0.05 measured at reference wavelength of $\lambda_0 = 355\,\text{nm}$ to correspond with the CLF's operational wavelength. For a given value of γ, a test track is calculated as a function of air mass as follows:

$$Test\ Track(AM) = \sum_i F_0'(\lambda_i) \times e^{-(\tau_{Ray}(\lambda_i)+\tau_{Mie}(\lambda_i))\times AM} \tag{7.25}$$

where F_0' is the flux of the star folded with the FD efficiency and τ_{Ray} is the Rayleigh optical depth (see Section 7.2.1). The value of τ_{aero} is evaluated as a function of λ_i according to Equation 7.16. The ratio of the test track and an

equivalent Rayleigh test track (essentially Equation 7.25, but with $\tau_{aero} = 0$) is then calculated, to which the following exponential function is fitted.

$$Fit\ Function(AM) = AC \times e^{-AOD \times AM} \tag{7.26}$$

The effect of a non-zero value of γ on the fitted parameters is summarised in Figure 7.35. The left hand plot suggests that the effect of a non-zero γ on the fitted absolute calibration is small. Even in the most extreme scenario ($\gamma = 2$) the fitted absolute calibration is only incorrect by $\sim 1\%$. On the other hand, the aerosol optical depth appears to be more sensitive to the value of γ, and can be underestimated by up to $\sim 15\%$ in the most extreme scenario[9].

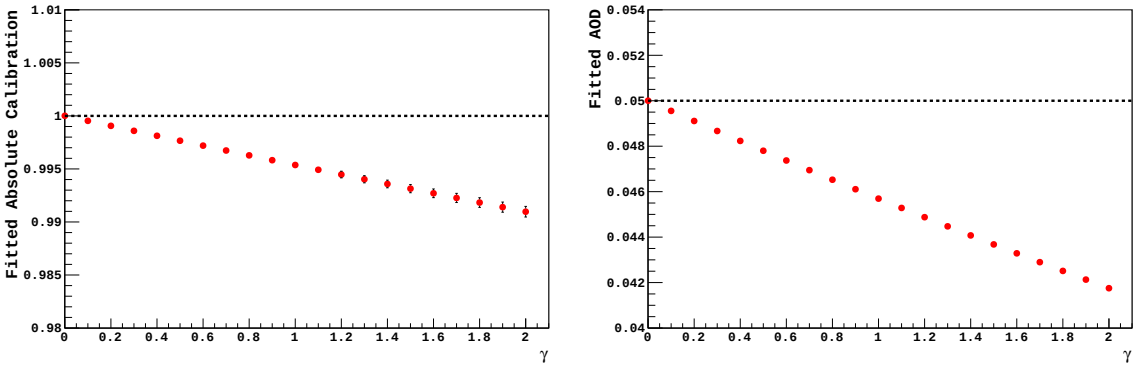

Figure 7.35: Left: The fitted absolute calibration for test tracks calculated using different γ values. Right: Fitted aerosol optical depth (τ_{aero}) for test tracks as a function of γ. The "true" values are indicated by the dashed lines in both graphs.

7.3.3.2 Choice of Template

In Section 7.2.2 we introduced the template as a function designed to characterise the efficiency of the observing FD telescope as a function of elevation. The adopted solution took the form of an empirically derived template which had been guided by a shape function provided through a ray tracing simulation. In this Section we compare calibration results estimated using different templates.

In the left hand plot of Figure 7.36 a comparison is made between the non-guided and guided empirical templates for Sirius as observed by CO 4. At first glance the two templates appear to agree well, especially between elevations of $\sim 10^\circ - 20^\circ$. At elevations below $\sim 10^\circ$ the non-guided template sits below the guided template, which is not surprising given the shape function (Figure 7.13). Similarly, above 20° the non-guided template is slightly above the guided template.

[9] As mentioned earlier, the aim of this analysis was not to quantify the aerosol atmosphere using star tracks. The result is simply a by-product of the analysis method.

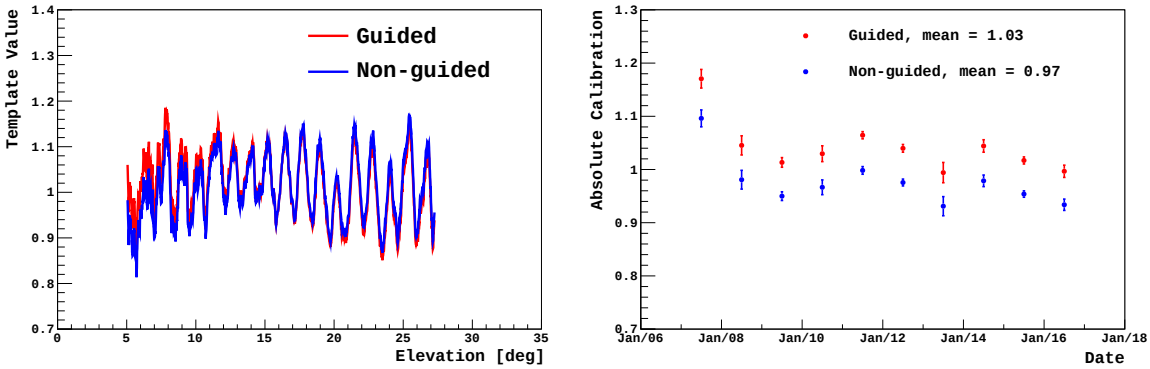

Figure 7.36: Left: The guided (red) and non-guided (blue) empirical templates for Sirius as observed by CO 4. Right: Comparison of the star calibration profiles estimated using the guided and non-guided templates.

In the right hand plot of Figure 7.36 the star calibration profiles using the two templates are compared. While the year to year fluctuations correlate with one another, the normalisation of the two profiles differ by $\sim 6\%$.

It should be noted that the magnitude of this discrepancy will vary depending on the shape function itself, which will depend on the star and telescope pairing of interest. For example, the path taken by a specific star across the field of view of an observing telescope may return a relatively flat shape function, for which the difference between the guided and non-guided templates is not expected to be significant. In such a case, it is not expected that the fitted calibration would be greatly affected by the choice of template.

The uncertainty of the shape function (recalling that this function was generated using an Offline ray tracing module) is estimated by shifting the telescope pointing direction[10] by the uncertainty of the FD pixel alignment, estimated to be 0.1° (Section 3.2.1). Two independent shifts of 0.1° are made to the pointing direction in both azimuth and elevation, with each shift providing a new underlying shape function. The shape functions are then used to calculate two guided templates which are then passed through the fitting algorithm. Both shifts resulted in a small increase (2%) in the average fitted absolute calibration compared to the scenario where the nominal telescope pointing direction is used. From these results, we estimate that the systematic effect on the fitted calibration introduced by the uncertainty in the shape function is of the order of 2%.

7.3.4 Systematics Summary

The contributions from the various systematic uncertainties on the fitted absolute calibration are summarised in Table 7.3. A small contribution related to the uncertainty in the Rayleigh optical depth (provided using GDAS) is included for com-

[10]Telescope pointing directions can be modified in *FTelescopeList.dtd*.

pleteness. Any uncertainty in the Rayleigh optical depth will propagate through to the Rayleigh model (effectively making the Rayleigh model appear brighter or dimmer) and consequently, the fitted calibration. Previous studies [142] have shown that data provided through GDAS can be adequately validated through local atmospheric measurements with radio soundings and weather stations.

For the case of Sirius the total systematic uncertainty on the value of the fitted absolute calibration is estimated to be $7 - 8\%$.

Source	**Contribution [%]**
Optical Halo	3.5
Star Spectrum	5*
FD Efficiency	2-5**
Fitting Algorithm	<1
Angstrom Coefficient	<1
Rayleigh Optical Depth	1
Template Estimate	2
Total	**7-8**

Table 7.3: Summary of systematic errors and their respective contributions. The total is given by the quadrature sum of the individual contributions. * for the case of Sirius. ** 2% for Coihueco, Los Morados and Loma Amarilla telescope and 5% for Los Leones.

7.4 Results and Discussion

Results obtained using several stars to estimate the calibration stability of individual FD telescopes are presented in this Section. For the case of Sirius, in which a measured stellar spectrum is used, the results can be used to monitor the long term stability of the absolute FD calibration. For all other stars the results can only be used to monitor the long term stability of the FD calibration in a relative sense, as a large uncertainty exists on their absolute scales. This Section will also include a comparison of the star calibration measurements obtained for multiple stars observed by the same telescope, as well as the measurements obtained for multiple telescopes within a single FD site and the implications of these results.

7.4.1 Sirius

Absolute star calibration measurements estimated for the four Sirius observing FD telescopes are presented in Figure 7.37. It should be noted that the lack of statistics for LL 1 (Figure 7.37b) can be attributed to two main factors. Firstly, there existed an issue with the NSB variance measurements for LL 1, which began in August 2010 lasting through to October 2011. We have chosen to omit data

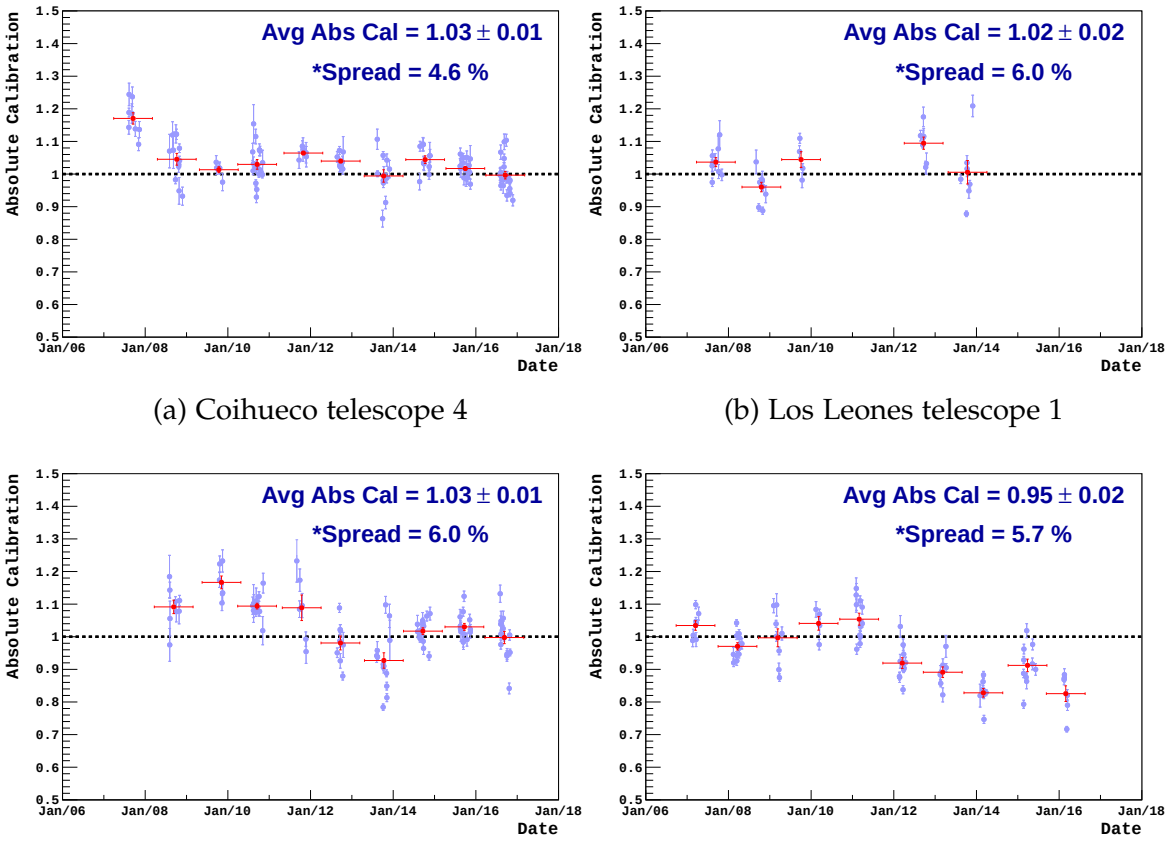

(a) Coihueco telescope 4

(b) Los Leones telescope 1

(c) Loma Amarilla telescope 6

(d) Los Morados telescope 5

Figure 7.37: The absolute star calibration profiles for CO 4, LL 1, LA 6 and LM 5 estimated using Sirius. Sirius is observed rising in the East by CO 4, LL 1 and LA 6 between August and November, and setting in the West by LM 5 between February and June. The quoted spread is with respect to the mean value of each year.

from this period as star tracks could not be reliably measured. Secondly, the FD calibration constants for LL 1 for the period after November 2014 were found to be unreliable [151]. Star tracks measured after this period were also omitted from the results.

The four measurements of Figure 7.37 are characteristically different as no two telescopes appear to be consistent with one another. For example, while the mean values of the absolute calibration for CO 4 and LA 6 may be compatible, the individual profiles do not appear to be consistent as a function of time. The profile for CO 4 (if the first time bin is ignored) appears to only have small deviations from a flat line, indicating an absolute calibration which is stable as a function of time. In contrast, the profile of LA 6 has greater variation as a function of time, most notably between the years 2008 to 2014, during which a significant downwards drift is observed. Finally, the profile for LM 5 indicates a stable absolute calibra-

tion for the period up until 2012, beyond which the calibration appears to rapidly change to a mean value well below 1. It should be noted that the average absolute calibration for all telescopes are consistent with 1 (after taking into account the systematic uncertainty of $7-8\%$ estimated in Section 7.3.4).

Since we know that the intrinsic brightness of Sirius is constant as a function of time, any fluctuations observed in the star calibration measurements can be attributed to the observing telescopes themselves. In that case, there is no expectation that the four telescopes (each belonging to a different FD site) should have identical results, as individual telescopes are not required to change in a similar way. In a later section (Section 7.4.4) comparisons will be made between the star calibration measurements using different stars for telescopes belonging to the same FD site.

7.4.2 Rigel

Rigel (also known as β *Orionis*) is a blue supergiant belonging to one of the most well known constellations in the sky, Orion. Rigel is classified as a type B8Iae star with a U-band magnitude of -0.56 [137, 152], making it one of the brightest stars in the night sky. During the months of August to November of each year, Rigel can be observed rising in the East (approximately 1 hour before Sirius) from CO 4 and LA 6. Rigel is also partially visible from LL 1 during the same period of year, but only reaches a maximum elevation of $\sim 14^{\circ}$ before leaving the telescope's field of view. As tracks formed in LL 1 do not reach a sufficiently high elevation (or low air mass), the value of the extrapolated function is prone to greater track to track variations, resulting in a larger spread in the final result. For this reason, we shall only focus on results obtained for CO 4 and LA 6 in this Section.

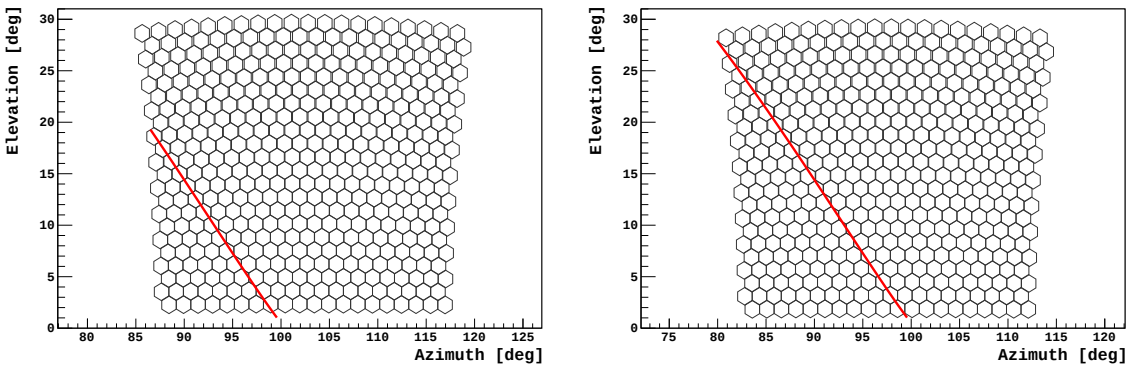

(a) Coihueco telescope 4 (b) Loma Amarilla telescope 6

Figure 7.38: The path of Rigel across the fields of view of CO 4 (left) and LA 6 (right).

Rigel is the first example of a star for which a measured stellar spectrum was not easily obtainable and so a scaled library spectrum was used as a compromise.

A library spectrum for a type B8I star was sourced from [147] and scaled to appropriately match the desired magnitude for Rigel. As mentioned in Section 7.3.2.1, a presumably large uncertainty (which is difficult to quantify) is introduced on the absolute value because of the use of a library spectrum and consequently, the star calibration measurements can only be analysed in a relative sense. The results for Rigel as observed by CO 4 and LA 6 are shown in Figure 7.39. It should be noted that the vertical axis of each profile has been normalised by the mean of all the data points.

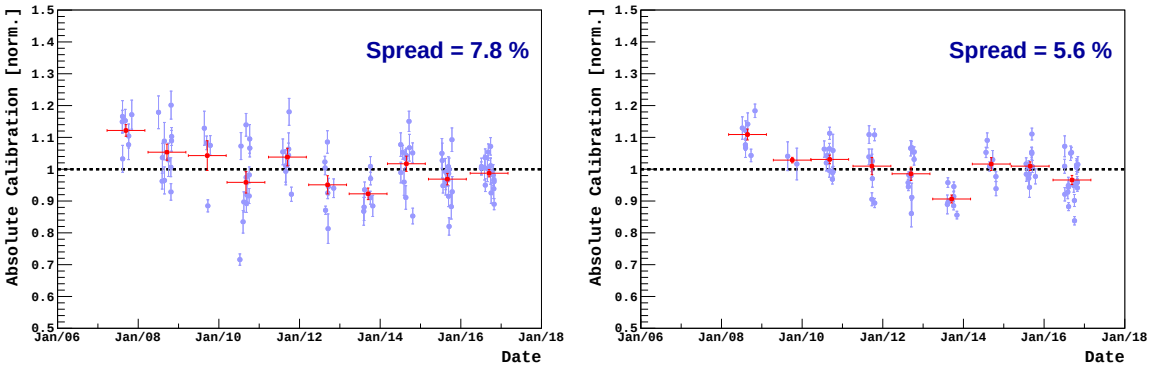

(a) Coihueco telescope 4

(b) Loma Amarilla telescope 6

Figure 7.39: Normalised star calibration profiles for CO 4 (left) and LA 6 (right) estimated using Rigel. The spread is calculated year by year. By construction, the mean of all data points in a given plot is 1.

Once again it is not expected that the two profiles of Figure 7.39 should correlate with one another, as two independent telescopes (from different FD sites) are being tested. The larger spread in the results for CO 4 (compared to LA 6) can be attributed to the geometric limitations imposed on individual star tracks for that specific telescope. From Figure 7.38a it can be seen that on a given night, Rigel is only able to reach a maximum elevation of $\sim 20^{\circ}$ in CO 4, corresponding to a minimum air mass of ~ 3. This particular geometry not only limits the maximum length of a star track in CO 4, but also imposes a minimum air mass which can potentially be reached by Rigel. In Section 7.2.4 it was discussed that the length of the track as well as its positioning in the field of view can affect the spread of the fitted nightly values. Given the inherently shorter tracks, as well as the greater degree of extrapolation required to reach zero air mass, it is expected that greater variation should exist in the results for CO 4 compared to LA 6.

7.4.3 Canopus

Canopus (α *Carinae*) is a bright giant star of spectral type A9II [153] belonging to the southern constellation, Carinae. Canopus has a U-band magnitude of -0.49 [137] and can be observed rising through the fields of view of CO 3 and LA 4

during the months of June through to November. The tracks formed by Canopus through these two telescopes are illustrated in Figure 7.40.

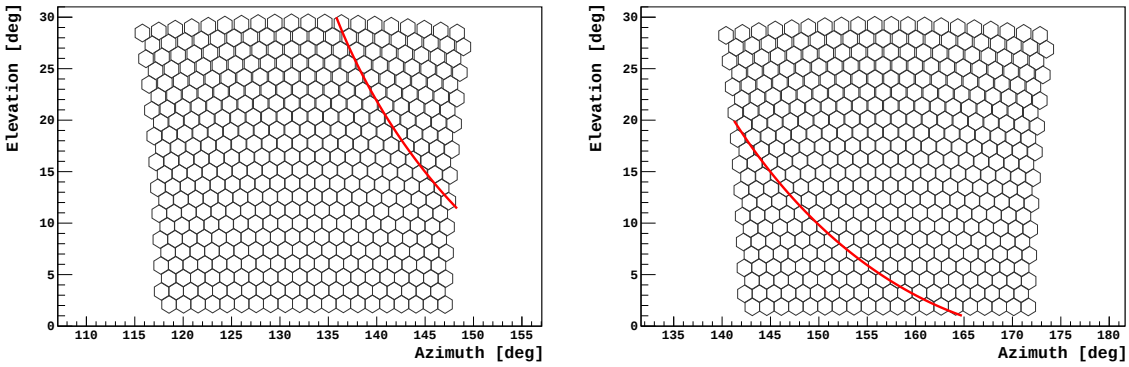

(a) Coihueco telescope 3 (b) Loma Amarilla telescope 4

Figure 7.40: The path of Canopus across the fields of view of CO 3 (left) and LA 4 (right).

A rescaled library spectrum corresponding to an F0I spectral type star was used for this analysis. Similar to the case for Rigel, the uncertainty due to the choice of spectrum introduced on the absolute scale of the star calibration measurement is large and the results can only be treated in a relative sense. The two normalised star calibration measurements for CO 3 and LA 4 are shown in Figure 7.41. The large track to track variations observed in Figures 7.41a and 7.41b can be attributed to the geometric limitations of the path of Canopus through the respective telescopes. The result for CO 3 indicates a calibration which is relatively stable as a function of time up until 2014, beyond which a large discontinuity is observed. The calibration following the discontinuity appears to be stable. For LA 4, the result indicates a rapidly decreasing calibration in the early years of the profile which appears to stabilise in 2010. Similar to the profile for CO 3, a discontinuity (albeit not as large) is also observed towards the beginning of 2014.

7.4.4 Comparisons of Star Calibration Measurements

In this Section we compare the star calibration measurements obtained using multiple stars for the same FD telescope. Comparisons will also be made between measurements for different telescopes (using different stars) within the same FD site.

7.4.4.1 Sirius and Rigel

As shown previously in Sections 7.4.1 and 7.4.2, Sirius and Rigel are observed by both CO 4 and LA 6 at approximately the same time of year. The respective paths

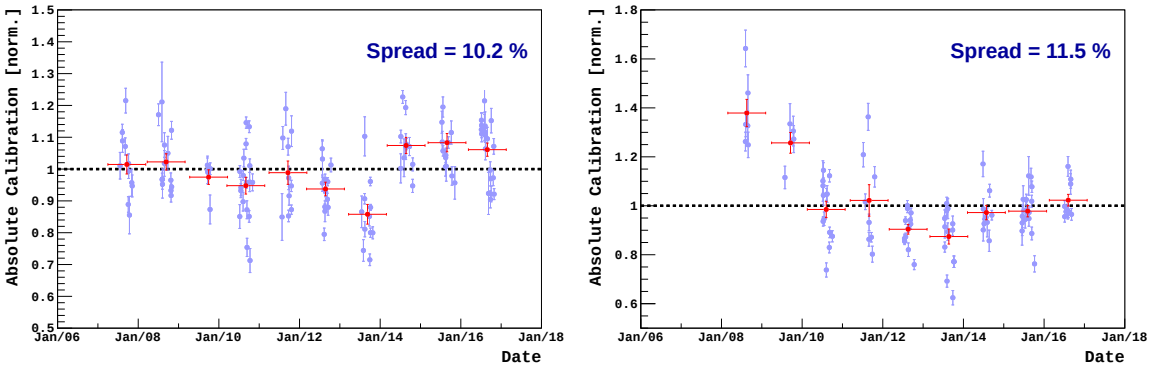

(a) Coihueco telescope 3 (b) Loma Amarilla telescope 4

Figure 7.41: Normalised star calibration profiles for CO 3 (left) and LA 4 (right) estimated using Canopus.

through the field of view of each of these telescopes are compared in Figures 7.42a and 7.42b.

The transits of Sirius and Rigel sample a different collection of FD pixels in each of these telescopes, with the results providing an opportunity to study the uniformity of the calibration evolution across individual telescopes. In Figure 7.42c the results from Sirius and Rigel observed by CO 4 are compared. Due to the uncertainty in the absolute scale of the fitted values, in particular for Rigel, each star calibration profile is normalised by its respective mean. The most striking feature is the strong correlation observed between the two measurements as a function of time. A similar observation is made for the two measurements of LA 6 in Figure 7.42d. These correlations are perhaps expected, as all pixels belonging to the same telescope are exposed to more or less the same operational and calibration conditions[11]. From these results we can conclude that the FD pixels belonging to a singe telescope will (on average) evolve in a similar manner.

7.4.4.2 Sirius and Canopus

Sirius and Canopus are observed by separate telescopes from both the Coihueco and Loma Amarilla detectors. The results from these two stars offers the opportunity to study the properties of the calibration evolution of different telescopes within the same FD site.

In Figure 7.43a a comparison is made between the star calibration measurements for Sirius and Canopus as observed by CO 4 and CO 3, respectively. A strong correlation is observed in the long term trends of both profiles, as both telescopes appear to have a steady downwards drift up until 2014, after which a discontinuity is observed. Similar correlations are observed for the measurements

[11] Both the nightly relative calibration and the absolute calibration are performed on a telescope by telescope basis.

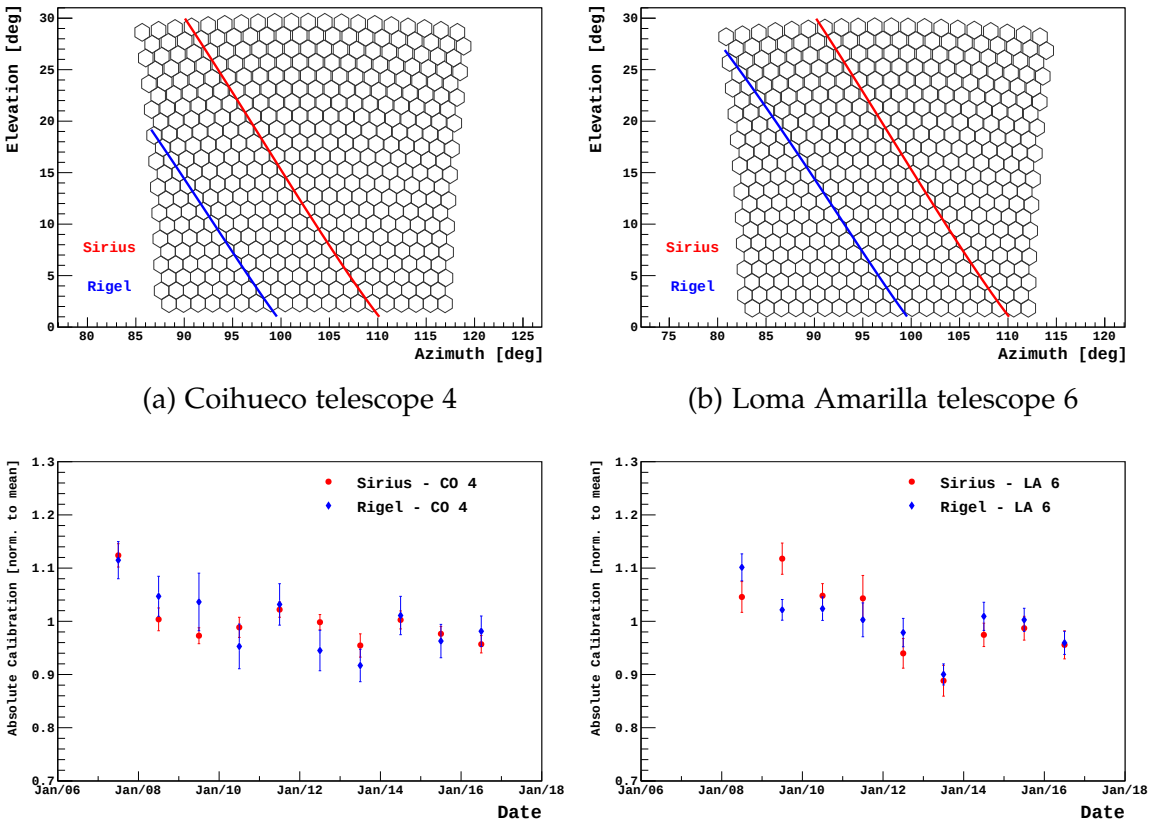

(a) Coihueco telescope 4

(b) Loma Amarilla telescope 6

(c) Coihueco telescope 4

(d) Loma Amarilla telescope 6

Figure 7.42: The paths of Sirius (red) and Rigel (blue) across the fields of view of CO 4 (top left) and LA 6 (top right). The normalised fitted star calibration profiles are compared for CO 4 (bottom left) and LA 6 (bottom right).

for the Loma Amarilla telescopes, as shown in Figure 7.43b. This result suggests that all telescopes belonging to the same FD site will (on average) evolve in a similar manner.

Unlike the case of Sirius and Rigel (for which both stars are observed through the same telescope) it is not immediately obvious why these correlations exist. The fact that the calibrations of two telescopes appear to correlate with one another suggests that the features of the respective profiles are likely due to a factor common to all telescopes within the same FD site. The light pulses used as part of the cal A calibration procedure (see Sections 3.2.2.2 and 5.1) for all telescopes within a single FD site are sourced from a common LED which is housed towards the rear of each FD building. Any changes to the performance of this LED can affect the calibration of all telescopes uniformly. Similarly, any significant calibration or maintenance campaigns (such as the cleaning of the UV filters or mirrors) can affect all telescopes uniformly[12].

[12] As long as these campaigns are performed for all telescopes at approximately the same time.

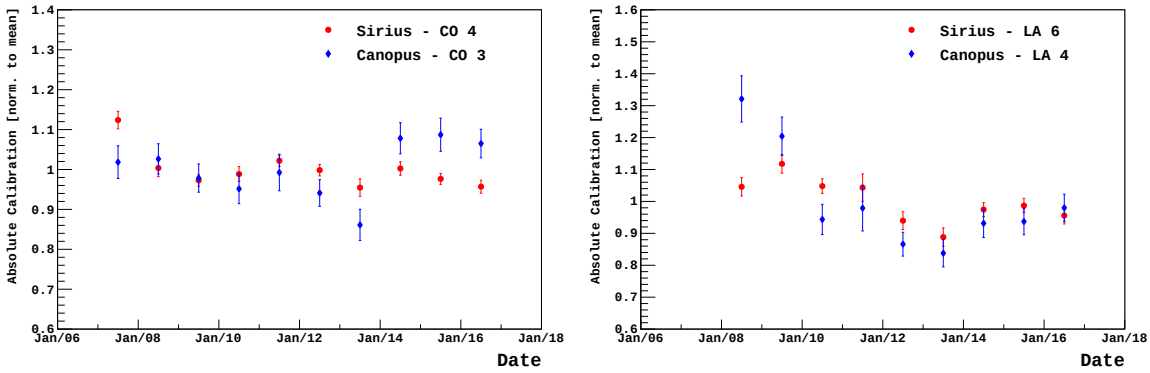

(a) Coihueco Telescopes 3 and 4 (b) Loma Amarilla Telescopes 4 and 6

Figure 7.43: The normalised fitted star calibration profiles for different telescopes of Coihueco (left) and Loma Amarilla (right) using Sirius and Canopus.

7.5 Comparisons with the Energy Scale Ratio

In Chapter 5 an extensive analysis of the long term stability of the Pierre Auger Observatory's energy scale was presented. Several unexpected features related to the evolution of the ESR (defined in Section 5.5) were noted, most notably the downwards drift of $\sim 1.6\%$ per year, the seasonal modulation of amplitude $\sim 5\%$ as well as a discontinuity beginning in 2014. After applying a series of FD and SD event reconstruction improvements, it was observed that the seasonal modulation improved to an amplitude of the order of $\sim 2\%$. The same improvements did not appear to significantly affect either the long term drift or the discontinuity. Through an independent study of the SD event rates, it was concluded that a small fraction of this drift ($\sim 0.3\%$ per year) may be attributed to the SD, with the residual drift most likely being related to the evolution of the FD. In this Section we will study any correlations between the long term stability of the ESR and the calibration stability of the FD using results obtained using the stellar photometry analysis.

The analysis presented in Chapter 5 used 8895 high quality hybrid events observed by at least one of the 24 main FD telescopes. The drift in the ESR can therefore be thought of as an average drift encompassing the evolution of the entire FD. As the stellar photometry analysis is only capable of monitoring the calibration stability on an individual telescope basis, then it would be appropriate if the stability of the ESR is studied separately for each FD site. The ESR using hybrid events detected by individual FD sites[13] is illustrated in Figure 7.44. The vertical axis of each Figure is normalised to have a mean of 1. The four ESR profiles share similarities in their evolutions, as each profile exhibits a drift of the order of $\sim -1.6\%$ followed by a significant discontinuity in 2014.

[13]From the completed Observatory (2008 onwards).

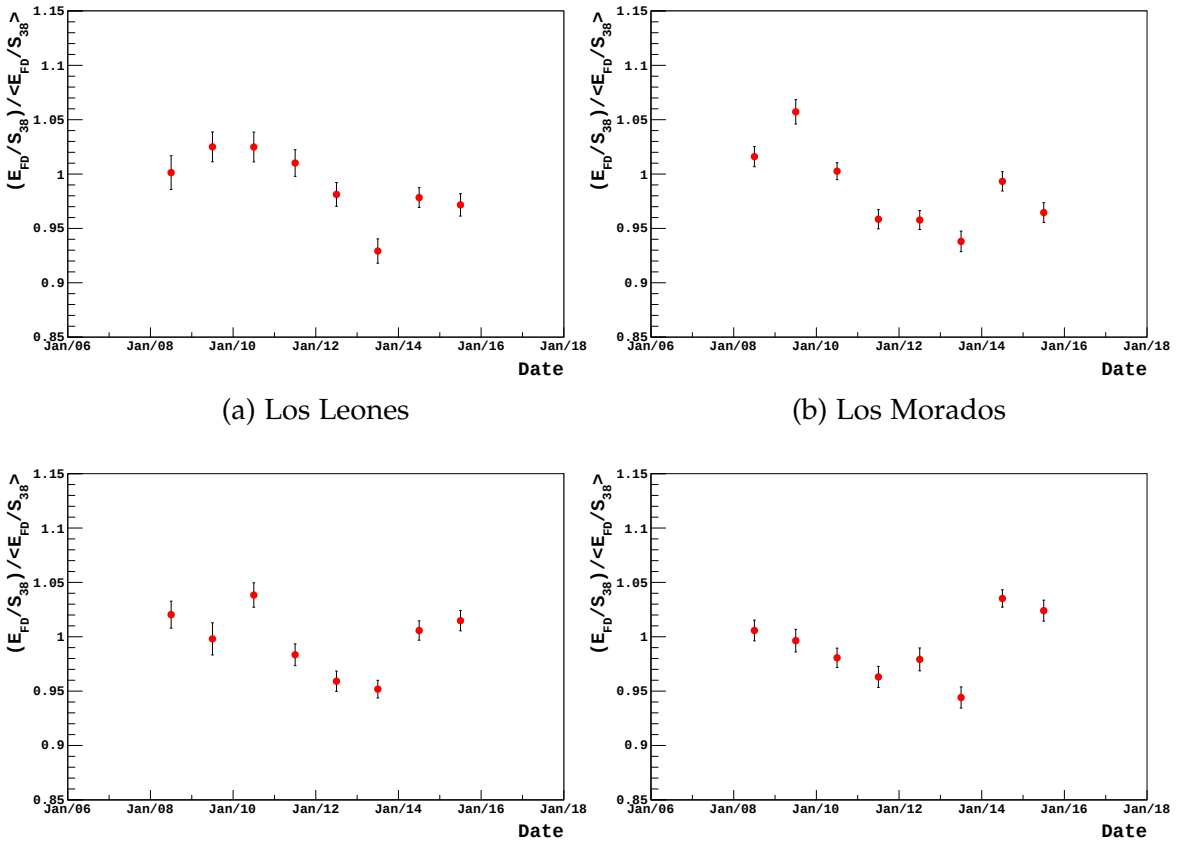

(a) Los Leones

(b) Los Morados

(c) Loma Amarilla

(d) Coihueco

Figure 7.44: ESR profiles for individual FD sites. The horizontal axis here has bin width equal to 1 year. All four FD sites have a similar trend in their respective profiles; a long term drift followed by a discontinuity of $5-10\%$ at the beginning of 2014.

In Section 7.4.4 it was concluded that the FD pixels belonging to a single telescope appear to evolve in a similar manner. It was also observed that changes between telescopes of the same FD site appear to correlate with one another. It is reasonable then to combine the star calibration measurements for individual telescopes (within the same FD) to form an average profile which can be generalised to a single FD site. By doing this we can overcome one of the obvious limitations of the stellar photometry technique, which only enables the study of the calibration of telescopes which observe bright U-band stars. The following comparisons are only made for the Coihueco and Loma Amarilla detectors, as we have only obtained star calibration measurements for multiple telescopes within those two detectors. Generalised star calibration profiles for Los Leones and Los Morados would be difficult to obtain given the shortage of suitable stars presented in this Chapter.

In Figure 7.45 a comparison is made between the ESR profile and star calibra-

tion measurements for the Coihueco FD. The red circles indicate the yearly average ratio of E_{FD}/S_{38} for hybrid events observed by the Coihueco FD telescopes. The black squares represent the weighted average FD star calibration measurements for Coihueco estimated using Sirius, Rigel and Canopus. Both profiles have been normalised by their respective means so that comparisons can be easily made. A remarkable correlation is observed in the evolution of the two profiles, which both appear to have a slight downwards drift up until the beginning of 2014 after which a step of the order of $\sim$ 10% is observed. Similar observations can be made for the case of the Loma Amarilla calibration and ESR profiles, as shown in Figure 7.46.

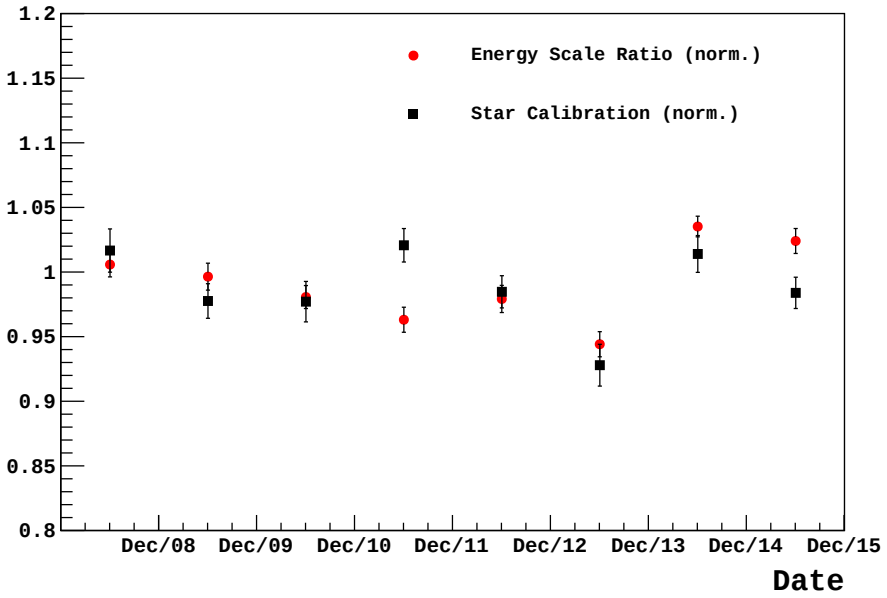

Figure 7.45: Comparison of the ESR and weighted average star calibration profiles for Coihueco (Sirius, Rigel and Canopus). Both vertical axis are normalised with their respective means.

The comparisons made in this Section confirm, at least for the Coihueco and Loma Amarilla detectors, that the residual features in the long term stability of the ESR are due to the evolution of the FD[14]. It is possible that the same trends exist for Los Leones and Los Morados, although additional star calibration measurements for telescopes belonging to those FD sites are required to confirm this.

7.5.1 Long Term Drift of the FD Calibration and Energy Scale Ratio

Part of the long term drift may be attributed to the ageing of the FD pixels through their continual operation and exposure to the NSB, an effect which appears to be

[14] An expected result as the SD event rate was shown to have no such features.

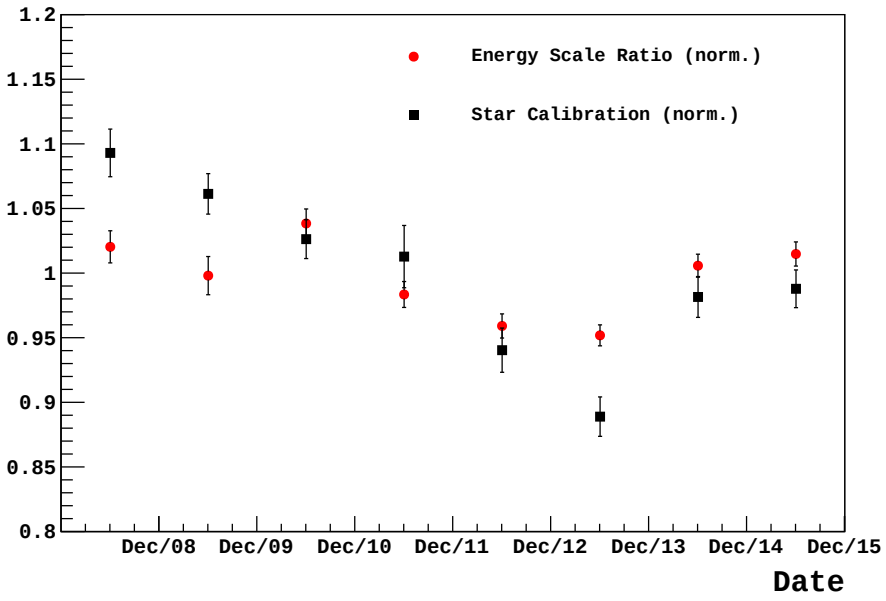

Figure 7.46: Comparison of the ESR and weighted average star calibration profiles for Loma Amarilla (Sirius, Rigel and Canopus).

common to all FD sites. The nightly calibration should, at least in theory, return calibration constants which appropriately compensate for such variations. It is possible that the LED (from which cal A pulses are sourced from) is slightly changing with time and not being monitored correctly. This could potentially contribute to the drift in the FD calibration.

Another, although perhaps not immediately obvious, origin of the drift could be the effect of the broadening of the PSF of the FD telescopes. This was discussed in some detail in Section 7.3.1. It is suspected that the extent of the broadening is proportional to the amount of dust deposited on the surface of the FD mirrors, with a thicker layer of dust corresponding to a broader PSF [146]. It is important to note that both the relative and absolute FD calibrations are blind to the broadening of the PSF. The relative calibration only illuminates the FD cameras and so any changes to the reflective properties of the mirrors are irrelevant. The absolute calibration involves the complete illumination of the entire FD camera, so the light lost from a given pixel (due to the broadening of the PSF) is compensated by the tails of the PSF from neighbouring pixels.

In Section 7.3.1 it was estimated that $\sim 7\%$ of the relevant star light remained undetected due to the choice of integration area adopted in the analysis. For simplicity, it was assumed that the magnitude of this correction was constant with time and independent of the position of the spot on the camera (and equivalent illuminated area on the mirror).

An analogous correction is made during the FD reconstruction of cosmic ray air showers. For a given event, the light collection area along the track of the

shower detector plane (SDP) is defined as all FD pixels enclosed within a particular region centred along the SDP. The angle between the centre of a pixel and the spot centre estimated at a given time t is labelled as ζ. The light collection area includes all pixels for which $\zeta < \zeta_{opt}$, where ζ_{opt} is the optimal ζ determined through the maximisation of the signal to noise ratio of the enclosed pixels. Previous studies have shown that a fraction of the total signal is observed by pixels beyond this area (where $\zeta > \zeta_{opt}$) requiring an additional correction [154]. Historically this correction was based on parametrised angular distributions for both the fluorescence and Cherenkov components of an air shower [155, 156]. Folding the intrinsic shower widths with the measured PSF of the FD telescopes [144] predicted that the parametrised distributions were underestimating the amount of additional light. The effect of this missing light took the form of a lateral width correction, which was parametrised through the analysis of real shower data which had been collected over several years of operation. The lateral width correction therefore encompasses the average broadening of the width of a shower convolved with the optical PSF [157].

Recent efforts have been made by members of the Collaboration to study the effect of the deposition of dust on the reflective properties of the FD mirrors [146]. More specifically, the study involved the measurement of the fraction of signal (from a portable light source) which was diffusely scattered off the mirror. This fraction, referred to as the diffusion reflectivity, is naturally anti-correlated with the specular scattering of light off the mirror. If it is assumed that all of the diffusely scattered light contributes to the broadening of the PSF, then the diffusion reflectivity can be interpreted as a measure of the broadening of the PSF. For the mirror monitored in [146][15] it was found that the dust layer which had accumulated on the mirror's surface after 12 years of operation caused the diffusion reflectivity to increase by 15% at a wavelength of 325 nm. This is equivalent to an increase in the broadening of the PSF of $\sim$ 1.25% per year (assuming this effect is linear in time), a rate which is comparable to the long term drift of the FD calibration.

In summary, the light collection algorithms of the stellar photometry analysis and FD event reconstruction attempt to correct for the effect of a broadened PSF. The stellar photometry analysis employs a one sided 7% systematic correction which is assumed to be constant in time. The FD reconstruction analysis addresses this problem through the lateral width correction which attempts to correct for the average effect of a broadened PSF. As the dust layer of the FD mirrors accumulates with time, the PSF presumably changes shape, resulting in less light being collected by the respective light collection algorithms. The lack of a dynamic correction in both analyses to account for this phenomenon can result in a systematic decrease in the measured signal, which may manifest in a downwards long term drift.

[15] Telescope 2 of Coihueco.

7.5.2 Discontinuity in the FD Calibration and Energy Scale Ratio

The discontinuity at the beginning of 2014 appears to be due to a source common to each of the 24 main FD telescopes. In Section 7.4.4.2 the possibility that (unmonitored) changes to the LED light source used as part of the nightly relative calibrations can affect all telescopes within the same FD site uniformly. While it is possible that changes to the LED can lead to a discontinuity in the ESR (and star calibration) profiles, it is extremely unlikely that the LEDs for each of the four FD sites underwent identical changes simultaneously. It is more likely that a global change capable of affecting all FD detectors is the cause of the discontinuity.

7.5.2.1 Significant Calibration Events

Significant calibration events which are performed on all FD telescopes at (approximately) the same time can potentially cause global calibration changes. For example, the absolute drum calibration involves the illumination of individual telescopes using a portable (pre-calibrated) light source. Several of these calibration campaigns have taken place throughout the lifetime of the FD [116, 135, 158]. If the calibration of the portable light source had changed for a particular calibration campaign, then it would be expected that the calibration of all FD telescopes would change accordingly. In addition to the absolute calibration, a spectral calibration campaign was also undertaken in March of 2014 with the goal of obtaining precise relative spectral response functions for individual FD telescopes [140].

In Figure 7.47 the ESR and star calibration profiles for Coihueco (left) and Loma Amarilla (right) are shown along with the approximate dates of significant calibration events. The absolute calibrations are indicated by the dashed black and red lines, and correspond to the January 2010 and April 2013 campaigns, respectively. The FD spectral calibration campaign is also labelled as the dashed blue line. It is understood that the results obtained from the January 2010 campaign were used to fill the full calibration database between 2004 and 2012 [159] with the database following this period being filled using the April 2013 results. Certain features in the respective profiles appear to coincide with the absolute calibration (for example, the downwards step of $\sim 5-10\%$ between 2012 and 2013 for Coihueco) but whether or not these are directly related to the absolute calibration (or due to some other factor) is uncertain.

Prior to the March 2014 campaign, it was assumed that all FD telescopes shared an identical spectral response which was initially derived from the convolution of separate transmission or reflection measurements of each optical component used in the first Los Leones telescopes [160]. This was later replaced with an end-to-end measurement of the spectral response (measured in 2006), which was obtained using the drum light source (used in the absolute calibration) which had been equipped with a xenon flasher and filter wheel. The result was a direct measurement of the FD's efficiency at five wavelengths across its operational bandpass [161]. The aim of the study of March 2014 was to obtain the spectral

response of different telescope configurations (recalling that the materials used to construct the FD telescope components vary due to different manufacturers) with a finer wavelength spacing of $\Delta\lambda = 5\,\text{nm}$.

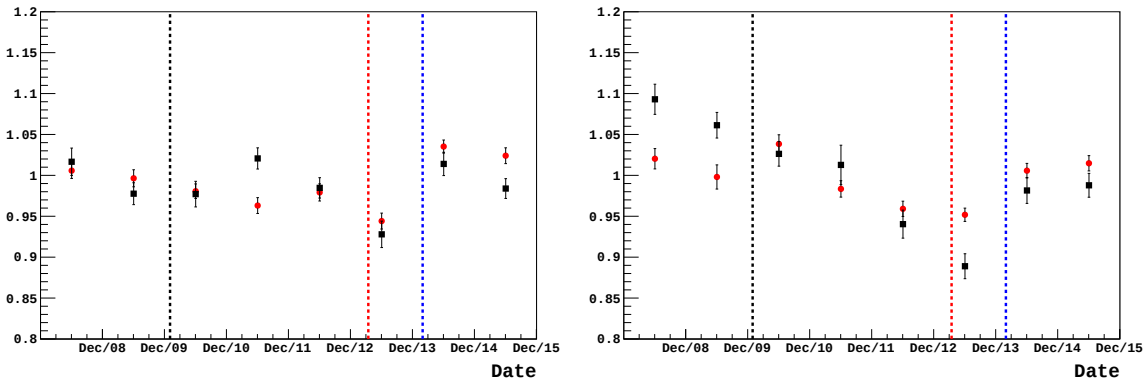

(a) Coihueco (b) Loma Amarilla

Figure 7.47: Normalised ESR and star calibration profiles are labelled by the red circles and black squares, respectively, for Coihueco (left) and Loma Amarilla (right). The dashed black, red and blue lines indicate the approximate dates of the January 2010 absolute calibration, April 2013 absolute calibration and spectral calibration campaigns, respectively.

Although the discontinuities in both the ESR and star calibration profiles appear to occur following the spectral calibration, it is unlikely that the two events are correlated. In the conclusions of [140] it was noted that the new calibration constants obtained from the spectral calibration campaign increased the primary cosmic ray energy by 1.8% to 2.8% for the Los Morados and Los Leones telescopes while having a negligible effect (less than 0.35%) for the telescopes of Coihueco and Loma Amarilla. The effect of the spectral calibration is obviously far too small to account for the discontinuities observed in Figure 7.47, which are of the order of 10%. Furthermore, the correction to FD energies derived from the spectral calibration is one which was applied back in time for all FD telescopes, so it is not expected to contribute any significant discontinuities in the ESR.

7.5.2.2 Introduction of the Running Calibration

In Section 5.2 the running cal A procedure was introduced as a means of tracking the gain evolution of individual FD pixels throughout data acquisition. The running calibration has been in regular operation since 2014 with the data being available from reference [162]. Unlike the standard cal A procedure, the running calibration can be performed without the need to close the FD shutters, so as to have a minimal impact on data acquisition. In the following we investigate the possibility that the introduction of these regular, bright LED pulses during data

acquisition has affected the calibration stability of the FD, resulting in a discontinuity in the energy scale.

If it is assumed that the running cal A measurements follow the same procedure as the standard cal A (50 rectangular shaped LED pulses, each 57 μs in duration emitted at a rate of 1/3 Hz) then the number of additional photons provided through the running cal A can be estimated:

1. A typical cal A pulse (see Figure 5.1) has a pulse height of approximately 400 ADC counts/100 ns.

2. The calibration constant for a pixel has an average value of $\sim$ 4 photons/ADC count. One cal A pulse therefore has a height of $\sim$ 1600 photons/100 ns.

3. Factoring in the duration of the pulse (57 μs = 570 100 ns time bins) it is estimated that a single cal A pulse will illuminate a given FD pixel with $\sim 9 \times 10^5$ photons.

The NSB flux observed by a single FD pixel has an average value of $\sim$ 70 photons/m^2/deg^2/μs (see Figure 5.12). Over the duration of a single cal A pulse this equates to $\sim 3 \times 10^4$ photons per pixel. For practical reasons it is reasonable that the cal A pulse is significantly brighter than the underlying NSB during the period of illumination. The fact that the running cal A measurements only occur every 30 minutes must also be taken into account when estimating the extra light contribution. Over a period of 30 minutes, the cal A measurement (of 50 pulses) will expose an FD pixel to $\sim 4.5 \times 10^7$ photons. In contrast, the integrated NSB over the same period is $\sim 10^{12}$ photons per pixel. Given these estimations, it can be seen that the running cal A pulses will typically only contribute a very small fraction ($\sim$ 0.005%) of additional photons to a given FD pixel, which is not expected to have a significant effect on the performance of the FD telescopes.

It is unlikely that the running cal A, which we have estimated to contribute a very small fraction of additional light, is capable of causing the discontinuity observed in the energy scale and star calibration profiles of the FD.

7.5.3 UV Filter and Mirror Cleaning Campaigns

Throughout the lifetime of the FD, significant quantities of dust and dirt may accumulate on the surface of the filters and mirrors, having an obvious effect on their transmission and reflective properties. An important detail is that the cal A procedure (recalling that this is the measurement used to track the calibration between consecutive absolute calibrations) is completely blind to such effects, as cal A only focusses on the illumination of the FD pixels and effectively ignores all other telescope components. Failing to account for the changing properties of the filter and mirror may introduce a systematic effect in the calibration of the FD.

The Collaboration has chosen to address this issue in recent years with the undertaking of filter and mirror cleaning campaigns. A log of filter and mirror cleaning campaigns can be found in reference [163]. Mirrors are significantly harder to clean compared to filters as individual mirror segments are removed, cleaned separately and then realigned. Consequently, far fewer mirror cleaning campaigns have been undertaken compared to filter cleaning campaigns. In the following we investigate the effect of any relevant (between 2008 and 2015) cleaning procedures on the star calibration and ESR profiles of Coihueco and Loma Amarilla.

The effect of cleaning the surface of the filters has been studied and documented in references [145, 164], with the results of a case study summarised in Figure 7.48. A dedicated filter cleaning campaign was undertaken in March of 2014 with telescope 1 of HEAT (HEAT 1) in a downwards position. In such a configuration, the fields of view of HEAT 1 and CO 3 overlap, allowing the relative detected signal from the CLF, as observed by the two telescopes, to be studied. The result shown in Figure 7.48 indicates a drop of the order of 10% in the ratio following the cleaning of the HEAT 1 filter. The ratio is later restored to its original value following the cleaning of the filter of CO 1. This result implies that the effect of cleaning the filters is an increase in the FD response of $\sim 10\%$.

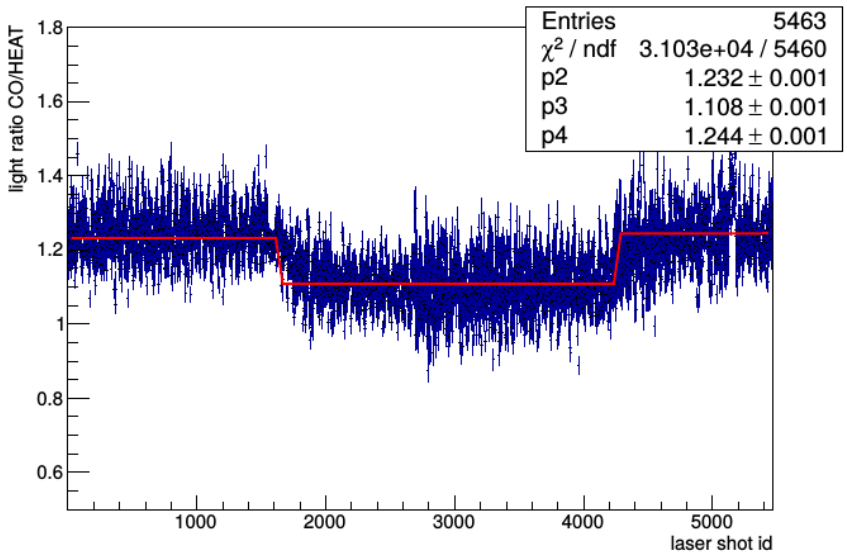

Figure 7.48: The ratio of CLF signals detected by CO 3 and HEAT 1 over an eight day period in March 2014. The downwards step corresponds to the filter of HEAT 1 being cleaned. The upwards step corresponds to the cleaning of the filter of CO 3 [164].

In Figure 7.49 the dates of several filter and mirror cleaning campaigns for Coihueco and Loma Amarilla are labelled on the respective ESR and star calibration profiles. For Coihueco, there appears to be an increase in the star calibration

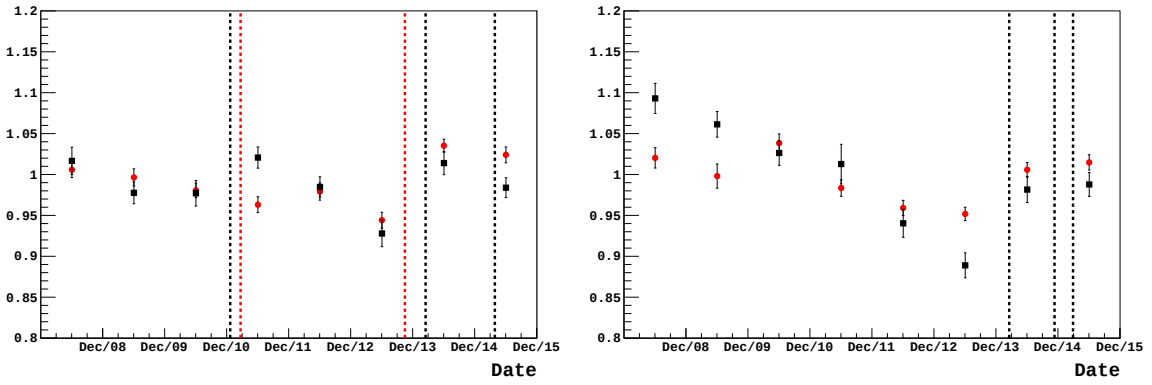

(a) Coihueco (b) Loma Amarilla

Figure 7.49: Normalised ESR (red circles) and star calibration (black squares) profiles for Coihueco and Loma Amarilla. The dashed black lines indicate the dates of the filter cleaning campaigns. The dashed red line indicates the date of a mirror cleaning campaign for Coihueco (no mirror cleaning campaigns for Loma Amarilla were listed over the time period considered here).

measurement following the dates of the filter and mirror cleaning campaigns in 2011. A similar observation can be made following the cleaning campaigns occurring in November 2013 and March 2014. The profiles following these cleaning campaigns appear to "recover" by $\sim 5-10\%$, which is comparable to the expected increase in the response of the FD depicted in Figure 7.48. The profiles of Loma Amarilla display a similar recovery following its filter cleaning campaign, which also occurred in March of 2014. Interestingly, the apparent stability of the respective measurements for both Coihueco and Loma Amarilla[16] may be a result of more regular filter cleaning campaigns in recent years.

For completeness ESR profiles for Los Leones and Los Morados with the recent filter cleaning campaigns have been included in Figure 7.50. Similar to Coihueco and Loma Amarilla, these two FD sites had their filters cleaned in March 2014. The discontinuity in the respective ESR profiles is consistent with the expected FD response to clean filters.

From the results presented in this Section, it appears that the effect of cleaning the UV filters may correlate with the discontinuity observed in the star calibration and ESR profiles of the FD. Furthermore, the magnitude of the discontinuity is consistent with that of a previous analysis where the effect of cleaning filters was studied using the CLF.

[16] A slight decrease is observed in 2015 for Coihueco, but this is not statistically significant.

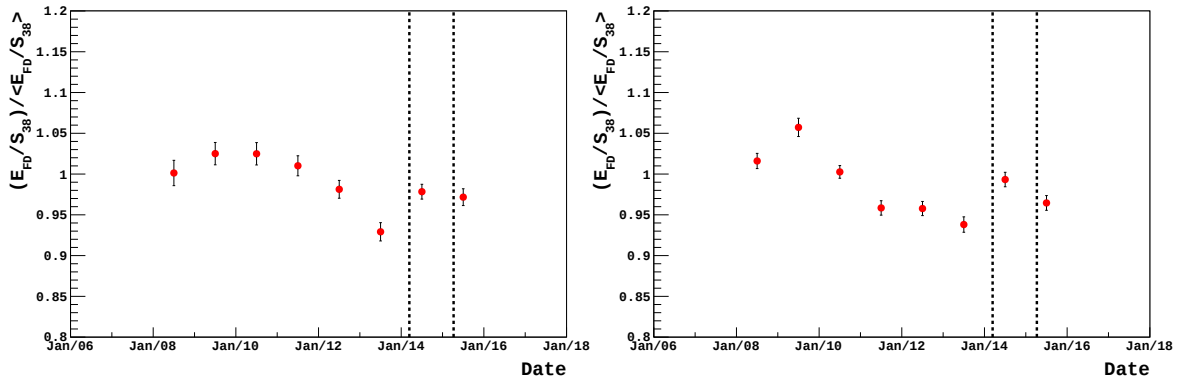

(a) Los Leones (b) Los Morados

Figure 7.50: Normalised ESR profiles for Los Leones and Los Morados. The dashed lines indicate the dates of the filter cleaning campaigns around the time of the discontinuity at the beginning of 2014.

7.6 Conclusions

In this Chapter we have presented a method to monitor the long term stability of the calibration of individual FD telescopes using stellar photometry. It was initially hoped that the signals associated with bright U-band stars observed by the FD could be used to monitor the absolute calibration of individual telescopes. Unfortunately, due to the apparent lack of measured stellar spectra for the bright stars of interest, the majority of the results presented in this Chapter can only be used to monitor the calibration stability of individual telescopes in a relative sense. Nonetheless the results can still be compared with the long term evolution of the Observatory's energy scale, which was discussed in Chapter 5.

For the case of Sirius, for which a measured spectrum is available, the results indicate that the average absolute calibration for the four Sirius observing FD telescopes (Los Leones 1, Los Morados 5, Loma Amarilla 6 and Coihueco 4) are consistent with that of a properly calibrated detector.

In addition to the star calibration measurements estimated using Sirius, two other stars (Rigel and Canopus) were also used to monitor the calibration stability of several FD telescopes. Through comparisons between measurements of different stars by the same telescope, it became apparent that the FD pixels belonging to a single telescope appeared to evolve in a similar manner. Furthermore, comparisons between measurements for separate telescopes (using different stars) within the same FD site suggested that telescopes belonging to the same FD evolved in a similar manner. This suggests that the absolute calibration of the four Sirius observing telescopes could be representative of the absolute calibration of all other telescopes belonging to the same eye (at least within the 1.8% uncertainty estimated through studies of the overlapping night sky background of neighbouring telescopes - see Chapter 6). Using this information, we were able to generalise

the results (for those FD sites which observed different stars through multiple telescopes) to estimate the average calibration as a function of time for a single FD site.

A strong correlation between the star calibration measurements as a function of time for Coihueco and Loma Amarilla with their respective ESR profiles was observed. This result confirmed that both the residual long term drift and the discontinuity in the ESR observed at the beginning of 2014 are related to the performance of the FD.

The long term drift may be associated the failure to account for the broadening of the PSF with time. The light collection algorithms used in the stellar photometry technique and FD event reconstruction both attempt to correct for the effect of the broadening of the PSF (which is believed to be caused by the deposition of dust on the FD mirrors). Neither of these corrections were formulated to take into account any change in the shape of the PSF with time, potentially resulting in a long term drift in the respective measurements.

The discontinuity is observed across all FD telescopes at the beginning of 2014 and is most likely the result of a global change which affected the entire FD. Two significant FD calibration events took place around the time of the discontinuity, these being the spectral FD calibration and the introduction of the running cal A measurements. Changes introduced by the spectral FD calibration were extended back in time, and resulted in a small increase in reconstructed FD energies. The pulses from the running cal A, although significantly brighter than the underlying NSB, only illuminate the FD pixels every 30 minutes during data acquisition. When the low duty cycle of the running cal A pulses is taken into account, it was estimated that the additional light introduced from the cal A pulses was insignificant relative to the integrated NSB. It was concluded that the changes introduced from these two calibration events had a negligible effect on the stability of the FD calibration and ESR.

The discontinuity appears to correlate in time with the UV filter cleaning campaign of March 2014. All four FD sites were covered in this campaign, with the magnitude of the discontinuity in the respective ESR profiles being consistent with that predicted by a previous case study.

Chapter 8

Conclusions and Future Work

This thesis has primarily focussed on the long term stability of the Pierre Auger Observatory's energy scale with a particular emphasis on the calibration of the FD. The goal of this work was to develop methods to cross check the stability of the relative and absolute calibration of the FD using the night sky background signal. The most important outcomes of this thesis are outlined here.

We began by defining the energy scale ratio (ESR) as a quantity which can be used to monitor the stability of the Observatory's energy scale. The ESR is given by the ratio of two independent measurements of the energy of the primary cosmic ray. For a hybrid event, these two measurements are the energy reconstructed by the FD (E_{FD}) and the zenith angle-corrected shower size measure by the SD (S_{38}). Several unexpected features became apparent in the evolution of the ESR, most notably the seasonal variation, a long term downwards drift and an upward discontinuity beginning at 2014. We note the following:

- A seasonal variation (of amplitude $\sim$ 5%), drift ($\sim -1.6\%$ per year) and discontinuity at the beginning of 2014 ($\sim 5-10\%$) was observed in the ESR.

- In recent years the collaboration has developed two significant event analysis improvements, these being the SD weather correction and an updated treatment of the analysis of atmospheric aerosols. The application of both of these improvements to the respective reconstruction chains significantly improved the amplitude of the seasonal variation, which is now of the order of $\sim$ 2%.

- The residual amplitude is likely to be related to the nightly gain fluctuations of the PMTs which comprise the FD telescopes. Through the recent implementation of a running calibration measurement (designed to monitor the gain of the FD telescopes during the course of data acquisition) it was observed that the gain of the FD telescopes can vary by as much as 4%. It is suspected that accounting for the nightly variations in the gain can further reduce the seasonal amplitude of the ESR, although additional years worth of running calibration measurements are required to evaluate this.

- Neither of the aforementioned reconstruction improvements had a significant improvement on the long term drift or the discontinuity. Through an independent analysis of the SD event rates, it was concluded that the SD only contributes a small fraction ($\sim 0.3\%$ per year) to the drift, with the majority of the drift being dominated by the evolution of the FD. Furthermore, no discontinuity at the beginning of 2014 was observed in the SD event rate, implying that the discontinuity in the ESR can also be attributed to the FD.

The stability of the calibration of the FD can be monitored by analysing the FD's response to a light source of known brightness. During data acquisition, the FD regularly samples the night sky background signal. It was initially hoped that the night sky background as a whole could be treated as a constant light source. Unfortunately, the uncertainty and natural time variation in various contributing night sky background sources would have made this specific task difficult. Nonetheless, the night sky background was still used to monitor the stability of the FD relative calibration.

- A cross check method which compares the observed night sky background photon flux across a region of overlapping field of view between adjacent FD telescopes was developed. To simplify the analysis, the overlapping region was defined as the neighbouring pixel columns on the edges of two FD telescopes.

- It was estimated that an uncertainty of 1.8% exists in the relative calibration between adjacent FD telescopes at any point in time. This value combines the calibration of all of the 24 main FD telescopes, and should be treated as an average estimate of the inter-calibration between telescopes across the entire FD.

By studying the night sky background photon flux it became apparent that sufficiently bright U-band stars could be treated as a constant light source. A method was developed to monitor the absolute FD calibration stability using stellar photometry. The main conclusions are as follows:

- The stellar photometry technique can be used to monitor the absolute FD calibration stability of a given telescope only if the absolute brightness of the star in question is known, for which a measured stellar spectrum is required. This is true for the star Sirius, for which we estimated the "absolute calibration" for Los Leones 1, Los Morados 5, Loma Amarilla 6 and Coihueco 4 to be $(1.02 \pm 0.02 \pm 0.08)$, $(0.95 \pm 0.02 \pm 0.07)$, $(1.03 \pm 0.01 \pm 0.07)$, $(1.03 \pm 0.01 \pm 0.07)$ $(\pm\text{stat.} \pm \text{sys.})$, respectively. These results are consistent with a properly calibrated detector (for which the absolute calibration has a value of unity) even before evoking the systematic uncertainty of the FD calibration of 9.9%.

An important note is that even though only 1 telescope from each FD site observes Sirius, the results obtained from the inter-calibration analysis (which indicate the relative calibration stability between adjacent telescopes is consistent within 1.8%) gives confidence in the absolute calibration of all other (non-Sirius observing) FD telescopes.

- The technique was used to obtain (generalised) star calibration measurements for the Coihueco and Loma Amarilla FD sites, as those two sites contain multiple telescopes which observe different stars. For cases in which a measured spectrum for the star of interest was difficult to obtain, the technique was used to monitor the calibration stability in a relative sense.

- The star calibration measurements as a function of time for Coihueco and Loma Amarilla were compared to their respective ESR profiles. A correlation was observed between the evolution of the two profiles, confirming that the residual long term drift and discontinuity in the ESR are related to the FD.

- The long term drift may be attributed to the the light collection algorithms employed in both the stellar photometry analysis and FD event reconstruction. Both algorithms require additional corrections to account for the broadening of the FD telescopes' point spread function (suspected to be correlated with the accumulation of dust on the surface of the FD mirrors). The relevant corrections were derived and applied in an average sense, and are not capable of accounting for any changes in the shape of the PSF with time. If the broadening of the PSF has a time dependency then this effect could result in a long term downwards drift in the ESR and star calibration measurements as a function of time. Recent mirror reflectivity measurements [146] seem to confirm that the diffusive mirror reflectivity has been increasing with time.

- The discontinuity appearing towards the beginning of 2014 is suspected to be related to the cleaning of the UV filters located at the aperture of each FD telescope. All FD telescopes had their filters cleaned in early 2014, and the magnitude of the discontinuities in their respective ESR profiles are consistent with that expected due to filter cleaning.

The results and analysis techniques presented in this thesis can be extended with the continual operation of the Pierre Auger Observatory's FD with the further collection of hybrid events, night sky background data, and calibration data. Future work may entail:

- Further monitoring of the evolution of the ESR with the accumulation of additional (hybrid) cosmic ray shower data. These results, in conjunction with the results from the stellar photometry analysis (for the stars presented

in this thesis as well as additional stars), can be used to monitor the stability of the Observatory's FD.

- Extension of the stellar photometry technique to include more telescopes from different FD sites. For example, HEAT telescope 2 observes Sirius shortly after it leaves the field of view of Coihueco telescope 4, offering the opportunity to compare the calibration and energy scales of HEAT and Coihueco.

- A study of the time variation of the point spread function of the FD telescopes using the stellar photometry technique. If the extent of the point spread function is correlated with the accumulation of dust on the FD mirrors, then it may be possible to study the evolution of this effect using signals from bright stars.

References

[1] R. Clay, B. Dawson, and P. Davies. *Cosmic Bullets: High Energy Particles in Astrophysics*. Frontiers of science. Perseus Books Group, 1997.

[2] CA de Coulomb. Troisième Mémoire sur l'Electricité et le Magnétism. *Histoire de l'Académie Royal des Sciences*, page 612, 1785.

[3] M. Faraday. *Experimental Researches in Electricity*. Number v. 2 in Experimental Researches in Electricity. Richard and John Edward Taylor, printers and publishers to the University of London, 1844.

[4] C. T. R. Wilson. On the Ionisation of Atmospheric Air. *Proceedings of the Royal Society of London*, 68:151–161, 1901.

[5] A. de Angelis. Atmospheric ionization and cosmic rays: studies and measurements before 1912. *Astroparticle Physics*, 53:19–26, January 2014.

[6] J. Blümer, R. Engel, and J. R. Hörandel. Cosmic rays from the knee to the highest energies. *Progress in Particle and Nuclear Physics*, 63:293–338, October 2009.

[7] C Patrignani, DH Weinberg, et al. Review of particle physics. *Chin. Phys.*, 40:100001, 2016.

[8] K. Greisen. End to the Cosmic-Ray Spectrum? *Physical Review Letters*, 16:748–750, April 1966.

[9] G. T. Zatsepin and V. A. Kuz'min. Upper Limit of the Spectrum of Cosmic Rays. *Soviet Journal of Experimental and Theoretical Physics Letters*, 4:78, August 1966.

[10] A. A. Penzias and R. W. Wilson. A Measurement of Excess Antenna Temperature at 4080 Mc/s. *Astrophys. J.*, 142:419–421, July 1965.

[11] G. R. Blumenthal. Energy Loss of High-Energy Cosmic Rays in Pair-Producing Collisions with Ambient Photons. *Physical Review D*, 1:1596–1602, March 1970.

[12] J. L. Puget, F. W. Stecker, and J. H. Bredekamp. Photonuclear interactions of ultrahigh energy cosmic rays and their astrophysical consequences. *Astrophys. J.*, 205:638–654, April 1976.

[13] O. E. Kalashev, V. A. Kuzmin, and D. V. Semikoz. Top-Down Models and Extremely High Energy Cosmic Rays. *ArXiv Astrophysics e-prints*, November 1999.

[14] The Pierre Auger Collaboration. Upper limit on the cosmic-ray photon flux above 10^{19} eV using the surface detector of the Pierre Auger Observatory. *Astroparticle Physics*, 29:243–256, May 2008.

[15] The Pierre Auger Collaboration. Upper limit on the cosmic-ray photon fraction at EeV energies from the Pierre Auger Observatory. *Astroparticle Physics*, 31:399–406, July 2009.

[16] R. J. Protheroe. Acceleration and interaction of ultra high energy cosmic rays. In M. A. Duvernois, editor, *Topics in Cosmic-Ray Astrophysics*, volume 230, page 247, 1999.

[17] A. M. Hillas. The Origin of Ultra-High-Energy Cosmic Rays. *Annual Review of Astron and Astrophys*, 22:425–444, 1984.

[18] T. Stanev. Ultra High Energy Cosmic Rays:. Origin and Propagation. In J. P. Wefel, T. Stanev, and M. M. Shapiro, editors, *Astrophysics at Ultra-High Energies*, pages 83–95, November 2007.

[19] D. F. Torres and L. A. Anchordoqui. Astrophysical origins of ultrahigh energy cosmic rays. *Reports on Progress in Physics*, 67:1663–1730, September 2004.

[20] F. Halzen and E. Zas. Neutrino Fluxes from Active Galaxies: A Model-Independent Estimate. *Astrophysical Journal*, 488:669–674, October 1997.

[21] E. Waxman. Cosmological Gamma-Ray Bursts and the Highest Energy Cosmic Rays. *Physical Review Letters*, 75:386–389, July 1995.

[22] M. Vietri. The Acceleration of Ultra–High-Energy Cosmic Rays in Gamma-Ray Bursts. *Astrophysical Journal*, 453:883, November 1995.

[23] H. Kang, D. Ryu, and T. W. Jones. Cluster Accretion Shocks as Possible Acceleration Sites for Ultra–High-Energy Protons below the Greisen Cutoff. *Astrophysical Journal*, 456:422, January 1996.

[24] L. A. Anchordoqui, G. E. Romero, and J. A. Combi. Heavy nuclei at the end of the cosmic-ray spectrum? *Physical Review D*, 60(10):103001, November 1999.

[25] J. P. Rachen and P. L. Biermann. Extragalactic Ultra-High Energy Cosmic-Rays - Part One - Contribution from Hot Spots in Fr-II Radio Galaxies. *Astronomy and Astrophysics*, 272:161, May 1993.

[26] P. Blasi, R. I. Epstein, and A. V. Olinto. Ultra-high-energy cosmic rays from young neutron star winds. *The Astrophysical Journal Letters*, 533(2):L123, 2000.

[27] T. Stanev. *High Energy Cosmic Rays*. Springer Praxis Books. Springer Berlin Heidelberg, 2010.

[28] The Pierre Auger Collaboration. The Pierre Auger Cosmic Ray Observatory. *ArXiv e-prints*, February 2015.

[29] P. Auger, P. Ehrenfest, R. Maze, J. Daudin, and R. A. Fréon. Extensive Cosmic-Ray Showers. *Reviews of Modern Physics*, 11:288–291, July 1939.

[30] W. Heitler. *Quantum theory of radiation*. 1954.

[31] J. Matthews. A Heitler model of extensive air showers. *Astroparticle Physics*, 22:387–397, January 2005.

[32] J. Alvarez-Muñiz, R. Engel, et al. Hybrid simulations of extensive air showers. *Physical Review D*, 66(3):033011, August 2002.

[33] L. Anchordoqui, T. Paul, S. Reucroft, and J. Swain. Ultrahigh Energy Cosmic Rays. *International Journal of Modern Physics A*, 18:2229–2366, 2003.

[34] J. Abraham, P. Abreu, et al. The fluorescence detector of the Pierre Auger Observatory. *Nuclear Instruments and Methods in Physics Research A*, 620:227–251, August 2010.

[35] L. Bonolis. From cosmic ray physics to cosmic ray astronomy: Bruno Rossi and the opening of new windows on the universe. *ArXiv e-prints*, November 2012.

[36] J. Linsley, L. Scarsi, and B. Rossi. Extremely Energetic Cosmic-Ray Event. *Physical Review Letters*, 6:485–487, May 1961.

[37] M. Nagano and A. A. Watson. Observations and implications of the ultrahigh-energy cosmic rays. *Reviews of Modern Physics*, 72:689–732, July 2000.

[38] J. Linsley. Primary cosmic rays of energy 10^{17} to 10^{20} ev, the energy spectrum and arrival directions. *International Cosmic Ray Conference*, 4:77, 1963.

[39] J. Linsley. Evidence for a Primary Cosmic-Ray Particle with Energy 10^{20} eV. *Physical Review Letters*, 10:146–148, February 1963.

[40] M. A. Lawrence, R. J. O. Reid, and A. A. Watson. The cosmic ray energy spectrum above $4*10^{17}$ eV as measured by the Haverah Park array. *Journal of Physics G Nuclear Physics*, 17:733–757, May 1991.

[41] C.J. Bell, A.D. Bray, et al. The upper end of the observed cosmic ray energy spectrum. *Journal of Physics A: Mathematical, Nuclear and General*, 7(8):990, 1974.

[42] L. J. Kewley, R. W. Clay, and B. R. Dawson. Arrival directions of the southern highest energy cosmic rays. *Astroparticle Physics*, 5:69–74, June 1996.

[43] A A Ivanov, S P Knurenko, and I Ye Sleptsov. Measuring extensive air showers with Cherenkov light detectors of the Yakutsk array: the energy spectrum of cosmic rays. *New Journal of Physics*, 11(6):065008, 2009.

[44] R. M. Baltrusaitis, R. Cady, et al. The Utah Fly's Eye detector. *Nuclear Instruments and Methods in Physics Research A*, 240:410–428, October 1985.

[45] S. Yoshida and H. Dai. TOPICAL REVIEW: The extremely high energy cosmic rays. *Journal of Physics G Nuclear Physics*, 24:905–938, May 1998.

[46] G. Sigl, D. N. Schramm, and P. Bhattacharjee. On the origin of highest energy cosmic rays. *Astroparticle Physics*, 2:401–414, October 1994.

[47] D. J. Bird, S. C. Corbato, et al. The cosmic-ray energy spectrum observed by the Fly's Eye. *Astrophys. J.*, 424:491–502, March 1994.

[48] N. Chiba, K. Hashimoto, et al. Akeno Giant Air Shower Array (AGASA) covering 100 km2 area. *Nuclear Instruments and Methods in Physics Research Section A: Accelerators, Spectrometers, Detectors and Associated Equipment*, 311(1):338 – 349, 1992.

[49] H. Ohoka, M. Takeda, et al. Further development of data acquisition system of the Akeno Giant Air Shower Array. *Nuclear Instruments and Methods in Physics Research Section A: Accelerators, Spectrometers, Detectors and Associated Equipment*, 385(2):268 – 276, 1997.

[50] M. Takeda, N. Hayashida, et al. Extension of the Cosmic-Ray Energy Spectrum beyond the Predicted Greisen-Zatsepin-Kuz'min Cutoff. *Physical Review Letters*, 81:1163–1166, August 1998.

[51] K. Shinozaki, M. Teshima, and the Agasa Collaboration. AGASA Results. *Nuclear Physics B Proceedings Supplements*, 136:18–27, November 2004.

[52] T. Abu-Zayyad et al. The prototype high-resolution Fly's Eye cosmic ray detector. *Nucl. Instrum. Meth.*, A450:253–269, 2000.

[53] P. Sokolsky and G. B. Thomson. TOPICAL REVIEW: Highest energy cosmic-rays and results from the HiRes experiment. *Journal of Physics G Nuclear Physics*, 34:R401–R429, November 2007.

[54] R. U. Abbasi, T. Abu-Zayyad, et al. First Observation of the Greisen-Zatsepin-Kuzmin Suppression. *Physical Review Letters*, 100(10):101101, March 2008.

[55] Y. Tsunesada. Highlights from Telescope Array. *International Cosmic Ray Conference*, 12:67, 2011.

[56] T. Abu-Zayyad, R. Aida, et al. The surface detector array of the Telescope Array experiment. *Nuclear Instruments and Methods in Physics Research A*, 689:87–97, October 2012.

[57] H. Tokuno, Y. Tameda, et al. New air fluorescence detectors employed in the Telescope Array experiment. *Nuclear Instruments and Methods in Physics Research A*, 676:54–65, June 2012.

[58] H. Tokuno et al. On site calibration for new fluorescence detectors of the telescope array experiment. *Nucl. Instrum. Meth.*, A601:364–371, 2009.

[59] G. B. Thomson, P. Sokolsky, et al. *The telescope array low energy extension (TALE)*, volume 3, pages 337–339. Institute of High Energy Physics, 2011.

[60] Hiroyuki Sagawa. Telescope Array extension. *Nucl. Part. Phys. Proc.*, 279-281:145–152, 2016.

[61] B. R. Dawson, M. Fukushima, and P. Sokolsky. Past, Present and Future of UHECR Observations. *ArXiv e-prints*, March 2017.

[62] K.-H. Kampert and A. A. Watson. Extensive air showers and ultra high-energy cosmic rays: a historical review. *European Physical Journal H*, 37:359–412, August 2012.

[63] D. Allard, I. Allekotte, et al. Aperture calculation of the Pierre Auger Observatory surface detector. *International Cosmic Ray Conference*, 7:71, 2005.

[64] I. Allekotte, A. F. Barbosa, and the Pierre Auger Collaboration. The surface detector system of the Pierre Auger Observatory. *Nuclear Instruments and Methods in Physics Research A*, 586:409–420, March 2008.

[65] Xavier Bertou et al. Calibration of the surface array of the Pierre Auger Observatory. *Nucl. Instrum. Meth.*, A568:839–846, 2006.

[66] J. Abraham, P. Abreu, et al. Trigger and aperture of the surface detector array of the Pierre Auger Observatory. *Nuclear Instruments and Methods in Physics Research A*, 613:29–39, January 2010.

[67] D. Newton, J. Knapp, and A. A. Watson. The optimum distance at which to determine the size of a giant air shower. *Astroparticle Physics*, 26:414–419, January 2007.

[68] M. Ave for the Pierre Auger Collaboration. Reconstruction accuracy of the surface detector array of the Pierre Auger Observatory. *ArXiv e-prints*, September 2007.

[69] J. Hersil, I. Escobar, et al. Observations of Extensive Air Showers near the Maximum of Their Longitudinal Development. *Physical Review Letters*, 6:22–23, January 1961.

[70] A. Schulz. The measurement of the energy spectrum of cosmic rays above 3×10^{17} eV with the Pierre Auger Observatory. In *Proceedings, 33rd International Cosmic Ray Conference (ICRC2013): Rio de Janeiro, Brazil, July 2-9, 2013*, page 27, 2013.

[71] P. Bauleo, J. Brack, and the Pierre Auger Collaboration. Absolute Calibration of the Auger Fluorescence Detectors. *International Cosmic Ray Conference*, 8:5, 2005.

[72] R Caruso. Nightly Relative Calibration of the Fluorescence Detector of the Pierre Auger Observatory. In *ICRC2009*, pages 1–4, 2009.

[73] J. Abraham, M. Aglietta, et al. Properties and performance of the prototype instrument for the Pierre Auger Observatory. *Nuclear Instruments and Methods in Physics Research A*, 523:50–95, May 2004.

[74] B. R. Dawson, H. Y. Dai, et al. Simulations of a giant hybrid air shower detector. *Astroparticle Physics*, 5:239–247, October 1996.

[75] L. Valore for the Pierre Auger Collaboration. Atmospheric Aerosol Attenuation Measurements at the Pierre Auger Observatory. *ArXiv e-prints*, February 2014.

[76] L Valore. *Atmospheric Aerosol Determination using Vertical Laser Tracks in the Pierre Auger Experiment*. PhD thesis, University of Naples Federico II, 2007.

[77] B. R. Dawson. Hybrid Performance of the Pierre Auger Observatory. *International Cosmic Ray Conference*, 4:425–428, 2008.

[78] F. Fenu. The cosmic ray energy spectrum measured by the Pierre Auger Observatory. In *The Pierre Auger Observatory: Contributions to the 35th International Cosmic Ray Conference (ICRC 2017)*, pages 9–16, 2017.

[79] The Pierre Auger Collaboration. Reconstruction of inclined air showers detected with the Pierre Auger Observatory. *Journal of Cosmology and Astroparticle Physics*, 8:019, August 2014.

[80] M. Unger. Highlights from the Pierre Auger Observatory. talk presented at 35th Int. Cosmic Ray Conf., Busan, Korea., 2017.

[81] C. Meurer, N. Scharf, and the Pierre Auger Collaboration. HEAT - a low energy enhancement of the Pierre Auger Observatory. *Astrophysics and Space Sciences Transactions*, 7:183–186, May 2011.

[82] T. Hermann-Josef Mathes. The HEAT telescopes of the Pierre Auger Observatory: Status and first data. In *Proceedings, 32nd International Cosmic Ray Conference (ICRC 2011): Beijing, China, August 11-18, 2011*, volume 3, page 153, 2011.

[83] F. Sánchez. The AMIGA detector of the Pierre Auger Observatory: overview. In *Proceedings, 32nd International Cosmic Ray Conference (ICRC 2011): Beijing, China, August 11-18, 2011*, volume 3, pages 149–152, 2011.

[84] B. Wundheiler. The AMIGA Muon Counters of the Pierre Auger Observatory: Performance and Studies of the Lateral Distribution Function. *PoS*, ICRC2015:324, 2016.

[85] F. Suarez. The AMIGA muon detectors of the Pierre Auger Observatory: overview and status. In *Proceedings, 33rd International Cosmic Ray Conference (ICRC2013): Rio de Janeiro, Brazil, July 2-9, 2013*, page 0712, 2013.

[86] C. Glaser. Results and Perspectives of the Auger Engineering Radio Array. In *European Physical Journal Web of Conferences*, volume 135 of *European Physical Journal Web of Conferences*, page 01006, March 2017.

[87] The Pierre Auger Collaboration. The Pierre Auger Observatory Upgrade - Preliminary Design Report. *ArXiv e-prints*, April 2016.

[88] T. Abu-Zayyad, R. Aida, et al. The Cosmic-Ray Energy Spectrum Observed with the Surface Detector of the Telescope Array Experiment. *The Astrophysical Journal Letters*, 768:L1, May 2013.

[89] V. Verzi. The Energy Scale of the Pierre Auger Observatory. In *Proceedings, 33rd International Cosmic Ray Conference (ICRC2013): Rio de Janeiro, Brazil, July 2-9, 2013*, page 0928.

[90] T. Abu-Zayyad, R. Aida, et al. Energy Spectrum of Ultra-High Energy Cosmic Rays Observed with the Telescope Array Using a Hybrid Technique. *ArXiv e-prints*, May 2013.

[91] C. Jui. Summary of Results from the Telescope Array Experiment. *PoS*, ICRC2015:035, 2016.

[92] D. Ivanov. Report of the Telescope Array - Pierre Auger Observatory Working Group on Energy Spectrum. In *Proceedings, 35th International Cosmic Ray Conference (ICRC 2017): Bexco, Busan, Korea, July 12-20, 2017*, volume ICRC2017, 2017.

[93] A. Aab, P. Abreu, et al. Depth of maximum of air-shower profiles at the Pierre Auger Observatory. I. Measurements at energies above 1 $0^{17.8}$ eV. *Physical Review D*, 90(12):122005, December 2014.

[94] R. U. Abbasi, M. Abe, et al. Study of Ultra-High Energy Cosmic Ray composition using Telescope Array's Middle Drum detector and surface array in hybrid mode. *Astroparticle Physics*, 64:49–62, April 2015.

[95] J. Bellido. Depth of maximum of air-shower profiles at the Pierre Auger Observatory: Measurements above $10^{17.2}$ eV and Composition Implications. In *The Pierre Auger Observatory: Contributions to the 35th International Cosmic Ray Conference (ICRC 2017)*, pages 40–47, 2017.

[96] W. Hanlon, D. Ikeda, et al. Telescope Array Composition Summary. In *Proceedings, 35th International Cosmic Ray Conference (ICRC 2017): Bexco, Busan, Korea, July 12-20, 2017*, volume ICRC2017, 2017.

[97] E. Barcikowski, J. Bellido, et al. Mass composition working group report. In *European Physical Journal Web of Conferences*, volume 53 of *European Physical Journal Web of Conferences*, page 01006, June 2013.

[98] A. Abbasi, J. Bellido, and et al. for the Pierre Auger Collaboration and the Telescope Array Collaboration. *Report of the Working Group on the Composition of Ultra High Energy Cosmic Rays*. 2014.

[99] V. de Souza for the Pierre Auger Collaboration and the Telescope Array Collaboration. Testing the agreement between the Xmax distributions measured by the Pierre Auger and Telescope Array Observatories. In *Proceedings, 35th International Cosmic Ray Conference (ICRC 2017): Bexco, Busan, Korea, July 12-20, 2017*, volume ICRC2017, 2017.

[100] A. Aab, P. Abreu, et al. Searches for Anisotropies in the Arrival Directions of the Highest Energy Cosmic Rays Detected by the Pierre Auger Observatory. *The Astrophysical Journal*, 804:15, May 2015.

[101] The Pierre Auger Collaboration. Observation of a Large-scale Anisotropy in the Arrival Directions of Cosmic Rays above 8×10^{18} eV. *ArXiv e-prints*, September 2017.

[102] The Pierre Auger Collaboration. Search for first harmonic modulation in the right ascension distribution of cosmic rays detected at the Pierre Auger Observatory. *Astroparticle Physics*, 34:627–639, March 2011.

[103] The Pierre Auger Collaboration. Large-scale Distribution of Arrival Directions of Cosmic Rays Detected Above 10^{18} eV at the Pierre Auger Observatory. *Astrophys. J. Suppl.*, 203:34, December 2012.

[104] The Pierre Auger Collaboration. Large Scale Distribution of Ultra High Energy Cosmic Rays Detected at the Pierre Auger Observatory with Zenith Angles up to 80°. *Astrophys. J.*, 802:111, April 2015.

[105] P. Erdogdu, J. P. Huchra, et al. The dipole anisotropy of the 2 micron all-sky redshift survey. *Monthly Notices of the Royal Astronomical Society*, 368(4):1515–1526, 2006.

[106] A. Calvez, A. Kusenko, and S. Nagataki. Role of Galactic Sources and Magnetic Fields in Forming the Observed Energy-Dependent Composition of Ultrahigh-Energy Cosmic Rays. *Physical Review Letters*, 105(9):091101, August 2010.

[107] D. Eichler, N. Globus, et al. Ultrahigh Energy Cosmic Rays: A Galactic Origin? *The Astrophysical Journal*, 821:L24, April 2016.

[108] The Pierre Auger Collaboration. Indication of anisotropy in arrival directions of ultra-high-energy cosmic rays through comparison to the flux pattern of extragalactic gamma-ray sources. Submitted to Astrophysical Journal, Letters, 2017.

[109] M. Ackermann, M. Ajello, et al. 2FHL: The Second Catalog of Hard Fermi-LAT Sources. *The Astrophysical Journal Supplement Series*, 222:5, January 2016.

[110] R. U. Abbasi, M. Abe, and T. Abu-Zayyad. Indications of Intermediate-scale Anisotropy of Cosmic Rays with Energy Greater Than 57 EeV in the Northern Sky Measured with the Surface Detector of the Telescope Array Experiment. *Astrophysical Journal, Letters*, 790:L21, August 2014.

[111] The Pierre Auger Collaboration. Correlation of the highest-energy cosmic rays with the positions of nearby active galactic nuclei. *Astroparticle Physics*, 29:188–204, April 2008.

[112] N. Hayashida, K. Honda, et al. The Anisotropy of Cosmic Ray Arrival Direction around 10^{18}eV. *ArXiv Astrophysics e-prints*, June 1999.

[113] K. Kawata et al. Ultra-High-Energy Cosmic-Ray Hotspot Observed with the Telescope Array Surface Detectors. *Proceedings of Science*, ICRC2015:276, 2016.

[114] J. T. Brack, R. Cope, et al. Absolute calibration of a large-diameter light source. *Journal of Instrumentation*, 8:P05014, May 2013.

[115] C. Delle Fratte, G. Matthiae, et al. On the stability of the FD cameras. *GAP-2007-111*, 2007. Pierre Auger Collaboration internal technical note.

[116] J. Brack, R. Cope, et al. Auger Fluorescence Detector Absolute Calibration January and June 2010. *GAP-2010-118*, 2010. Pierre Auger Collaboration internal technical note.

[117] N. Grant, R. Clay, et al. Ageing Tests of Auger FD Photomultipliers. *GAP-2008-002*, 2008. Pierre Auger Collaboration internal technical note.

[118] R. Clay, B. Dawson, et al. Ageing and Other Gain Variations of Auger Fluorescence Detector Photomultipliers. *GAP-2009-026*, 2009. Pierre Auger Collaboration internal technical note.

[119] K. Daumiller, M. Del Rio, et al. Towards a continuous calibration A during FD data taking. *GAP-2016-009*, 2016. Pierre Auger Collaboration internal technical note.

[120] G. Salina. FD Calibrations: Some News. talk presented at Pierre Auger Collaboration Meeting, Malargüe, Argentina, November 2014.

[121] C. Delle Fratte et al. On the stability of the FD cameras - update #1. *GAP-2008-129*, 2008. Pierre Auger Collaboration internal technical note.

[122] M. Malacari. Improvements to aerosol attenuation measurements at the Pierre Auger Observatory. In *The Pierre Auger Observatory: Contributions to the 35th International Cosmic Ray Conference (ICRC 2017)*, pages 193–200, 2017.

[123] The Pierre Auger Collaboration. Atmospheric effects on extensive air showers observed with the surface detector of the Pierre Auger observatory. *Astroparticle Physics*, 32:89–99, September 2009.

[124] The Pierre Auger Collaboration. Impact of atmospheric effects on the energy reconstruction of air showers observed by the surface detectors of the Pierre Auger Observatory. *ArXiv e-prints*, February 2017.

[125] K Greisen. Progress in cosmic ray physics. *JG Wilson, Amsterdam, Netherlands*, 1956.

[126] I. Valino for the Pierre Auger Collaboration. The flux of ultra-high energy cosmic rays after ten years of operation of the Pierre Auger Observatory. In *34th International Cosmic Ray Conference (ICRC2015)*, volume 34 of *International Cosmic Ray Conference*, page 271, July 2015.

[127] The Pierre Auger Collaboration. The effect of the geomagnetic field on cosmic ray energy estimates and large scale anisotropy searches on data from the Pierre Auger Observatory. *Journal of Cosmology and Astroparticle Physics*, 11:022, November 2011.

[128] C.R. Benn and S.L. Ellison. Brightness of the night sky over La Palma. 42:503–507, November 1998.

[129] S. F. Sánchez, J. Aceituno, et al. The Night Sky at the Calar Alto Observatory. *Publications of the ASP*, 119:1186–1200, October 2007.

[130] R. Smida et al. Measured ADC variances on FD cameras. *GAP-2009-074*, 2009. Pierre Auger Collaboration internal technical note.

[131] R. Caruso and S. Petrera. Measurement of the sky photon background flux at Los Leones. *GAP-2004-072*, 2004. Pierre Auger Collaboration internal technical note.

[132] A. Segreto. Night sky background measurements by the Pierre Auger fluorescence detectors and comparison with simultaneous data from the UVscope instrument. In *Proceedings, 32nd International Cosmic Ray Conference (ICRC 2011): Beijing, China, August 11-18, 2011*, volume 3, page 129, 2011.

[133] M. Kleifges, A. Menshikov, et al. Statistical current monitor for the cosmic ray experiment pierre auger. *IEEE Transactions on Nuclear Science*, 50:1204–1207, August 2003.

[134] A. Menshikov, M. Kleifges, and H. Gemmeke. Fast gain calibration of photomultiplier and electronics. *IEEE Transactions on Nuclear Science*, 50:1208–1213, August 2003.

[135] A. Dorofeev, B. Gookin, et al. FD Absolute Calibration, April 2013. *GAP-2013-058*, 2013. Pierre Auger Collaboration internal technical note.

[136] P. Kervella, F. Thévenin, et al. The interferometric diameter and internal structure of Sirius A. 408:681–688, September 2003.

[137] J. R. Ducati. VizieR Online Data Catalog: Catalogue of Stellar Photometry in Johnson's 11-color system. *VizieR Online Data Catalog*, 2237, 2002.

[138] A. Young. Air mass and refraction. *Appl. Opt.*, 33(6):1108–1110, Feb 1994.

[139] Space Telescope Science Institute. CALSPEC Calibration Database. Available at `http://www.stsci.edu/hst/observatory/crds/calspec.html`, Accessed: October 2016.

[140] The Pierre Auger Collaboration. Spectral calibration of the fluorescence telescopes of the Pierre Auger Observatory. *Astroparticle Physics*, 95:44–56, October 2017.

[141] B Gookin. *Calibration of the Pierre Auger Observatory Fluorescence Detectors and the Effect on Measurements*. PhD thesis, Colorado State University, 2015.

[142] The Pierre Auger Collaboration. Description of atmospheric conditions at the Pierre Auger Observatory using the Global Data Assimilation System (GDAS). *Astroparticle Physics*, 35:591–607, April 2012.

[143] M. Hedge. Giovanni. Available at `https://giovanni.gsfc.nasa.gov/giovanni/`, Accessed: October 2016.

[144] J. Bäuml. Measurement of the optical properties of the auger fluorescence telescopes. *Proceedings of the 33rd ICRC*, pages 15–18, 2013.

[145] L. Tománková. *Optical Properties and Calibration of the Pierre Auger Fluorescence Detector*. PhD thesis, Karlsruhe Institute of Technology, 2016.

[146] L. Nozka, H. Hiklova, et al. Monitoring of the optical performance of primary mirrors at the Pierre Auger Observatory. Submitted to Journal of Instrumentation, 2017.

[147] Space Telescope Science Institute. Pickles atlas. Available at `http://www.stsci.edu/hst/observatory/crds/pickles_atlas.html`, Accessed: October 2016.

[148] A. J. Pickles. A Stellar Spectral Flux Library: 1150-25000 Å. 110:863–878, July 1998.

[149] J. Ely et al. STIS Instrument Handbook, 2011. Version 11.0, (Baltimore: STScI).

[150] K. Louedec and R. Losno. Atmospheric aerosols at the Pierre Auger Observatory and environmental implications. *European Physical Journal Plus*, 127:97, August 2012.

[151] G. Salina. FD Calibrations: Some News. talk presented at the Pierre Auger Observatory Collaboration Meeting, Malargüe, Argentina, March 2017.

[152] P. W. Merrill and C. G. Burwell. Supplement to the Mount Wilson Catalogue and Bibliography of Stars of Classes B and A whose Spectra have Bright Hydrogen Lines. *Astrophysical Journal*, 98:153, September 1943.

[153] R. O. Gray and R. F. Garrison. The early F-type stars - Refined classification, confrontation with Stromgren photometry, and the effects of rotation. *Astrophysical Journal, Supplement*, 69:301–321, February 1989.

[154] B. Dawson, C. Di Giulio, et al. Proposal for an update of the Auger Energy Scale. *GAP-2012-124*, 2012. Pierre Auger Collaboration internal technical note.

[155] D. Góra, R. Engel, et al. Universal lateral distribution of energy deposit in air showers and its application to shower reconstruction. *Astroparticle Physics*, 24(6):484 – 494, 2006.

[156] M. Giller and G. Wieczorek. Influence of the scattered Cherenkov light on the width of shower images as measured in the EAS fluorescence experiments. *Astroparticle Physics*, 31:212–219, April 2009.

[157] V. Verzi. *Measurement of the Energy Spectrum of Cosmic Rays with the Pierre Auger Observatory*. 2014.

[158] B. Gookin, J. Brack, et al. November Absolute Calibration, Addendum to GAP 2010-118. *GAP-2011-037*, 2011. Pierre Auger Collaboration internal technical note.

[159] J. Brack and M. Sutherland. Fluorescence Detector Absolute Calibration Database Update. *GAP-2012-095*, 2012. Pierre Auger Collaboration internal technical note.

[160] J. A. J. Matthews. Optical calibration of the Auger fluorescence telescopes. In P. W. Gorham, editor, *Particle Astrophysics Instrumentation.*, volume 4858 of *Proceedings of the SPIE*, pages 121–130, February 2003.

[161] A. C. Rovero, P. Bauleo, et al. Multi-wavelength calibration procedure for the pierre Auger Observatory Fluorescence Detectors. *Astroparticle Physics*, 31:305–311, May 2009.

[162] INFN Roma Group. Pierre Auger Observatory Calibration Production and Data Base. Available at `http://aa-calib.auger.org.ar/CalibrationDisplay/`, Accessed: November 2017.

[163] The Pierre Auger Collaboration. List of Cleanings. Available at `https://www.auger.unam.mx/AugerWiki/ListOfCleanings`, Accessed: December 2017.

[164] J. Debatin. Investigation of optical properties of the fluorescence telescopes of the Pierre Auger Observatory. Master's thesis, Karlsruhe Institute of Technology, 2015.

[165] J. Parrisius, R. Engel, et al. Comparison of telescope simulations with flasher data. talk presented at Pierre Auger Analysis Meeting, Lecce, Italy, June 2010.

Appendix A

Event Quality Cuts

Cuts used to determine which hybrid events are of suitable quality for the analysis presented in Section 5.5.

Quality Cuts on the SD reconstruction

- The SD station which recorded the strongest signal is surrounded by 6 working stations (6T5 trigger).
- The SD reconstruction successfully fits a lateral distribution function to the detected signal.
- The shower has a zenith angle less than 60°.
- The shower was not detected during a *bad period* - known time periods during which problems with the SD prevented the acquisition of reliable data.

Quality Cuts on the FD reconstruction

- The energy reconstructed by the FD is greater than 3 EeV.
- Atmospheric aerosol measurements exist for the time of the event.
- The vertical aerosol optical depth (VAOD) is greater than 0 and less than 0.1.
- Cuts to reject weak showers being mistakenly fit with a good Gaisser-Hillas function
  - The reduced χ^2 for the Gaisser-Hillas profile should be less than 2.5.
  - (χ^2 for a linear profile - χ^2 for the Gaisser-Hillas profile) > 4
- Less than 50% of the received light is from Cherenkov light.
- Relative uncertainty in the reconstructed FD energy is less than 0.2.
- Uncertainty in shower maximum less than $40\,\mathrm{g\,cm^{-2}}$.

Additional cuts are made on the reconstructed hybrid geometry.

Appendix B

Photon Flux Uncertainty

For simplicity we will assume that the photon flux uncertainty ($\Delta\Phi_\gamma$) is dominated by fluctuations in the photoelectron statistics. This can be written as

$$\Delta\Phi_\gamma^2 = \left(\frac{\partial\Phi_\gamma}{\partial n_{phe}}\right)^2 \times \Delta n_{phe}^2 \tag{B.1}$$

using Equation 6.5 this can be simplified to

$$\Delta\Phi_\gamma = \frac{\Delta n_{phe}}{Q \times f \times A \times \Delta t} \tag{B.2}$$

Photoelectron statistics are Poissonian in nature, allowing the uncertainty in n_{phe} to be expressed as (using Equation 6.4)

$$\Delta n_{phe} = \sqrt{n_{phe}} = \sqrt{\frac{\sigma_{phe}^2}{1+V_G}} \tag{B.3}$$

Finally, combining Equations 6.2, 6.3, B.2 and B.3 it can be shown that

$$\Delta\Phi_\gamma = \frac{C_{FD} \times \sqrt{\sigma_{ADC}^2}}{A \times \Delta t \times \sqrt{1+V_G}} \qquad [\text{photons}/\text{m}^2/\text{deg}^2/\mu\text{s}] \tag{B.4}$$

In reality, the uncertainty in the calculated photon flux has contributions from the Poisson fluctuations in the number of NSB photons arriving at the telescope aperture (N_{ph}), as well as fluctuations in the number of photoelectrons emitted from the photocathode (n_{phe}). The number of photons incident on the PMT face is given by

$$N_{ph,PMT} = N_{ph} \times \epsilon_{opt} \tag{B.5}$$

where ϵ_{opt} is the product of the respective efficiencies of the filter, mirror and corrector ring. By taking into account the fluctuations in the number of photons, Equation B.5 can be written as

$$N_{ph,PMT} = N_{ph}\epsilon_{opt} \pm \sqrt{N_{ph}\epsilon_{opt}} \tag{B.6}$$

The number of photoelectrons emitted at the photocathode of a given PMT is

$$n_{phe} = N_{ph,PMT} \times Q = N_{ph}\epsilon_{opt} \times Q \tag{B.7}$$

where Q is the quantum efficiency of the PMT. The uncertainty in n_{phe} is given by

$$\Delta n_{phe}^2 = \left(\frac{\partial n_{phe}}{\partial N_{ph}}\right)^2 \Delta N_{ph}^2 \tag{B.8}$$

Substituting in Equation B.6,

$$\Delta n_{phe}^2 = \epsilon_{opt}^2 Q^2 (N_{ph}\epsilon_{opt}) \tag{B.9}$$

and therefore,

$$\Delta n_{phe} = \epsilon_{opt} Q \sqrt{N_{ph}\epsilon_{OPT}} \tag{B.10}$$

Appendix C

Additional Figures

Presented here are additional figures for results discussed in Section 6.4. Overlapping night sky background ratio profiles for Los Leones, Los Morados and Loma Amarilla are shown in Figures C.1, C.2 and C.3, respectively.

Distributions of the $\sqrt{\text{Photon Flux Ratio}}$ for individual telescope pairs are also provided. A handful of these distributions appear to be bimodal (for the Identical Pixel method). The bimodal features are removed for the equivalent distribution using the K_v method.

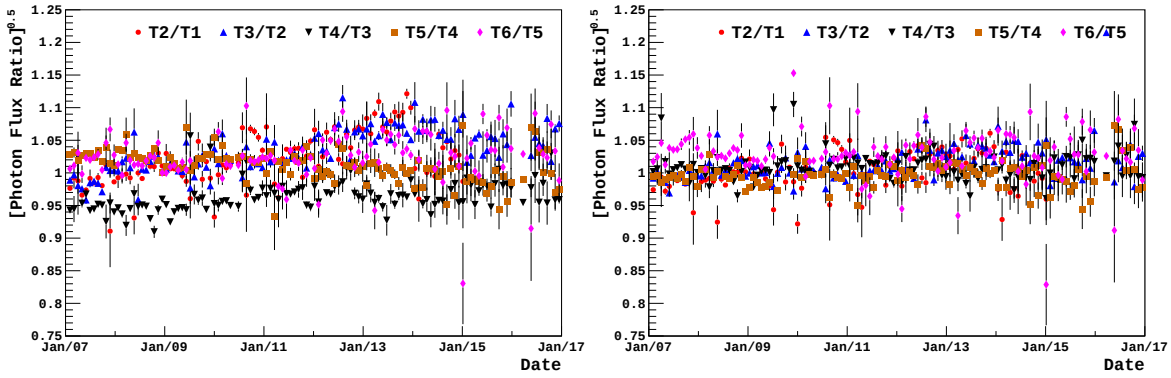

Figure C.1: Results for Los Leones using the Identical Pixel Method (Kv Method) are presented on the left (right).

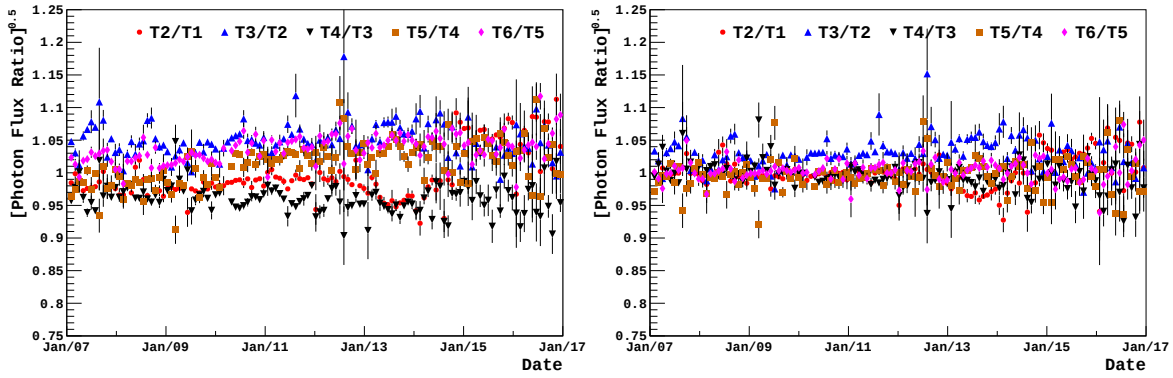

Figure C.2: Results for Los Morados using the Identical Pixel Method (Kv Method) are presented on the left (right).

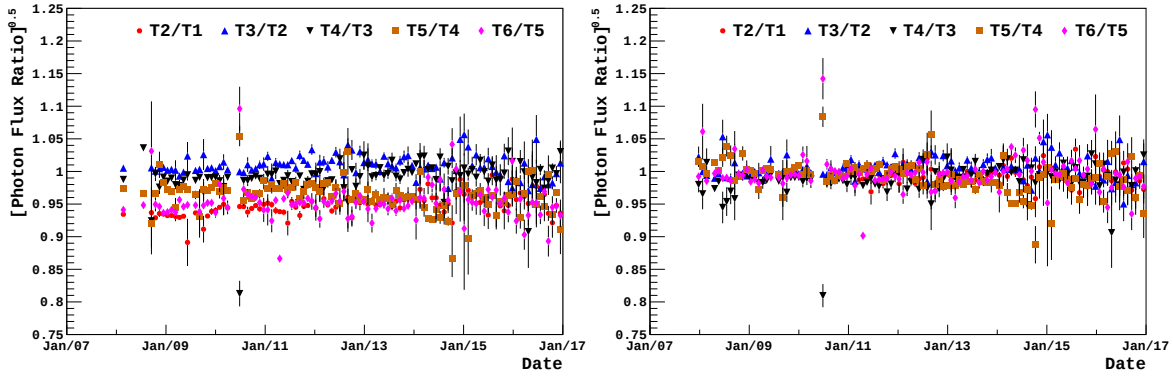

Figure C.3: Results for Loma Amarilla using the Identical Pixel Method (Kv Method) are presented on the left (right).

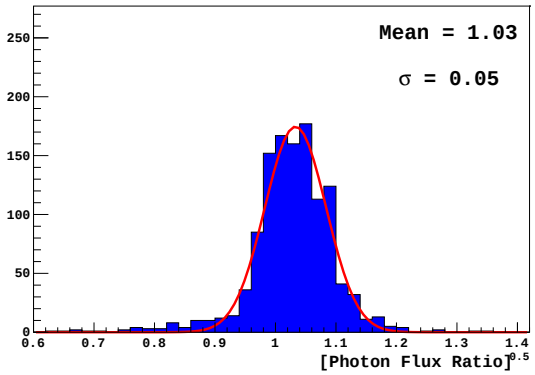

(a) T2/T1

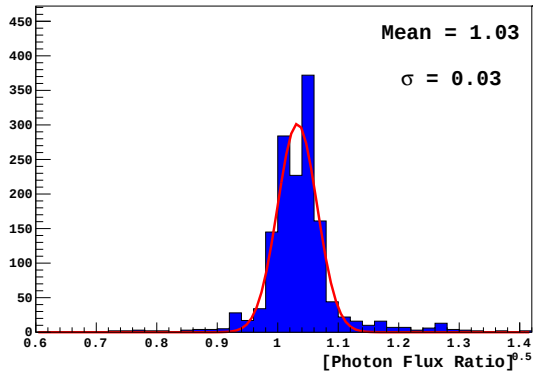

(b) T3/T2

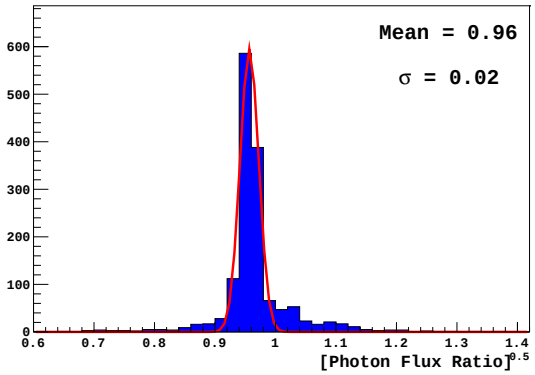

(c) T4/T3

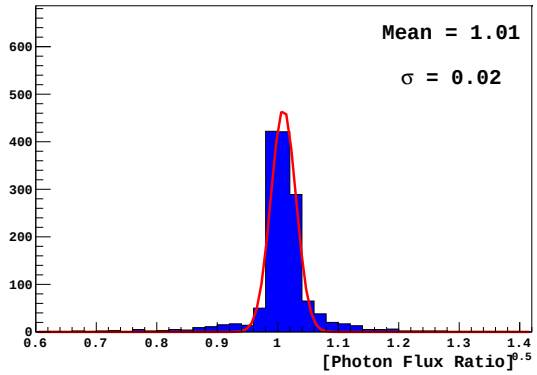

(d) T5/T4

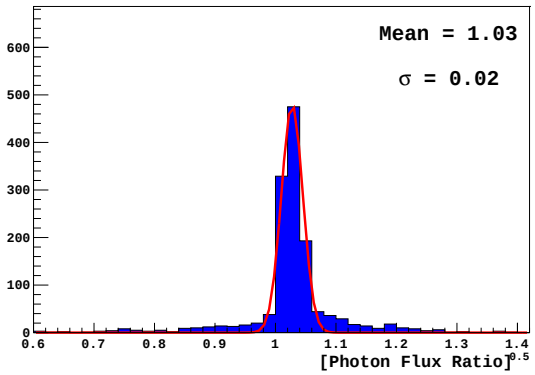

(e) T6/T5

Figure C.4: Los Leones distributions using the Identical Pixel method.

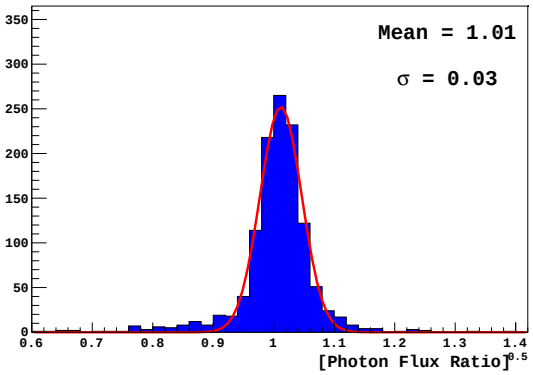

(a) T2/T1

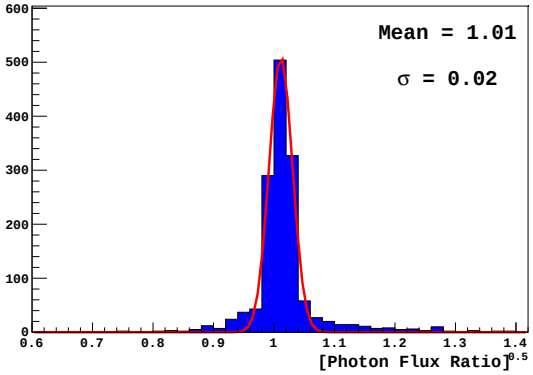

(b) T3/T2

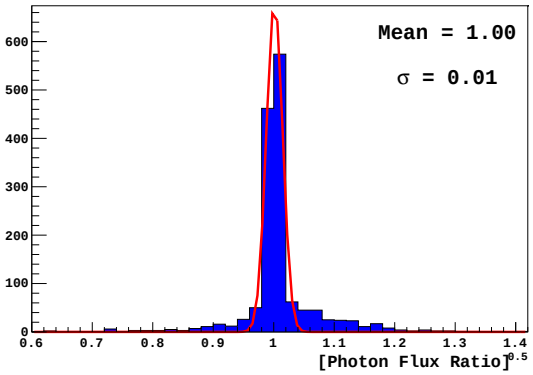

(c) T4/T3

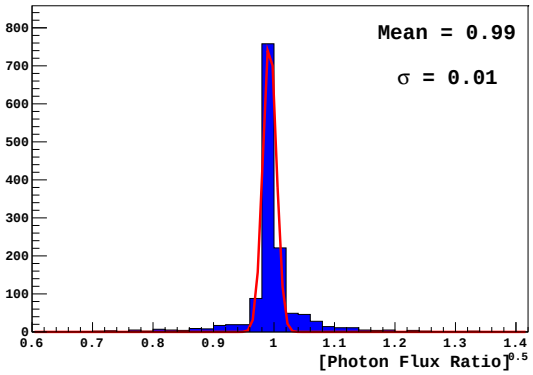

(d) T5/T4

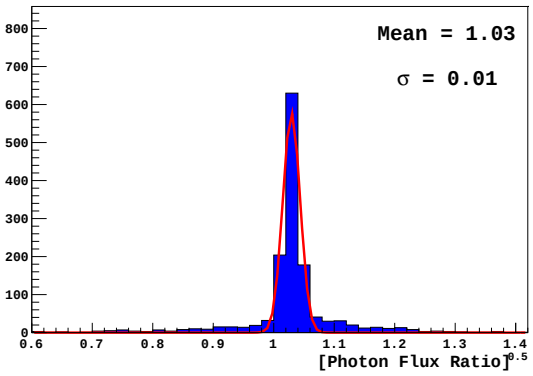

(e) T6/T5

Figure C.5: Los Leones distributions using the K_v method.

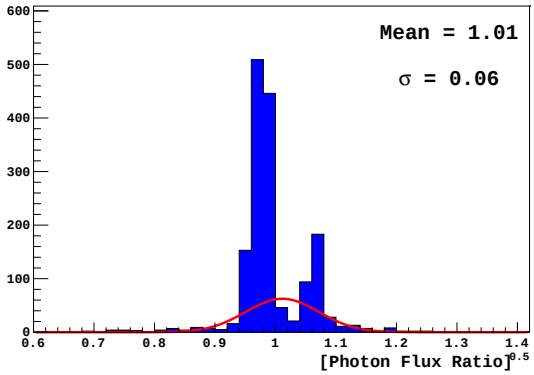

(a) T2/T1

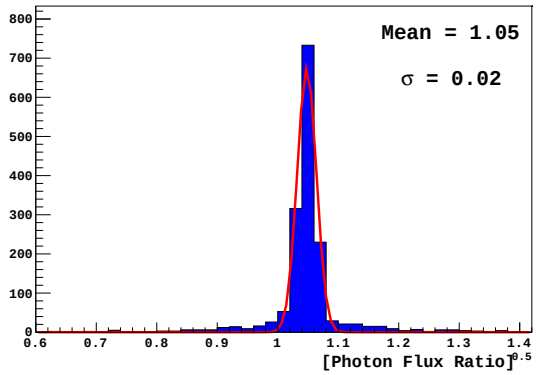

(b) T3/T2

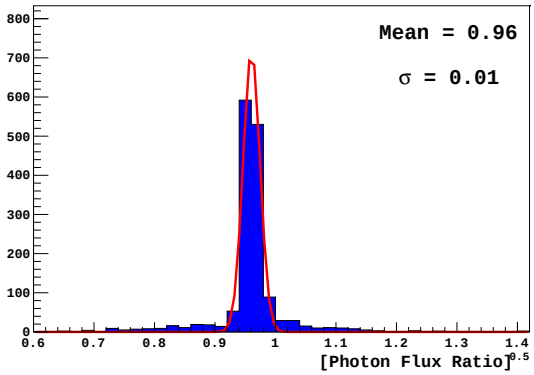

(c) T4/T3

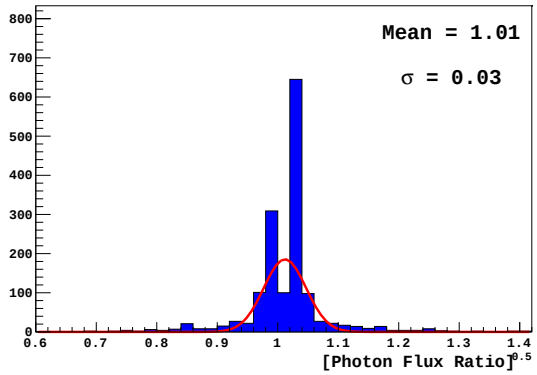

(d) T5/T4

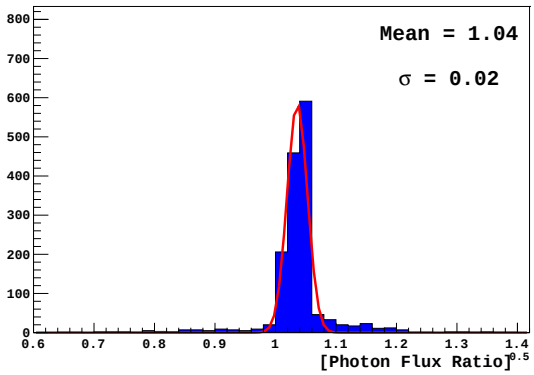

(e) T6/T5

Figure C.6: Los Morados distributions using the Identical Pixel method.

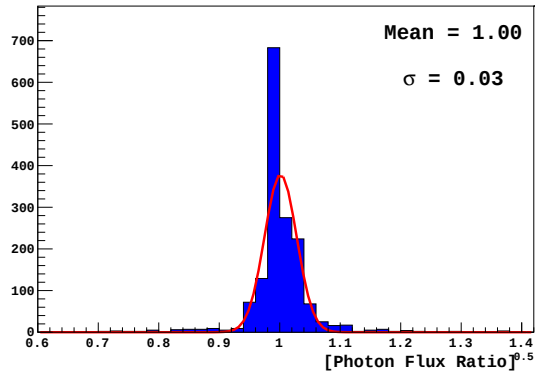

(a) T2/T1

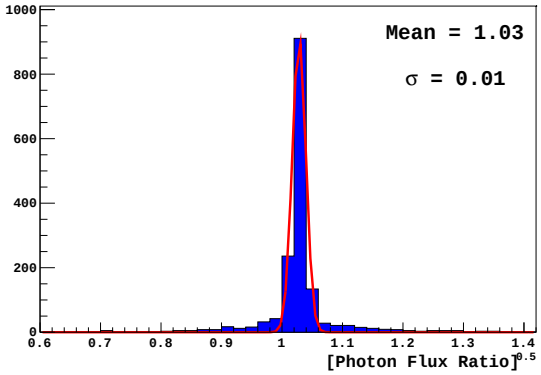

(b) T3/T2

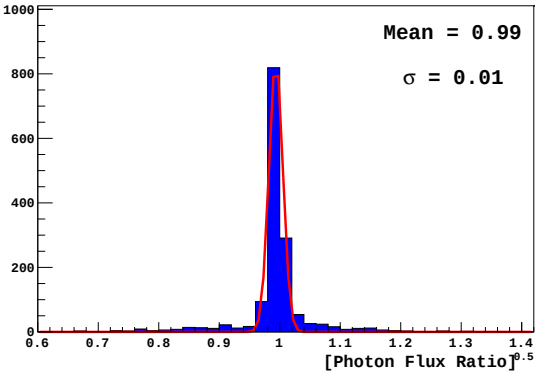

(c) T4/T3

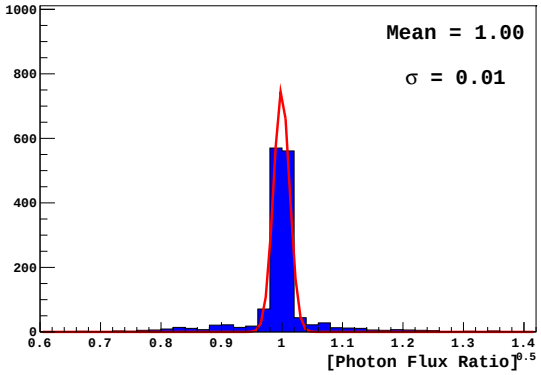

(d) T5/T4

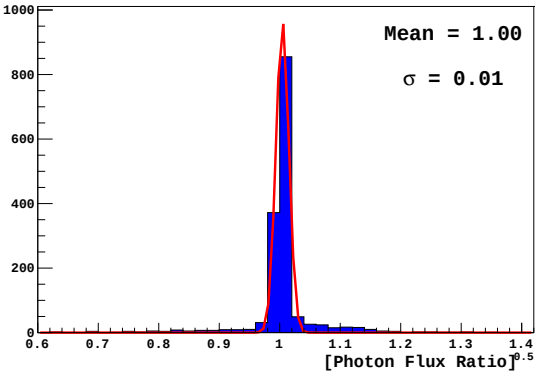

(e) T6/T5

Figure C.7: Los Morados distributions using the K_v method.

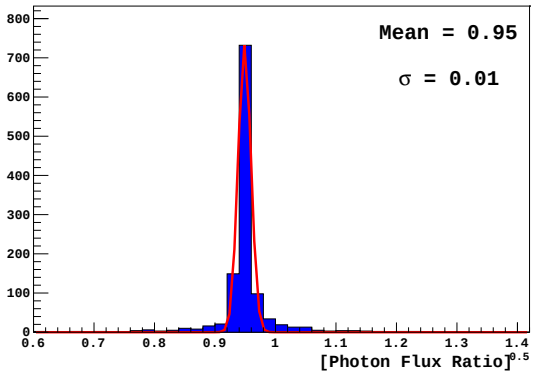

(a) T2/T1

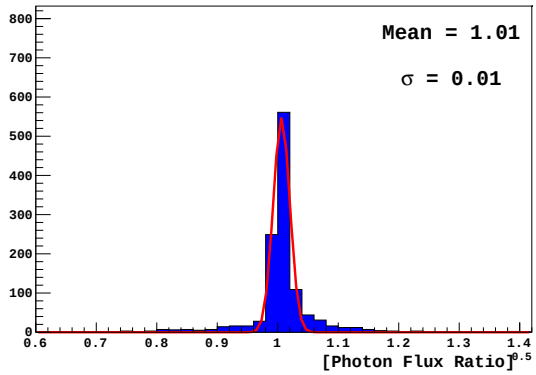

(b) T3/T2

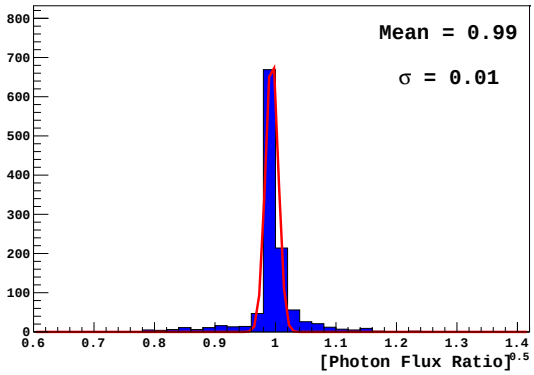

(c) T4/T3

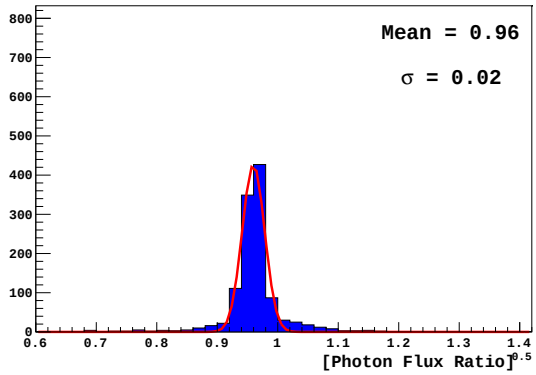

(d) T5/T4

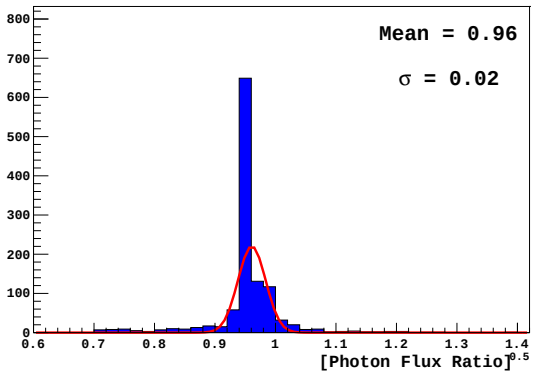

(e) T6/T5

Figure C.8: Loma Amarilla distributions using the Identical Pixel method.

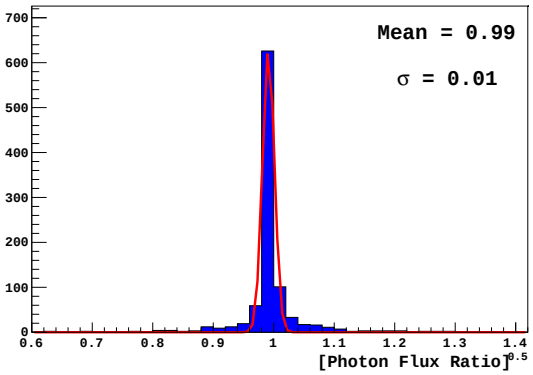

(a) T2/T1

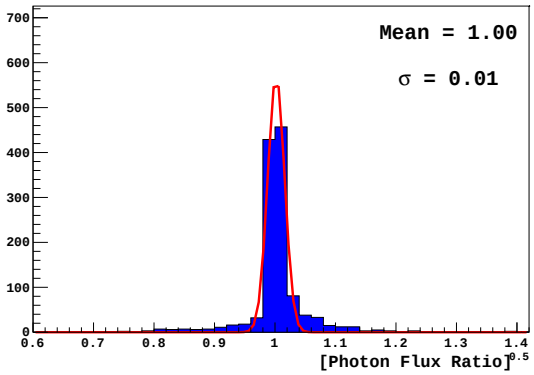

(b) T3/T2

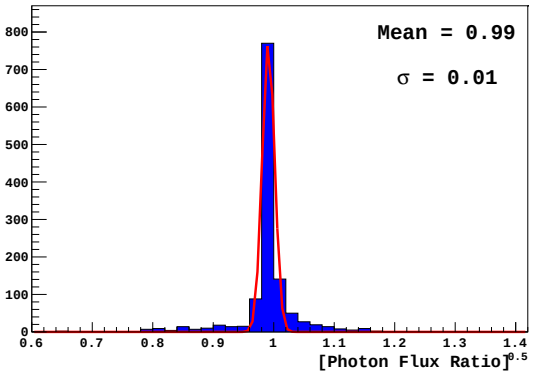

(c) T4/T3

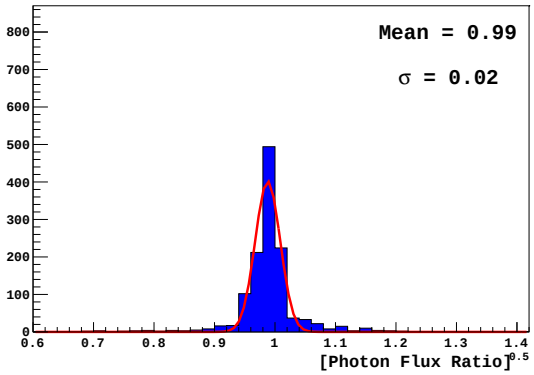

(d) T5/T4

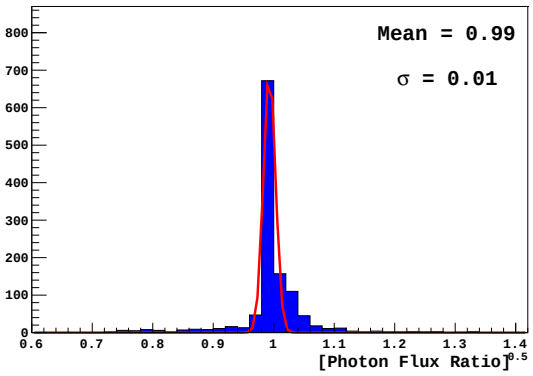

(e) T6/T5

Figure C.9: Loma Amarilla distributions using the K_v method.

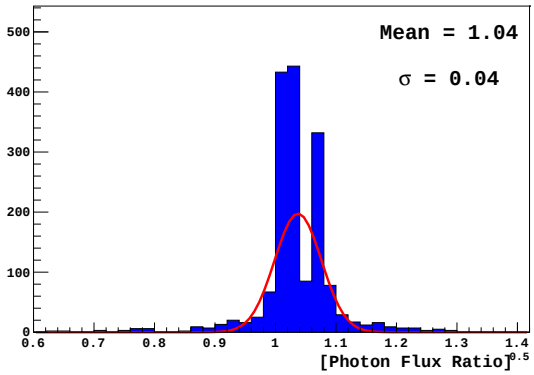

(a) T2/T1

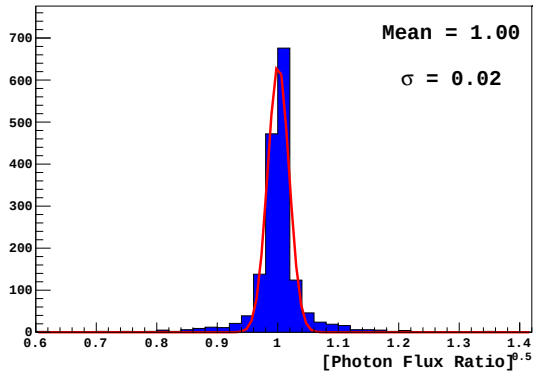

(b) T3/T2

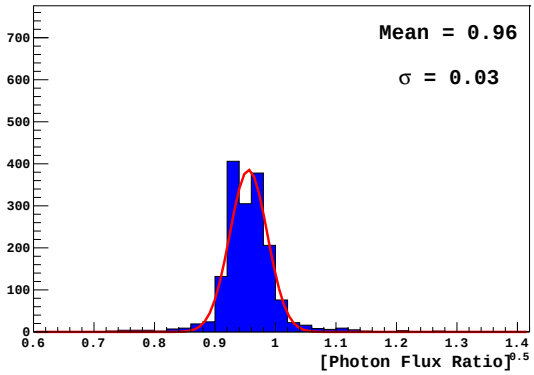

(c) T4/T3

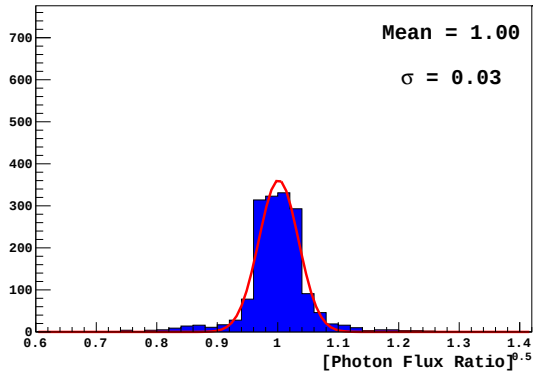

(d) T5/T4

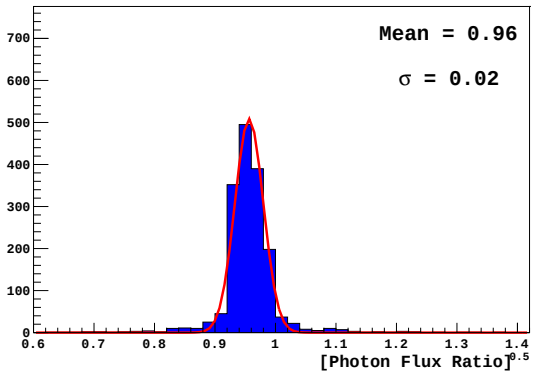

(e) T6/T5

Figure C.10: Coihueco distributions using the Identical Pixel method.

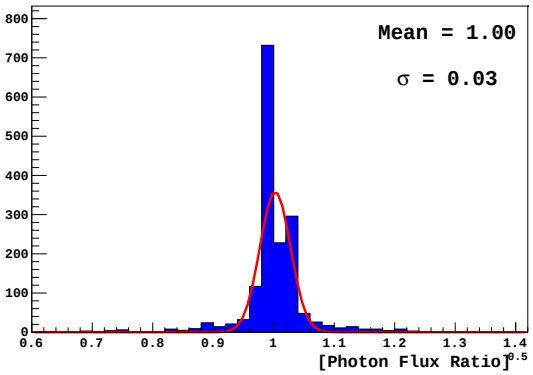

(a) T2/T1

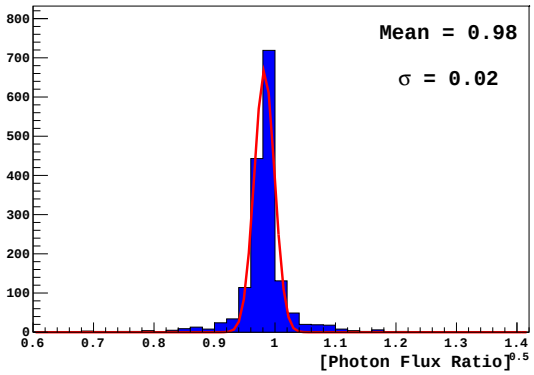

(b) T3/T2

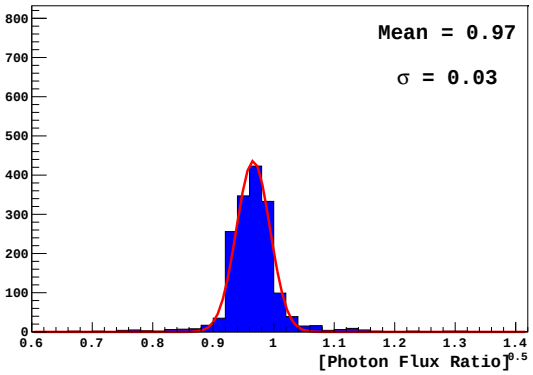

(c) T4/T3

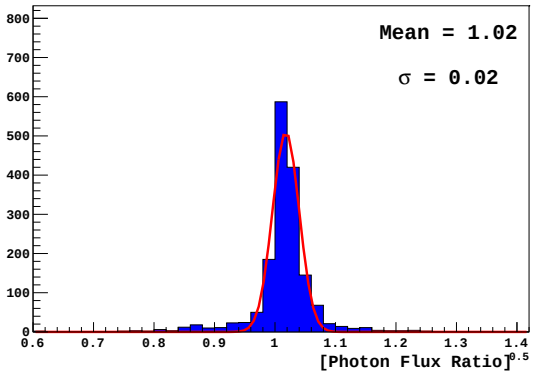

(d) T5/T4

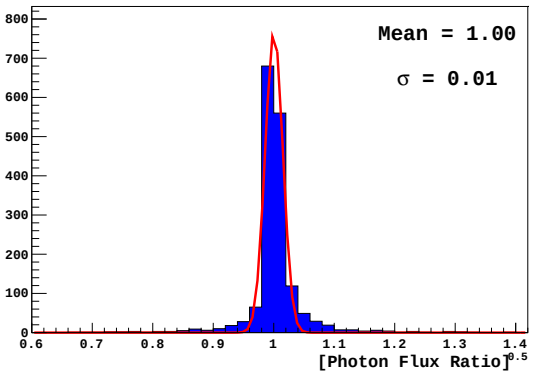

(e) T6/T5

Figure C.11: Coihueco distributions using the K_v method.

Appendix D

Broadening of the Optical Spot

The following is a discussion of the broadening of the optical spot (or point spread function, PSF) on the camera face. This broadening will be referred to as the halo and can be treated as the combination of two types:

- The broadening of the PSF caused by an optical aberration of some sort. It is suspected that the accumulation of dust on the surface of the FD mirrors can disrupt the specular reflection of incident photons. The result is a diffusive reflection which can act to spread the expected light from a source over a larger area of the camera. Call the halo originating from this effect *TypeA*.
- Photons incoming towards the camera may be reflected off the surface of the PMTs (the reflectivity has been measured in lab experiments and was found to be $\sim 20\%$ [144]). A fraction of these photons will make their way back to the mirror, only to be reflected back towards the camera. The returning light results in a broad (and flat) distribution across the camera. In this case, the camera will observe more light than expected for a light source as a fraction of photons will have a second opportunity to produce a photoelectron upon reaching a PMT. Call this halo type *TypeB*.

Figure 7.27 compares the differential light distributions obtained through real measurements and a simulation. The two distributions do not agree within the intermediate region between $\sim 2^\circ < \zeta < 15^\circ$. The halo within this region is most likely to be attributed to *TypeA*, and the discrepancy due to the fact that the simulation does not account for diffusive reflections off the mirror surface. Beyond this region (where *TypeB* is of most importance), in the extended tail of the halo, the measured and simulated distributions appear to agree with one another.

During an absolute (drum) FD calibration the entire camera is illuminated by the portable light source. The effect of the two halo types on the absolute calibration is as follows:

- *TypeA*: The broadening of the optical spot implies that (for a given pixel) the observed light is dimmer than what would be expected if the spot were fully contained within the pixel. This is (at least partially) compensated by the tails of the PSF of all other pixels of the camera, but the compensation will not be total due to light loss off the edges of the mirror.

  For example, consider an exercise where the measured differential light distribution (see Figure 7.27) is thrown onto the centre of each FD pixel on the camera (note that one should also include "phantom" pixels beyond the camera border). By totalling the light in each pixel, it becomes apparent that the light lost in a given pixel is only partially compensated by the PSF of the surrounding pixels i.e. the total signal within a pixel is not equal to unity. Further compensation is achieved with the addition of phantom pixels, although the exact number of additional pixels is not immediately obvious (phantom pixels should at least extend to those angles that would be captured by the mirror). The magnitude and importance of this effect is still to be determined.

  Overall the effect of the diffusive scattering will likely make the drum appear slightly dimmer than the expectation.

- *TypeB*: This effect has been previously studied [165] and a correction ranging between $\sim 2-4\%$ has been applied to the calibration constants [159] (this appears as the *Halo* term in the calibration constant equation, Equation 5.6, and has value ranging between $\sim 1.02-1.04$). The effect of this correction is an increase in the calibration constants, as the camera would see more photons than would be expected from the true calibrated brightness of the drum (there are no "second chance photons" in the lab calibration of the drum brightness).

Currently, calibration constants are explicitly corrected for the *TypeB* halo.

The effect of the two halos on shower energies is as follows:

- *TypeA*: It is assumed that the remaining halo (not corrected for with the *Halo* factor) is (partially) corrected with the lateral width correction. This correction attempts to account for the broadening of the PSF along with any inadequacies in the treatment of the intrinsic shower width. This may only be a partial correction as it is only measured out to $\zeta = 4^{\circ}$, given that it is an empirical correction made using read-out pixels around the shower track, and pixel information beyond this range is lacking.

  The remaining light beyond $\zeta = 4^{\circ}$ is ignored (discussed in further detail in [154]). Justification for this includes:

  - There is a lack of halo light beyond this region, although this is unlikely.

  - The light may be multiple scattered shower light which should not be counted - also thought to be unlikely.
  - The systematic error in the lateral width correction is half of the correction itself, so it will likely account for the missing light.
  - The light may be due to the *TypeB* halo and should not be counted.
  - The drum calibration may partially correct for the halo light. Since the *TypeA* halo is not corrected for during the drum calibration, the calibration constants may be slightly larger than what they should be. For a given ADC count a larger photon count will be returned, partially correcting for the missing light.

- *TypeB*: Should not be of any concern as the effect is only important at large values of ζ (far from the shower track), and the calibration constants are compensated appropriately (assuming that the simulations used to derive the $2-4\%$ *Halo* factor are correct).

When correcting for the effect of the broadening of the optical spot in the stellar photometry analysis, it makes sense to only integrate the differential light distribution up to $\zeta = 15^{\circ}$ (giving a one sided systematic correction of $\sim 7\%$). The contributions to the halo beyond this point are due to reflections off the surface of the PMTs, an effect which has already been compensated due to the *Halo* correction applied to the calibration constants.

Appendix E

Rescaling Library Spectra

The method used to rescale library spectra for stars without an easily accessible U-band spectrum is presented here. In the following example, a library spectrum for a star of spectral type B8I is rescaled for Rigel.

Figure E.1 illustrates the spectrum for an B8I star. It should be noted that spectra from [147] have fluxes calculated by normalising the original fluxes in the V-band to 0 magnitude in the *vegamag* system. In this system, Vega has a magnitude of zero in all bands.

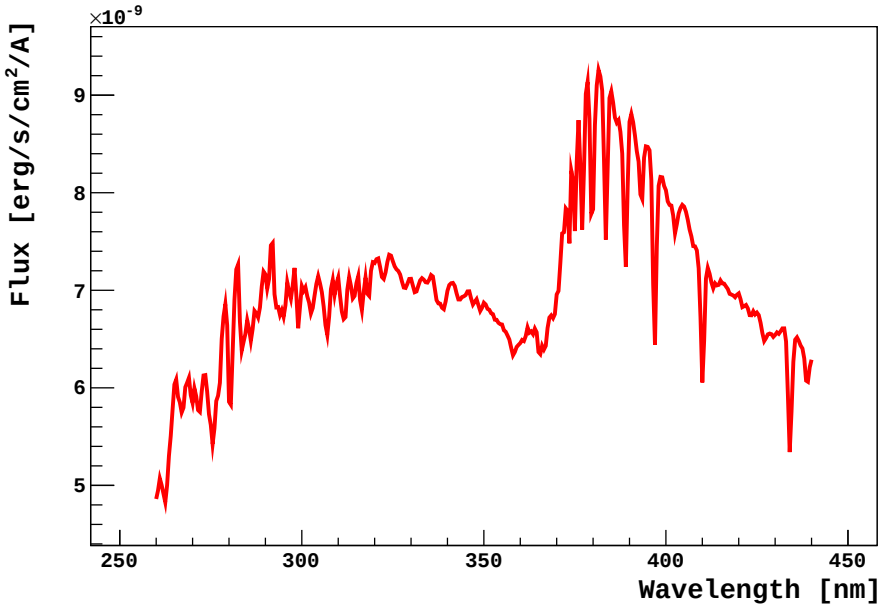

Figure E.1: The library spectrum for a star of spectral type B8I. Spectra available from [147] are in units of [ergs/s/cm^2/A].

The flux presented in Figure E.1 is first rescaled to have units equivalent to the relevant units (photons/m^2/μs/nm). The rescaled spectrum is shown in Figure E.2.

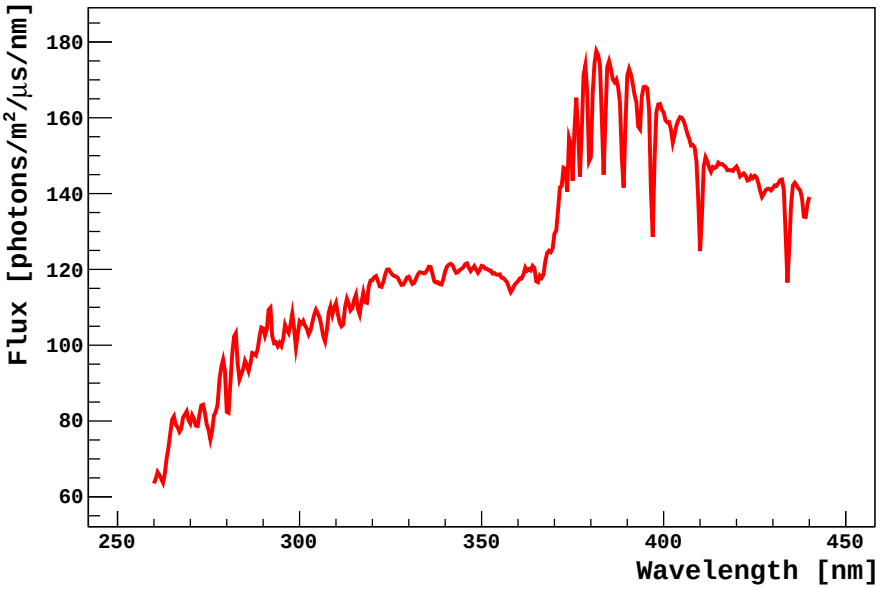

Figure E.2: The flux is rescaled to have units of photons/$m^2/\mu s/nm$.

The final step is to calculate a correction factor to scale the flux (now in the appropriate units) to the desired magnitude for the star of interest. As the library spectra are defined in terms of the *vegamag* system, it is the V-band magnitude of Sirius that is of importance here and not that of the U-band. The correction factor is calculated as follows:

Consider two stars, A and B, of magnitude m_A and m_B and intensity I_A and I_B, respectively. The difference in the magnitude of the two stars is given by

$$m_A - m_B = 2.5 \log\left(\frac{I_B}{I_A}\right) \tag{E.1}$$

which can be rearranged to give

$$\frac{I_B}{I_A} = 10^{\left(\frac{m_A - m_B}{2.5}\right)} \tag{E.2}$$

The ratio I_B/I_A is the ratio of the brightness between two spectra and provides the necessary correction factor. It should be noted that, by the definition of the *vegamag* system, the V-band magnitude for Vega is 0. For the case of Rigel (which has a V-band magnitude of 0.13) the correction factor is given by

$$Correction\ Factor = 10^{\left(\frac{-0.13}{2.5}\right)} \tag{E.3}$$

Applying this correction factor to the spectrum shown in Figure E.2 gives the rescaled library spectrum for a star of type B8I.